OCEAN MODEL VALIDATION AND DOWNSCALING FOR SUBSEASONAL-TO-SEASONAL PREDICTION

by

Christoph Renkl

Submitted in partial fulfillment of the requirements
for the degree of Doctor of Philosophy

at

Dalhousie University
Halifax, Nova Scotia
November 2020

To whom it may concern.

TABLE OF CONTENTS

LIST OF TABLES

LIST OF FIGURES

ABSTRACT

Subseasonal-to-seasonal (S2S) prediction is a global effort to forecast the state of the atmosphere and ocean with lead times between two weeks and a season. This thesis explores the feasibility of S2S prediction of the ocean using a variety of tools including statistical analysis, a statistical-dynamical mixed layer model, and regional, high-resolution ocean circulation models based on physical principles.

First, ocean predictability on S2S timescales is analyzed by compositing winter sea surface temperature (SST) anomalies in the North Atlantic with respect to the Madden-Julian Oscillation (MJO). It is found that statistically significant, large-scale SST changes, particularly along the eastern seaboard of North America, can be related to the MJO. This signal is shown to be driven by anomalous air-sea heat fluxes caused by atmospheric perturbations in response to the MJO.

Next, the suitability of a high-resolution model of the Gulf of Maine and Scotian Shelf (GoMSS) as a tool for S2S prediction is demonstrated through extensive validation with a focus on the mean state and low-frequency changes. The mean dynamic topography (MDT) predicted by GoMSS is shown to be in good agreement with novel observations of geodetically referenced sea levels from coastal tide gauges. It is shown that the alongshore tilt of MDT can be used to make inferences about coastal circulation, and also upwelling averaged over an adjacent offshore region. A new method is developed for evaluating model predictions of MDT in shallow, tidally dominated regions using observations of overtides and mean currents. This is useful in regions where no sufficiently long sea level records exist for application of the geodetic approach to estimating coastal MDT.

Finally, the validated GoMSS model is used to predict the mean ocean response to the MJO. The model is able to capture the observed relationship between the MJO and SST in the northwest Atlantic. It is also shown that the anomalous atmospheric circulation in response to the MJO leads to anomalous upwelling on the Scotian Shelf. Overall, this thesis demonstrates that it is feasible, and of value, to use regional ocean models for S2S prediction.

List of Abbreviations and Symbols Used

Abbreviation	Description
ADCP	Acoustic Doppler Current Profiler
BIO	Bedford Institute of Oceanography
B1, B2, B3	Runs of UBoF with interpolated GoMSS bathymetry
CD	Chart Datum of tide gauge
CFSR	Climate Forecast System Reanalysis
CFSv2	Climate Forecast System model version 2
CGG2013a	Canadian Gravimetric Geoid Model of 2013 - Version A
CHS	Canadian Hydrographic Service
COARE	Ocean-Atmosphere Response Experiment
CORE	Coordinated Ocean-Ice Reference Experiment
CTRL	Control Run of UBoF
DFO	Department of Fisheries and Oceans Canada
DJF	December, January, and February
ENSO	El-Niño Southern Oscillation
EOF	Empirical orthogonal function
ETOPO2v2	2-minute Gridded Global Relief Data
FES2004	Finite Element Solution global tide model
GEBCO	General Bathymetric Chart of the Oceans
GLORYS12v1	Global Ocean Physics Reanalysis
GoMSS	Gulf of Maine and Scotian Shelf regional model
GPS	Global Positioning System
GRS80	Geodetic Reference System 1980 ellipsoid
HTDP	Horizontal Time-Dependent Positioning tool
HYCOM	Hybrid Coordinate Ocean Model
ISCCP	International Satellite Cloud Climatology Project
ITRF2008	International Terrestrial Reference System realization of 2008
JEBAR	Joint effect of baroclinicity and relief

Abbreviation	Description
MEDS	Marine Environmental Data Section
MDT	Mean dynamic topography
MJO	Madden-Julian Oscillation
MLLW	Mean Lower Low Water
MSE	Mean squared error
MSL	Mean sea level
NABD	Northwest Atlantic Bathymetry Dataset
NAD83	North American Datum
NAO	North Atlantic Oscillation
NCEP	National Center for Environmental Prediction
NCODA	Navy Coupled Ocean Data Assimilation
NEMO	Nucleus for European Modelling of the Ocean
NGS	National Geodetic Service
NOAA	National Oceanic and Atmospheric Administration
NRCAN	Natuaral Ressources Canada
OA	Objective analysis
OAFlux	Objectively Analyzed Air-Sea Fluxes
OI	Optimal Interpolation
OISSTv2	Optimal Interpolation Sea Surface Temperature, version 2
OLR	Outgoing longwave radiation
OPUS	Online Positioning User Service
PNA	Pacific/North American Pattern
P0, P3, P7	Sensitivity runs of GoMSS depending on forcing on S2S timescales
RMM	Real-Time Multivariate MJO index
RMSE	Root mean squared error
“S” runs	Sensitivity runs of UBoF
SLP	Sea level pressure
SST	Sea surface temperature
S2S	Subseasonal-to-seasonal
UBoF	Barotropic ocean model for the upper Bay of Fundy
WMO	World Meteorological Organization

Symbol	Description	Units
$A_{\mathrm{h}}^{\mathrm{m}}$	Laplacian lateral eddy viscosity coefficient	$\mathrm{m\,s^{-2}}$
A_{RMM}	Amplitude of RMM index	
A'_k	Corrected complex amplitude of M_4 elevation	m
$\mathbf{B}$	Error covariance matrix of background	
$C = C_{\mathrm{c}} + C_{\mathrm{o}}$	Closed integration path	
c_{h}	turbulent exchange coefficients for latent heat	
c_{e}	turbulent exchange coefficients for sensible heat	
$c_{p,\mathrm{a}}$	Specific heat capacity of air at constant pressure	$\mathrm{J\,kg^{-1}\,K^{-1}}$
$c_{p,\mathrm{w}}$	Specific heat capacity of seawater at constant pressure	$\mathrm{J\,kg^{-1}\,K^{-1}}$
c_{d}	Bottom drag coefficient	
$\mathbf{D}$	Eddy mixing term of horizontal momentum	
$\overline{\mathbf{D}}_{\mathrm{l}}$	Depth-averaged lateral mixing term	
$\overline{F}$	Climatological model forcing	various
$\hat{F}$	Composites of model forcing conditioned on MJO	various
F'_{a}	High-frequency atmospheric model forcing	various
$\tilde{F}_{\mathrm{o}}$	Tidal forcing at lateral ocean boundaries	various
F_{n}	Tidal forcing at lateral ocean boundaries	various
f	Coriolis parameter	$\mathrm{rad\,s^{-1}}$
g	Acceleration due to Earth's gravity	$\mathrm{m\,s^{-2}}$
h	Total water depth	m
h_{e}	GPS ellipsoidal height	m
H	Water depth below geoid	m
H_{m}	Mixed layer Depth	m
$\mathbf{H}$	Linear observation operator	
$\mathcal{H}$	Forward observational operator	
$\hat{\boldsymbol{\imath}}, \hat{\boldsymbol{\jmath}}, \hat{\mathbf{k}}$	Unit vectors in zonal, meridional, and vertical direction	
L_{e}	Latent heat of evaporation	
N	Geoid height above reference ellipsoid	m
$\hat{\mathbf{n}}$	Unit vector perpendicular to the surface A	
o_t	Observed variable	various
p	Pressure	Pa

Symbol	Description	Units
p_{a}	Atmospheric pressure at sea level	Pa
Q_{l}	Latent air-sea heat flux	W m^{-2}
Q_{lw}	Outgoing long-wave radiation	W m^{-2}
Q_{net}	Net air-sea heat flux	W m^{-2}
Q_{s}	Sensible air-sea heat flux	W m^{-2}
Q_{sw}	Incoming short-wave radiation	W m^{-2}
q_{air}	Specific humidity of air at 2 m	
q_{s}	Saturation humidity at T	
R^2	Metric to assess fit of mixed layer model	
r	Fraction of Q_{sw} that reaches the base of mixed layer	
$\mathbf{R}$	Error covariance matrix of observations	
S	Salinity	
T	Sea surface temperature	°C
T_{c}	Sea surface temperature climatology	°C
T_{a}	Sea surface temperature anomaly	°C
$\overline{T}_{\mathrm{a}}$	SST composite with respect to MJO	°C
T_{air}	Air temperature at 2 m	°C
t	Time	s
u, v, w	Zonal, meridional, and vertical fluid velocity	m s^{-1}
$\mathbf{u}$	Two-dimensional, horizontal fluid velocity vector	m s^{-1}
$\mathbf{U}$	Volume transport vector	m^2 s^{-1}
$\mathbf{u}_{\mathrm{g,b}}$	Geostrophically balanced fluid velocity at $z = -H$	m s^{-1}
$\overline{\mathbf{u}}$	Depth-averaged fluid velocity vector	m s^{-1}
$\overline{\mathbf{u}}_{\mathrm{g}}$	Depth-averaged, geostrophic velocity vector	m s^{-1}
$\mathbf{u}^*$	Corrected depth-averaged fluid velocity vector	m s^{-1}
U, V	Zonal and meridional volume transport	m^2 s^{-1}
U_{wind}	Wind speed at 10 m	m s^{-1}
$\mathbf{v}$	Three-dimensional fluid velocity vector	m s^{-1}
W	Set of daily time indices for each winter	
$\mathbf{W}$	Weight matrix in OI procedure	
w_{E}	Ekman pumping velocity	m s^{-1}

Symbol	Description	Units
w^*	Upwelling velocity	$\mathrm{m\,s^{-1}}$
$\mathbf{x}$	Location vector	m
$\mathbf{x}_\mathrm{a}$, $\mathbf{x}_\mathrm{b}$	Analysis and background field in OI procedure	various
x, y, z	Spatial coordinates	m
y_t	Predicted variable	various
$\overline{y}_t$	Time-mean of predicted variable	various
β	β-plane coefficient	$\mathrm{m^{-1}\,s^{-1}}$
ΔL	Alongshore distance between two points	m
γ^2	Metric to evaluate model fit	
$\Delta\eta$	Large-scale MDT slope in the upper Bay of Fundy	cm
$\Delta\eta_\mathrm{c}$	Alongshore tilt of MDT at the coast	cm
$\Delta\eta_\mathrm{w}$	Wind setup of sea level along the coast	cm
$\Delta\tilde{\eta}_\mathrm{c}$	Wind-corrected alongshore tilt of MDT at the coast	cm
δ	Time lag after MJO phase	days
δ_O	Timescale of ocean response to atmospheric anomaly	days
δ_T	Atmospheric teleconnection timescale	days
ϵ	Normalized density perturbation of seawater	
ζ	Relative vorticity	$\mathrm{s^{-1}}$
η	Sea surface height above geoid, MDT	m
η_BF	MDT contribution by bottom friction	m
η_BM	Mean sea level relative to GPS benchmark	m
η_IB	Inverse barometer correction of sea level	cm
η_LM	MDT contribution by lateral mixing	m
η_s	Steric height	m
η_W	MDT contribution by wind stress	m
λ	Damping rate in mixed layer model	$\mathrm{s^{-1}}$
λ	Linear bottom friction coefficient	$\mathrm{m\,s^{-1}}$
ν	Kinematic viscosity	$\mathrm{m^2\,s^{-1}}$
ξ	Area-averaged upwelling rate	$\mathrm{s^{-1}}$
ρ	Density of seawater	$\mathrm{kg\,m^{-3}}$
ρ_a	Density of air	$\mathrm{kg\,m^{-3}}$

Symbol	Description	Units
ρ_0	Constant reference density of seawater	$\mathrm{kg\,m^{-3}}$
ρ'	Density Perturbation of seawater	$\mathrm{kg\,m^{-3}}$
σ	In-situ density	$\mathrm{kg\,m^{-3}}$
$\boldsymbol{\tau}^{\mathrm{b}}$	Kinematic bottom stress vector	$\mathrm{m^2\,s^{-2}}$
$\boldsymbol{\tau}^{\mathrm{w}}$	Kinematic wind stress vector	$\mathrm{m^2\,s^{-2}}$
Φ_{RMM}	Integer phase of RMM index	
ϕ	Latitude	$^\circ$
ϕ_{RMM}	Phase angle of RMM index	rad
χ	Vertically integrated potential energy anomaly	$\mathrm{m^3\,s^{-2}}$
ψ	Stream function of volume transport	$\mathrm{m\,s^{-1}}$
Ω	Angular velocity of the Earth	$\mathrm{rad\,s^{-1}}$
$\boldsymbol{\Omega}$	Earth's rotation vector	$\mathrm{rad\,s^{-1}}$
ω	Frequency	$\mathrm{rad\,s^{-1}}$

ACKNOWLEDGEMENTS

This thesis marks the end of a outstanding, challenging, and inspiring endeavour. I would not have been able to get to this point without the contributions from many individuals and I want to take the opportunity to thank them.

First and foremost, I would like to thank my advisor Keith Thompson for his continued support, encouragement, and patience throughout the years. I am immensely grateful for his guidance, openness to new ideas, and endless optimism that *"this has to work"*. I would like to extend my sincere thanks to the members of my advisory committee, Katja Fennel, David Barclay, Youyu Lu, and Eric Oliver, for many constructive discussions and their helpful advice along the way.

Many thanks to the faculty and staff of the Department of Oceanography. In particular, I would like to thank Daniel Morrison and Balagopal Pillai for their technical support that kept the computer clusters and servers up and running. Special thanks also to Lori Lawton and Jackie Hurst, who have gone above and beyond to remove any bureaucratic hurdles in my way.

I gratefully acknowledge the assistance of David Greenberg, Shannon Nudds, Phillip MacAulay, and Yongsheng Wu in obtaining observation data that have been very valuable to my thesis work. I also very much appreciate the many insightful suggestions and comments from Hai Lin that have helped me to shape this research. Furthermore, thank you to Anna Katavouta, Fatemeh Chegini, and Shiliang Shan for helping me get up to speed with the NEMO model. I would also like to recognize the effort of the countless people who spend their (spare) time to develop and maintain the open-source Python packages that have been used extensively for the data analysis in this thesis.

The funding for my research and studies was provided by Dalhousie University, the Natural Sciences and Engineering Research Council (NSERC), the Nova Scotia Graduate Scholarship program, and the Marine Environmental Observation Prediction and Response Network (MEOPAR).

I consider myself extremely lucky that, during all these years, I was surrounded by many supportive and inspiring colleagues and fellow graduate students, many of whom have become good friends. Thank you to Hansen Johnson, Nadine Lehmann, Krysten

Rutherford, Lorenza Raimondi, Colleen Wilson, Myriam Lacharité, and Jonathan Izett for many stimulating discussions and all the moments we have shared.

This whole endeavour would not have been possible without the unwavering support of my family near and far, for which I am tremendously grateful. In particular, I would like to thank my partner Mays for her encouragement, patience, and for being a rock I can hold on to whenever the current is getting too strong.

CHAPTER 1

INTRODUCTION

Subseasonal-to-seasonal (S2S) prediction refers to forecasting the state of the atmosphere and ocean on intraseasonal timescales with lead times between two weeks and a season *Vitart and Robertson* (2019). These predictions can provide valuable, early information for decision makers to ensure public safety, energy security, and protection of marine infrastructure (e.g., *White et al.*, 2017). Over the last decade, S2S prediction has become a research priority of the climate community with particular emphasis on meteorological high-impact events. This thesis explores the feasibility of S2S predictions of the ocean using a variety of approaches ranging from simple, statistically based models to regional, high-resolution ocean circulation models based on physical principles.

1.1 S2S Prediction and Predictability

Efforts to predict weather and climate date back to early civilizations. Around 340 BC, the philosopher Aristotle wrote his *Meteorologica* in which he summarized the contemporaneous meteorological knowledge (*Frisinger*, 1972). Around the same time, the astronomer and explorer Pytheas made the observation that tides in the ocean are controlled by the Moon (*Ekman*, 1993). However, it took millennia to develop the theories that form our current understanding of the climate system.

The governing equations describing the motion of fluids, often referred to as the Navier-Stokes equations, were derived during the 19th century (*Navier*, 1821, 1827; *Stokes*, 1848). At the beginning of the 20th century, *Bjerknes* (1904) recognized that this set of equations could be solved as an initial-value problem to predict the weather for short periods of time.

Richardson (1922, pp. 181) made an attempt to forecast the pressure over Europe by

discretizing and solving the governing equations by hand. Although his effort failed, this proved to be the foundation of numerical weather prediction.

With the advent of the first electronic computers during the late 1940s, numerical weather prediction became feasible and *Charney et al.* (1950) presented the first successful forecast based on the barotropic vorticity equation and observed data. Numerical weather prediction soon became routine and the underlying models have been improved continuously (e.g., *Bauer et al.*, 2015).

Interestingly, theories of the wind-driven ocean circulation were also developed in the 1940s and used to explain, for the first time, the origin of western boundary currents (e.g., *Sverdrup*, 1947; *Stommel*, 1948; *Munk*, 1950). Besides regional numerical models for tides and storm surges (e.g., *Hansen*, 1956; *Heaps and Proudman*, 1969), the first global ocean circulation models were developed by *Bryan and Cox* (1967) and *Bryan* (1969) as part of a coupled climate model. This not only demonstrates that oceanography is a young science, but also that the ocean modelling community has long benefited from advances in numerical weather prediction.

Spatial scales in the ocean are generally smaller compared to the atmosphere and this increases the computational demand placed on the development of numerical ocean models (*Semtner*, 1995). Increasing computing capacity, constant model improvement, and the availability of more observations have all led to better predictions of both the atmosphere and ocean. Global ocean circulation models are now generally able to resolve mesoscale eddies and can be coupled usefully with models for sea ice and biology.

Based on the fundamental work of *Lorenz* (1963), it became apparent in the 1960s that there are limits as to how far in advance weather can be predicted. Using a set of three coupled, ordinary differential equations representing a simplified model for atmospheric convection, he showed that small perturbations in the initial conditions can grow over time and result in large discrepancies in the predicted state. Later, *Lorenz* (1965) applied this idea to a low-order model representing the atmosphere and estimated the predictability limit for weather forecasts to be two weeks.

Generally, predictability refers to the theoretical, model-independent potential to predict a phenomenon (*Kantz et al.*, 2006). In comparison to the atmosphere, the characteristic timescales and thus the predictability limit of the ocean are generally longer. However, it is important to recognize that the upper bounds of predictability based on initial conditions

strongly depend on the process of interest. Mesoscale eddies, the oceanic equivalent to synoptic weather systems in the atmosphere, are predictable multiple weeks and up to a month in advance (*Pinardi et al.*, 2017, and references therein). Since the extratropical surface ocean is predominantly forced by the atmosphere (*Peña et al.*, 2003), the predictability limit of resulting anomalies is shorter (*Bach et al.*, 2019). On the other hand, given sufficient observations, ocean tides can be predicted indefinitely due to their well defined periodicities. The assessment of predictability, and an understanding of its physical origins are an essential and ongoing research effort.

On seasonal to decadal timescales, initial conditions become less important and predictability is determined by slowly varying processes resulting from anomalies in the large-scale state of the climate system (e.g., *Yuan et al.*, 2018; *Merryfield et al.*, 2020). While it is not possible to predict the daily weather over such long lead times, a statement can be made about the average state of the climate system over a season or decade, given the large-scale boundary conditions. Hence, it is possible to perform future climate projections which primarily depend on forcing scenarios for the development of greenhouse gas concentrations. This is sometimes referred to as "predictability of the second kind" as opposed to "predictability of the first kind" which describes the sensitivity to initial conditions (*Lorenz*, 1975).

Based on the different kinds of predictability, two timescales can be defined to describe the difference between weather and climate. Accordingly, weather describes short-term fluctuations of the atmosphere-ocean system, while climate refers to average conditions over a period of time. This is also captured by the quote *"Climate is what on average we may expect, weather is what we actually get"* (*Herbertson*, 1901, p. 118). Consequently, weather forecasting refers to the prediction of atmospheric and oceanic variations on timescales up to two weeks, whereas seasonal outlooks or climate projections aim to predict the conditions averaged over a season or longer (e.g., *Vitart and Robertson*, 2019).

The gap between these timescales is filled by subseasonal-to-seasonal (S2S) time range. With lead times ranging from 2 weeks up to a season (e.g., *Vitart and Robertson*, 2019), the S2S timescale covers the lead time of extended-range and the first part of long-range forecasts as defined by the *World Meteorological Organization* (WMO, 2018, p. 5).

S2S prediction has become an important focus of recent research efforts by the climate community with the first subseasonal forecasts dating back to the early 1980s (*Miyakoda*

et al., 1983, 1986). The challenge for such extended-range predictions is that they depend on both the initial conditions as well as as external forcing by slowly varying processes which can be considered constant on shorter timescales (*Von Neumann*, 1960; *White et al.*, 2017; *Mariotti et al.*, 2018).

Significant advances in S2S prediction have been made by the atmospheric community, but the ocean has received relatively little attention (*Merryfield et al.*, 2020). Ongoing research efforts are focusing not only on model improvement and validation, but also the identification of sources of predictability which will enable predictions on longer timescales, beyond the two-week limit postulated by *Lorenz* (1965). The sources of such atmospheric predictability are typically associated with slowly evolving atmosphere, ocean, and land processes.

While it is recognized that the ocean directly influences the atmospheric predictability on S2S timescales, less is known about the predictability of the ocean on such timescales (e.g., *DeMott et al.*, 2015; *Saravanan and Chang*, 2019; *Merryfield et al.*, 2020, and references therein). This is in part related to the lack of sufficient observations of the subsurface ocean which are needed to fully understand the processes at play (*Subramanian et al.*, 2019).

1.2 Interaction Across Scales

The atmosphere-ocean system is characterized by modes of variability that vary on timescales of order seconds to centuries and space scales from meters to global (*Stommel*, 1963; *Hoskins*, 2013). In general, low-frequency variability acts as a background state around which variations on shorter timescales occur.

Persistent and recurring spatial patterns of atmospheric variability that link weather and climate anomalies around the globe, either directly or indirectly, are referred to as teleconnections (*Feldstein and Franzke*, 2017). The global interaction of these patterns can enhance or suppress processes on smaller scales and vice versa. This can result in anomalous conditions and ultimately lead to extreme events (e.g., *Lin et al.*, 2009; *Marshall and Hendon*, 2014; *Lee et al.*, 2019). Furthermore, interactions across scales can create temporal "windows of opportunity" of enhanced predictability during which time more accurate predictions can be made.

Empirical modes of climate variability have also been defined for limited regions, e.g., the North Atlantic Oscillation (NAO) describes the meridional dipole of sea level pressure

in the Atlantic and European sector (*Wallace and Gutzler*, 1981). The NAO is the dominant pattern of atmospheric variability in the northern hemisphere and varies on intraseasonal to multidecadal timescales (e.g., *Woollings et al.*, 2015). The associated circulation anomalies in the atmosphere can lead to basin-wide changes in the surface ocean (*Visbeck et al.*, 2003), and also the hydrography on continental shelves (e.g., *Petrie*, 2007).

Further examples of climate modes of variability include, with increasing period, the Indian Ocean Dipole ($\sim$2 years, *Saji et al.*, 1999), the El-Niño Southern Oscillation (2–8 years, e.g., *Clarke*, 2008), the Pacific Decadal Oscillation (12–25 years, *Mantua and Hare*, 2002), and the Atlantic Multidecadal Oscillation (60–80 years, *Schlesinger et al.*, 2000). All of these modes describe large-scale patterns of sea surface temperature (SST) which are intrinsically linked to robust anomalies in the atmosphere. This illustrates the importance of treating the ocean and atmosphere as one coupled system, especially beyond weather timescales.

Due to their low frequency, teleconnections provide a source of predictability for extended- and long-range forecasts. A particularly important example for S2S prediction is the Madden-Julian Oscillation (MJO, *Madden and Julian*, 1971, 1972). This is the dominant driver of intraseasonal climate variability in the tropics and it has been shown that teleconnections exist with modes of variability at higher latitudes (*Zhang*, 2013; *Stan et al.*, 2018; *Lin et al.*, 2019). The MJO is a large-scale convective dipole anomaly in the atmosphere propagating eastward along the equator with a period of 40–60 days (*Woolnough*, 2019). Significant advances have been made recently in understanding the predictability of the MJO (e.g., *Vitart*, 2014). Estimated timescales of MJO predictability based on statistical and dynamical models range from 2–3 weeks (*Waliser*, 2005) up to 45 days (*Neena et al.*, 2014). Generally, these timescales for the MJO are longer than the predictability limit of most weather phenomena (1–2 weeks) and can therefore provide a potential source of predictability on S2S timescales.

The anomalous large-scale, deep atmospheric convection and resulting divergent outflow aloft associated with the MJO induce a Rossby wave train which alters the circulation in the atmosphere at higher latitudes. Due to the propagating nature of the MJO, the extratropical response is generally a result of constructive and destructive interference and, as a result, teleconnections can vary with the phase of the MJO (*Stan et al.*, 2018).

Robust statistical relationships between the MJO and atmospheric circulation patterns

in the northern hemisphere (e.g., NAO and winter blocking) have been identified (e.g., *Cassou*, 2008; *Lin et al.*, 2009; *Henderson et al.*, 2016). Additionally, variability in the stratosphere, which is the atmospheric layer between 10 and 50 km height, can influence the circulation in the troposphere below (e.g., *Kidston et al.*, 2015; *Butler et al.*, 2019; *Klotzbach et al.*, 2019). Resulting changes in the atmospheric circulation can have an influence on the ocean. For example, an anomalous position of the atmospheric jet stream can alter the air-sea heat flux leading to extreme ocean temperature anomalies (*Chen et al.*, 2014). Concurrent shifts in the position of the Gulf Stream (*Gawarkiewicz et al.*, 2012) can create persistent anomalous initial conditions which can serve as an additional source of predictability (*Chen et al.*, 2016).

Tidal oscillations in the atmosphere are generally small (on the order equivalent to 1 cm changes in sea level) and primarily induced by the thermal effect of solar radiation (*Cartwright*, 1977). By way of contrast, in the ocean, tides are a dominant driver of high-frequency variability. Their spatial scales can reach up to 1000 km, but tidal variations also play a dominant role on much smaller scales, in particular where they interact with bottom topography or the coastline. Resonant modes of oscillation can significantly amplify tides in regions like the Gulf of Maine and Bay of Fundy system where the period of the dominant tidal mode is close to the period of the semi-diurnal lunar tidal constituent M_2 resulting in an extreme tidal range (*Garrett*, 1972).

Through processes like tidal rectification, vertical mixing, and horizontal advection, tides can have a direct influence on the long-term mean of the local hydrography and circulation (*Katavouta et al.*, 2016). In shallow, tidally dominated regions, nonlinear interactions between the tidal flow and bottom topography create overtides at higher frequencies which covary with the mean, tidal residual circulation. In this case, the high-frequency overtides can act as a proxy for the mean circulation.

Due to interactions with sea floor topography, seasonal changes in stratification can also alter tidal elevation and the vertical structure of currents (*Katavouta and Thompson*, 2016). This is an example of nonlinear interaction between tidal and seasonal timescales which can be important for S2S predictions of the ocean. There are also implications for space scales: the generation and propagation of internal tides require an accurate representation of local bathymetric features like banks and channels on scales of kilometers.

Tidal mixing acts against stratification by breaking down vertical density gradients and

changing the thermal inertia of the water column (*Sharpies et al.*, 1996). This is likely to have an influence on the air-sea heat flux and underscores the importance of including the tides when undertaking S2S predictions.

1.3 Ocean Downscaling and Model Validation

The resolution of global ocean models is generally too coarse to represent all relevant processes and furthermore, they do not resolve coastal areas which are of great interest for many practical applications. Mesoscale eddies play an important role in the energy exchange between the ocean and atmosphere (*Byrne et al.*, 2016) and can contribute to the time-mean heat transport (*Jayne and Marotzke*, 2002). However, in many regions of the globe, the local baroclinic deformation radius is smaller than the grid spacing of most global ocean circulation models (*Hallberg*, 2013). This is of particular concern for coastal and shelf seas (*Holt et al.*, 2017).

High-resolution models, however, require large computational resources and, even with today's supercomputers, they are not feasible on a global scale. This is where "downscaling" comes into play. Regional ocean circulation models are now being used to downscale large-scale information from global ocean models through physically consistent open boundary conditions. This one-way nesting approach allows for representation of processes on a wider range of spatial and temporal scales, including tides, and their interactions over a specific region of interest. Significant improvements have been made and regional ocean models have become a valuable tool for operational ocean forecasting as well as research (*Haidvogel et al.*, 2008). In addition, statistical approaches, can be used to combine information from low-resolution (global) ocean circulation models and observations, and thereby improve predictions on finer spatial scales (e.g., *Oliver et al.*, 2014; *Vanhatalo et al.*, 2016; *Towe et al.*, 2017). This is referred to as "statistical downscaling", as opposed to the dynamical downscaling mentioned above.

Most global ocean models do not include tides which are an important source of high-frequency variability and a generator of seasonal mean, tidal residual circulation and stratification. Tides can also enhance vertical mixing locally and, as mentioned above, this can have direct consequences for the air-sea fluxes and hence the transfer of atmospheric predictability into the ocean.

Recent advances in S2S prediction by the atmospheric community can improve ocean

forecasts on S2S timescales in two ways. First, new and improved atmospheric predictions can be used to force high-resolution ocean circulation models with realistic fluxes of heat, momentum, and moisture at the air-sea interface. Second, atmospherically generated S2S variability expressed in the large-scale ocean circulation can enter through the open boundaries of regional ocean models. This can lead to improved S2S predictions of the ocean as well as deepen understanding of the dynamical basis of the predictability.

Before using an ocean model for downscaling, it is important to assess its ability to capture all relevant processes. This is referred to as model validation which is more formally defined as *"the process of formulating and substantiating explicit claims about the applicability and accuracy of computational results, with reference to the intended purposes of the model as well as to the natural system it represents"* (*Dee*, 1995, p. 4). As noted above, coupling across scales is of particular importance for S2S prediction and it is hence important to validate the representation of a wide range of scales and their interactions in ocean models.

Ocean observations are relatively scarce and therefore traditional point-to-point validation is often restricted to a few locations. The availability of new observing platforms allows for more effective validation, e.g., satellite altimetry can be used to validate sea level variability as well as surface circulation, and ocean gliders can be used to validate the vertical structure of the water column with high spatial resolution.

Advances in other disciplines can also be utilized by oceanographers when validating models. An exciting recent example is the satellite-based measurements of the Earth's gravity field which have led to geoid models with unprecedented accuracy. Coastal sea level measured by tide gauges, in combination with the new geoid models, give more accurate estimates of mean dynamic topography (MDT) along the coast (*Huang*, 2017).

Here, MDT refers to the mean sea level (MSL) above the geoid corrected for the inverse barometer effect and averaged over a period of time to remove tidal and meteorological variations. MDT is also referred to as ocean dynamic sea level and is solely defined by ocean dynamics and density (*Gregory et al.*, 2019).

In the open ocean mean surface currents are approximately in geostrophic balance leading to a very simple relationship between MDT and mean circulation. As the coast is approached the interpretation of alongshore changes in MDT becomes more subtle because the geostrophic balance is no longer dominant and frictional processes become

important. The variations in MDT near the coast are still however useful. A particularly simple illustration is provided by considering a constant density ocean in a rectangular basin of constant depth lying on a mid-latitude β-plane. If the ocean circulation is forced by a steady, purely zonal wind stress, the meridional Sverdrup flow integrated across the basin is balanced by a return flow in a narrow western boundary current (e.g., *Stommel*, 1948; *Munk*, 1950). It is straightforward to show, using simple vorticity arguments, that the tilt of MDT along the western boundary is proportional to the meridional transport of the boundary current and independent of the details of the frictional dissipation in the model (*Stewart*, 1989). As will be shown in this thesis, similar arguments can be used on shelves to show that the tilt of MDT along the coast is related to net upwelling over the adjacent offshore region.

Given the value of MDT as an integrated measure of the mean state of the coastal ocean, the new measurements of the tilt of coastal MDT have the potential to be particularly useful for validating downscaled ocean predictions, and understanding scale interactions.

1.4 Objectives and Outline of Thesis

As indicated above, most research efforts around S2S prediction and predictability focus on the atmosphere. In this context, the ocean is mostly discussed in terms of its role as forcing for the atmosphere. It is reasonable to assume that atmospheric S2S variability has a direct influence on the ocean and thus its predictability.

The overall objectives of this thesis are to (i) improve the understanding of extratropical ocean variability and predictability on S2S timescales and (ii) increase the predictive skill of high-resolution, regional ocean models. This requires a realistic and validated ocean model which can resolve processes operating over a wide range of temporal and spatial scales as well as their interactions. Here, the Gulf of Maine and Scotian Shelf model (GoMSS) developed by *Katavouta and Thompson* (2016) will be used.

The thesis is broadly divided into three themes:

1.4.1 Theme 1: Identification of "Windows of Opportunity"

Given the dominant role of the MJO and its known atmospheric teleconnections on S2S timescales, the surface ocean response to the MJO is analyzed using observations of sea surface temperature (SST) as well as statistical and physically based models. This will

provide insight into the predictability of ocean variability on S2S timescales. The research questions which guide this analysis are:

- Does the MJO influence SST in the North Atlantic on S2S timescales?
- Are there specific locations and temporal "windows of opportunity" for S2S predictions of the ocean?
- How does this response differ between coastal regions, continental shelves, and the deep ocean? Where does the strongest response occur?
- What are the underlying physical processes?

1.4.2 Theme 2: Model Validation

In order to demonstrate the suitability of GoMSS as a tool for S2S prediction of the ocean, a significant part of the thesis is concerned with the validation of the model with a particular focus on the mean state and low-frequency changes. Emphasis will be put on predictions of MDT which will be evaluated using new methods and new observations. This will also allow for analysis of the role of the alongshore MDT in coastal and regional ocean dynamics. The following technical and scientific questions will be answered:

- Can new observations of geodetically referenced coastal sea level help validate high-resolution regional ocean models?
- How can model predictions of the mean state be evaluated in the absence of sufficiently long records of observed sea level and currents?
- What does the alongshore tilt of MDT at the coast tell us about circulation in the nearshore and also over the adjacent shelf? What are the implications for ocean monitoring?

1.4.3 Theme 3: Downscaling Case Studies

Based on the results of the first two themes, the feasibility of ocean downscaling for S2S prediction will be addressed using sensitivity model experiments with GoMSS. The following research questions will be addressed:

- Can GoMSS reproduce the three-dimensional, time-varying response of the ocean to the MJO?

- What are the main physical processes that shape the mean ocean response to the MJO?
- How is the effect of atmospheric forcing in response to the MJO vertically projected into the ocean interior?
- What is the importance of including forcing at higher frequencies than the MJO (e.g., tides and weather)?

A common theme that occurs throughout this work is the interaction across space and timescales. Overall, this thesis covers spatial scales from the global atmosphere to tidal bays in the coastal ocean, and temporal scales from hours to years.

The remainder of the thesis is structured as follows: Chapter 2 deals with the identification of "windows of opportunity" based on the SST response to the MJO in the North Atlantic. Chapter 3 provides a brief summary of the governing equations and a detailed description of the GoMSS model configuration. In Chapter 4, new observations of geodetically referenced sea levels are used to validate GoMSS and the dynamical role of coastal MDT is discussed. In Chapter 5, a new method for validating model predictions of MDT is proposed which is based on observations of overtides and mean currents. In Chapter 6, the nearshore and sub-surface ocean response to the MJO is explored with model sensitivity experiments using GoMSS and the feasibility of ocean downscaling for S2S prediction is discussed. Chapter 7 provides a summary of the main research results and guidance for further work.

CHAPTER 2

THE RESPONSE OF NORTH ATLANTIC SEA SURFACE TEMPERATURE TO THE MADDEN-JULIAN OSCILLATION

2.1 Introduction

Subseasonal-to-seasonal (S2S) prediction relies considerably on teleconnections as a source of predictability which can often be traced back to the tropics (*Lin et al.*, 2019). On S2S timescales, variability in the tropics is dominated by the Madden-Julian Oscillation (MJO, *Madden and Julian*, 1971, 1972) which can influence the atmospheric circulation around the globe (e.g., *Zhang*, 2013; *Woolnough*, 2019). The MJO is a large-scale convective anomaly in the atmosphere which propagates eastward along the equator with a period of 40–60 days. This convective signal is characterized by variations of zonal winds in the lower and upper troposphere as well as anomalies in outgoing longwave radiation (OLR) and precipitation.

Upward motion associated with the deep atmospheric convection near the equator leads to divergent outflow aloft creating a source for Rossby waves which propagate poleward and eastward (*Sardeshmukh and Hoskins*, 1988). Consequently, a wave train is established which influences the extratropical circulation (e.g., *Matthews et al.*, 2004; *Seo and Son*, 2012; *Seo and Lee*, 2017; *Stan et al.*, 2018). It has been shown that this teleconnection is most effective when the MJO has a dipole structure with enhanced convection over the eastern Indian Ocean and suppressed convection over the western Equatorial Pacific, and vice versa (*Lin et al.*, 2010). Most of the known MJO teleconnections are documented for winter (*Stan et al.*, 2018) when the MJO activity is stronger and the westerly waveguide

is not interrupted (e.g., *Zhang and Dong*, 2004; *Adames et al.*, 2016). There is growing evidence that the MJO also influences the extratropical atmospheric circulation through a stratospheric pathway based on interaction with the polar vortex (e.g., *Barnes et al.*, 2019).

In the extratropics, the coherent circulation anomalies related to the MJO interact with modes of climate variability and have direct influence on weather (see *Stan et al.*, 2018, for a comprehensive review). For example, *Cassou* (2008) and *Lin et al.* (2009) showed that the North Atlantic Oscillation (NAO) is more likely to occur in its positive (negative) phase about 5–15 days after the enhanced MJO-related convection reaches the eastern Indian Ocean (western Equatorial Pacific). The MJO has also been shown to influence surface air temperature in the northern hemisphere (e.g., *Vecchi and Bond*, 2004; *Lin and Brunet*, 2009; *Zhou et al.*, 2012; *Baxter et al.*, 2014; *Seo et al.*, 2016; *Hu et al.*, 2019) and precipitation across North America (e.g., *Lin et al.*, 2010; *Jones and Carvalho*, 2012; *Baxter et al.*, 2014; *Klotzbach et al.*, 2016). This can ultimately lead to extreme events like heat waves and flooding related to the MJO.

The influence of the MJO on the extratropical surface ocean has received relatively little attention (*Merryfield et al.*, 2020). The ocean and atmosphere exchange heat and momentum through fluxes across the air-sea interface. It is therefore likely that the atmospheric anomalies in response to the MJO also affect the surface ocean. *Marshall et al.* (2015) showed that outside the tropics, the MJO has an impact on ocean wind wave characteristics in the North Pacific and North Atlantic. They conclude that zonal wind anomalies related to the NAO response to the MJO lead to anomalies in significant wave height in the eastern North Atlantic. However, they also point out that some anomalous wave conditions occur before the NAO pattern is established in the atmosphere.

In this chapter, the response of sea surface temperature (SST) in the extratropical North Atlantic to the MJO will be analyzed using observations and simple statistical and physically based models. This will help identify temporal "windows of opportunity" of enhanced predictability which can be utilized for S2S prediction of the ocean. In particular, the following research questions will be tackled: (i) Does the MJO influence SST in the North Atlantic on S2S timescales? (ii) How does this response differ between coastal regions, continental shelves, and the deep ocean? Where does the strongest response occur? (iii) What are the underlying physical mechanisms causing the SST response? (iv) What are the implications for S2S predictions of the North Atlantic Ocean?

The remainder of the chapter is structured as follows. Section 2.2 gives a description of the Real-Time Multivariate MJO (RMM) index and the observations of SST and air-sea heat fluxes used in this study. In Section 2.3, a composite analysis is applied to identify the relationship between the MJO and both SST and net heat fluxes in the North Atlantic. A simple surface mixed layer model is used in Section 2.4 to explore if air-sea heat flux variations are a significant driver of SST variability in the study area on S2S timescales. Section 2.5 describes the physical mechanism behind the teleconnection linking the MJO and SST in the North Atlantic. In Section 2.6, the results are summarized and implications for S2S prediction of the ocean are discussed.

2.2 Data

This section provides an overview of the data used in this study. First, the Real-Time Multivariate MJO (RMM) index will be described and the gridded observations of SST and air-sea heat fluxes will be introduced.

2.2.1 Real-Time Multivariate MJO (RMM) Index

The state of the MJO is characterized by the daily Real-Time Multivariate MJO (RMM) index (*Wheeler and Hendon*, 2004) obtained from the Australian Bureau of Meteorology. This index is based on satellite observations of outgoing longwave radiation (OLR) and reanalysis fields of zonal wind at 850 hPa and 200 hPa in the tropics (15°S–15°N). Before the index is calculated, the seasonal cycle and interannual variability are removed and the resulting anomalies are averaged in the meridional direction. The bivariate MJO index is defined by the principal components associated with the first two combined empirical orthogonal functions (EOFs) referred to as RMM1 and RMM2. Figure 2.1a shows a time series of RMM1 and RMM2 for 2012 to illustrate the quasi-periodicity of the MJO. Both components are approximately normally distributed and, by construction, have zero mean and unit variance. For this reason, a component magnitude of 2 is considered large in the sense that this value will be exceeded with probability 0.046.

Note that due to the quasi-periodicity of the MJO, the RMM index is strongly autocorrelated. The autocorrelation function of the complex RMM index $(\text{RMM1} + i\,\text{RMM2})$ is 0.3 at a lag of 20 days.

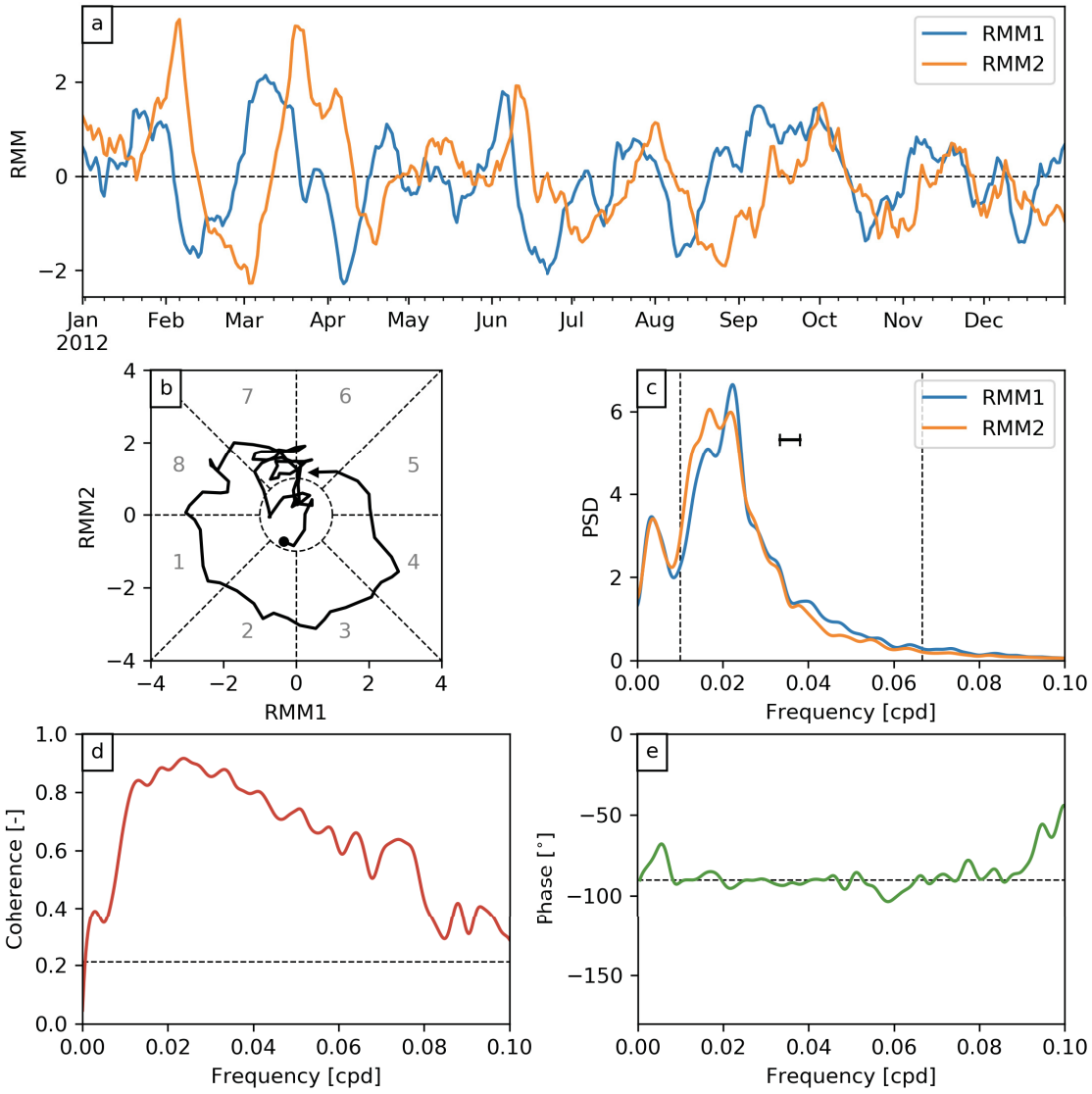

Figure 2.1: Time series and spectra of the RMM index. (a) Time series of the two index components RMM1 and RMM2 for 2012. (b) Representation of MJO in RMM phase space for the period from 1 January to 14 April 2012. Numbers indicate the eight integer MJO phases Φ_{RMM}. (c) Power spectra of RMM1 and RMM2 which have been smoothed using a 400-point Parzen window. The bandwidth of the kernel function is indicated by the horizontal bar. Vertical dashed lines mark the frequency band of the 15–100-day bandpass filter. (d) Coherence between RMM1 and RMM2. The dashed line indicates the threshold above which the coherence is considered statistically different from zero at the 5% significance level. (e) Spectrum of phase lag between RMM1 and RMM2. The spectral analyis was performed for the period 1981–2019.

Table 2.1: Summary statistics of the RMM index during boreal winter (DJF) for the period 1981–2019. The MJO is considered active when $A_{\text{RMM}} > 1$.

Phase (Φ_{RMM})	1	2	3	4	5	6	7	8	Inactive
Days	176	252	322	294	296	319	389	270	1,111
Percentage	5.1%	7.3%	9.4%	8.6%	8.6%	9.3%	11.3%	7.9%	32.4%
Mean A_{RMM}	1.61	1.67	1.79	1.72	1.74	1.74	1.84	1.75	0.64

The amplitude of the RMM index is given by

$$A_{\text{RMM}}(t) = \sqrt{\text{RMM1}^2(t) + \text{RMM2}^2(t)} \tag{2.1}$$

and the MJO is considered to be active when $A_{\text{RMM}} > 1$. The angle

$$\phi_{\text{RMM}}(t) = \tan^{-1}\left(\frac{-\text{RMM2}(t)}{\text{RMM1}(t)}\right) \tag{2.2}$$

is typically quantized into eight integer phases Φ_{RMM} which describe the geographic position of the convective anomaly associated with the MJO (Figure 2.1b). On average, the MJO stays in one phase for 6 days. It is important to note that a particular MJO cycle does not necessarily start in phase 1 nor does it progress through all phases.

Daily values of the RMM index are available continuously from 1979 to present. In this study the focus will be on boreal winter months (December through February, DJF) for the period 1981–2019. Table 2.1 provides summary statistics of the RMM index. For about one third of the study period, the MJO is inactive, i.e., $A_{\text{RMM}} < 1$. When the MJO is active it is mostly in phase 7 which corresponds to enhanced (reduced) convection over the western equatorial Pacific (eastern Indian Ocean). This is followed by phases 3 and 6 which is consistent with the pentad statistics of *Lin and Brunet* (2009). Note that phase 3 corresponds to the reversed spatial pattern of the convective MJO dipole during phase 7. During these phases, the mean RMM amplitude is typically at its maximum.

Figure 2.1c shows the smoothed power spectra of daily RMM1 and RMM2. The bandwidth of the kernel function of the 400-point Parzen window (*Priestley*, 1981, pp. 443), that was used for the smoothing, is indicated by the horizontal bar. Most of the energy is concentrated at periods between 30 and 100 days with a tail towards higher frequencies. Additionally, enhanced low-frequency variability is visible for timescales with period of

one year which indicates the seasonal cycle of the MJO.

The coherence between RMM1 and RMM2 is shown in Figure 2.1d. Across the spectrum, the indices are strongly coherent with values up to 0.9 at the frequencies that contain the most energy. The phase lag between RMM1 and RMM2 is around –90° (Figure 2.1e) which shows that the two indices are roughly in quadrature corresponding to a counterclockwise rotation in phase space (Figure 2.1b). This quadrature relationship is consistent with the zero correlation between RMM1 and RMM2 at zero lag.

2.2.2 NOAA Optimal Interpolation Sea Surface Temperature

Version 2 of the Optimal Interpolation Sea Surface Temperature dataset (OISSTv2, *Reynolds et al.*, 2007) produced by the National Oceanic and Atmospheric Administration (NOAA) provides statistically interpolated satellite observations of SST supplemented with in-situ measurements. Daily SST values are available on a global grid with 0.25° spacing from September 1981 to present. In this study, the focus is on the North Atlantic region between 15–65°N and 262–360°E for the period from December 1981 to February 2019. In the following, these daily SST fields will be denoted by $T(\mathbf{x}, t)$, where $\mathbf{x}$ is the location vector of a given grid cell and t is time.

At each grid point in the study area, the climatology $T_{\mathrm{c}}(\mathbf{x}, t)$ was computed using a methodology similar to that of *Hobday et al.* (2016). First, the mean for each day of the year is calculated over the climatology period (here 1982–2018) and then a running mean with an 11-day window centered around the day of interest is applied. (Note that year end effects are taken into account, e.g., the climatological value for January 1 is the mean value over the period from December 27 to January 6 over all years). For leap years, the value for February 29 is computed as the arithmetic mean of the values for 28 February and 1 March.

Anomalies were computed by subtracting the smoothed daily climatology from the daily SST fields

$$T_{\mathrm{a}}(\mathbf{x}, t) = T(\mathbf{x}, t) - T_{\mathrm{c}}(\mathbf{x}, t). \tag{2.3}$$

In order to extract the SST variability on S2S timescales, a third order digital Butterworth bandpass filter (*Butterworth*, 1930) with a 15–100-day passband was applied to the SST anomaly time series at each grid point. For the remainder of the study, $T_{\mathrm{a}}(\mathbf{x}, t)$ refers to the bandpass filtered SST anomalies.

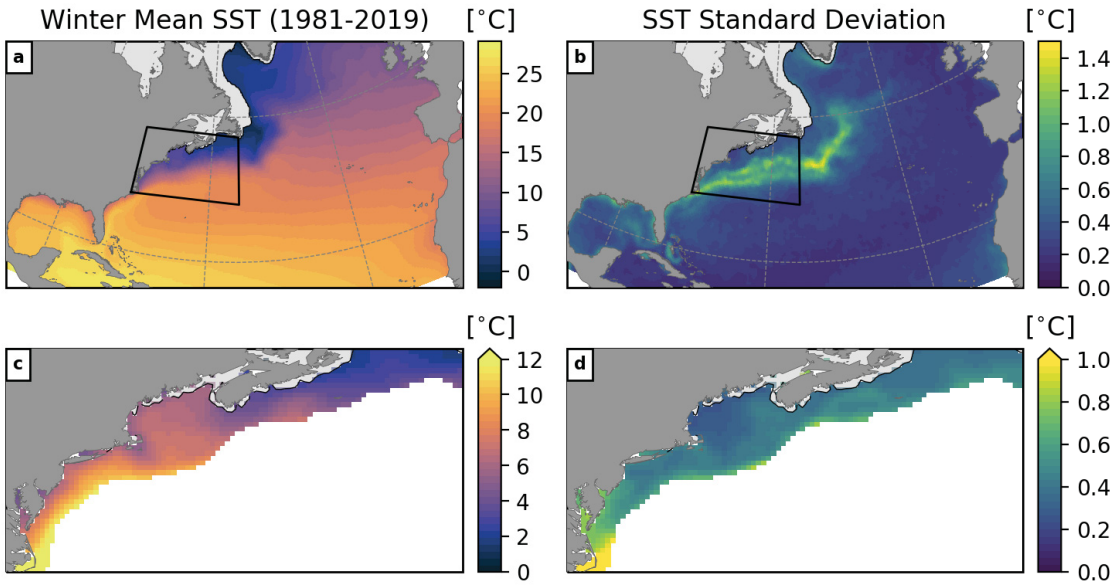

Figure 2.2: (a) OISSTv2 winter mean SST, and (b) standard deviation of bandpass-filtered SST anomalies $T_\mathrm{a}(\mathbf{x}, t)$ for the period 1981–2019. (c) & (d) Enlarged view of the Middle Atlantic Bight, Gulf of Maine, and Scotian Shelf regions indicated by the black quadrangle. In these panels, values are only shown at grid points with water depth less than or equal to 1000 m. The light area near the coast shows the climatological sea ice cover.

Figure 2.2 shows the winter mean SST and standard deviation of $T_\mathrm{a}(\mathbf{x}, t)$ for the whole study area and as an enlarged view of the Middle Atlantic Bight, Gulf of Maine, and Scotian Shelf (bottom panels). The dominant feature in the domain is the Gulf Stream indicated by strong gradients and high variability in SST. Note that the regions with a high standard deviation are confined to the deep ocean.

2.2.3 Objectively Analyzed Air-Sea Fluxes (OAFlux)

Gridded fields of turbulent heat fluxes between the ocean and atmosphere are taken from the third version of Objectively Analyzed Air-Sea Fluxes (OAFlux, *Yu and Weller*, 2007). This dataset is a synthesis of satellite observations and reanalysis products of four atmospheric and ocean variables which were combined using variational objective analysis (OA). The four variables are sea surface temperature T, air temperature T_air and specific humidity q_air at 2 m, and wind speed U_wind at 10 m. Each field of these variables was computed independently using the OA procedure to yield the best estimates in a least squares sense. From these fields, air-sea heat fluxes were computed using the Coupled Ocean-Atmosphere Response Experiment algorithm (COARE, *Fairall et al.*, 2003) based on following bulk

formulae for sensible heat flux

$$Q_{\mathrm{s}} = \rho_{\mathrm{a}} c_{p,\mathrm{a}} c_{\mathrm{h}} U_{\mathrm{wind}} \left(T - T_{\mathrm{air}}\right) \tag{2.4}$$

and latent heat flux

$$Q_{\mathrm{l}} = \rho_{\mathrm{a}} c_{\mathrm{e}} L_{\mathrm{e}} U_{\mathrm{wind}} \left(q_{\mathrm{s}} - q_{\mathrm{air}}\right), \tag{2.5}$$

where ρ_{a} is the density of air, q_{s} is the saturation humidity at T taking into account the reduced vapor pressure caused by salt water (*Yu*, 2009), and $c_{p,\mathrm{a}}$ is the specific heat capacity of air at constant pressure. c_{h} and c_{e} are the turbulent exchange coefficients for latent and sensible heat, respectively, and L_{e} is the latent heat of evaporation.

Daily mean fields of turbulent air-sea heat fluxes are available for the period 1985–2019 on grid a global grid with 1° spacing. In addition, surface radiation data of incoming shortwave Q_{sw} and outgoing longwave radiation Q_{lw} from the International Satellite Cloud Climatology Project (ISCCP, *Zhang et al.*, 2004) as well as net heat flux

$$Q_{\mathrm{net}} = Q_{\mathrm{sw}} - Q_{\mathrm{lw}} - Q_{\mathrm{s}} - Q_{\mathrm{l}}. \tag{2.6}$$

were obtained on the same grid from the OAFlux database. This equation reflects the sign convention of the OAFlux dataset. These data are only available for the years 1985–2009 and therefore, the heat flux analysis in this study is limited to this period. Anomalies of the heat flux components were calculated in the North Atlantic region the same way as for SST. The same Butterworth bandpass filter was applied to extract the heat flux variability on S2S timescales.

2.3 Composite Analysis

In order to statistically analyze the relationship between SST of the North Atlantic and the MJO, a composite analysis is applied. Composites are created by computing the mean T_{a} conditioned on MJO phase. (Although T_{a} is bandpass-filtered, any potentially remaining seasonal mean anomaly was subtracted for each winter season prior to the compositing.) Consider the bandpass-filtered SST anomaly at a fixed location $T_{\mathrm{a}}(\mathbf{x}, t)$ to be a random variable of a stationary process. The conditional mean (e.g., *Priestley*, 1981, p. 74) of T_{a} at

lag δ is defined by

$$\mu(\mathbf{x}, j, \delta) = \mathrm{E}\left[T_{\mathrm{a}}(\mathbf{x}, t+\delta) | \Phi_{\mathrm{RMM}}(t) = j, A_{\mathrm{RMM}}(t) \geq 1\right]. \tag{2.7}$$

Here, E$[\cdot]$ is the expectation operator which is applied to the subset of T_{a} defined by the time when the integer MJO phase $\Phi_{\mathrm{RMM}} = j$, where j = 1, 2, ..., 8, and $A_{\mathrm{RMM}} > 1$. It is clear from (2.7) that the conditional mean is a function of location, MJO phase, and lag.

For each combination of integer MJO phase $\Phi_{\mathrm{RMM}} = j$ and lag δ, the conditional means were calculated using (2.7) where the expectation operator was replaced by the sample mean. These estimates will henceforth be referred to as composites and denoted by $\overline{T}_{\mathrm{a}}$. The maximum lag considered in this study is $\delta = 42$ days which approximately corresponds to the time it takes the MJO to propagate through seven phases. This means the lagged composites also contain data for the months of March and April. It is important ot recognize that the samples in each composite are not independent because they can be from consecutive days and therefore are autocorrelated (Figure 2.1c).

In order to test if a composite is significantly different from zero, a moving-blocks bootstrap is applied following *Henderson et al.* (2016). This significance test preserves the autocorrelation structure of the samples in each composite. For each MJO phase, $N_{\mathrm{c}}/6$ potentially overlapping 6-day blocks of the full record of T_{a} are randomly selected with replacement where N_{c} is the number of samples in each composite. These blocks constitute a bootstrap sample with the same number of days as the MJO composite expected for a specific phase. The length of the blocks was chosen based on the average time the MJO spends consecutively in each phase. This process was repeated 1000 times and the mean of each bootstrap sample was computed. From the 1000 bootstrap means, the quantiles of the underlying probability distribution were estimated and then compared to $\overline{T}_{\mathrm{a}}$. Here, the composited anomalies are considered statistically different from zero at the 10% significance level if they are below or above the 5th and 95th percentile of the bootstrap distribution, respectively.

2.3.1 SST Composites

Previous studies have shown that the MJO leads to an increased near-surface air temperature over the eastern US and Canada 5–20 days after phase 3 (e.g., *Lin and Brunet*, 2009; *Baxter et al.*, 2014). It is possible that this leads to an increased sensible heat flux into the ocean

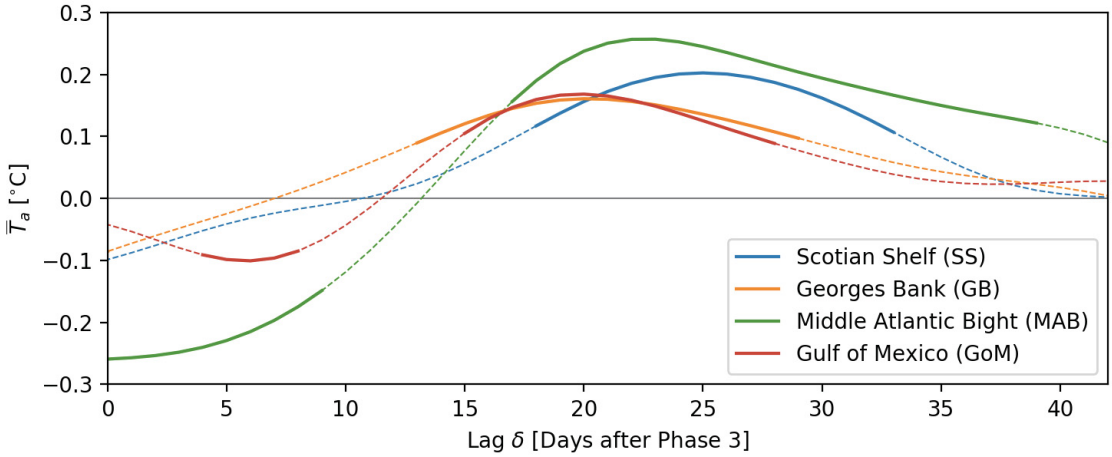

Figure 2.3: SST composites with respect to MJO phase 3 during winter when $A_{\text{RMM}} > 1$. Each composite is for one of the four representative locations along the east coast of North America and in the Gulf of Mexico shown in Figure 2.4. Solid lines indicate anomalies statistically different from zero at the 10% significance level.

which would be associated with elevated SST along the east coast of North America. Figure 2.3 shows composites with respect to MJO phase 3 at four representative locations along the east coast of North America and in the Gulf of Mexico. At $\delta = 0$, when the MJO is in phase 3, the SST at these locations is about 0.1 °C colder than normal except for the Middle Atlantic Bight (MAB) where $\overline{T}_{\text{a}} = -0.26$ °C. A warm anomaly develops after 2 weeks reaching its maximum 20–25 days after phase 3 depending on the location. The maximum anomaly is about 0.2 °C with the strongest response in the Middle Atlantic Bight of 0.26 °C. This indicates that there is a lagged relationship between the MJO and SST at these locations.

What is the spatial extent of the SST anomalies in response to the MJO? Figure 2.4 shows composite maps for the whole study area (top panels) and for the Middle Atlantic Bight, Gulf of Maine, and Scotian Shelf region (bottom panels). Each map is a composite for lags $\delta = 0$, 6, ..., 30 days after phase 3. Only composites statistically different from zero at the 10% significance level are shown. The shaded areas in the Gulf of St. Lawrence and western Labrador Sea are mostly covered by sea ice during the winter months (sea ice concentration greater than 15% during at least 90% of days in DJF) and are therefore excluded from the analysis. Black dots mark the four locations discussed above.

The contemporaneous composite ($\delta = 0$ days) shows that the cold anomaly along the eastern seaboard of North America and in the Gulf of Mexico is only significant in

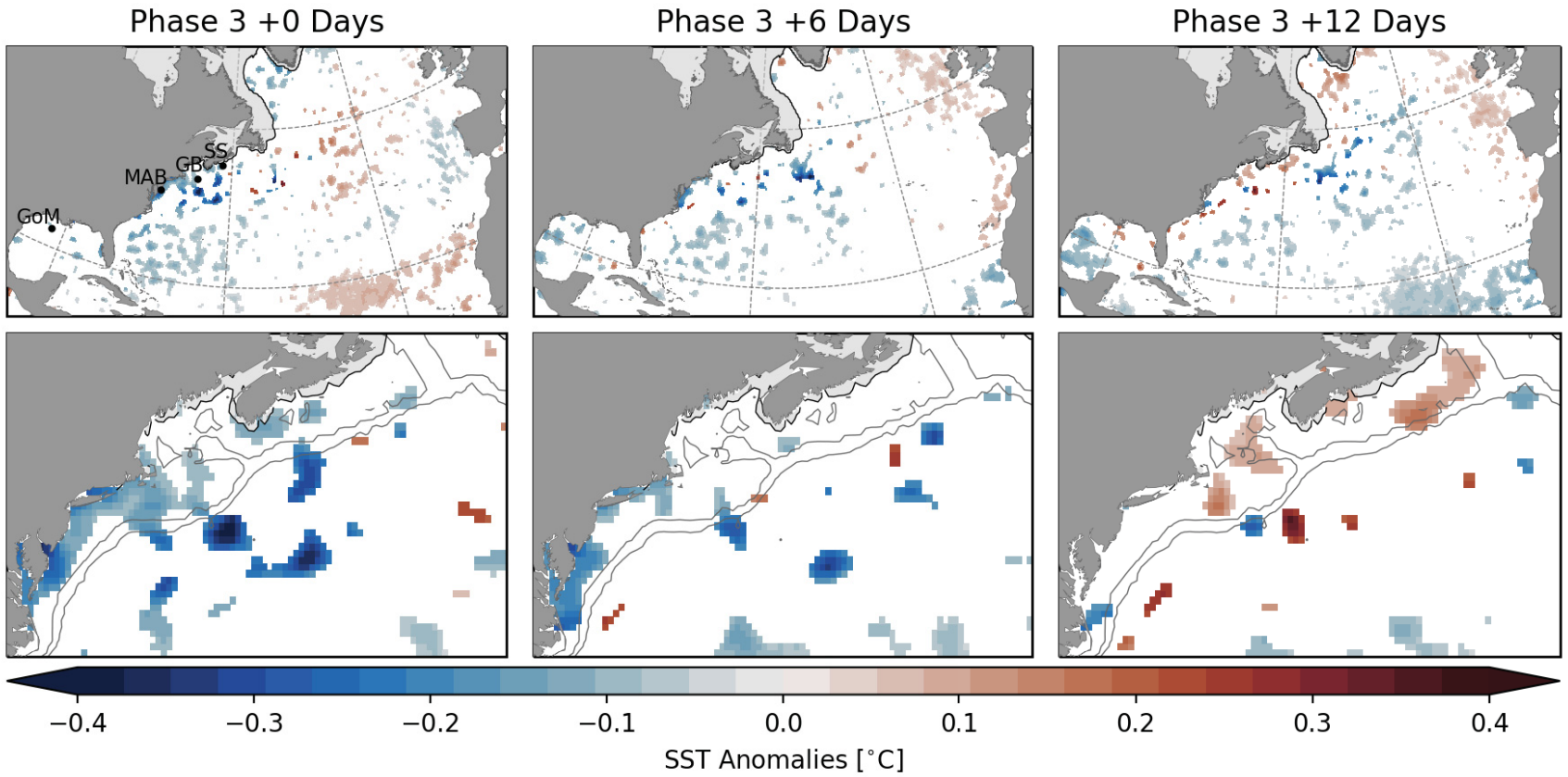

Figure 2.4: Lagged composites of bandpass-filtered SST anomalies $\overline{T}_{\mathrm{a}}$ with respect to MJO phases 3 during winter when $A_{\mathrm{RMM}} > 1$. Maps show the spatial structure of the composites for the whole study area (top panels) and in the Middle Atlantic Bight, Gulf of Maine, and Scotian Shelf region (bottom panels). Each map is a composite for lags $\delta = 0$, 6, ..., 30 days after phase 3. Only anomalies statistically different from zero at the 10% significance level are shown. Shaded areas near the coast show the climatological sea ice cover.

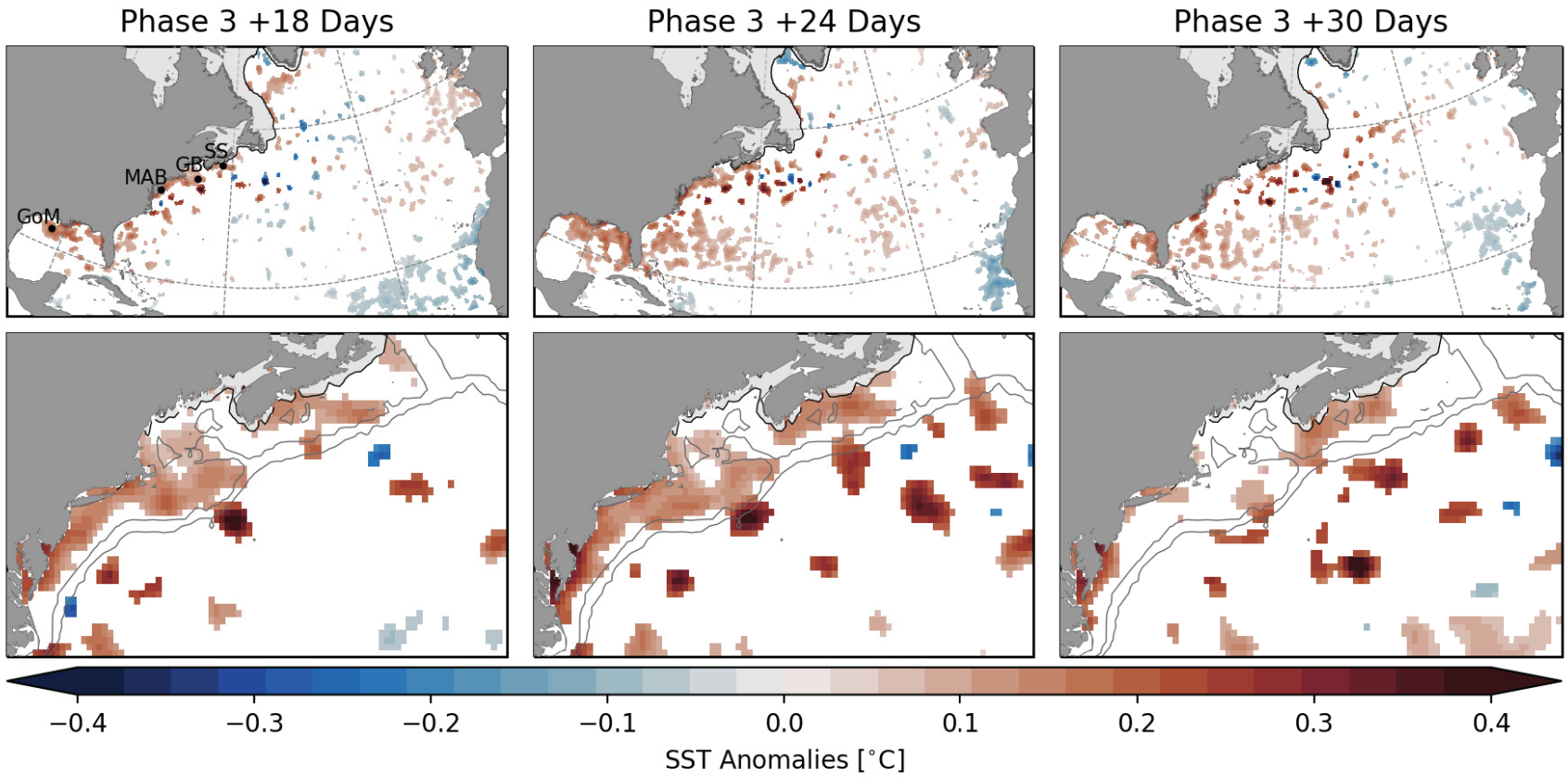
Phase 3 +18 Days
Phase 3 +24 Days
Phase 3 +30 Days
GoM
MAB
GB
SS
−0.4
−0.3
−0.2
−0.1
0.0
0.1
0.2
0.3
0.4
SST Anomalies [˚C]

the Middle Atlantic Bight where it is confined to shallow areas along the coast. In the offshore, weak and scattered negative anomalies occur in the Sargasso Sea. Additionally, a widespread increase in SST of about 0.1 °C can be observed in the tropical North Atlantic.

The significant anomalies in the Middle Atlantic Bight, Gulf of Maine, and Scotian Shelf region only occur on the continental shelf. The largest response occurs in Chesapeake Bay and Delaware Bay which are shallow estuaries with water depths of order 20 m. Composite maps disregarding the statistical significance of the anomalies show a large-scale response extending to the deep ocean (see Figure A.1 in Appendix A). However, the mesoscale eddy variability associated with the Gulf Stream (Figure 2.2) increases the background noise level which masks the response to the MJO.

Overall, a statistically significant, spatially coherent SST signal in the North Atlantic that covaries with the MJO has been identified. The structure of the large-scale SST response is reminiscent of the well known tripole pattern which has been related atmospheric to forcing on monthly and seasonal timescales (e.g., *Cayan*, 1992a,b; *Seager et al.*, 2000). Spatial irregularities in the signal, especially in the deep ocean, can be explained by mesoscale processes not directly affected by the MJO. On the other hand this may also be due to the spatial smoothing which was applied in the statistical interpolation of OISSTv2 to fill gaps where no observations were available (see *Reynolds et al.*, 2007).

It is expected that the extratropical response will occur at some lag with respect to the time when the MJO reaches a phase which is favourable for teleconnections (e.g., *Cassou*, 2008; *Henderson et al.*, 2016). Note that the lag at which the maximum ocean response to the MJO occurs can, conceptually, be considered, the sum of two components:

$$\delta = \delta_{\mathrm{T}} + \delta_{\mathrm{O}}, \tag{2.8}$$

where δ_{T} is the time for the atmospheric signal to propagate from the tropics to the North Atlantic region and δ_{O} is the timescale for the surface ocean to respond to an atmospheric perturbation. This can include the effects of turbulent heat exchange at the sea surface and advection by ocean currents. The teleconnection timescale of the atmosphere δ_{T} is on the order of 1–2 weeks (e.g., *Cassou*, 2008; *Lin and Brunet*, 2009; *Lin et al.*, 2009; *Baxter et al.*, 2014; *Lin et al.*, 2019). A similar timescale is plausible for the upper ocean response (e.g., *Deser and Timlin*, 1997) which leads to a total lag of $\delta = 2$–4 weeks which is in agreement with the results of the composite analysis above. Note that, based on the

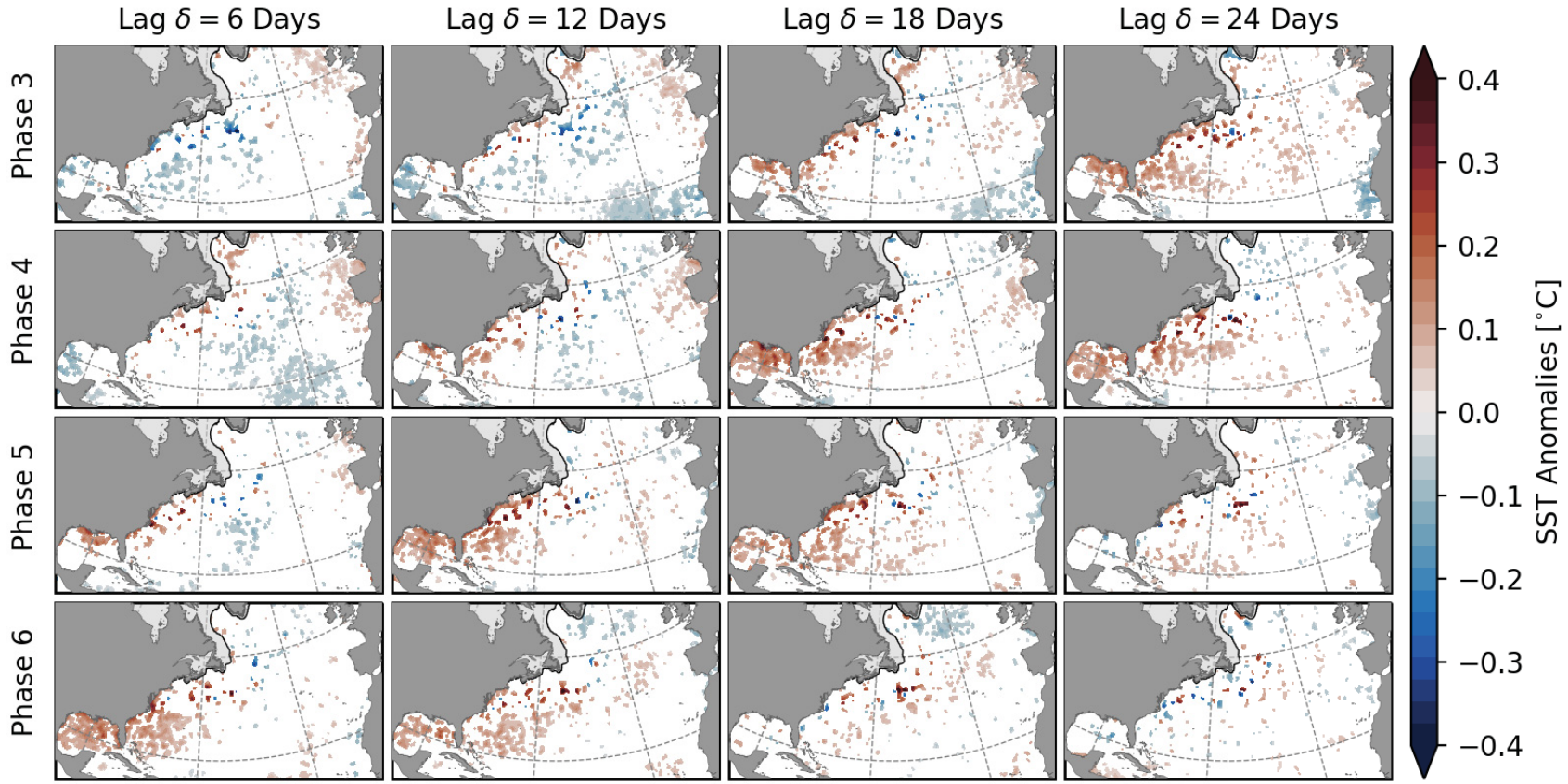

Figure 2.5: SST composites with respect to MJO phases 3–6 during winter when $A_{\mathrm{RMM}} > 1$. Each row represents a certain phase and the columns refer to lags $\delta = 6$, 12, 18, and 24 days after that phase. All shown anomalies are statistically different from zero at the 10% significance level. Shaded areas near the coast show the climatological sea ice cover.

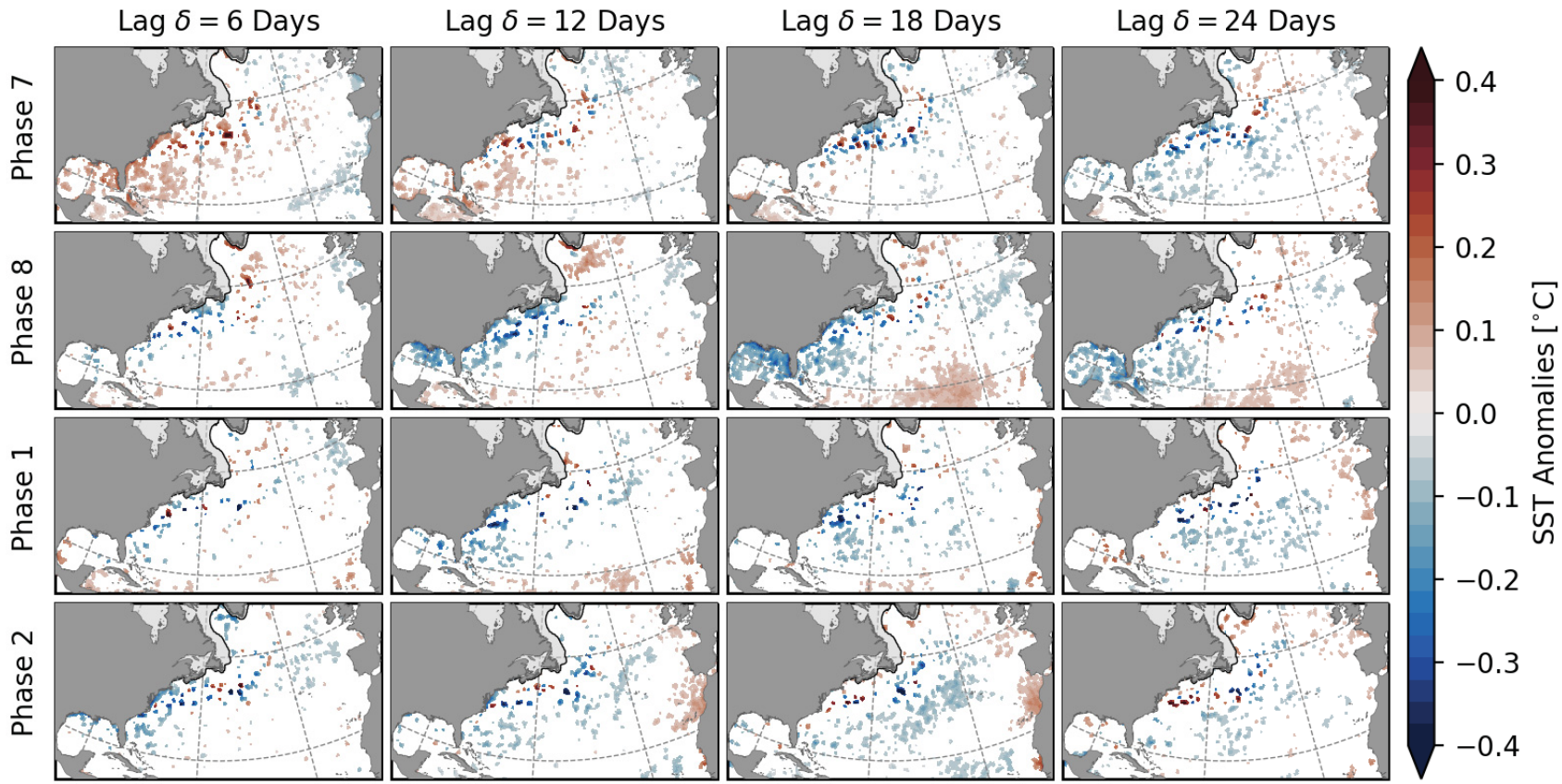

Figure 2.5: Continued for MJO phases 7–8, and 1–2.

average time the MJO spends in a particular phase (6 days), the total lag $\delta = 20$–25 days corresponds to roughly half a cycle.

Given this delay, it is likely that the anomalies occurring at $\delta = 0$ days are a lagged response to the MJO phase half a cycle before, i.e., phase 7. This is consistent with previous studies which showed that a negative near-surface air temperature anomaly occurs in eastern North America 10–20 days after the MJO is in phase 7 (e.g., *Lin and Brunet*, 2009; *Baxter et al.*, 2014; *Hu et al.*, 2019). The opposite responses to MJO phases 3 and 7 can be related to the tropical convection anomaly dipole associated with the MJO which reverses sign between the two phases (e.g., *Lin et al.*, 2010) and will be further discussed in Section 2.5.

The results presented above illustrate the relationship between the SST and one particular phase of the MJO. What is the response and timing to the other phases? This leads to a known issue: the quasi-periodicity of the MJO creates an ambiguity between MJO phases and the time lag at which the teleconnection occurs. This is illustrated in Figure 2.5 which shows SST composites with respect to all eight phases of the MJO. The first row shows the same maps as in the top panels of Figure 2.4. Each row represents a certain phase and the columns refer to lags of $\delta = 6$, 12, 18, and 24 days. Note that the composites for $\delta = 0$ days are not presented here because they are assumed to indicate a lagged response to a previous phase. It is important to point out the similarity of the anomaly patterns in the panels along the diagonals.

The warm anomaly in the western North Atlantic and in the Gulf of Mexico developing 2–3 weeks after phase 3 can also be seen at shorter lags with respect to phases 4–7. Note that this anomaly appears to be more pronounced at $\delta = 18$ days after phase 4. Based on the mean period of the MJO, this timing is in agreement with the composite 24 days after phase 3 described above because, on average, the MJO spends six consecutive days in one phase before it moves to the next. Therefore, a relationship with a particular phase and lag appears to be similar to the relationship of the next phase with δ about 6 days shorter. However, this duration varies and it is possible that the MJO skips a phase or decays before completing a full cycle. Thus, the composites along the diagonals are not completely identical.

The same issue occurs for the other half of the MJO cycle (second part of Figure 2.5). At $\delta = 18$ days after phase 8, significantly lower SST can be observed along the North

American east coast and in the Gulf of Mexico. In terms of offshore extent, this cold anomaly is unique compared to the other phases and lags, however, in coastal regions, a similarity of the response along the diagonals is apparent. This shows again that the anomalies at $\delta = 0$ with respect to phase 3 shown in Figure 2.4 are a delayed response.

Although the SST composites are generally small ($< 0.5\,^{\circ}$C), it is important to note that they present a climatological average and the response to individual MJO episodes are expected to be much stronger. Due to the varying propagation speed of the MJO and response time, the averaging of multiple impulses leads to a further attenuation of the signal. Additionally, the spatial averaging due to the gridding as well as the filtering of the data will also attenuate the SST signal. Given the ambiguity in the lag due to the quasi-periodicity of the MJO, and the multiple timescales involved, it is not straightforward to quantify the relationship between a single MJO episode and the resulting SST anomalies.

The spatial scales of the SST composites suggest large-scale atmospheric anomalies to drive the observed variations in the surface ocean. This is now explored using the same composite analysis on the net heat fluxes in the North Atlantic.

2.3.2 Net Air-Sea Heat Flux Composites

Composites of net air-sea heat flux anomalies with respect to the MJO were computed using (2.7) by replacing the SST with bandpass-filtered Q_{net} anomalies from the OAFlux dataset. The statistical significance of the heat flux composites was assessed using the moving-blocks bootstrapping method described in Section 2.3.

Figure 2.6 shows the spatial structure of Q_{net} composites at lags $\delta = 6$, 12, and 18 days (columns) for all MJO phases (rows). Only anomalies which are statistically different from zero at the 10% significance level are shown. Positive values refer to increased heat flux from the atmosphere into the surface ocean.

Focusing again on the response to phase 3, it can be seen that a strong positive heat flux anomaly occurs along the eastern seaboard of North America and in the eastern Gulf of Mexico at lag δ = 6 days. This anomaly persists for several days, most notably north of the Gulf Stream. At $\delta = 18$ days after phase 3, the positive anomaly is slightly weaker, but more widespread, covering large parts of the western North Atlantic. Generally, the strongest anomalies can be observed along the Gulf Stream.

Clearly, the relationship between the MJO and net surface heat flux in the North Atlantic is complex and depends on location. Figure 2.7 shows Q_{net} composites with respect to

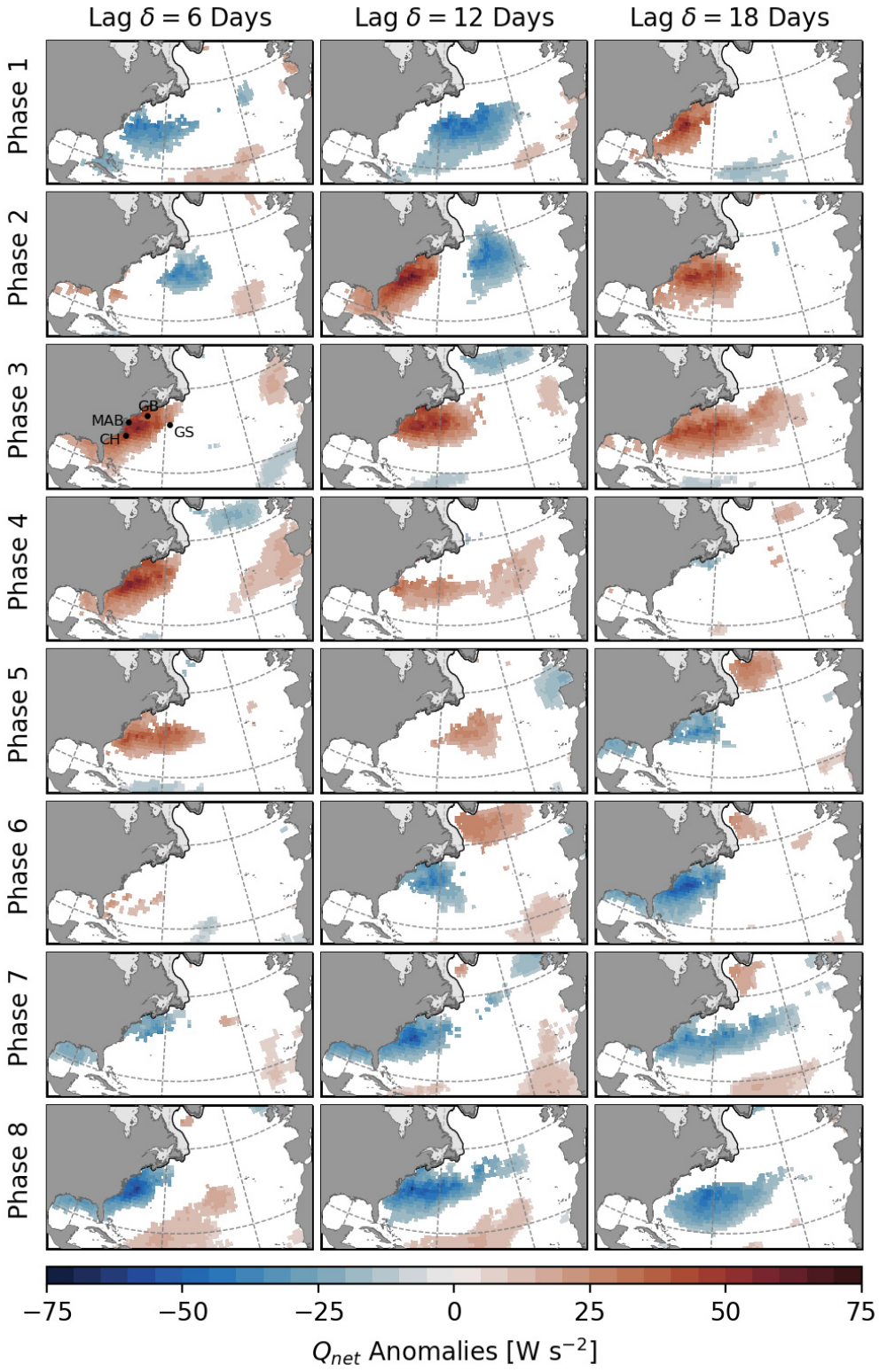

Figure 2.6: Composites of bandpass-filtered Q_{net} anomalies for all MJO phases during winter when $A_{\text{RMM}} > 1$. All shown anomalies are statistically different from zero at the 10% significance level. Shaded areas near the coast show the climatological sea ice cover.

phase 3 at four representative locations which have been chosen to illustrate the propagation of the signal. A maximum positive anomaly of 48 W m^{-2} along the North American east coast first occurs around Cape Hatteras at $\delta = 6$ days after phase 3 and then moves northward and reaches Georges Bank at a lag of $\delta = 9$ days after phase 3. Subsequently, the anomaly propagates eastward along the Gulf Stream where it persists for about 10 days. After the anomaly reaches its maximum, it slowly decays at all locations except for Cape Hatteras where it reintensifies at $\delta = 20$ days.

The spatial pattern of net heat flux composites with respect to MJO phase 7 is, to first order, a mirror image of the anomalies for phase 3 at the same lags, but with reversed sign (Figure 2.6). The negative Q_{net} anomaly in the northern Gulf of Mexico and along the North American east coast occurs at $\delta = 12$ days after phase 7. However, the mirror imaging is not perfect. For example, the weak positive anomaly off the west coast of Africa "misses" its negative counterpart in the respective composite with respect to phase 3.

Overall, the composites show that there is a statistical relationship between the MJO and the net air-sea heat flux in the North Atlantic. The same composite analysis was conducted for the individual heat flux components in (2.6) and this indicated that the Q_{net} signal is primarily due to anomalies in sensible and latent heat flux (see Figures A.2 and A.3 in Appendix A). This will be further discussed in Section 2.5 where the heat flux composites are interpreted with respect to the large-scale atmospheric circulation linked to the MJO. The composites of incoming shortwave and outgoing longwave radiation are negligible and not statistically different from zero at the 10% significance level (not shown).

As already discussed for the SST composites, the quasi-periodicity of the MJO leads to an ambiguity as to which phase initiates the teleconnection between the tropics and the North Atlantic. This is again illustrated by the similarity of the anomaly response patterns along the diagonals in Figure 2.6. The lagged responses to phases 3 and 7 are also present in the contemporaneous composites ($\delta = 0$) with respect to phases 4 and 8, respectively (not shown). Given that the teleconnection timescale δ_{T} is on the order of 1–2 weeks (*Cassou*, 2008; *Lin et al.*, 2009) and also supported by the Q_{net} composites, the atmospheric perturbations leading to the heat flux anomalies are likely initiated by earlier phases.

Generally, the spatial structure of the heat flux and SST composites are similar. The difference in lags can be explained by the additional timescale δ_{O} for the SST to respond

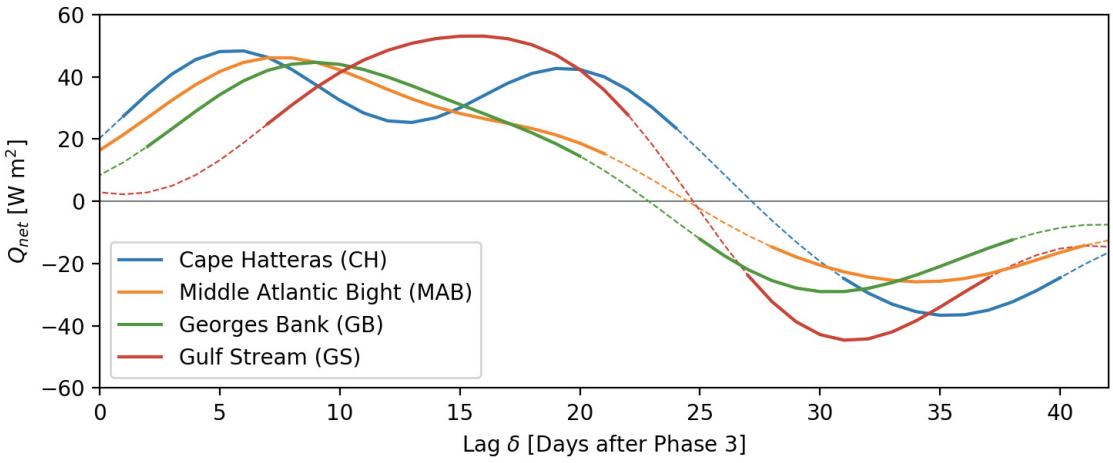

Figure 2.7: Composites of bandpass-filtered Q_{net} anomalies with respect to MJO phase 3 during winter when $A_{\text{RMM}} > 1$. Each composite is for one of the four representative locations along and off the east coast of North America shown in Figure 2.6. Solid lines indicate anomalies statistically different from zero at the 10% significance level.

to the anomalous heating or cooling. This supports the hypothesis that the SST anomalies are driven by large-scale atmospheric perturbations in response to the MJO. However, the Q_{net} anomalies are more spatially coherent than the SST composites suggesting that other processes, e.g., mesocale eddies or advection, and spatial variations in mixed layer depth, contribute to the spatial structure of the SST. Furthermore, the different spatial resolution of the datasets may also contribute to the discrepancy in the spatial scales of the composites.

The SST anomalies are an integrated response to the net air-sea heat flux into the ocean. In the following, a surface mixed layer model will be used to predict SST anomalies based on the observed heat fluxes. These predictions will be used to test the hypothesis that heat flux variations drive SST variability on S2S timescales and can explain the observed SST composites conditioned on the MJO.

2.4 Statistical-Dynamical Modelling of SST Anomalies

A surface mixed layer model is now used to test if air-sea heat flux variations related to the MJO are a significant driver of winter SST variability on S2S timescales for the North Atlantic.

2.4.1 Surface Mixed Layer Model

A simple one-dimensional surface mixed layer heat budget can be written (e.g., *Lagerloef et al.*, 1998)

$$\frac{\partial T_{\mathrm{a}}}{\partial t} = \frac{Q_{\mathrm{net}} - rQ_{\mathrm{sw}}}{\rho_0 c_{p,\mathrm{w}} H_{\mathrm{m}}} + M, \tag{2.9}$$

where T_{a} is the vertically averaged temperature anomaly in the mixed layer with depth H_{m}, Q_{net} is the net air-sea heat flux anomaly (positive downwards), and r is the fraction of incoming shortwave radiation Q_{sw} that reaches the base of mixed layer. $\rho_0 = 1026\,\mathrm{kg\,m^{-3}}$ and $c_{p,\mathrm{w}} = 3985\,\mathrm{J\,kg^{-1}\,K^{-1}}$ are the density and specific heat capacity of seawater, respectively. Other ocean processes, e.g., horizontal advection, vertical mixing, or entrainment, that cause dissipation of heat from the mixed layer are summarized by M.

During winter, the mixed layer in the North Atlantic is assumed to be deep enough that the penetrating Q_{sw} is negligibly small and therefore $r = 0$. The processes in M are parameterized as $-\lambda T_{\mathrm{a}}$. They include the effects of horizontal and vertical diffusion of T_{a} in restoring the temperature back to its climatology. As a result, (2.9) can be approximated by a first-order autoregressive model (e.g., *Lagerloef et al.*, 1998)

$$\frac{\partial T_{\mathrm{a}}}{\partial t} = \frac{Q_{\mathrm{net}}}{\rho_0 c_{p,\mathrm{w}} H_{\mathrm{m}}} - \lambda T_{\mathrm{a}}. \tag{2.10}$$

Note that (2.10) does not include advection which could also lead to SST anomalies and may play a role on S2S timescales.

Because the net heat flux associated with synoptic variability of the atmosphere has a shorter characteristic timescale in comparison to SST anomalies, Q_{net} can be considered as stochastic forcing of the surface ocean. The constant damping rate $\lambda > 0$, which has units time^{-1}, causes the model to have a statistically stationary response to stationary stochastic forcing (*Frankignoul and Hasselmann*, 1977). The response to an impulse is an exponential decay with an e-folding time λ^{-1}. If Q_{net} is purely stationary, the absence of dissipation ($\lambda = 0$) would lead to a linear increase of the SST anomaly variance over time. On the other hand, if $\lambda \to \infty$, any input of heat is rapidly dissipated and the predicted SST anomaly would tend to zero.

Using a simple, explicit forward differencing scheme, the discrete form of (2.10) becomes

$$T_{\mathrm{a}}^{t+1} = \frac{Q_{\mathrm{net}}^{t}}{\rho_0 c_{p,\mathrm{w}} H_{\mathrm{m}}^{t}} \Delta t + (1 - \lambda \Delta t)\, T_{\mathrm{a}}^{t}, \tag{2.11}$$

where Δt is the time difference between the model time steps denoted by superscript $t = 0, 1, ..., N$. Here, $\Delta t = 1$ day is used.

Based on the assumption that the temperature is constant throughout the surface mixed layer, the model in (2.11) can be applied to predict SST variations due to heat fluxes across the air-sea interface. Here, the observed daily bandpass-filtered Q_{net} anomalies are used as forcing to predict the resulting SST anomalies on S2S timescales at each grid point of the OAFlux dataset.

In order to determine the unknown model parameters H_{m} and λ that best describe the observed SST variability, the model in (2.11) was fit to the bandpass-filtered OISSTv2 anomalies. Alternatively, H_{m} could have been treated as a forcing variable, e.g., by using data from reanalyses or climatologies (e.g., *Deser et al.*, 2003). By treating the mixed layer depth as a model parameter, the predicted SST variability can be directly attributed to the heat fluxes.

Prior to the model fitting, the SST observations were linearly interpolated to the OAFlux grid and then bandpass-filtered using the same Butterworth filter mentioned in Section 2.2.2. Generally, the mixed layer depth can vary throughout the year, but here, H_{m} is assumed constant because the focus is on the winter months and the model was fit for this season only. This assumption has been shown to be suitable for predictions of low frequency SST variations (*Lagerloef et al.*, 1998). (Sensitivity experiments with time-varying mixed layer depth H_{m} did not yield a significant improvement of the model fit to the observations.)

The fitting procedure is based on an optimization algorithm that minimizes the mean squared error (e.g., *Wilks*, 2011, p. 325)

$$\text{MSE} = \frac{1}{N_W} \sum_{t \in W} (y_t - o_t)^2 \tag{2.12}$$

during winter, where y_t and o_t are the predicted and observed SST anomalies, respectively, and W is the set of N_W daily time indices for each winter from 1985 to 2009. This minimization technique corresponds to maximum likelihood estimation under the assumption that the errors have a Gaussian distribution.

The parameter estimation was conducted independently for all OAFlux grid points in the North Atlantic where both the interpolated SST and Q_{net} anomalies are available. To ensure physically interpretable results, the parameters were constrained as follows: 1 m

$\leq H_\mathrm{m} \leq 4000\,\mathrm{m}$ and $\lambda > 0\ \mathrm{day}^{-1}$.

For each grid point, SST anomalies were predicted using (2.11) with the optimized model parameters for the whole period 1985–2009 starting from an initial value of zero. The agreement between the observed and predicted winter SST anomalies was assessed using

$$R^2 = 1 - \frac{\sum_{t \in W} (y_t - o_t)^2}{\sum_{t \in W} (y_t - \overline{y})^2}, \tag{2.13}$$

where $R^2 = 0$ and $R^2 = 1$ mean no and perfect agreement, respectively. This measure of fit is motivated by the coefficient of determination (e.g., *Wilks*, 2011, p. 222) used to assess the fit of multiple linear regression models. In the present case, the predictions by the mixed layer model (2.11) do not vary linearly with the two model parameters and so it is possible for R^2 defined by (2.13) to become negative.

In order to test if R^2 is significantly different from zero, a bootstrapping method was applied. The predicted time series was divided into blocks of 90 days for each winter from 1 December through 28 February. These blocks were randomly shuffled to create an synthetic time series which was then compared to the observed winter SST anomalies using (2.13). This process was repeated 1000 times and from the resulting R^2 values, the quantiles of the underlying probability distribution were estimated. The R^2 of the original prediction is considered statistically different from zero at the 5% significance level if it is above the 95th percentile of the bootstrap distribution.

Figure 2.8a shows the model fit at the grid points in the study domain where R^2 is greater than the significance threshold. Generally, R^2 varies between 0.17 and 0.66 over large parts of the study domain. The best agreement of the predictions with the observations can be found along the coast in the Gulf of Mexico. Other areas of good model fit can be found on the continental shelf along the eastern seaboard of North America, in the Sargasso Sea, and southwest of the Azores. However, there are some regions (e.g., Gulf Stream, subpolar gyre) where there is no significant agreement between the model and the observations. Here, oceanographic processes which are not captured directly by the model, such as advection by large-scale currents, stirring by mesoscale variability and convective mixing, are more important determinants of temperature changes in the surface mixed layer. Overall, the significant values of R^2 demonstrate where net heat flux is important for determining the SST variability on S2S timescales in the North Atlantic.

As shown in Figure 2.8b, the estimated mixed layer depth H_m varies between 50–150 m

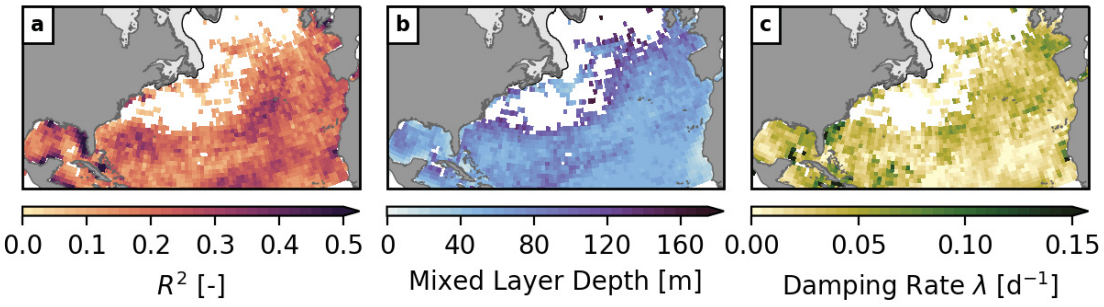

Figure 2.8: Estimated parameters and fit of the surface mixed layer model during winter. (a) Measure of model fit R^2 defined by (2.13). (b) Mixed layer depth H_m in meters. (c) Damping rate λ in day^{-1}. Note that the color scales have been clipped. Shaded areas near the coast show the climatological sea ice cover. Results are only shown at grid points where R^2 is statistically different from zero at the 5% significance level.

over most parts of the study domain where the model fit is significant. Along the coasts of North Africa and the Gulf of Mexico, lower values can be identified. The estimated H_m and its spatial distribution are in general qualitative agreement with available climatologies for the winter months (*Kara et al.*, 2003; *de Boyer Montégut et al.*, 2004).

Figure 2.8c shows the estimated damping rate λ. Over large areas of the North Atlantic $\lambda^{-1} = 25$–100 days and shorter relaxation timescales occur in the eastern Gulf of Mexico, in the South Atlantic Bight, and in the Bay of Biscay. These decay timescales for SST anomalies in response to forcing by air-sea heat fluxes are shorter than previously documented values of 3–6 months (e.g., *Frankignoul*, 1985; *Deser and Timlin*, 1997; *Deser et al.*, 2003). This discrepancy is likely related to the bandpass-filtering of the net heat flux which excludes variations on timescales longer than 100 days.

Overall, the simple one-dimensional surface mixed layer model forced by net heat flux anomalies is able to capture a significant part of the observed SST variability in the MJO frequency band in the study region. This demonstrates that air-sea heat flux variations over the North Atlantic are a major driver of the observed winter SST variability on S2S timescales. In the following section, a composite analysis of the SST predictions by the mixed layer model will be used to analyze if they also capture the observed relationship between SST and the MJO.

2.4.2 Composites of SST Predictions with Respect to the MJO

So far, it has been shown that the net heat flux Q_net accounts for a significant part of the SST variability on S2S timescales using a simple mixed layer model. As demonstrated in

Section 2.3.2, there is a statistical relationship between the MJO and Q_{net} in the extratropical North Atlantic. The predictions by the mixed layer model are now used to test if the simple dynamics in that model can explain the observed SST signal with respect to the MJO. The focus will be on the predicted SST anomalies with respect to phases 3 and 7 which have been shown to initiate robust teleconnections in the northern hemisphere.

Using the same procedure described in Section 2.3, composites of SST anomalies predicted by the mixed layer model were computed with respect to the MJO. Figure 2.9 shows composites of observed and predicted SST anomalies at lag $\delta = 24$ days after phases 3 and 7 during winter when the RMM amplitude $A_{\text{RMM}} > 1$.

Following MJO phase 3, the composite of the SST predictions shows a large-scale positive temperature anomaly in the northern Gulf of Mexico and spanning the entire mid-latitude North Atlantic. The largest anomalies generally occur near the coast. Additionally, a weak cold anomaly can be seen across the northern tropical Atlantic.

At lag $\delta = 24$ days after phase 7, the predicted SST composite shows a negative anomaly in the northern Gulf of Mexico and in the western North Atlantic. To the north and south of it, widespread warm anomalies are visible in the subpolar gyre and toward the equator. This similar to the well known SST tripole pattern which has been associated with anomalies in sensible and latent heat flux on monthly to seasonal timescales (e.g., *Cayan*, 1992a).

Similar patterns can also be seen in the composites of the predicted SST at lag $\delta = 18$ days after MJO phases 4 and 8 when the observed SST composites are more spatially coherent (Figure 2.10). This is again due to the quasi-periodicity of the MJO which, on average, spends 6 days in one phase. Therefore, the composites in Figures 2.9 and 2.10 roughly correspond to the same time.

The spatial structure of the predicted and observed SST composites are remarkably similar, but the predicted anomalies are generally smaller. One possible reason is the mixed layer model predicts an average temperature over the surface mixed layer while the observations in OISSTv2 are corrected to represent a "bulk" SST at about 0.5 m depth (*Reynolds et al.*, 2007). Another reason is that all parameters of the mixed layer model have been kept constant through time.

From the observed composites, it can be seen that the strongest SST anomalies occur in shallow regions near the coast. Due to the relatively coarse spatial resolution of the OAFlux dataset (1° grid spacing) the predicted SST anomalies are representative of a

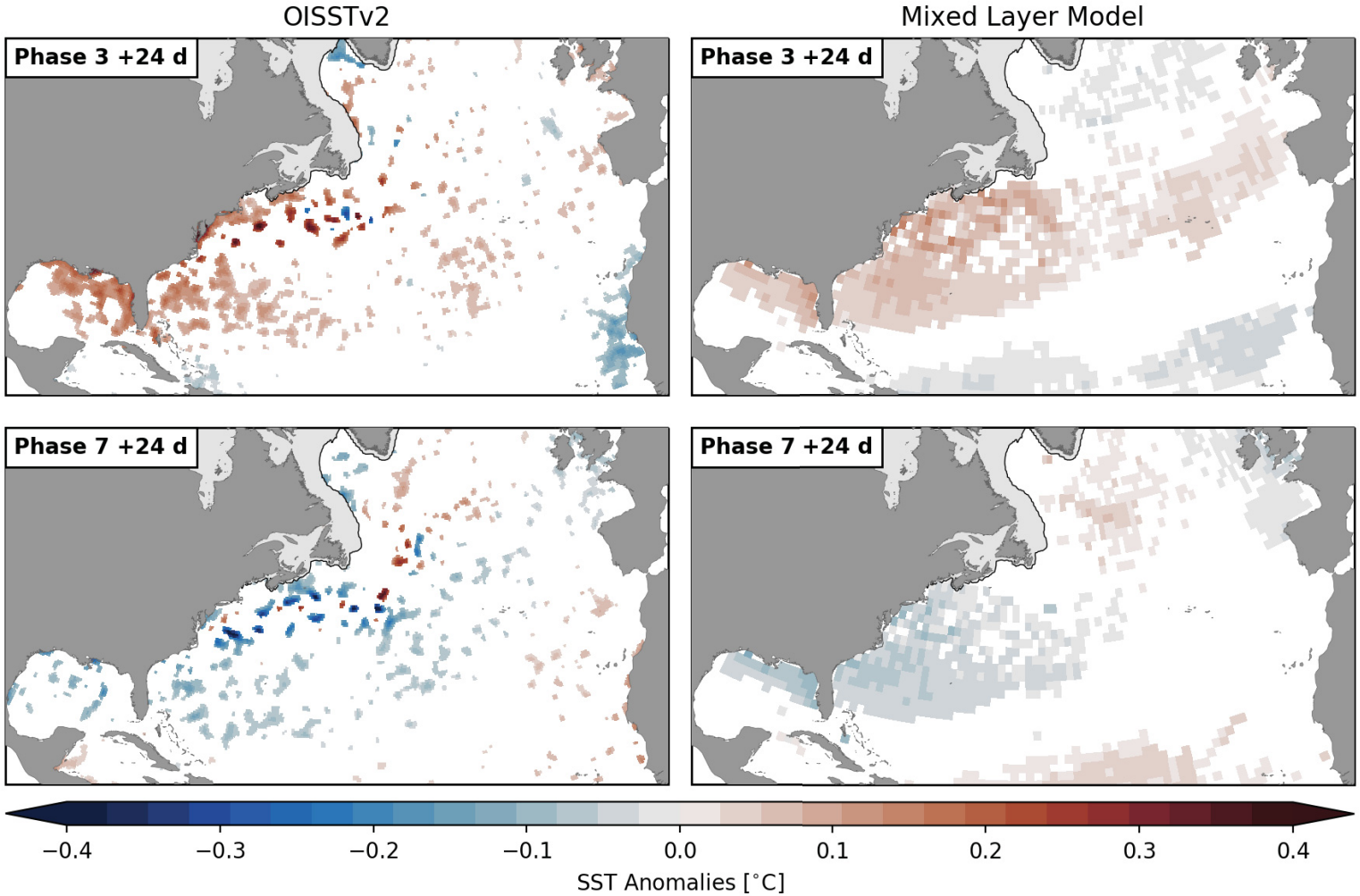

Figure 2.9: Composites of observed and predicted SST anomalies at lag $\delta = 24$ days after phases 3 and 7 during winter when the RMM amplitude $A_{\text{RMM}} > 1$. Only anomalies statistically different from zero at the 10% significance level are shown. Shaded areas near the coast show the climatological sea ice cover. Note that the composites of the observations were computed for the period 1981–2019 and are the same as in Figure 2.5.

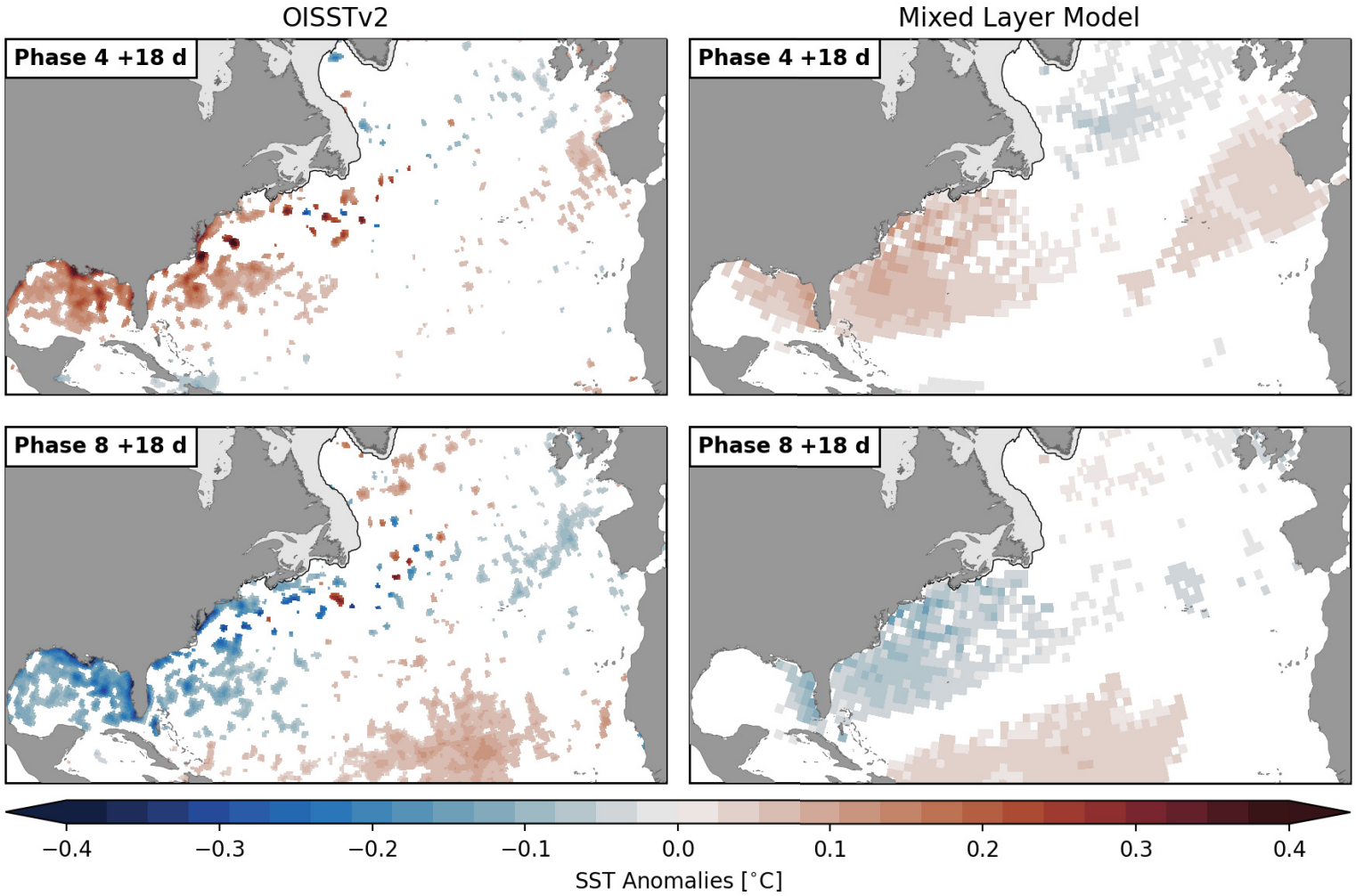

Figure 2.10: Same as Figure 2.9, but for lag $\delta = 18$ days after phases 4 and 8. Note that the composites in both figures roughly correspond to the same time due to the quasi-periodicity of the MJO.

larger area which, on the continental shelves, can cover water depths ranging from 10 to 100 m. This can lead to an underestimation of the SST anomalies.

Additionally, the predicted SST signal is generally smoother, and spatially more coherent, than the observed composites. This could be in part due to the different horizontal resolutions of the OISSTv2 and OAFlux. More importantly, it suggests that processes which are not captured in the mixed layer model, e.g., advection, also contribute to the response of SST to the MJO.

The remarkable agreement of the sign and overall spatial structure of the observed and predicted composites supports the hypothesis that the large-scale SST anomalies linked to the MJO are driven by the atmosphere.

2.5 Physical Mechanisms of the MJO/SST Teleconnection

As shown above, the net air-sea heat flux determines the SST variability on S2S timescales in large parts of the North Atlantic and can explain the observed anomalies in response to the MJO. In order to link the heat flux composites to the MJO, Figure 2.11 shows composites of atmospheric circulation anomalies during and after MJO phases 3 (left column) and 7 (right column). Rows correspond to lags $\delta = 0$, 6, ..., 24 days after these phases. The top panels also show composites of daily bandpass-filtered NOAA interpolated outgoing longwave radiation (OLR, *Liebmann and Smith*, 1996, obtained from the NOAA Physical Sciences Laboratory) anomalies over the Indian Ocean, Maritime Continent, and western Pacific which is a proxy for the large-scale atmospheric convection associated with the MJO. Phase 3 is characterized by a dipole of enhanced convection over the eastern Indian Ocean and suppressed convection over the western tropical Pacific. Half a MJO cycle later, during phase 7, the sign of this dipole is reversed.

Composites of 500 hPa daily geopotential height anomalies from the NCEP-DOE AMIP-II Reanalysis (*Kanamitsu et al.*, 2002) are shown as contours with dashed lines indicating negative values. In the North Atlantic, composites of net heat flux anomalies Q_{net} are shown. These fields are a subset of the composites shown in Figure 2.6, but without masking of statistically insignificant anomalies.

During phase 3 ($\delta = 0$ days), a series of alternating positive and negative anomalies of geopotential height span from the subtropical Pacific to the North Atlantic sector.

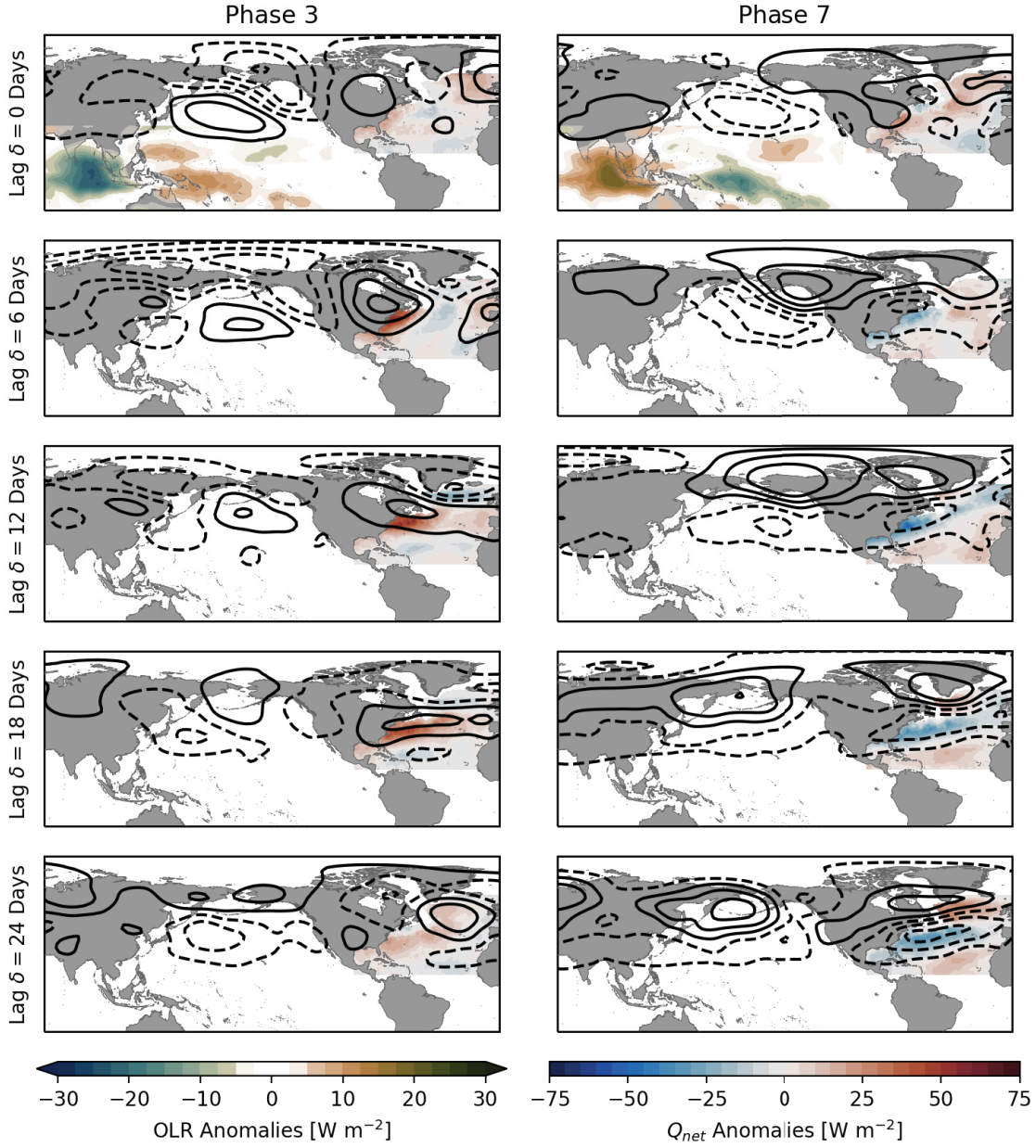

Figure 2.11: Atmospheric circulation anomalies during and after MJO phases 3 (left) and 7 (right). Bandpass-filtered outgoing longwave radiation (OLR, left color scale) anomalies are only shown at lag $\delta = 0$ days over the Indian Ocean, Maritime Continent, and western Pacific to illustrate the large-scale convection anomaly associated with the MJO. Negative (positive) values refer enhanced (suppressed) convection. Contours show anomalies of 500 hPa geopotential height (interval 20 m, zero line omitted) which illustrate the Rossby wave train propagating from the tropics to the North Atlantic region in response to the MJO. Dashed lines refer to negative values. In the North Atlantic, composites of net heat flux (Q_{net}, right color scale) are shown. These fields are a subset of the composites shown in Figure 2.6.

Comparing with the composites for $\delta > 0$ days it can be seen that the pattern propagates westward over time. This is the Rossby wave train that is induced by anomalous diabatic heating and cooling associated with the MJO convective dipole (e.g., *Sardeshmukh and Hoskins*, 1988) and has been shown to influence the extratropical atmospheric circulation (e.g., *Lin and Brunet*, 2009; *Lin et al.*, 2010; *Seo et al.*, 2016).

At lag $\delta = 6$ days after phase 3 a dipole can be observed with negative and positive anomalies of geopotential height over western and eastern North America, respectively. Together with the above normal geopotential height over the North Pacific, this is similar to the negative phase of the Pacific/North American Pattern (PNA), a prominent mode of extratropical variability in the northern hemisphere (*Wallace and Gutzler*, 1981). This is consistent with previous studies that have demonstrated a teleconnection between this PNA-like circulation and the MJO (e.g., *Riddle et al.*, 2013; *Seo and Lee*, 2017).

The corresponding anomalies in sea level pressure (SLP) and the associated gradient over North America are shifted westward with respect to the geopotential height anomalies shown in Figure 2.11. There is further deviation of the surface geostrophic flow field from the geostrophic flow at 500 hPa (not shown). Consequently, there is an anomalous northward geostrophic advection of warm and moist air over eastern North America at lag $\delta = 6$ days after MJO phase 3. This warm advection has been shown to lead to a significant increase in surface air temperature over Northeast America (*Seo et al.*, 2016). As illustrated in Figure 2.11, this also results in an increased net air-sea heat flux into the surface ocean along the eastern seaboard of North America. Similarly, the southwesterly surface geostrophic flow over the eastern North Atlantic leads to warm advection and slightly increased warming of the surface ocean in that region. The northwesterly flow over the Labrador sea advects cold and dry air masses from polar regions causing a small heat loss of the surface ocean in the subpolar North Atlantic which is not statistically significant (see Figure 2.6).

During and after MJO phase 7, the large-scale atmospheric circulation is, to first order, a mirror image of the response to phase 3 with reversed sign (right column in Figure 2.11). This results in a southward flow over North America and the western North Atlantic advecting cold and dry air masses from polar regions which leads to a negative heat flux anomaly along the eastern seaboard and in the northern Gulf of Mexico at lag $\delta = 6$ days. The positive heat flux anomaly in the eastern North Atlantic can be explained by

advection of warm and humid air from the south in agreement with the shown atmospheric circulation.

With increasing lag after both phase 3 and 7, the geopotential height anomalies over the North Atlantic intensify and a pattern reminiscent of the North Atlantic Oscillation (NAO) emerges in agreement with previous studies (e.g., *Cassou*, 2008; *Lin et al.*, 2009). The corresponding spatial structure of the net heat flux composites at lags $\delta = 12$ and 18 days is also similar to known patterns of the response to the atmospheric circulation related to the NAO on monthly to seasonal timescales (e.g., *Cayan*, 1992a,b; *Visbeck et al.*, 2003; *Somavilla Cabrillo et al.*, 2011). In the extratropics, these patterns can be largely explained by changes in sensible and latent heat flux due to differences in temperature and humidity, respectively, between the surface ocean and near-surface atmosphere caused by meridional advection of air masses. The heat flux anomalies in the northern tropical Atlantic can be attributed to changes in wind speed (*Cayan*, 1992a). On seasonal to interannual timescales, the anomalies of sensible and latent heat flux lead to the well know SST tripole pattern associated with the NAO (e.g., *Visbeck et al.*, 2003). This is also partly evident in the lagged SST composites with respect to the MJO shown in Figure 2.5.

The circulation anomalies can also explain the secondary peak of net heat flux near Cape Hatteras discussed in Section 2.3.2 (Figure 2.7). During the transition from the PNA-like to the NAO-like circulation, the advection of warm and humid air masses from the south is interrupted at a lag $\delta = 12$ days after phase 3. This is due to a general westward shift of the circulation pattern leading to the delayed arrival of the heat flux anomaly in the Gulf Stream region. As the positive geopotential height anomaly spreads across the North Atlantic at $\delta = 18$ days after phase 3, the southerly geostropic flow along the eastern seaboard of North America is re-established.

Overall, the atmospheric circulation in response to the MJO can explain the spatial structure of the net heat flux composites in the extratropical North Atlantic. This provides a physical mechanism for the teleconnection between the MJO and SST composites shown in Figure 2.5. Furthermore, it explains why the strongest SST response to the MJO occurs along the eastern seaboard of North America. This region is influenced by changes in the atmospheric circulation due to the Rossby wave train only a few days after it is induced in the tropics. As the atmospheric response spreads and intensifies across the North Atlantic, the heating or cooling of the surface ocean continues and therefore, a strong SST anomaly

develops.

2.6 Summary and Discussion

Based on composite analysis, a statistically significant relationship has been found between the MJO and SST anomalies in the North Atlantic. A widespread positive anomaly develops in the northern Gulf of Mexico, along the eastern seaboard of North America, and extending to the Sargasso Sea which reaches its maximum 20–25 days after MJO phase 3 depending on the location. Due to the quasi-periodicity of the MJO, a similar anomaly pattern can also be observed after phases 4–7, but at shorter lags, which illustrates the ambiguity between MJO phases and the time lag at which teleconnection occurs. The same issue arises after the other half of the canonical MJO cycle when a large-scale negative anomaly occurs in the same regions after MJO phases 7 and 8.

Clearly, the composite analysis cannot determine cause and effect. However, the large-scale structure of the SST anomalies suggests that they are driven by atmospheric perturbations in response to the MJO. This is supported by composites of net air-sea heat fluxes conditioned on the MJO which revealed anomalous heat exchange between the ocean and atmosphere prior to the SST anomalies. Additionally, predictions by a simplified surface mixed layer model demonstrated that a significant part of the SST variability in the North Atlantic on S2S timescales is determined by net heat flux anomalies. Composites of the predicted SST anomalies showed a remarkable agreement with the observed relationship with the MJO. Overall, these results are consistent with *Deser and Timlin* (1997) who demonstrated a strong relationship between heat fluxes and SST tendencies in the North Atlantic on weekly timescales. The spatial structure of both the SST and heat flux composites can be related to other modes of climate variability in the northern hemisphere (e.g., PNA and NAO) that have been shown to be linked to the MJO through a Rossby wave train.

Let us now return to the questions raised in the Introduction: *(i) Does the MJO influence SST in the North Atlantic on S2S timescales? (ii) How does this response differ between coastal regions, continental shelves, and the deep ocean? Where does the strongest response occur?* As outlined above, the MJO influences the SST in the North Atlantic with a lag $\delta = 3$–4 weeks. However, this relationship is indirect as the resulting SST anomalies are caused by local atmospheric perturbations which are a response to the MJO.

Consistent with atmospheric forcing, the spatial structure of the resulting SST anomalies is large-scale, but mostly focused on the western Atlantic. Along the path of the Gulf Stream, the SST response to the MJO is masked by mesoscale eddy variability which increases the background noise level in that region. The strongest SST anomalies occur in the northern Gulf of Mexico and in shallow, coastal regions along the eastern seaboard of North America, particularly in the Middle Atlantic Bight. A significant part of this signal also extends offshore to the Sargasso Sea where the surface ocean variability is predominantly determined by local air-sea heat fluxes and convergence of Ekman heat transport (e.g., *Buckley et al.*, 2014).

Note that δ is the sum of the timescales δ_{T} for the Rossby wave train to be established between the tropics and the Atlantic Sector and δ_{O} for the ocean to respond to anomalies in the atmospheric circulation. It is well established that δ_{T} is on the order of 1–2 weeks (e.g., *Cassou*, 2008; *Lin et al.*, 2009; *Riddle et al.*, 2013). Similarly, it has been shown that there is a 2–3 week lag between large-scale atmospheric modes of variability and corresponding SST anomalies on weekly timescales *Deser and Timlin* (1997). This shows that the estimated δ from the composite analysis is plausible and furthermore helps determine which phase is more likely to initiate the teleconnection between the MJO and SST in the North Atlantic.

(iii) What are the underlying physical mechanisms causing the SST response? The results presented in this chapter demonstrate that air-sea heat flux is the primary driver of SST variability on S2S timescales and can explain the spatial structure and timing of the SST composites with respect to the MJO. These heat fluxes arise from advection of warm and humid or cold and dry air masses which lead to anomalous sensible and latent heat exchange between the ocean and the atmosphere. Note that this study only focused on the response of the surface ocean to atmospheric perturbations related to the MJO. A possible feedback from the resulting SST anomalies to the atmosphere and potential downstream coupling with the tropics (e.g., *Lin et al.*, 2009) is beyond the scope of this study.

This leads to the last question raised in the introduction: *(iv) What are the implications for S2S predictions of the North Atlantic Ocean?* Through the teleconnection described in Section 2.5, the MJO acts as a source of predictability for SST variations in the North Atlantic on S2S timescales. The lagged nature of the relationship between the MJO and SST creates a temporal "window of opportunity" of enhanced predictability which

ultimately can lead to more accurate S2S forecasts of the ocean. In order to utilize this teleconnection, it is important that models are able to capture the interaction between the deep atmospheric convection in the tropics and the midlatitude circulation, and also the resulting heat flux anomalies. All of these processes involve air-sea interactions which underlines the importance for the atmosphere and ocean components of global S2S models to be coupled. For ocean circulation models to correctly capture the nearshore response to changes in air-sea fluxes, they need to have high spatial resolution and include tides which influence the thermal inertia through mixing. Additionally, it is important that the models correctly represent low-frequency variability on S2S timescales and longer including the mean state of the ocean circulation.

With regard to the overall objectives of this thesis, the results presented in this chapter provide an improved understanding of the extratropical ocean variability and predictability on S2S timescales. The documented air-sea interactions in the MJO frequency band are an encouraging first step toward the feasibility of S2S predictions of the ocean. Based on the strong SST response close to shore, it remains to be explored in more detail how the MJO influences the ocean circulation in coastal areas and on continental shelves. This will be addressed using the high-resolution ocean circulation model for the Gulf of Maine and Scotian Shelf (GoMSS) which includes all relevant physical processes.

CHAPTER 3

OCEAN DYNAMICS AND MODELS

In this chapter, the governing equations for ocean circulation referred to throughout the remainder of the thesis are discussed. The Gulf of Maine and Scotian Shelf regional ocean model is also introduced.

3.1 Equations of Motion

The governing equations for motion of an incompressible fluid in a rotating reference frame are (e.g., *Gill*, 1982, p. 75)

$$\frac{\partial \mathbf{v}}{\partial t} + \mathbf{v} \cdot \nabla \mathbf{v} + 2\boldsymbol{\Omega} \times \mathbf{v} = -\frac{1}{\rho}\nabla p - \mathbf{g} + \nu \nabla^2 \mathbf{v}, \tag{3.1}$$

$$\nabla \cdot \mathbf{v} = 0, \tag{3.2}$$

where $\mathbf{v}(\mathbf{x}, t) = u\hat{\boldsymbol{\imath}} + v\hat{\boldsymbol{\jmath}} + w\hat{\mathbf{k}}$ is the fluid velocity at a given location $\mathbf{x}$ varying with time t. The horizontal unit vectors $\hat{\boldsymbol{\imath}}$ and $\hat{\boldsymbol{\jmath}}$ in zonal and meridional direction, respectively, are perpendicular to the orientation of local gravity indicated by the unit vector $\hat{\mathbf{k}}$. The vector $\boldsymbol{\Omega}$ has a magnitude equal to the constant angular velocity of the reference frame and is parallel to its axis of rotation. $\rho(\mathbf{x}, t)$ is the fluid density, $p(\mathbf{x}, t)$ is the fluid pressure, $-\mathbf{g} = -g\hat{\mathbf{k}}$ is the vertical acceleration due to gravity with magnitude g, and ν is the kinematic viscosity.

The large-scale ocean circulation is characterized by a small aspect ratio and therefore, the Coriolis terms in the horizontal components of (3.1) involving the vertical velocity can be neglected (e.g., *Vallis*, 2017, p. 65). Additionally, the vertical component of (3.1) can be approximated by the hydrostatic balance between the vertical pressure gradient and the

gravitational term. Thus, the momentum equation (3.1) can be written

$$\frac{\partial \mathbf{u}}{\partial t} + \mathbf{u} \cdot \nabla_z \mathbf{u} + w \frac{\partial \mathbf{u}}{\partial z} + f\hat{\mathbf{k}} \times \mathbf{u} = -\frac{1}{\rho} \nabla_z p + \mathbf{D}, \tag{3.3}$$

$$\frac{\partial p}{\partial z} = -\rho g, \tag{3.4}$$

where $\mathbf{u}(\mathbf{x}, t) = u\hat{\boldsymbol{\imath}} + v\hat{\boldsymbol{\jmath}}$ is the horizontal velocity at a given point and ∇_z is taken to be the two-dimesional gradient operator at a constant value of z (e.g., *Vallis*, 2017, p. 106). $f = 2\Omega \sin \phi$ is the Coriolis parameter at latitude ϕ and Ω is the Earth's angular velocity and $\mathbf{D}$ describes the combined effect of lateral and vertical mixing of horizontal momentum.

The coordinate system is chosen such that the surface at $z = 0$ is the geoid. The geoid is defined as a surface of constant geopotential that describes the shape of the sea level in the absence of winds and tides (*Gregory et al.*, 2019). This hypothetical surface is purely defined by the combined gravitational and centrifugal potential due to the Earth's mass and rotation (*Hughes et al.*, 2006). If the ocean were at rest, the air-sea interface would coincide with this surface, but dynamical processes cause the sea level, in the following denoted by η, to generally deviate from the geoid.

The density can be written as the sum of a constant reference density and a pertubation, $\rho = \rho_0 + \rho'$. In the following, the Boussinesq approximation is applied where ρ' is neglected, except when multiplied by g (*Spiegel and Veronis*, 1960).

Integrating the hydrostatic balance (3.4) from z to the sea surface η, the horizontal pressure gradient term can be written as

$$\frac{1}{\rho_0} \nabla_z p = \frac{1}{\rho_0} \nabla_z p_\mathrm{a} + g \nabla_z \eta + g \nabla_z \int_z^\eta \epsilon \, dz, \tag{3.5}$$

where p_a is the atmospheric pressure at the air-sea interface and $\epsilon = \rho'/\rho_0$ is the normalized density perturbation. This equation splits the oceanic pressure gradient into a barotropic and baroclinic part. Note that instead of a constant reference density, a mean profile can be chosen around which the pertubations are defined (e.g., *Sheng and Thompson*, 1996).

Substituting (3.5) into (3.3) gives

$$\frac{\partial \mathbf{u}}{\partial t} + \mathbf{u} \cdot \nabla_z \mathbf{u} + w \frac{\partial \mathbf{u}}{\partial z} + f\hat{\mathbf{k}} \times \mathbf{u} = -\frac{1}{\rho_0} \nabla_z p_\mathrm{a} - g \nabla_z \eta - g \nabla_z \int_z^\eta \epsilon \, dz + \mathbf{D}. \tag{3.6}$$

3.2 Depth-Averaged Momentum and Vorticity Equations

Integrating (3.6) from the sea floor at $z = -H$ to the sea surface and dividing by the total water depth

$$h = H + \eta \tag{3.7}$$

yields the depth-averaged horizontal momentum equation which explicitly includes kinematic wind stress $\boldsymbol{\tau}^{\mathrm{w}}$ and bottom friction $\boldsymbol{\tau}^{\mathrm{b}}$ (*Robinson*, 1983, p. 333):

$$\begin{aligned}\frac{\partial \overline{\mathbf{u}}}{\partial t} + \overline{\mathbf{u}} \cdot \nabla_z \overline{\mathbf{u}} + f\hat{\mathbf{k}} \times \overline{\mathbf{u}} \\ = -\frac{1}{\rho_0}\nabla_z p_{\mathrm{a}} - g\nabla_z \eta - \frac{g}{h}\int_{-H}^{\eta} \nabla_z \int_z^{\eta} \epsilon \, dz' \, dz + \frac{\boldsymbol{\tau}^{\mathrm{w}} - \boldsymbol{\tau}^{\mathrm{b}}}{h} + \overline{\mathbf{D}}_{\mathrm{l}}.\end{aligned} \tag{3.8}$$

Here,

$$\overline{\mathbf{u}} = \frac{1}{h}\int_{-H}^{\eta} \mathbf{u} \, dz \tag{3.9}$$

is the depth-averaged current and $\overline{\mathbf{D}}_{\mathrm{l}}$ denotes the depth-averaged lateral mixing term. Note that the terms arising from depth-averaging the advection term due to vertical structure of the horizontal flow have been neglected (e.g., *Robinson*, 1983, p. 332).

The depth-averaged baroclinic horizontal pressure gradient in (3.8) can be written

$$\frac{g}{h}\int_{-H}^{\eta} \nabla_z \int_z^{\eta} \epsilon \, dz' \, dz = g\nabla_z \int_{-H}^{\eta} \epsilon \, dz + \frac{1}{h}\nabla_z \int_{-H}^{\eta} g\epsilon z \, dz = -g\nabla_z \eta_{\mathrm{s}} + \frac{1}{h}\nabla_z \chi, \tag{3.10}$$

where

$$\eta_{\mathrm{s}} = -\int_{-H}^{\eta} \epsilon \, dz \tag{3.11}$$

is the steric contribution to the sea level and

$$\chi = g\int_{-H}^{\eta} z\epsilon \, dz \tag{3.12}$$

is the vertically integrated potential energy anomaly (e.g., *Olbers et al.*, 2012, p. 460). Note is has been assumed that the factor in front of the steric height gradient is approximately equal to one (see Appendix B for a discussion of this assumption).

Using the vector identity $\nabla(\mathbf{A}\cdot\mathbf{B}) = (\mathbf{A}\cdot\nabla)\mathbf{B}+(\mathbf{B}\cdot\nabla)\mathbf{A}+\mathbf{A}\times(\nabla\times\mathbf{B})+\mathbf{B}\times(\nabla\times\mathbf{A})$, the advection term in (3.8) can be rewritten as (e.g., *Pedlosky*, 1987, p. 35)

$$\overline{\mathbf{u}}\cdot\nabla_z\overline{\mathbf{u}} = \nabla_z\left(\frac{|\overline{\mathbf{u}}|^2}{2}\right) + \zeta\hat{\mathbf{k}}\times\overline{\mathbf{u}}, \tag{3.13}$$

where

$$\zeta = \hat{\mathbf{k}}\cdot\nabla\times\overline{\mathbf{u}} \tag{3.14}$$

is the vertical component of relative vorticity of the depth-averaged flow.

Combining (3.8)–(3.13) leads to the vector-invariant form

$$\underbrace{\frac{\partial\overline{\mathbf{u}}}{\partial t}}_{\text{A}} + \underbrace{\nabla_z\left(\frac{|\overline{\mathbf{u}}|^2}{2}\right)}_{\text{B}} + \underbrace{(f+\zeta)\hat{\mathbf{k}}\times\overline{\mathbf{u}}}_{\text{C}} = \underbrace{-g\nabla_z\left(\eta-\eta_{\text{s}}+\frac{p_{\text{a}}}{g\rho_0}\right)}_{\text{D}} \underbrace{-\frac{1}{h}\nabla_z\chi}_{\text{E}} + \underbrace{\frac{\boldsymbol{\tau}^{\text{w}}-\boldsymbol{\tau}^{\text{b}}}{h}}_{\text{F}} + \underbrace{\overline{\mathbf{D}}_{\text{l}}}_{\text{G}}\ . \tag{3.15}$$

The terms on the left-hand side in (3.15) are the local rate of change of the depth-averaged current (A), the gradient of the Bernoulli setdown (B), and the Coriolis term modified to include the effect of relative vorticity (C). These terms are balanced by the gradient of total sea level including the inverse barometer effect (D), the gradient of depth-integrated potential energy anomaly (E), the difference between wind and bottom stress (F), and lateral mixing (G).

Taking the curl of (3.15), leads to the following equation for the vorticity of the depth-averaged flow:

$$h\frac{D}{Dt}\left(\frac{f+\zeta}{h}\right) = J\left(\chi, h^{-1}\right) + \hat{\mathbf{k}}\cdot\nabla\times\left(\frac{\boldsymbol{\tau}^{\text{w}}-\boldsymbol{\tau}^{\text{b}}}{h}\right) + \hat{\mathbf{k}}\cdot\nabla\times\overline{\mathbf{D}}_{\text{l}}. \tag{3.16}$$

The left-hand side can be written as

$$h\frac{D}{Dt}\left(\frac{f+\zeta}{h}\right) = \frac{\partial}{\partial t}(f+\zeta) + \overline{\mathbf{u}}\cdot\nabla_z(f+\zeta) - \frac{(f+\zeta)}{h}\overline{\mathbf{u}}\cdot\nabla_z h \tag{3.17}$$

which is the total change of potential vorticity following a fluid column. The right-hand side expresses this term as a sum of contributions by the local rate of change and advection of absolute vorticity as well as vortex tube stretching by flow across isobaths.

The first term on the right-hand side of (3.16) is the joint effect of baroclinicity and relief (JEBAR, *Sarkisyan and Ivanov*, 1971)

$$J\left(\chi, h^{-1}\right) = \frac{\partial \chi}{\partial x}\frac{\partial h^{-1}}{\partial y} - \frac{\partial \chi}{\partial y}\frac{\partial h^{-1}}{\partial x}. \tag{3.18}$$

As shown by *Mertz and Wright* (1992), this can be interpreted as the curl of a horizontal force exerted on the fluid by the bottom. They furthermore showed that JEBAR acts as a correction to the vortex stretching term in (3.16) by removing the nonphysical contribution of the geostrophic flow referenced to the bottom. Note that JEBAR vanishes in the case of constant water depth. The remaining terms in (3.16) describe the net torque exerted by the difference between wind stress and bottom friction, and vorticity dissipation due to lateral mixing.

3.3 Gulf of Maine and Scotian Shelf Model (GoMSS)

The Gulf of Maine and Scotian Shelf model, henceforth referred to as GoMSS, was initially developed by *Katavouta and Thompson* (2016) in an effort to downscale ocean conditions in the Northwest Atlantic. The model domain covers the continental shelf from the western Grand Banks to Cape Cod including the Gulf of Maine and Bay of Fundy as well as adjacent parts of the Atlantic Ocean. In the north, an open boundary exists across Cabot Strait (Figure 3.1). In the region of the model domain, the bottom topography is complex with a series of deep channels and basins (*Thompson and Sheng*, 1997). Tides, wind stress, buoyancy fluxes, and deep ocean circulation cause the hydrography to vary across a variety of temporal and spatial scales (e.g., *Smith and Schwing*, 1991).

Originally, the model was based on version 3.1 of the Nucleus for European Modelling of the Ocean (NEMO, *Madec et al.*, 2017). As part of this thesis, the GoMSS model has been updated to version 3.6 of the NEMO ocean model. Additional modifications have been made as detailed below.

Within the NEMO framework, the continuity equation 3.2 and the momentum equations (3.3)–(3.4) in their vector-invariant form are discretized on a curvilinear Arakawa C-grid (*Arakawa and Lamb*, 1977, see Figure 3.2) where scalar quantities, e.g., sea level, temperature, and salinity, are defined at the center of each grid cell (T-points). The velocity components are defined in the middle of the right (u-points) and upper edge (v-points),

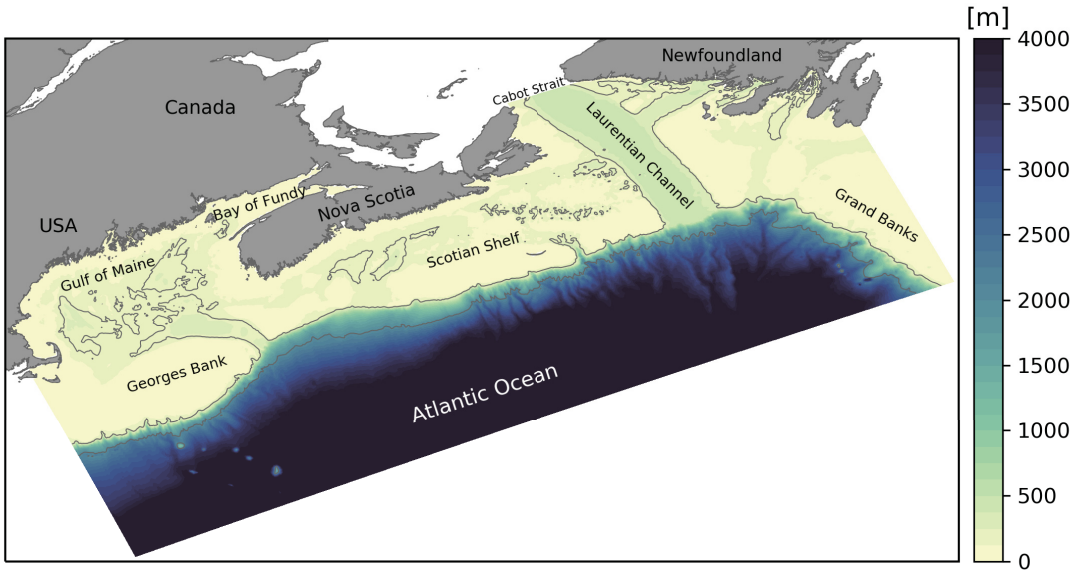

Figure 3.1: Model domain and bathymetry of the Gulf of Maine and Scotian Shelf regional ocean model GoMSS. The contours indicate the 200 and 2000 m isobaths.

respectively. In the model, the coastline is defined along the edges of the grid cells and thus, it is straightforward to invoke the boundary condition of no normal flow.

The x-axis of the coordinate system in GoMSS is broadly aligned with the large-scale orientation of the coastline with an anti-clockwise rotation angle of 23.6°. The horizontal grid spacing is 1/36° which corresponds to 2.1–2.5 km in the x-direction and 2.9–3.6 km in the y-direction. In the vertical, the model grid consists of 52 levels which, in a state of rest, increase in thickness from 0.72 m at the surface to 235.33 m at the bottom. The maximum depth of the bathymetry is clipped at 4000 m. GoMSS uses a variable volume formulation of the nonlinear free surface (z*-coordinates) which means the thickness of all model levels varies over time, scaled by sea surface height (*Levier et al.*, 2007). At the bottom, partial cells are applied to better resolve the bathymetry.

Based on model test runs, the TKE turbulent closure scheme in the original configuration of GoMSS was replaced by the k-ϵ-closure scheme (*Rodi*, 1987) through the Generic Length Scale (GLS) formulation (*Umlauf and Burchard*, 2003, 2005). The enhanced vertical diffusion of momentum applied in the original configuration was turned off. Furthermore, an iso-level Laplacian diffusion operator is applied instead of a biharmonic operator for stability reasons. The background lateral eddy viscosity coefficient $A_{\mathrm{h}}^{\mathrm{m}} = 50\,\mathrm{m^2\,s^{-1}}$.

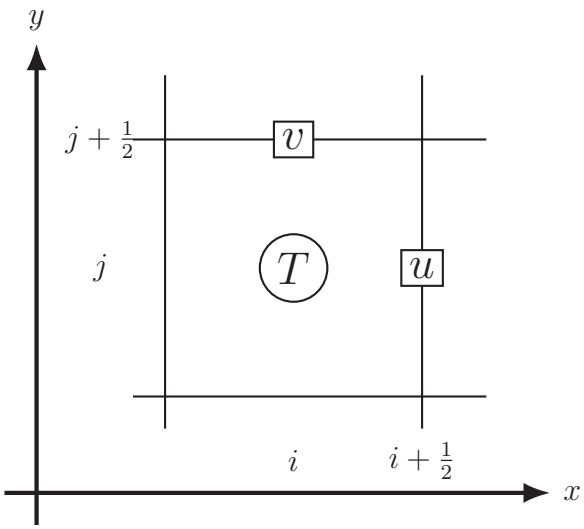

Figure 3.2: Schematic of the staggering of variables on an Arakawa C-grid (*Arakawa and Lamb*, 1977). Scalar quantities are evaluated in the center of each grid cell. The vector components are defined at the edges of each grid cell.

A nonlinear parameterization of bottom friction with enhancement in the logarithmic boundary layer is used. That means the drag coefficient c_{d} is dependent on the thickness of the model grid cell above the bottom. The minimum value was set to $c_{\mathrm{d}} = 2.5 \times 10^{-3}$. At the coast, a partial slip boundary condition with a value of 0.5 is applied which introduces lateral friction to reduce the tangential velocity at the coast.

Along the open boundaries, GoMSS is forced either with output from the data-assimilative HYCOM-NCODA analysis system (1/12°, approximately 7 km grid spacing, *Chassignet et al.*, 2007) or the Global Ocean Physical Reanalysis product (GLORYS12v1, 1/12° grid spacing, *Fernandez and Lellouche*, 2018). Sea level, currents, ocean temperature, and salinity are prescribed using the Flow Relaxation Scheme (*Davies*, 1976; *Engedahl*, 1995) which smoothly introduces the external data over 10 grid cells adjacent to the open boundaries. Additionally, tidal elevation and depth-averaged currents for five constituents (M_2, N_2, S_2, K_1, O_1) from the barotropic Finite Element Solution global tide model (FES2004, *Lyard et al.*, 2006) are prescribed using the Flather radiation scheme (*Flather*, 1994). No nudging or data assimilation is applied in the interior of the model domain.

At the air-sea interface, GoMSS is forced with data from the NCEP Climate Forecast System Reanalysis (CFSR, *Saha et al.*, 2010, for period 1979 to 2010) and its successor the Climate Forecast System model version 2 (CFSv2, *Saha et al.*, 2014, for the period

2011 to present). The atmospheric forcing is calculated in GoMSS using the Coordinated Ocean-Ice Reference Experiment (CORE) bulk formulae (*Large and Yeager*, 2004) for air-sea fluxes of heat and momentum using the following variables: wind at 10 m above ground, air temperature and specific humidity at 2 m above the ground, precipitation rate, as well as longwave and incoming short wave radiation.

The model equations are integrated in time using a split-explicit, free surface formulation following *Shchepetkin and McWilliams* (2005). This approach evaluates separately the fast-moving barotropic (depth-averaged) and slower baroclinic motions using different time steps. In GoMSS, the barotropic and baroclinic timesteps are 6 s and 180 s, respectively.

As demonstrated by *Katavouta and Thompson* (2016) and *Katavouta et al.* (2016), GoMSS improves the representation of shelf circulation compared to HYCOM, a global system with lower resolution. They furthermore showed that GoMSS provides realistic predictions of the tidal variability in the region as well as their dynamical interaction on tidal and seasonal timescales.

However, GoMSS predicts an unexpectedly large setdown of MDT in the upper reaches of the Bay of Fundy. This raised concern about the ability of GoMSS to predict the quasi-steady circulation on S2S timescales. Therefore, a lot of effort has gone into validating the model using newly available geodetic estimates of MDT based on sea level measurements by coastal tide gauge and one of the latest generation geoid model (Chapter 4). The cause of the MDT setdown in the Bay of Fundy is examined in Chapter 5.

CHAPTER 4

COASTAL MDT AND IMPLICATIONS FOR MODEL VALIDATION AND OCEAN MONITORING

4.1 Introduction

It has long been recognized that the alongshore tilt of mean dynamic topography (MDT) plays an important role in the dynamics of shelf circulation (e.g., *Scott and Csanady*, 1976; *Csanady*, 1978; *Hickey and Pola*, 1983; *Werner and Hickey*, 1983; *Lentz*, 2008). On the inner shelf (the region just outside the surf zone in water depths of order ten meters) frictional effects are dominant. Furthermore, due to the coastal constraint of no normal flow, currents in the nearshore mostly vary in alongshore direction (*Lentz and Fewings*, 2012). It has been shown that this results in continental shelves acting as a low wave number filter (*Huthnance*, 2004). This implies that mesoscale variations of sea level in the deep ocean are attenuated and only signals with large length scales on the order of thousand kilometers can be detected at the coast.

On the shelf, a multitude of drivers including wind stress, input of freshwater by rivers, and tidal rectification contribute to the circulation and thus impact the sea level at the coast (*Lentz and Fewings*, 2012). It is important to note that the coast acts as a waveguide and the effect of these drivers can be felt long distances "downstream" in the sense of coastal trapped wave propagation (*Csanady*, 1978; *Thompson*, 1986; *Thompson and Mitchum*, 2014; *Frederikse et al.*, 2017; *Hughes et al.*, 2019). The large number of drivers, and the possibility of remote effects, has resulted in debate about the origin of the observed alongshore pressure gradient at the coast (e.g,. *Csanady*, 1978; *Chapman et al.*, 1986; *Xu*

and Oey, 2011).

MDT appears in the momentum equation in the form of a gradient term and thus is an integrated measure of the mean circulation. This makes MDT a potentially useful variable for the validation of ocean models. The direct observation of MDT is complicated by the need to specify the geoid. However, recent advances in geodesy have led to new and improved models of the geoid which can be used to get reliable estimates of MDT at coastal tide gauges (*Woodworth et al.*, 2012). These independent measurements are accurate on the centimeter level (*Huang*, 2017) and thus provide potentially valuable information for the validation of ocean and shelf circulation models.

Higginson et al. (2015) compared multiple global ocean models with geodetically referenced sea level observations along the east coast of North America using different geoid models. While they showed a general convergence between the estimates of MDT, they also pointed out that some models predicted a drop near Cape Hatteras which is not evident in the observations. They concluded that these models did not capture the attenuation of the deep ocean signal over the shelf. A similar analysis was done by *Lin et al.* (2015) for the Pacific coasts of North America and Japan. They demonstrated a good agreement between the two approaches and furthermore used an analysis of the momentum budget along the coasts to illustrate the dominant dynamics behind the observed MDT. These studies as well as others (e.g., *Hughes et al.*, 2015; *Ophaug et al.*, 2015; *Woodworth et al.*, 2015; *Filmer et al.*, 2018) illustrate the value of the newly available geodetic estimates of coastal MDT for model validation. On the other hand, the overall convergence of the geodetically estimated and predicted MDT simultaneously also increases confidence in the geoid models (*Huang*, 2017).

Most of the previous studies, including the ones mentioned above, focus on global and basin-scale variability of MDT at the coast. There are however significant variations on smaller scales that are on the same order of magnitude as the accuracy of the geoid models. This chapter focuses on the Gulf of Maine and Scotian Shelf (GoMSS) model described in Section 3.3 of the previous chapter. The circulation in the GoMSS region is part of a large-scale buoyancy-driven coastal circulation originating along the south coast of Greenland (*Chapman and Beardsley*, 1989). It is also strongly influenced on smaller scales by tidal rectification which can generate mean currents up to $20\,\mathrm{cm\,s^{-1}}$ (*Loder*, 1980). These small-scale features, including the mean effect of tides, are included in the

GoMSS model. (The horizontal resolution of this model is significantly higher, by a least a factor three, than the global and basin-scale models referenced above.) This leads to the first question addressed in this chapter: Can new observations of geodetically referenced coastal sea level help validate high-resolution regional ocean models like GoMSS?

The second question is what can the alongshore tilt of MDT at the coast tell us about shelf circulation, followed by, what are the implications for coastal monitoring? These questions are of practical importance because (i) MDT provides an integrated measure of the mean circulation, (ii) tide gauges are cheap to deploy and maintain compared to many other oceanographic observing platforms (e.g., ships and gliders), and (iii) long records (several decades of hourly data) exist for some locations thereby providing background against which to interpret more recent variability. Using GoMSS and several idealized models, it will be shown that alongshore MDT can be used to estimate not only flow along the coast, but also area-integrated measures of upwelling offshore.

The remainder of this chapter is structured as follows. Section 4.2 provides a description of the approaches to estimate coastal MDT from sea level observations and ocean models. In Section 4.3, two views of the dynamical role of the alongshore tilt of MDT at the coast are introduced. These views are illustrated in Section 4.4 using idealized models of ocean circulation. In Section 4.5, the mean circulation and MDT predicted by GoMSS are presented and validated using geodetically referenced sea level measurements by tide gauges. The mean alongshore momentum balance predicted by GoMSS is discussed in Section 4.6. Section 4.7 provides an analysis of the predicted tilt of MDT along the coast of Nova Scotia with respect to the two dynamical interpretations. In Section 4.8, the results are summarized an implications for ocean monitoring are discussed.

4.2 Estimating the Alongshore Tilt of Coastal MDT

The alongshore tilt of MDT can be estimated using two independent approaches based on sea level observations and ocean circulation models. In this section, these approaches are outlined and information about data used in this study is presented.

4.2.1 Geodetic Approach

In the geodetic approach, sea level measurements by tide gauges relative to tidal benchmarks are referenced to a common vertical datum which traditionally is estimated by

spirit levelling (*Huang*, 2017). Recent advances by the geodetic community have led to new and improved high-resolution geoid models with an accuracy of several centimeters. These geoid models provide the geoid height relative to a reference ellipsoid. Through satellite-based navigation systems (e.g., Global Positioning System, GPS), sea level heights measured by tide gauges relative to the same ellipsoid can be determined. Subtracting the local geoid height yields an estimate of the MDT

$$\eta = \eta_{\mathrm{BM}} + h_{\mathrm{e}} - N, \tag{4.1}$$

where η_{BM} is the mean sea level (MSL) relative to the GPS tidal benchmark with height h_{e} above the reference ellipsoid and N is the geoid height above the same ellipsoid.

MSL values were computed from hourly observations of sea level at available tide gauges in the Gulf of Maine and Scotian Shelf area for the period 2011–2013. These tide gauges measure the real, observed height of the air-sea interface using acoustic, microwave radar, or air pressure-compensated pressure sensors. Since the focus of this study is on the regional-scale MDT signal, only tide gauges which are not influenced by highly localized effects were considered (see below). Table 4.1 gives a summary of the stations used in this study and their locations are shown in Figure 4.1. Overall, the proportion of missing values over the study period is less than 3% at all stations.

The tide gauge for Saint John, NB, Canada (CHS ID #65) was excluded because it is situated in the mouth of St. John River which is sheltered by breakwaters. It follows that sea level variations at this tide gauge are likely to be dominated by local processes (e.g., tides and river discharge). Furthermore, the tide gauge in Chatham, Lydia Cove, MA (NOAA ID #8447435) was excluded because of its location in a shallow lagoon behind a series of sandbars.

The permanent tide gauges located in Halifax, NS, Canada (CHS ID #490) and at the Bedford Insitute of Oceanography, Dartmouth, NS, Canada (CHS ID #491) are only a few kilometers apart. Here, the record at the latter will be used because it has fewer missing values and is closer to the GPS benchmark. (The resulting MDTs agree within millimeters.)

Table 4.1: Summary of geodetic MDT observations in the study area for the period 2011–2013. The numbers in parentheses after the station name are the IDs in the NOAA and CHS databases, respectively. The columns Lat. and Lon. list coordinates of the tide gauges. BM ID refers to the permanent identifiers of the GPS benchmarks assigned by NGS and NRCAN and the ellipsoidal height at these benchmarks are listed under h_e. The geoid height N interpolated to the benchmark locations are listed in column CGG2013a. In the last column, the resulting geodetic estimates of MDT are presented. Their error is a combination of the errors in h_e and N and were calculated using standard error propagation rules.

	Name	Lat. [°N]	Lon. [°E]	BM ID	h_e [m]	CGG2013a [m]	MDT [m]
SYD	North Sydney (612)	46.2167	-60.2500	NS29101	29.502840 $\pm$ 0.010	-13.180 $\pm$ 0.012	-0.201 $\pm$ 0.016
BIO	Bedford Institute (491)	44.6833	-63.6167	961000	3.099574 $\pm$ 0.000	-21.469 $\pm$ 0.012	-0.224 $\pm$ 0.012
YAR	Yarmouth (365)	43.8333	-66.1167	XXN9007	-19.457698 $\pm$ 0.015	-23.201 $\pm$ 0.011	-0.260 $\pm$ 0.019
EAS	Eastport (8410140)	44.9033	-66.9850	PD1179	-18.828134 $\pm$ 0.006	-23.303 $\pm$ 0.013	-0.321 $\pm$ 0.015
CFW	Cutler Farris Whf (8411060)	44.6570	-67.2047	PD0497	-16.757344 $\pm$ 0.014	-23.243 $\pm$ 0.022	-0.309 $\pm$ 0.026
BAR	Bar Harbor (8413320)	44.3917	-68.2050	BBGN12	-18.875490 $\pm$ 0.004	-24.797 $\pm$ 0.016	-0.305 $\pm$ 0.017
POR	Portland (8418150)	43.6567	-70.2467	AJ2726	-24.168144 $\pm$ 0.004	-26.996 $\pm$ 0.012	-0.298 $\pm$ 0.012
WEL	Wells (8419317)	43.3200	-70.5633	BBCF81	-23.691065 $\pm$ 0.007	-27.333 $\pm$ 0.013	-0.312 $\pm$ 0.015
BOS	Boston (8443970)	42.3539	-71.0503	AJ4030	-26.394000 $\pm$ 0.005	-28.666 $\pm$ 0.010	-0.266 $\pm$ 0.011

For stations in the US, hourly water level records with respect to Mean Lower Low Water (MLLW) were retrieved from the National Oceanic and Atmospheric Administration (NOAA). GPS ellipsoidal heights at nearby benchmarks were obtained from the Online Positioning User Service (OPUS) provided by the National Geodetic Survey (NGS). Their shared solutions list benchmark coordinates relative to the North American Datum, NAD83(2011) epoch 2010.0. They were converted to the International Terrestrial Reference System, ITRF2008 epoch 2010.0 (*Altamimi et al.*, 2011), using the Horizontal Time-Dependent Positioning tool (HTDP, *Pearson and Snay*, 2013) provided by NGS. At benchmarks where multiple OPUS shared solutions were available, the one with the smallest uncertainty in observed ellipsoidal height was chosen. Using information from benchmark sheets about the relative height of the benchmarks with respect to MLLW, the sea level observations were expressed relative to the GRS80 ellipsoid.

For tide gauges in Canada, hourly water level records with respect to chart datum (CD) were obtained from the Canadian Hydrographic Service (CHS). GPS ellipsoidal heights were obtained for nearby benchmarks of the Natural Resources Canada (NRCAN) High Precision 3D Geodetic Network in the ITRF2008 epoch 2010.0 reference frame. Generally, the height of the benchmark relative to CD is not known, but can be inferred from orthometric height differences with tidal benchmarks of NRCAN's Vertical Passive Control Network which are published by CHS. Using this information, the MSL can be expressed relative to the GRS80 ellipsoid.

Geodetic estimates of coastal MDT were then computed using (4.1). Here, the Canadian Gravimetric Geoid model of 2013 - Version A (CGG2013a, *Véronneau and Huang*, 2016) was used to provide the geoid height N relative to the GRS80 ellipsoid in the ITRF2008 epoch 2010.0 reference frame as well as a measure of its accuracy. The CGG2013a geoid heights are available on a grid with $2'$ spacing. These were linearly interpolated to the benchmark locations and then subtracted from the MSL referenced to the benchmarks.

Uncertainties in the geodetic MDT estimates for the study period arise from errors in the GPS ellipsoidal heights as well as geoid height. These uncertainties are independent and their standard deviations are known. It was therefore possible to use conventional error propagation rules to estimate the standard error of the geodetically determined MDT. The main source of uncertainty is the estimated error in the CGG2013a geoid height which is generally one order of magnitude higher compared to errors in the ellipsoidal heights.

Overall, the uncertainties in MDT are typically less than 1.6 cm (Table 4.1).

GPS coordinates are generally expressed in a tide-free coordinate system (*Woodworth et al.*, 2012) as is the geoid model CGG2013a. In order to make geodetically referenced MSL observations comparable to ocean circulation models, mean tidal effects on the coordinate systems have to be considered. Following *Ekman* (1989), the geodetic MDT estimates were converted from tide-free to mean tide coordinates. Note that the minus sign error reported by *Woodworth et al.* (2012) was taken into account.

Since MDT is solely defined by ocean dynamics and density (*Gregory et al.*, 2019), the geodetic MDT estimates were corrected for the inverse barometer effect following *Andersen and Scharroo* (2011). Here, 6-hourly data of air pressure reduced to MSL from the NCEP Climate Forecast System Version 2 (CFSv2, *Saha et al.*, 2014) were used. The time-mean air pressure p_a at the grid point closest to the tide gauges was used to compute the mean inverse barometer correction in centimeters

$$\eta_\mathrm{IB} = \frac{p_\mathrm{a} - p_\mathrm{ref}}{\rho_0 g} = 0.994\,85\,\mathrm{cm\,hPa^{-1}}\,(p_\mathrm{a} - p_\mathrm{ref})\,, \tag{4.2}$$

which was added to the geodetic MDT estimates. Here, $p_\mathrm{ref} = 1013.0\,\mathrm{hPa}$ is the atmospheric reference pressure. The difference in the mean inverse barometer effect between the tide gauges in Boston and North Sydney is 2 cm.

4.2.2 Hydrodynamic Approach

Ocean circulation models typically have their vertical coordinate system expressed relative to an equipotential surface assumed to be the geoid. Therefore, the MSL predicted by the model is equal to the MDT and can be directly compared to the geodetic estimates. This is referred to as the hydrodynamic or ocean approach (e.g., *Woodworth et al.*, 2012).

Here, the GoMSS model described in Section 3.3 in the previous chapter is used to estimate the MDT. In comparison to the original configuration by *Katavouta and Thompson* (2016), the bathymetry was replaced with a combination of the 30″ GEBCO bathymetry (*Weatherall et al.*, 2015) and high-resolution in-situ measurements. The optimal interpolation procedure used to create the new bathymetry is described in Appendix C. This was done to ensure the bathymetry is accurately represented in GoMSS, particularly in shallow regions.

Both the initial conditions and lateral boundary forcing are based on water temperature,

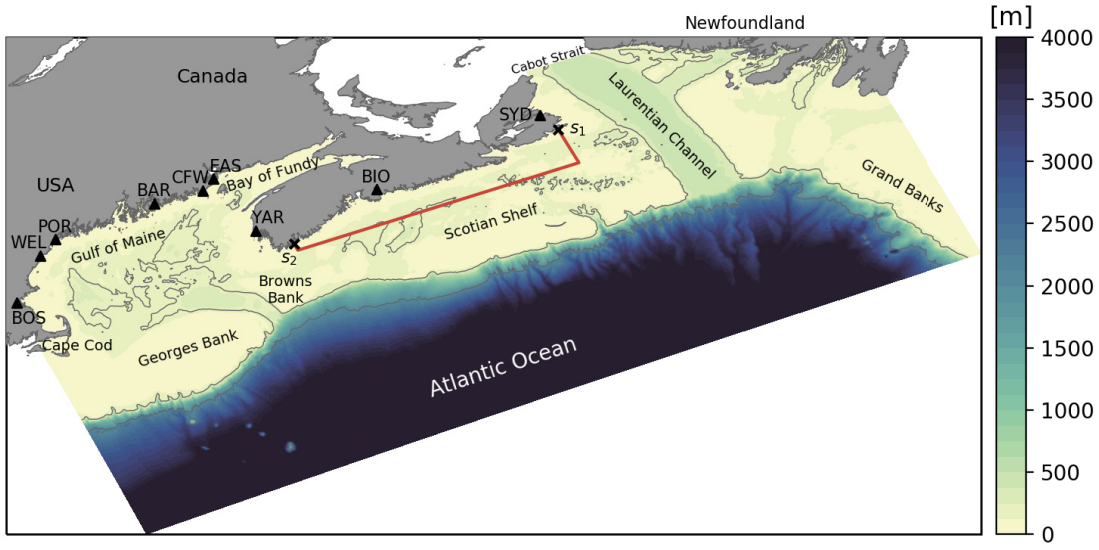

Figure 4.1: GoMSS model domain and tide gauge locations for the Scotian Shelf, Gulf of Maine and Bay of Fundy. Contours indicate the 200 and 2000 m isobaths. The triangles indicate the tide gauge locations with the abbreviations referring to the stations listed in Table 4.1. The area enclosed by the red polygon and the coastline illustrates the region over which the regional view is evaluated and the markers s_1 and s_2 indicate reference points along the coast.

salinity, sea surface height, and currents from the GLORYS12v1 reanalysis (*Fernandez and Lellouche*, 2018). Additionally, tidal elevation and currents for five tidal constituents (M_2, N_2, S_2, K_1, O_1) from FES2004 (*Lyard et al.*, 2006) were prescribed along the lateral boundaries. Atmospheric forcing at the air-sea boundary was based on CFSv2 (*Saha et al.*, 2014).

The following analysis is based on daily mean output fields of a hindcast for the period 2011–2013. Note that GoMSS does not include forcing by atmospheric pressure (see Section 3.3) and therefore no corrections for the inverse barometer effect have to be applied to the model output.

Model predictions of the alongshore MDT from the hydrodynamic approach are based on the predicted MSL over the three-year period. The coastal MDT is taken at the wet (non-land) grid cell closest to the coast and the alongshore tilt of MDT, in the following denoted by $\Delta\eta_\mathrm{c}$, is the difference in MDT between two points along the coast.

4.3 Dynamical Interpretation of $\Delta\eta_\mathrm{c}$

In the steady limit, the depth-averaged momentum equation (3.15) derived in Chapter 3 can be written

$$g\nabla_z\left(\eta-\eta_\mathrm{s}+\frac{|\overline{\mathbf{u}}|^2}{2g}+\frac{p_\mathrm{a}}{g\rho_0}\right)=-(f+\zeta)\hat{\mathbf{k}}\times\overline{\mathbf{u}}-\frac{1}{h}\nabla_z\chi+\frac{\boldsymbol{\tau}^\mathrm{w}-\boldsymbol{\tau}^\mathrm{b}}{h}+\overline{\mathbf{D}}_\mathrm{l}. \tag{4.3}$$

On the left-hand side, all gradient terms have been combined and therefore (4.3) can be considered an equation for the gradient of the dynamically active component of sea level.

In the following, this equation will be used to explore the role of $\Delta\eta_\mathrm{c}$ in coastal and shelf circulation.

4.3.1 Interpretation of $\Delta\eta_\mathrm{c}$ in Terms of Coastal Circulation

At the coast, the depth-averaged momentum balance (4.3) simplifies. Due to the condition of no flow across the coastal boundary, the first term on the right-hand side vanishes. Furthermore, it is assumed that density variations along the coast can be neglected. This assumption will be shown to be reasonable in the analysis of the alongshore momentum balance predicted by GoMSS in Section 4.6. It follows from (4.3), under the assumption

of steady state, that the momentum equation in *alongshore direction* reduces to

$$g\nabla_z\left(\eta + \frac{p_\mathrm{a}}{g\rho_0} + \frac{|\overline{\mathbf{u}}|^2}{2g}\right) = \frac{\boldsymbol{\tau}^\mathrm{w} - \boldsymbol{\tau}^\mathrm{b}}{h} + \overline{\mathbf{D}}_\mathrm{l}. \tag{4.4}$$

Given the inverse barometer effect has been removed from the observations and is not included in GoMSS, the atmospheric pressure term in (4.4) will be ignored. The left-hand side is the gradient of sea level corrected for the Bernoulli effect. The Bernoulli term is typically only significant where changes in current speed occur over small distances, e.g., around headlands and in channels (see Chapter 5). Thus, the large-scale alongshore gradient of MDT at the coast, is primarily balanced by the sum of wind stress, bottom drag, and horizontal mixing.

Suppose for now that the Bernoulli term can be neglected. In that case, the integral of (4.4) along a curve C_c following the coastline between two points (see Figure 4.2) gives the large-scale alongshore balance of the tilt of MDT in vector form

$$g\Delta\eta_\mathrm{c} = \int_{C_\mathrm{c}} \left[\frac{\boldsymbol{\tau}^\mathrm{w} - \boldsymbol{\tau}^\mathrm{b}}{h} + \overline{\mathbf{D}}_\mathrm{l}\right] \cdot d\mathbf{r}. \tag{4.5}$$

This is one interpretation of $\Delta\eta_\mathrm{c}$ in terms of coastal circulation. From (4.5) it is clear that, along the coast, the tilt of MDT is in frictional equilibrium. In the following, this interpretation is referred to as the *coastal view*.

In the special case when the wind setup along the coast

$$g\Delta\eta_\mathrm{w} = \int_{C_\mathrm{c}} \frac{\boldsymbol{\tau}^\mathrm{w}}{h} \cdot d\mathbf{r} \tag{4.6}$$

is known, a new variable $\tilde{\eta}$ can be defined as the wind-corrected MDT. More generally, $\tilde{\eta}$ can also incorporate corrections for the Bernoulli effect and atmospheric pressure variations. Thus, (4.5) becomes

$$g\Delta\tilde{\eta}_\mathrm{c} = -\int_{C_\mathrm{c}} \left[\frac{\boldsymbol{\tau}^\mathrm{b}}{h} - \overline{\mathbf{D}}_\mathrm{l}\right] \cdot d\mathbf{r}. \tag{4.7}$$

If $\boldsymbol{\tau}^\mathrm{b}$ is parameterized in terms of the depth-averaged current, $\overline{\mathbf{D}}_\mathrm{l}$ can be neglected, and the wind setup along the coast is known, it will be shown that $\Delta\tilde{\eta}_\mathrm{c}$ can be interpreted as a measure of the average alongshore flow between two points along the coast.

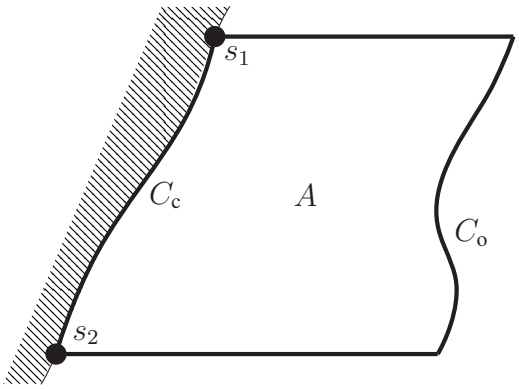

Figure 4.2: Schematic of closed curve along which the momentum balance is integrated. The hatched area is the land and the bold line illustrates the closed integration path C which can be divided into a coastal (C_c) and offshore part (C_o). The area enclosed by C is denoted by A.

4.3.2 Interpretation of $\Delta\eta_\mathrm{c}$ in Terms of Regional Circulation

Instead of integrating the momentum balance along the coast, it is also possible to define an offshore curve C_o from s_2 to s_1 along which (4.3) can be integrated. Together with the coastal integration path, this forms a closed curve $C = C_\mathrm{c} + C_\mathrm{o}$ (Figure 4.2). Note that the closed line integral of the sea level gradient term along C is zero and so

$$\int_{C_\mathrm{c}} \nabla_z \eta \cdot d\mathbf{r} + \int_{C_\mathrm{o}} \nabla_z \eta \cdot d\mathbf{r} = 0. \tag{4.8}$$

This demonstrates that the tilt of MDT along the coast $\Delta\eta_\mathrm{c}$ must equal the drop along the offshore integration path $\Delta\eta_\mathrm{o}$:

$$\Delta\eta_\mathrm{c} = -\Delta\eta_\mathrm{o}.$$

It follows that $\Delta\eta_\mathrm{c}$ can also be interpreted in terms of the regional ocean dynamics.

Using Green's theorem (*Green*, 1828), the line integral of a two-dimensional vector field $\mathbf{F}$ along a closed curve C is equal to the surface integral of the curl of the field over the enclosed area A,

$$\oint_C \mathbf{F} \cdot d\mathbf{r} = \iint_A (\nabla \times \mathbf{F}) \cdot \hat{\mathbf{n}}\, dA, \tag{4.9}$$

where $\hat{\mathbf{n}}$ is the unit vector perpendicular to the surface A.

For the case of depth-averaged ocean circulation, the term under the area integral is the relative vorticity of the flow field. Therefore, the circuit integral of the momentum equation is equal to the area integral of the vorticity equation. Combining (4.3) and (4.9)

with the steady form of the vorticity equation (3.16) introduced in Chapter 3 gives

$$\oint_C \left[\frac{\boldsymbol{\tau}^{\mathrm{w}} - \boldsymbol{\tau}^{\mathrm{b}}}{h} + \overline{\mathbf{D}}_{\mathrm{l}} \right] \cdot d\mathbf{r} = \iint_A \left[h \frac{D}{Dt} \left(\frac{f+\zeta}{h} \right) - J\left(\chi, h^{-1}\right) \right] dA. \tag{4.10}$$

The left-hand side is the closed line integral of the frictional terms which is balanced by the area integral of total change of potential vorticity and the JEBAR term. Note that all the gradient terms, including the sea level gradient, have dropped out.

The circuit integral on the left-hand side can be split into a coastal and offshore part. Note that the line integral along the coast is equal to $g\Delta\eta_{\mathrm{c}}$. Hence, substituting (4.5) in (4.10) gives

$$g\Delta\eta_{\mathrm{c}} = \iint_A \left[h \frac{D}{Dt} \left(\frac{f+\zeta}{h} \right) - J\left(\chi, h^{-1}\right) \right] dA - \int_{C_{\mathrm{o}}} \left[\frac{\boldsymbol{\tau}^{\mathrm{w}} - \boldsymbol{\tau}^{\mathrm{b}}}{h} + \overline{\mathbf{D}}_{\mathrm{l}} \right] \cdot d\mathbf{r}. \tag{4.11}$$

This is another interpretation of $\Delta\eta_{\mathrm{c}}$, this time in terms of regional ocean dynamics. It shows that the alongshore tilt of MDT at the coast can also be interpreted as an integrated measure of the regional ocean circulation. In the following this interpretation will be referred to as the *regional view*.

Both the coastal and regional views of $\Delta\eta_{\mathrm{c}}$ are complementary and dynamically consistent: the offshore circulation drives the coastal dynamics, and on the other hand, the dynamics along the coast act as a boundary condition for the offshore circulation.

A case of special interest assumes steady state, small Rossby number, constant Coriolis parameter f, and $\eta \ll H$. Under these assumptions, the vortex stretching term in (4.11) is given by the depth-averaged flow across isobaths:

$$h \frac{D}{Dt} \left(\frac{f+\zeta}{h} \right) = -\frac{f}{H} \overline{\mathbf{u}} \cdot \nabla_z H. \tag{4.12}$$

Consider now the JEBAR term, $J\left(\chi, H^{-1}\right)$. *Mertz and Wright* (1992) showed

$$J(\chi, H^{-1}) = -\frac{f}{H} (\overline{\mathbf{u}}_{\mathrm{g}} - \mathbf{u}_{\mathrm{g,b}}) \cdot \nabla_z H, \tag{4.13}$$

where $\mathbf{u}_{\mathrm{g}}(z)$ is a geostrophically balanced horizontal velocity defined in terms of the

density field according to the following thermal wind equation

$$f\hat{\mathbf{k}} \times \frac{\partial \mathbf{u}_{\mathrm{g}}}{\partial z} = g\nabla_z \epsilon \tag{4.14}$$

with bottom boundary condition $\mathbf{u}_{\mathrm{g}}(-H) = \mathbf{u}_{\mathrm{g,b}}$. *Mertz and Wright* (1992) used (4.13) to show the JEBAR term *"represents precisely the geostrophic component of the correction to the topographic stretching term to account for the fact that the bottom velocity, not the depth-averaged velocity, yields topographic vortex-tube stretching"*.

Combining (4.12) and (4.13) gives

$$h\frac{D}{Dt}\left(\frac{f+\zeta}{h}\right) - J\left(\chi, h^{-1}\right) = -\frac{f}{H}\mathbf{u}^* \cdot \nabla_z H, \tag{4.15}$$

where

$$\mathbf{u}^* = \overline{\mathbf{u}} - \overline{\mathbf{u}}_{\mathrm{g}} + \mathbf{u}_{\mathrm{g,b}} \tag{4.16}$$

can be interpreted as the depth-averaged current corrected for the geostrophic current at the bottom. The upwelling velocity caused by $\mathbf{u}^*$ running across a sloping seafloor is

$$w^* = -\mathbf{u}^* \cdot \nabla_z H. \tag{4.17}$$

With this definition of w^*, the regional view expressed by (4.11) can be written as

$$g\Delta\eta_{\mathrm{c}} \approx f \iint_A \frac{w^*}{H}\, dA - \int_{C_{\mathrm{o}}} \left[\frac{\boldsymbol{\tau}^{\mathrm{w}} - \boldsymbol{\tau}^{\mathrm{b}}}{h} + \overline{\mathbf{D}_{\mathrm{l}}}\right] \cdot d\mathbf{r}. \tag{4.18}$$

In the following sections, several idealized ocean models are used to dynamically interpret $\Delta\eta_{\mathrm{c}}$ and illustrate the potential of the tilt of MDT for ocean monitoring.

4.4 $\triangle\eta_{\mathbf{c}}$ in Idealized Ocean Models

In this section the coastal and regional views of $\Delta\eta_{\mathrm{c}}$ are illustrated using idealized ocean models. First, the model of a wind-driven basin circulation of *Stommel* (1948) is discussed. Second, two conceptual models of coastally trapped shelf circulation based on *Csanady* (1982) are illustrated. These models highlight the usefulness of $\Delta\eta_{\mathrm{c}}$ for the validation of ocean models.

4.4.1 Wind-Driven Gyre

The seminal model of *Stommel* (1948) describes the steady wind-driven circulation in an idealized, rectangular ocean basin on a β-plane (i.e., Coriolis parameter f is a function of latitude) with dimensions L_x and L_y in x- (zonal) and y-direction (meridional), respectively. The water depth H is assumed to be constant. Variations in atmospheric pressure are ignored and advection, density variations as well as lateral mixing are neglected.

Under these assumptions, the depth-averaged momentum equation (4.3) becomes

$$g\nabla_z \eta = f\hat{\mathbf{k}} \times \overline{\mathbf{u}} + \frac{\boldsymbol{\tau}^{\mathrm{w}} - \boldsymbol{\tau}^{\mathrm{b}}}{H}, \tag{4.19}$$

where the Coriolis parameter $f = \beta y$ is a linear function of latitude. Bottom friction is assumed to be a linear function of the depth-averaged current, that is $\boldsymbol{\tau}^{\mathrm{b}} = \lambda \overline{\mathbf{u}}$, where λ is the bottom friction coefficient with units $\mathrm{m\,s^{-1}}$. The wind forcing is taken to be purely zonal and prescribed as a sinusoidal function of latitude:

$$\tau_x^{\mathrm{w}} = -F \cos\left(\frac{\pi y}{L_y}\right) \quad \text{and} \quad \tau_y^{\mathrm{w}} = 0, \tag{4.20}$$

where τ_x^{w} and τ_y^{w} are the zonal and meridional components, respectively, of $\boldsymbol{\tau}^{\mathrm{w}}$ and F is the maximum amplitude of the wind stress (see grey arrows in Figure 4.3).

Multiplying by H and taking the curl of (4.19) yields the vorticity equation of the *Stommel* (1948) model

$$\beta V = -\frac{\partial \tau_x^{\mathrm{w}}}{\partial y} - \frac{\lambda}{H}\left(\frac{\partial V}{\partial x} - \frac{\partial U}{\partial y}\right), \tag{4.21}$$

where $U = \overline{u}H$ and $V = \overline{v}H$ are the volume transports in zonal and meridional direction, respectively. Introducing a stream function ψ, the components of the volume transport vector can be written as

$$U = \frac{\partial \psi}{\partial y} \quad \text{and} \quad V = -\frac{\partial \psi}{\partial x}. \tag{4.22}$$

Substituting these expressions in (4.21) gives

$$\nabla_z^2 \psi + \frac{H\beta}{\lambda}\frac{\partial \psi}{\partial x} = \frac{F\pi}{\lambda L_y} \sin\left(\frac{\pi y}{L_y}\right), \tag{4.23}$$

which can be integrated to obtain a solution for the stream function.

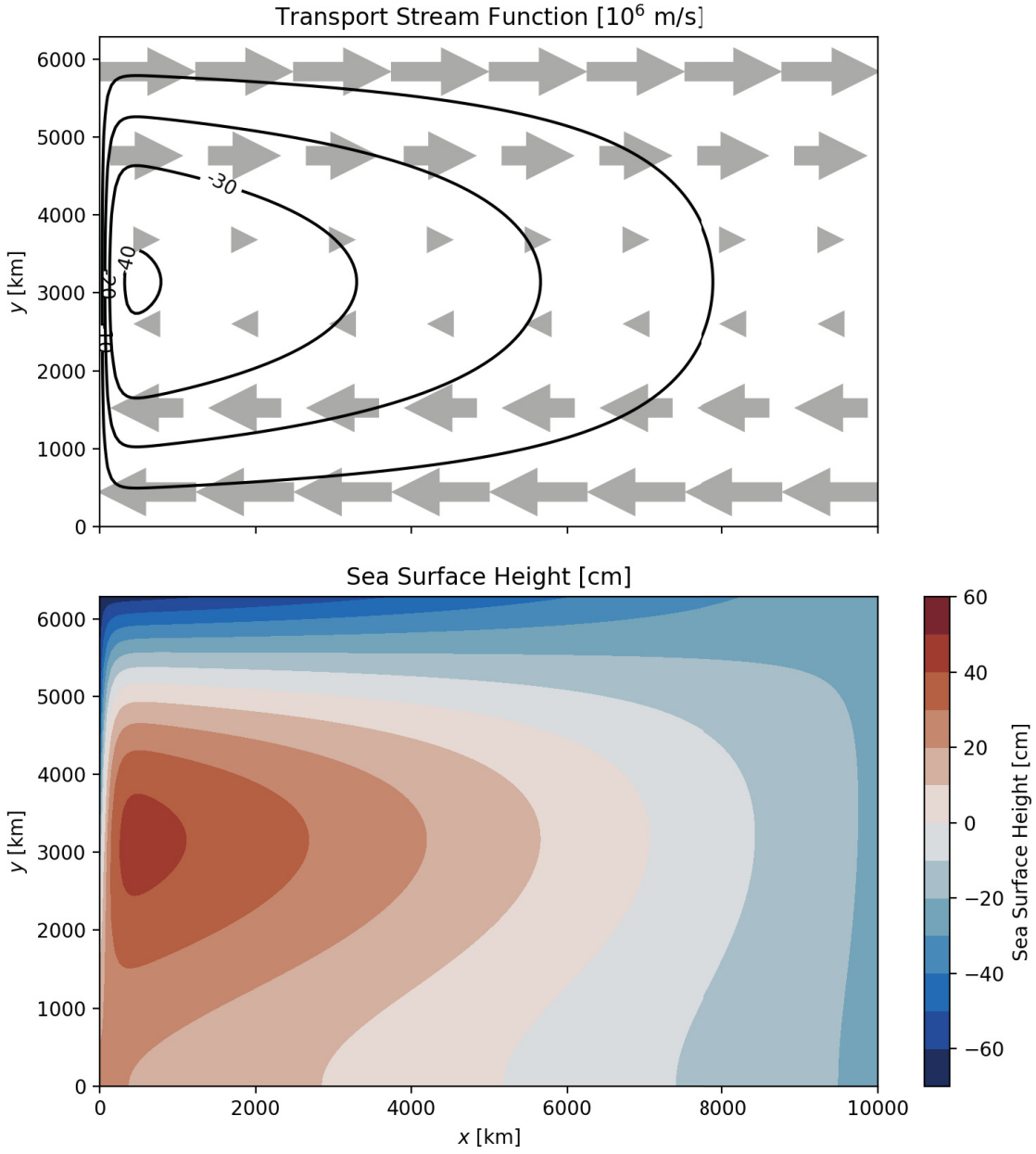

Figure 4.3: Transport stream function and sea surface height predicted by the *Stommel* (1948) model with maximum wind stress of $F = 0.1\,\mathrm{N\,m^{-2}}$ and bottom friction coefficient $\lambda = 0.02\,\mathrm{m\,s^{-1}}$.

Figure 4.3 shows the spatial structure of ψ and the associated sea level for the Stommel model. Based on the Sverdrup relation (*Sverdrup*, 1947), the curl of the wind stress leads to convergence of the Ekman transport in the surface layer. As a result, downwelling (vortex squashing) occurs causing overall southward transport in the ocean interior to conserve potential vorticity. This southward transport is balanced by a swift and narrow current along the western boundary. Along this boundary, the model predicts a sea level tilt of about 1 m.

Let the integration path C be defined along the domain boundaries where the Coriolis term is zero because of the no-flow coastal boundary condition. Based on the assumptions above, the coastal view in (4.5) for the Stommel model becomes

$$\Delta\eta_{\mathrm{c}} = \frac{\lambda}{gH} \int_0^{L_y} \overline{v}(0, y)\, dy. \tag{4.24}$$

This shows that $\Delta\eta_{\mathrm{c}}$ is a measure of the mean alongshore current.

Similarly, the regional view in (4.11), applied over the whole model domain, reduces to

$$\Delta\eta_{\mathrm{c}} = \frac{L_x}{gH} \left[\tau^{\mathrm{w}}(L_y) - \tau^{\mathrm{w}}(0)\right]. \tag{4.25}$$

Note that the Sverdrup transport in the ocean interior is balanced by the volume transport in the western boundary current and therefore, its area integral over the whole domain is zero. From (4.25) it is clear that $\Delta\eta_{\mathrm{c}}$ is also equal to the sea level setup due to the wind along the northern and southern boundary and hence a measure of the circulation offshore. It is important to point out that in this interpretation, $\Delta\eta_{\mathrm{c}}$ only depends on the wind stress and basin dimensions, but is independent of the bottom friction coefficient.

The right-hand side of (4.25) is equal to the area-integrated curl of the wind stress which is directly related to the Ekman pumping velocity w_{E} at the base of the surface Ekman layer (*Gill*, 1982, p. 326)

$$w_{\mathrm{E}} = \hat{\mathbf{k}} \cdot \nabla \times \left(\frac{\boldsymbol{\tau}^{\mathrm{w}}}{f}\right). \tag{4.26}$$

Hence, the regional interpretation of $\Delta\eta_{\mathrm{c}}$ can be written as

$$\Delta\eta_{\mathrm{c}} = \frac{1}{gH} \iint_A f w_{\mathrm{E}}\, dx\, dy. \tag{4.27}$$

This demonstrates that, from a regional perspective, the tilt of MDT along the coast is a

measure of the net surface downwelling over the whole basin.

Instead of applying the regional view in (4.11) over the entire model domain, it is also possible to define C such that C_o is along the outer edge of the western boundary current, where $V = 0$. Integrating the vorticity equation (4.21) with respect to x and substituting the alongshore momentum equation gives

$$g\frac{\partial \eta}{\partial y}\bigg|_{x=0} = -\frac{\beta}{gH}\int_0^L V\,dx. \tag{4.28}$$

This shows that, the alongshore gradient of MDT is also a measure of volume transport in the western boundary current. As shown by *Stewart* (1989), this idea can also be extended to inertial boundary currents.

By continuity, the volume transport in the western boundary current is equal to the southward Sverdrup transport in the interior of the domain. This in turn is proportional to the wind stress curl and also the overall downwelling in the model. This shows that all interpretations of the alongshore tilt of MDT are physically consistent.

4.4.2 Coastally Trapped Circulation

The role of the alongshore tilt of MDT in the circulation on continental shelves can be illustrated with the conceptual models discussed by *Csanady* (1982, pp. 186) which focus on flow trapped within the coastal boundary layer. Consider a coordinate system where the y-axis is aligned with a straight coastline and the x-axis pointing offshore. Without lateral mixing and assuming the flow to be steady, linear, and barotropic, the governing equations (4.3) can then be written in component form as

$$g\frac{\partial \eta}{\partial x} = \frac{f}{H}V + \frac{\tau_x^\mathrm{w}}{H}, \tag{4.29}$$

$$g\frac{\partial \eta}{\partial y} = -\frac{f}{H}U + \frac{\tau_y^\mathrm{w} - \tau_y^\mathrm{b}}{H}, \tag{4.30}$$

where U and V are the x- and y-components of the transport vector $\mathbf{U} = \overline{\mathbf{u}}H$. The Coriolis parameter f is assumed to be constant and bottom friction is taken to be linearly proportional to the depth-averaged alongshore current, $\tau_y^\mathrm{b} = \lambda\overline{v}$. Under the long-wave approximation that the alongshore current is much larger than the cross-shore current, the bottom friction in x-direction can be neglected.

Cross-differentiating (4.29) and (4.30) yields the vorticity equation of this model

$$f\frac{\overline{u}}{H}\frac{\partial H}{\partial x} = -\frac{\partial}{\partial x}\left(\frac{\tau_y^{\mathrm{w}}}{H}\right) + \frac{\partial}{\partial y}\left(\frac{\tau_x^{\mathrm{w}}}{H}\right) + \frac{\partial}{\partial x}\left(\frac{\tau_y^{\mathrm{b}}}{H}\right). \tag{4.31}$$

The net torque exerted by the wind stress and bottom drag (right-hand side), is balanced by vortex stretching/squashing through movement into deeper or shallower water, respectively. This flow across isobaths results in convergence or divergence near the seafloor leading to bottom stress-induced Ekman pumping.

Equation (4.30) can be rearranged to get an expression for $\overline{u}$ which can be substituted in (4.31). Parameterizing bottom friction with the alongshore geostrophic current times a drag coefficient λ yields a single governing equation for the sea level

$$\frac{\partial^2\eta}{\partial x^2} + \frac{f}{\lambda}\frac{\partial H}{\partial x}\frac{\partial \eta}{\partial y} = \frac{f}{g\lambda}\left(\frac{\partial \tau_y^{\mathrm{w}}}{\partial x} - \frac{\partial \tau_x^{\mathrm{w}}}{\partial y}\right). \tag{4.32}$$

Csanady (1982, pp. 192) pointed out the similarity of (4.32) to the heat conduction equation with downstream direction $-y$ corresponding to time. He furthermore used this analogy to discuss coastally trapped flow fields with respect to different forcing. In the following, two cases will be explored and the role of $\Delta\eta_{\mathrm{c}}$ discussed.

4.4.2.1 Wind Stress Along Portion of Coast

Assume water depth increases linearly with distance from shore as $H(x) = H_0 + sx$ where s is a constant slope. The wind stress along the part of the domain where $0 \leq y \leq Y$ is taken to be constant and in alongshore direction only, $\boldsymbol{\tau}^{\mathrm{w}} = (0, \tau_y^{\mathrm{w}})$.

As shown above the dashed line in Figure 4.4, this wind stress causes an Ekman transport toward the coast. From (4.31) it can be seen that the wind stress over the sloping shelf as well as the flow across isobaths into shallower water exert a negative torque on the water column. Thus, the flow is steered to the left resulting in an alongshore current at the coast in the direction of the wind. Consequently, sea level piles up in the downstream direction.

Applying the assumptions above to (4.5), the coastal view of $\Delta\eta_{\mathrm{c}}$ becomes

$$\Delta\eta_{\mathrm{c}} = \frac{\tau_y^{\mathrm{w}} Y}{gH_0} - \frac{\lambda}{gH_0}\int_0^Y \overline{v}(0,y)\,dy. \tag{4.33}$$

The first term on the right-hand side is the wind setup along the coast. As expected, $\Delta\eta_{\mathrm{c}}$ is in frictional equilibrium and balances the difference between wind stress and bottom drag.

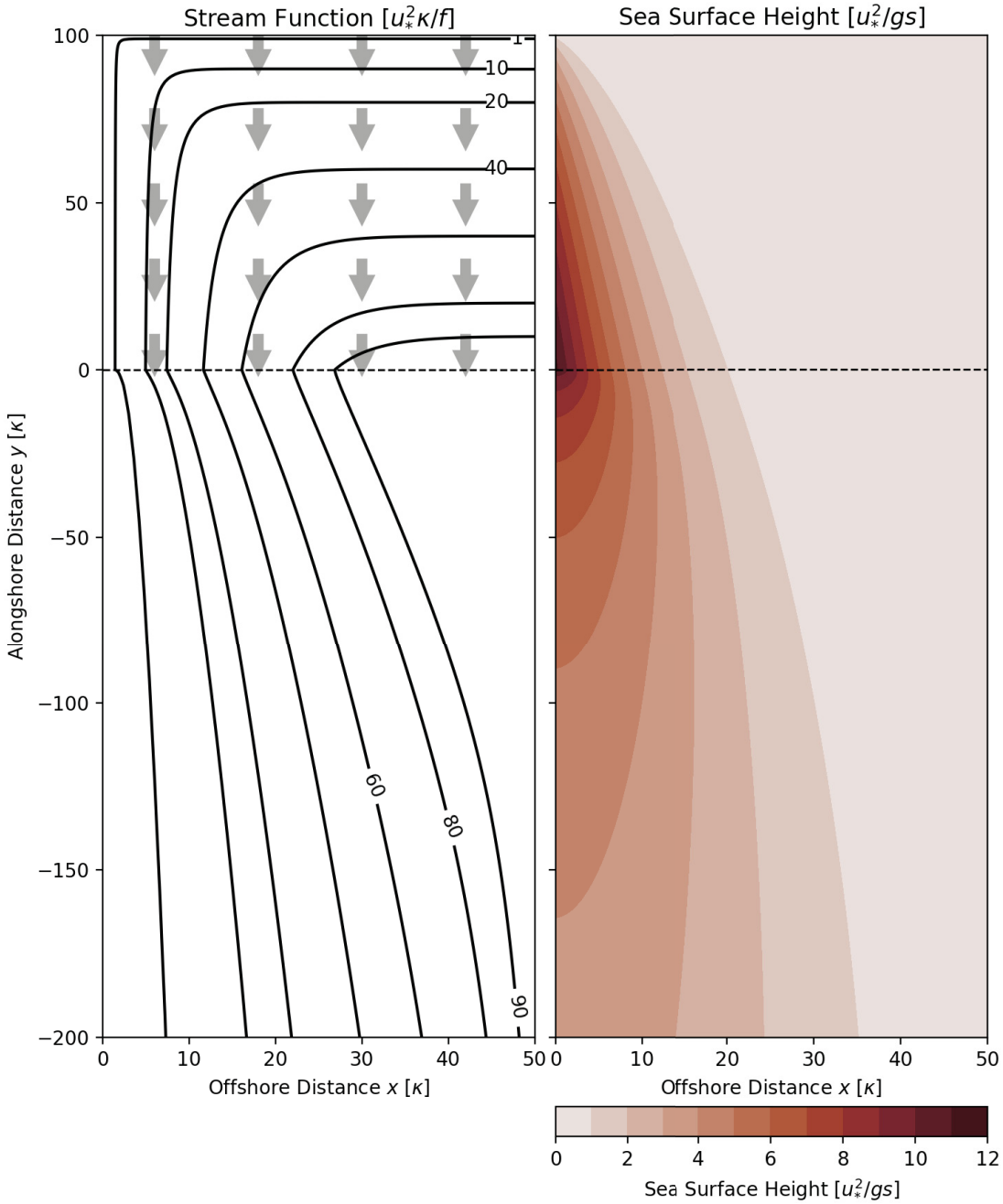

Figure 4.4: Stream function and sea surface height for two models of coastally trapped circulation. Water depth is increasing in x-direction as $H(x) = sx$, the bottom friction coefficient is $\lambda = 0.5 \times 10^{-3}\,\mathrm{m\,s^{-1}}$, and the Coriolis parameter $f = 10^{-4}\,\mathrm{s^{-1}}$. For $y > 0$, a spatially uniform wind stress $\tau_y^{\mathrm{w}} = u_*^2 = -0.01\,\mathrm{m\,s^{-2}}$ (grey arrows) is applied (adapted from *Csanady*, 1982).

If the wind setup along the coast is known, the corrected tilt of MDT along the coast $\Delta\tilde{\eta}_c$ can be used as a direct measure of the mean alongshore current.

The regional view can be directly obtained from (4.18) under the assumption of barotropic flow which implies $\mathbf{u}^* = \overline{\mathbf{u}}$. If the offshore integration path is chosen to be in deep water where the wind stress and bottom friction terms are negligible due to their inverse dependence on H, (4.18) becomes

$$\Delta\eta_c = -\frac{fs}{g}\int_0^Y \int_0^{L_x} \frac{\overline{u}}{H}\, dx\, dy. \tag{4.34}$$

This shows that, from a regional perspective, $\Delta\eta_c$ is equal to the cross-shore Ekman transport due to the wind forcing and the associated flow across isobaths. This onshore flow implies an overall upwelling in the area which can be monitored by observing the sea level at the coast.

4.4.2.2 Coastal Mound

Assume that the wind stress vanishes for $y < 0$ and the flow field is established by prescribing a cross-shore sea level distribution $\eta = \eta_0(x)$ at $y = 0$ which is the result of some upstream process e.g., wind-driven onshore transport as discussed above. It can be seen from (4.29) that the corresponding alongshore current is in geostrophic balance.

Figure 4.4 shows the resulting stream function and the associated sea surface height. The streamlines indicate a predominantly alongshore flow, but they also show a spreading in offshore direction further downstream. Equation (4.31) shows that this cross-shore flow is caused by the frictional torque at the sea floor acting on the alongshore current.

From (4.5) and (4.18), this offshore flow across isobaths can be directly related to the alongshore tilt of MDT at the coast

$$\Delta\eta_c = \underbrace{\frac{\lambda}{gH_0}\int_{-y}^{0} \overline{v}(0,y)\, dy}_{\text{coastal}} = \underbrace{-\frac{fs}{g}\int_{-y}^{0}\int_0^{L_x} \frac{\overline{u}}{H}\, dx\, dy}_{\text{regional}}. \tag{4.35}$$

This shows again that, from a coastal point of view, $\Delta\eta_c$ is proportional to the mean alongshore current driven by the pressure gradient. In the regional interpretation, $\Delta\eta_c$ is a measure of the area-integrated vortex stretching due to cross-isobath flow and is thus a measure of the net upwelling in the region.

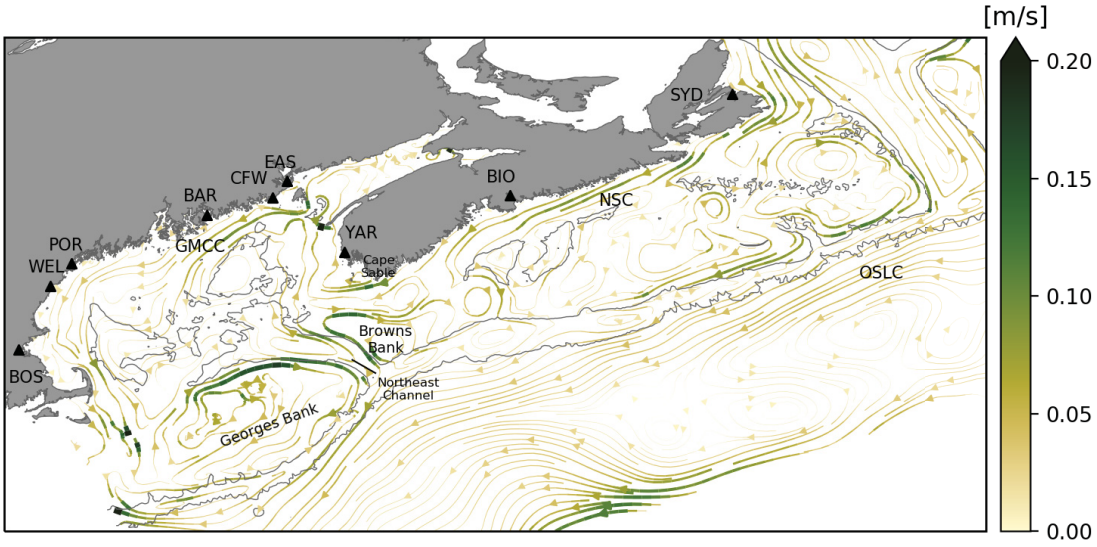

Figure 4.5: Streamlines of mean depth-averaged circulation predicted by GoMSS for the period 2011–2013. Grey contours mark the 200 and 2000 m isobaths and triangles show the locations of the tide gauges listed in Table 4.1. Acronyms indicate circulation features described in the text. NSC: Nova Scotia Current; OSLC: Offshore Labrador Current; GMCC: Gulf of Maine Coastal Current.

4.5 Model Prediction of Mean Circulation and Validation Using Geodetically Estimated MDT

Before the dynamical role of $\Delta\eta_c$ is explored in the realistic, high-resolution regional ocean model GoMSS, its predictions of the MDT and mean circulation are presented. To illustrate the main features of the circulation in the Scotian Shelf and Gulf of Maine region, the mean depth-averaged currents predicted by GoMSS for the period 2011–2013 are shown in Figure 4.5.

GoMSS is able to capture the main features of the mean circulation which are closely connected to the complex bathymetry in the region and have been documented in numerous studies. The nearshore outflow from the Gulf of Saint Lawrence through Cabot Strait is the origin of the Nova Scotia Current (NSC) which follows the coastline toward the Gulf of Maine. This outflow is associated with relatively fresh and cold water originating from the inshore Labrador Current and runoff from the Saint Lawrence River (e.g., *Smith and Schwing*, 1991; *Hannah et al.*, 2001; *Dever et al.*, 2016; *Rutherford and Fennel*, 2018). Another part of the outflow through Cabot Strait follows the western side of the Laurentian

Channel and joins the offshore branch of the Labrador Current (OSLC) flowing along the shelf break. The strong current along the offshore boundary of GoMSS is related to mesoscale eddies associated with the Gulf Stream outside the model domain and is also present in the forcing data from GLORYS12v1 (not shown).

On the shelf and in the Gulf of Maine, the mean circulation is dominated by rectified tidal flow which is aligned with bathymetric features. Most notable is the clockwise gyre on Georges Bank with predicted residual currents up to 20 cm s^{-1} along its northern flank. This is consistent with previous studies and can be explained by tidal rectification and baroclinic processes associated with strong tidal mixing (*Loder*, 1980; *Butman et al.*, 1982; *Greenberg*, 1983; *Naimie et al.*, 1994; *Naimie*, 1996).

GoMSS also predicts a clockwise gyre over Browns Bank which is caused by the same mechanisms (e.g., *Greenberg*, 1983; *Smith*, 1983; *Tee et al.*, 1993; *Hannah et al.*, 2001). These two gyres create an inflow-outflow pattern in the Northeast Channel.

In the vicinity of Cape Sable, strong tidal currents generate a tidally rectified mean flow that locally enhances the Nova Scotia Current. It has been shown that this is also associated with permanent topographic upwelling in that region (*Garrett and Loucks*, 1976; *Greenberg*, 1983; *Tee et al.*, 1988, 1993; *Chegini et al.*, 2018).

In the Gulf of Maine, GoMSS predicts a generally counter-clockwise circulation. One dominant feature is the Gulf of Maine Coastal Current (GMCC) which flows from the Bay of Fundy along the coast of Maine and splits into two branches south of Bar Harbor (BAR). This pattern is consistent with observations and is primarily driven by a pressure gradient force (*Pettigrew et al.*, 1998, 2005).

The circulation features described above are also expressed in the MDT predicted by GoMSS (Figure 4.6a). Note that the spatial median over the shelf regions (water depths $<$ 200 m) has been removed. Contours indicate the 200 m and 2000 m isobaths which mark the shelf break as well as important banks and channels on the shelf. Triangles show the locations of the tide gauges listed in Table 4.1.

The strong signal in the deep ocean is related to eddies associated with the Gulf Stream and the offshore branch of the Labrador Current. On the shelves, gradients in MDT are generally aligned with bathymetric features which is consistent with the topographically driven and tidally rectified circulation described above.

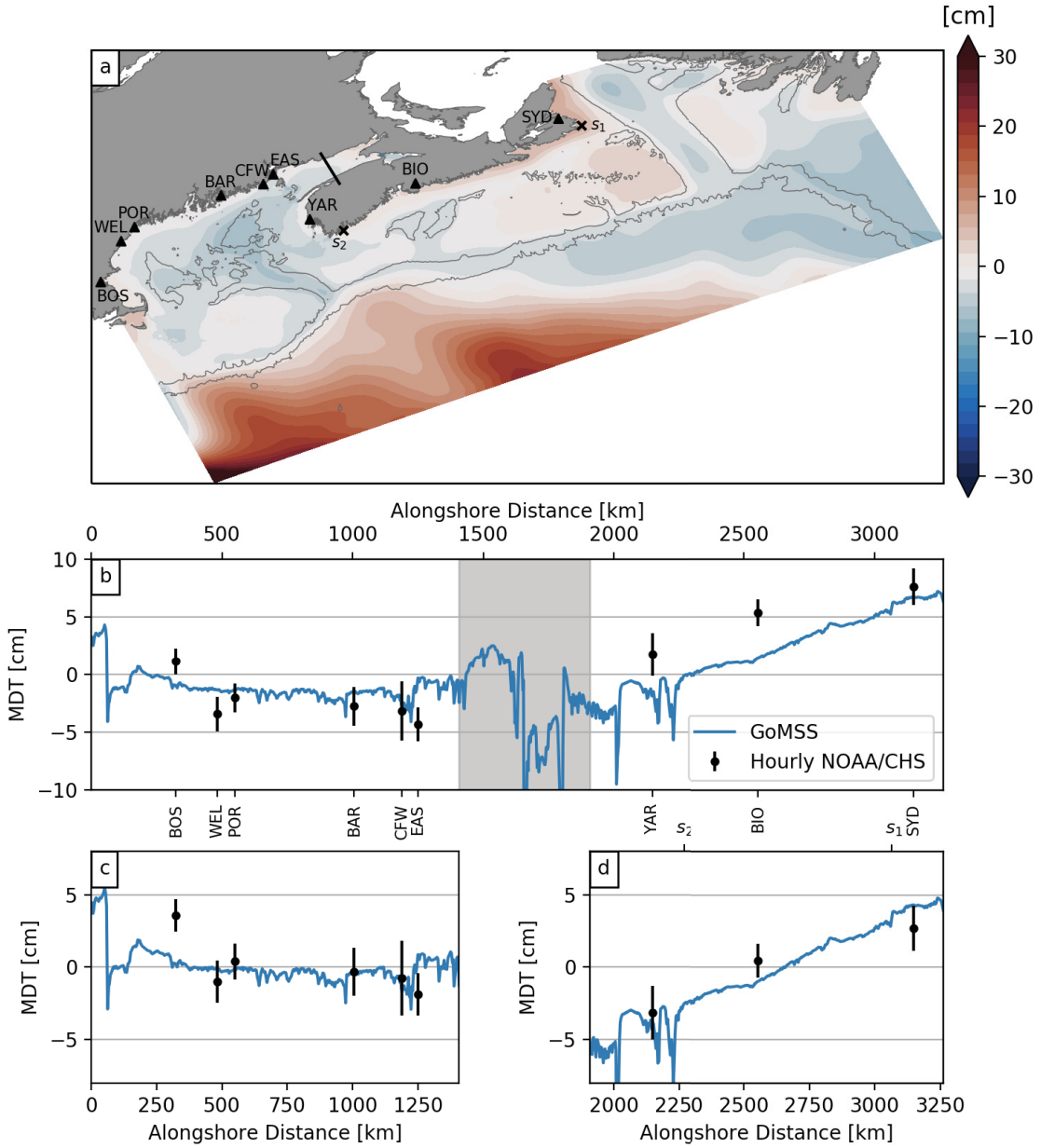

Figure 4.6: Predicted and observed mean dynamic topography (MDT). (a) MDT predicted by GoMSS (spatial median value over area where water depth < 200 m removed). Markers indicate the locations of the coastal tide gauges listed in Table 4.1. The line separates the upper Bay of Fundy where the model has difficulty resolving the residual circulation due to the limited resolution. (b) Coastal MDT as a function of distance along the coast of Gulf of Maine and Nova Scotia. The minima in Minas Passage (-28 cm and -25 cm, respectively) are not shown. Geodetic estimates of MDT are shown with their respective uncertainty. The shaded area indicates the coast along the upper Bay of Fundy. (c) and (d) Enlarged views of either side of the shaded area in (b). In panels (b)–(d), the means of the respective observations and predictions at the grid points closest to the tide gauges have been removed.

Relatively high values of MDT are predicted on the western side of Cabot Strait associated with the outflow from the Gulf of Saint Lawrence. The offshore gradient of MDT indicates a geostrophic balance with the Nova Scotia Current. Additionally, areas of elevated MDT are apparent over the banks on the shelf driven by tidal rectification.

In the Gulf of Maine, MDT is generally lower toward the center which is consistent with the overall counterclockwise circulation. This is also in agreement with observations (*Li et al.*, 2014a).

As will be shown in Chapter 5, the predicted MDT in the upper Bay of Fundy has to be treated with caution because of the limited spatial resolution of GoMSS in that region. An attempt was made to exclude this area from the model domain by introducing an open boundary where tidal elevation and currents were prescribed. However, this caused a strong steric setup because the exchange of temperature and salinity across the boundary, and thus mixing with waters in Minas Basin, was prohibited. Baroclinic boundary data from GLORYS12v1 are not suitable because of its coarse resolution and the lack of tides, both of which are important in the Bay of Fundy.

4.5.1 Model Validation Using Geodetic Tilt Estimates

In Figure 4.6b, the predicted and observed MDT along the coast are shown as a function of alongshore distance from Cape Cod to Cabot Strait. The means of the observations and predictions of coastal MDT at the grid points closest to the tide gauges have been removed.

The shaded area marks the coastline in the upper Bay of Fundy and illustrates more clearly the strong setdown in that area. As discussed above, the MDT prediction in that region has to be treated with caution and therefore, the coastline is separated in two parts along the Gulf of Maine (Figure 4.6c) and Nova Scotia (Figure 4.6d), respectively. In both panels, the means of the respective observations and predictions at the grid points closest to the tide gauges have been removed.

Along the coast of the Gulf of Maine, the predicted coastal MDT is mostly flat, with a small increase toward Cape Cod Bay due to wind setup. The small-scale variability originates from local interactions between the flow and bathymetry in tidal inlets which are part of the rugged coastline. While the predicted local minimum near Cutler Farris Wharf (CFW) and Eastport (EAS) is due to local processes, the overall difference in MDT either side of this setdown is associated with the Gulf of Maine Coastal Current.

The alongshore MDT predicted along the coast of the Gulf of Maine agrees well with the

geodetic estimates. The largest discrepancy is found at Boston (BOS) where the tide gauge is located inside the harbor, sheltered from the open ocean. Therefore, it is likely that the strong setup seen in the observations is a manifestation of local processes. However, it cannot be ruled out that the wind setup toward Cape Cod Bay is underestimated in GoMSS.

Along the coast of Nova Scotia (Figure 4.6d), both the observations and predictions show a strong tilt of coastal MDT. The observed difference in MDT between the tide gauges in Sydney (SYD) and Yarmouth (YAR) is $\Delta\eta_c = 5.9 \pm 2.0$ cm. GoMSS predicts a tilt of $\Delta\eta_c = 8.3$ cm. This is slightly larger than the geodetically estimated tilt, but within two standard deviations of the observed value. Note that a local setdown near YAR is predicted which is related to strong tidal currents in that region. The tide gauge itself is located inside Yarmouth Harbour which is not resolved in the model. This will lead to discrepancies between the model and observations.

Rather than stating $\Delta\eta_c$ as a difference between two fixed locations, it is often reported as the alongshore gradient consistent with its expression in the momentum equation. However, it is not straightforward to calculate the coastal MDT gradient because the irregular shape of the coastline leads to uncertainty in the distance between the fixed locations (*Mandelbrot*, 1982, pp. 25). For example, using an alongshore distance of $\Delta L = 999$ km computed from the coastline in GoMSS results in a predicted MDT gradient $\Delta\eta_c/\Delta L = 8.4 \times 10^{-8}$ (equivalent to 0.8 cm per 100 km). If the interest is the large-scale gradient, this value is arguably an underestimation. If instead one were to use $\Delta L = 650$ km based on three straight line segments from SYD to YAR, the gradient is $\Delta\eta_c/\Delta L = 1.3 \times 10^{-7}$. This gradient is comparable to the values used by *Smith* (1983) in his diagnostic model to describe the circulation off southwest Nova Scotia. However, the above discussion highlights the subjectivity that can be introduced by focusing on gradients rather than $\Delta\eta_c$ between two fixed locations.

In addition to the large-scale tilt, GoMSS predicts local minima of MDT around YAR and just southeast of it at Cape Sable. As discussed above in relation to the mean circulation, these setdowns can be explained by the strong tidal currents and the curvature of the coastline in that region (e.g., *Greenberg*, 1983; *Smith*, 1983; *Tee et al.*, 1993; *Chegini et al.*, 2018). Localized features like these will be discussed in detail in the next chapter.

The above discussion answers the first major question raised in the Introduction: Can new observations of geodetically referenced coastal sea level help validate high-resolution

regional ocean models? The good agreement of $\Delta\eta_c$ estimated independently by the hydrodynamic and geodetic approaches provides validation of the ocean model. The agreement gives confidence that GoMSS captures the mean circulation, including the effect of tidal rectification, on the Scotian Shelf and in the Gulf of Maine. In the next two sections, the following questions will be addressed: What can the alongshore tilt of MDT at the coast tell us about shelf circulation? What are the implications for coastal monitoring?

4.6 Predicted Mean Alongshore Momentum Balance

As discussed in Section 4.3.1, the large-scale tilt of alongshore MDT at the coast is expected to be balanced by the sum of wind stress, bottom friction, and lateral mixing. Using output from GoMSS, it is possible to check if this balance holds in the model and identify the dominant processes that lead to the predicted alongshore tilt of MDT. This is a necessary step before using $\Delta\eta_c$ to make inferences about coastal and regional circulation.

Here, the approach of *Lin et al.* (2015) is adopted, where each term in the alongshore momentum equation is integrated separately along the coast to yield an equivalent change in sea level. This approach is preferable over the comparison of the actual terms in the momentum equation which can be noisy due to local variations in bathymetry and coastline. Alongshore integration smooths out these small-scale fluctuations and makes results easier to interpret.

The alongshore integration path C_c is defined such that it connects all T-points closest to the coast where MDT is defined in the model (Figure 4.7). Note that the coastline in the model follows the edges of the grid cells and therefore, C_c is half a grid cell away from the coast. Due to the grid structure, the coastline in the model has a step-like shape, however, the integration path runs diagonally as indicated in the schematic.

Due to the staggering of the variables on the Arakawa C-grid, the alongshore integral of the momentum equation is straightforward. The approximation of the line integral $\int \mathbf{u}(x,y) \cdot d\mathbf{r}$ is illustrated by the schematic in Figure 4.2. The x- and y-components of the momentum equation are defined at the u- and v-points, respectively, on the model grid (see Figure 3.2 in Section 3.3 of the previous chapter). Each component is multiplied by the appropriate grid spacing Δx or Δy and summed up along the integration path. For increments in x-direction, $\Delta y = 0$ and for steps in y-direction, $\Delta x = 0$. Diagonal

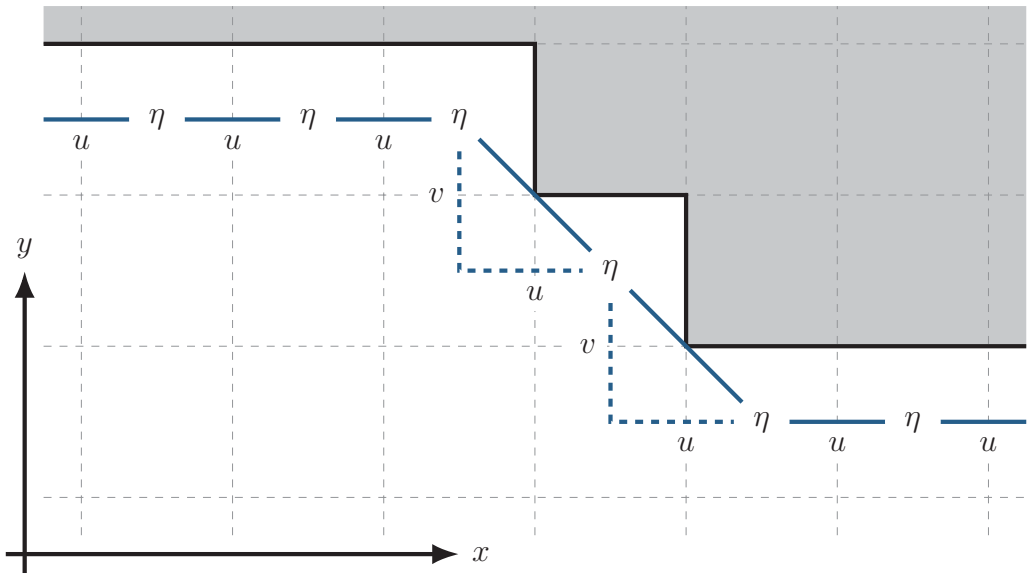

Figure 4.7: Schematic of the alongshore integration path in GoMSS. The gray area marks the land and the solid black line illustrates the coastline. Solid blue lines illustrate segments of the integration path between grid cells and dashed lines indicate components of diagonal segments.

elements include both the u- and v-component as shown in Figure 4.2.

Prior to the alongshore integration, the output fields of the three-dimensional momentum trends were first depth-averaged and then averaged over the period 2011–2013.

Figure 4.8 shows the alongshore MDT as well as mean sea level contributions by the individual terms in the momentum equation at the coast on the Scotian Shelf. Note that the mean of each term over the shown segment was subtracted to center the curves around zero. The red line shows the sum of the contributions of wind stress, bottom friction, and lateral mixing. It is clearly in close agreement with the MDT along the coast predicted by GoMSS. Including the remaining terms effectively closes the momentum balance defined by (4.3).

The alongshore wind stress causes the large-scale setup of MDT (η_{W}) with higher values toward Cabot Strait. The wind setup is partially balanced by bottom friction (η_{BF}) acting on the current at the coast. In the region around Sydney, bottom drag is strongest and associated with the Nova Scotia Current flowing close to the coast as it exits the Gulf of Saint Lawrence. Further downstream, the Nova Scotia Current veers offshore and bottom friction at the coast becomes negligible except in the region around YAR where it balances local MDT minima. These features are due to the Bernoulli effect caused by strong tidal

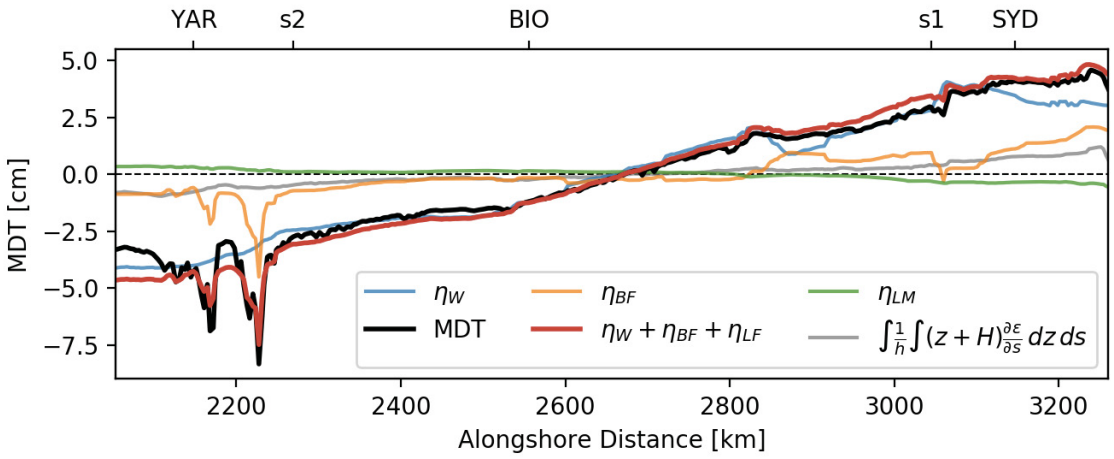

Figure 4.8: MDT (black line) and contributions by individual terms in the alongshore, depth-averaged momentum balance at the coast on the Scotian Shelf: wind stress (η_{W}), bottom friction (η_{BF}), and lateral mixing (η_{LM}) as well as their sum. The contribution from the depth-averaged baroclinic pressure gradient is also shown. Note that the mean of each term has been subtracted to center the curves around zero. Alongshore locations of the tide gauges are shown by their respective abbreviation.

currents around Cape Sable mentioned above. Variations of the sea level equivalent due to lateral mixing (η_{LM}) are relatively small along the coast of Nova Scotia. These results show that $\Delta\eta_{\mathrm{c}}$ is primarily a response to local Ekman dynamics and spatial variations of bathymetry (*Lentz and Fewings*, 2012). It is important to note that the bottom friction term depends on the alongshore current and thus implicitly includes the effect of large-scale, non-local forcing (e.g., JEBAR).

The close agreement between the coastal MDT and the sum of sea level equivalents due to the wind stress, bottom friction, and lateral mixing predicted by GoMSS is consistent with observational studies for other regions along the eastern seaboard of North America (e.g., *Scott and Csanady*, 1976; *Fewings and Lentz*, 2010). They show that the coastal circulation is generally in "frictional equilibrium" (*Lentz and Fewings*, 2012). The overriding importance of wind stress and bottom friction also justifies the choice of Csanady's arrested topographic wave model in Section 4.4.

Previous studies have shown that the wind forcing is the dominant driver of sea level variability on the Scotian Shelf on synoptic to interannual timescales (e.g., *Thompson*, 1986; *Schwing*, 1989; *Li et al.*, 2014b). Many of these studies also demonstrate the influence of remote forcing and coastally trapped waves propagating along the Scotian

Shelf. This is evident in Figure 4.8 for alongshore distances >3100 km which corresponds to the coastline between SYD and the open boundary across Cabot Strait. Here, the wind-driven sea level tilts in the opposite direction compared to the MDT which is primarily balanced by bottom friction.

The steric contribution to the alongshore tilt of MDT at the coast is small (0.9 cm between s_1 and s_2, about half of the contribution by bottom friction). This justifies the assumption made in the simplified alongshore momentum equation (4.4). In the cross-shore direction, a large density gradient exists which is related to the geostrophic outflow from the Gulf of Saint Lawrence with a coastal setup of MDT on the western side of Cabot Strait (*El-Sabh*, 1977). According to the idealized model of *Csanady* (1982, p. 193), this setup "diffuses" in the downstream direction, with the flow trapped within a widening coastal boundary layer. Note that the associated fanning out of MDT contours is evident in Figure 4.6a which can be compared with the region $y < 0$ in Figure 4.4.

4.7 Coastal and Regional Interpretations of $\Delta\eta_{\mathrm{c}}$

In Section 4.3 it was shown that the alongshore tilt of MDT at the coast can be interpreted in terms of the coastal and the regional circulation. Using idealized models, it was demonstrated that $\Delta\eta_{\mathrm{c}}$ is a measure of the mean alongshore current at the coast (coastal view), but can also be related to the net upwelling due to vortex stretching offshore (regional view). Here, it will be tested whether these views hold in GoMSS with a focus on the nearshore region between the reference points s_1 and s_2 outlined by the red polygon in Figure 4.1. Note that the coastal and regional views are based on time-averaged dynamics and can therefore be applied to shelf circulation on timescales where a quasi-steady state can be assumed.

4.7.1 Coastal View

Based on (4.5), $\Delta\eta_{\mathrm{c}}$ can be related to the integrated frictional effects along the coast. As shown above, alongshore wind stress is the main contributor to the MDT difference at the coast of Nova Scotia. Since the sea level equivalent due to wind stress can be computed from the GoMSS model output, the special case in (4.7) will be used. Given the negligible role of lateral mixing and assuming linear bottom friction $\tau_s^{\mathrm{b}} = \lambda\overline{u}_s$, the wind-corrected

tilt of MDT is proportional to the mean depth-averaged alongshore current

$$\langle u_s \rangle = \frac{1}{\Delta L} \int_{s_1}^{s_2} \overline{u}_s \, ds. \tag{4.36}$$

It follows from (4.7) that the predicted mean depth-averaged alongshore current based on the $\Delta\tilde{\eta}_c$ is

$$\langle \tilde{u}_s \rangle = -\frac{gH_0}{\lambda \Delta L} \Delta\tilde{\eta}_c, \tag{4.37}$$

where H_0 is the mean depth of the model along the coast.

It is to be expected that λ changes with seasonal stratification of the water column and therefore a time-varying friction coefficient is defined by

$$\lambda = \lambda_0 \{1 + \alpha \cos[(t - t_0)\omega]\}, \tag{4.38}$$

where λ_0 is a constant drag coefficient, α is a factor that controls the amplitude of the seasonal variations with frequency $\omega = 2\pi/365$ days^{-1}, and t_0 corresponds to the time when stratification is at its maximum.

Furthermore, defining $\kappa = gH_0/\lambda_0 \Delta L$, (4.37) becomes

$$\langle \tilde{u}_s \rangle = -\frac{\kappa}{1 + \alpha \cos[(t - t_0)\omega]} \Delta\tilde{\eta}_c, \tag{4.39}$$

which is a model with three parameters which can be applied to estimate the mean alongshore current based on $\Delta\tilde{\eta}_c$.

Figure 4.9a shows time series of $\langle u_s \rangle$ and $\langle \tilde{u}_s \rangle$ based on daily mean model output from GoMSS with realistic values of $H_0 = 23.4$ m, $\lambda_0 = 1.3 \times 10^{-3}$ m s^{-1}, $\alpha = 0.5$, $t_0 = 30$ d, and $\Delta L = 774$ km. The value for the drag coefficient was chosen to yield maximum agreement between the time series and is comparable to literature values (e.g., *Csanady*, 1982, p. 191). Based on the definition in (4.36), positive values correspond to a southwest flow from s_1 to s_2. Periodograms were analyzed to check if the time series contain an aliased signal from tidal variations. It was found that there is no significant energy at the alias frequencies. A third order Butterworth lowpass filter with cutoff frequency of 15 days was applied to the time series to remove high-frequency variability and thereby allow a quasi-steady state to be assumed.

Both time series show coherent low-frequency variability with correlation $r = 0.92$. The

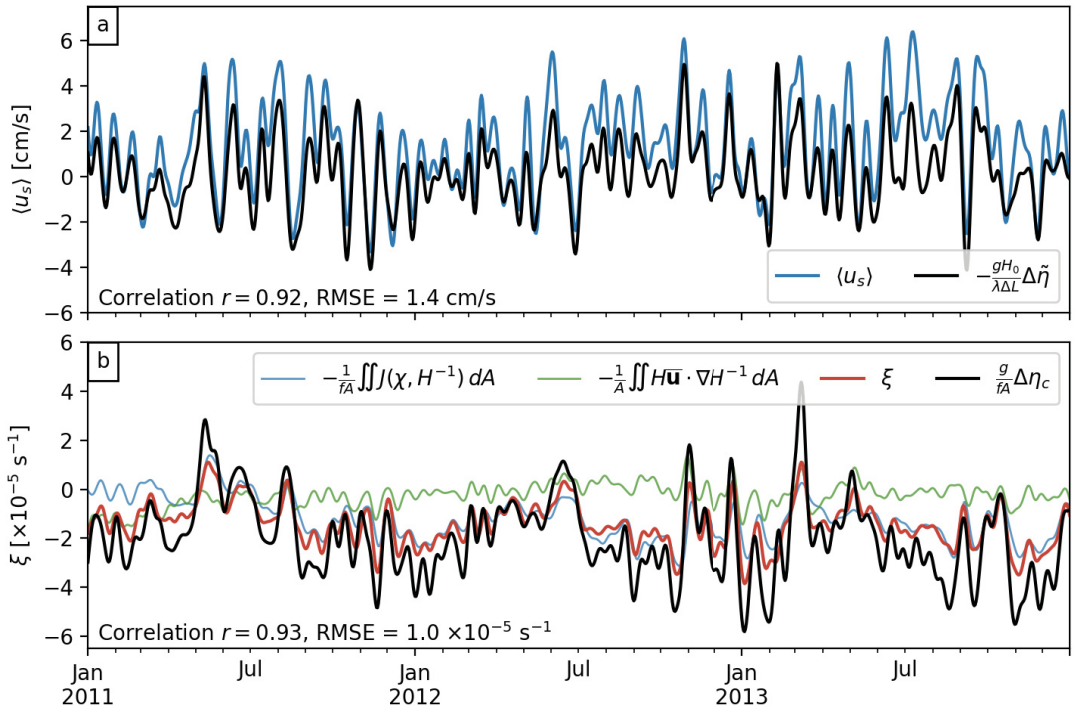

Figure 4.9: Lowpass-filtered time series of the alongshore tilt of MDT at the coast of Nova Scotia and related quantities. a) Mean alongshore depth-averaged current predicted by GoMSS and estimated from wind-corrected tilt of predicted MDT. b) Area-integrated JEBAR (blue) and flow across isobaths (green) as well as resulting upwelling rate (red). The estimated upwelling rate based on $\Delta\tilde{\eta}_c$ is shown in black.

RMSE between the time series is 1.4 cm s^{-1}. The good agreement between the two time series indicates that mean strength of the alongshore current can be estimated by the MDT difference at the coast after correction for the local wind effect.

4.7.2 Regional View

Equation (4.18) relates coastal MDT to area integrated upwelling as well as wind stress and frictional forces projected along the offshore boundary. Assuming the wind stress and frictional terms are negligible in deep water because of their inverse dependence on H, the tilt of sea level along the coast is then given by

$$g\Delta\eta_c = f \iint_A \frac{w^*}{H}\, dA. \tag{4.40}$$

To physically interpret this equation, note H/w^* is the time it takes for a water parcel moving vertically at w^* to travel from the seafloor to the surface. This motivates the

following definition of an area mean "upwelling" rate:

$$\xi = \frac{1}{A} \iint_A \frac{w^*}{H}\, dA. \tag{4.41}$$

Substituting this definition of ξ into (4.40) gives the following expression for the upwelling rate in terms of the tilt of MDT along the coast:

$$\xi = \frac{g}{fA} \Delta\eta_{\mathrm{c}}. \tag{4.42}$$

This equation can be used to estimate the upwelling rate directly from the alongshore tilt of MDT at the coast.

Equation (4.41) has been used to estimate time series of ξ from daily mean output from GoMSS integrated over the area enclosed by the red polygon in Figure 4.1. High-frequency variability was removed using the same lowpass filter described above. The resulting time series is shown by the red line in Figure 4.9b. ξ was also estimated from $\Delta\eta_{\mathrm{c}}$ using (4.42) with and $A = 27\,536.7\,\mathrm{km}^2$ and $f = 1 \times 10^{-4}\,\mathrm{s}^{-1}$. This estimate will henceforth be denoted by $\tilde{\xi}$.

There is clearly close agreement between ξ and $\tilde{\xi}$ in terms of both correlation ($r = 0.93$) and RMSE ($1.0 \times 10^{-5}\,\mathrm{s}^{-1}$). The estimate $\tilde{\xi}$ is generally larger than ξ during extreme events. This can be explained by the assumptions underlying (4.42), i.e., the neglect of the wind stress and frictional terms in deep water. Additional analysis (not shown) indicates that the wind setup along the offshore boundaries is not necessarily zero and explains most of the differences between ξ and $\tilde{\xi}$. However, the good agreement of the time series demonstrates that $\Delta\eta_{\mathrm{c}}$ is an effective measure of the net regional upwelling in a realistic model.

Figure 4.9b also shows the two components of ξ defined by (4.15): the area-averaged JEBAR and the vortex stretching due to depth-averaged flow across isobaths. Clearly, the JEBAR contribution is dominant thereby highlighting the importance of baroclinicity in driving the Nova Scotia Current. The relatively fresh outflow from the Gulf of Saint Lawrence through Cabot Strait causes a strong cross-shore density gradient leading to a geostrophic flow along the coast.

In general, ξ is negative which is consistent with an overall vortex squashing by an onshore flow across isobaths. Episodes where $\xi > 0$ can be identified which correspond to

periods of offshore flow and associated net downwelling.

As shown above, the mean alongshore wind stress leads to a MDT setup along the coast, but it also causes an offshore Ekman transport in the surface boundary layer. Below, a mean onshore flow leads to upwelling of subsurface water at the coast. Although the wind stress can be uniform over a large area, the increase in water depth offshore leads to an input of negative vorticity into the water column. The cross-isobath flow towards shallower water depth ensures that potential vorticity is conserved.

Similarly, frictional forces at the bottom as well as JEBAR exert a torque on the water column and generate relative vorticity. While bottom friction leads to an offshore flow across isobaths (see idealized case in Section 4.4.2.2), JEBAR is dominant along the coast of Nova Scotia. Here it drives an onshore flow which is captured in the time series of the upwelling rate ξ.

4.8 Summary and Discussion

In this chapter, newly available geodetic estimates of coastal MDT have been used to validate the GoMSS regional ocean model. In addition, the relationship between coastal MDT and shelf circulation has been studied using a combination of theory, idealized models and GoMSS.

It was first shown that GoMSS predicts the main features of the mean circulation that are known to exist on the Scotian Shelf and in the Gulf of Maine, including the effect of outflow from the Gulf of Saint Lawrence and tidal rectification. While the coastal MDT is generally flat in the Gulf of Maine, GoMSS predicts a MDT difference between North Sydney and Yarmouth of $\Delta\eta_c = 8.3\,\text{cm}$. This is slightly larger than the geodetically determined value of $\Delta\eta_c = 5.9 \pm 2.0\,\text{cm}$, but the difference is not statistically significant.

These results lead to an affirmative answer to the first question raised in the Introduction: *Can new observations of geodetically referenced coastal sea level help validate high-resolution regional ocean models like GoMSS?* The good agreement of the independent estimates of MDT derived from the hydrodynamic and geodetic approaches provides validation of both the ocean and geoid models used in this study.

The other questions addressed in this chapter focuses on the physical interpretation of $\Delta\eta_c$: *What can the alongshore tilt of MDT at the coast tell us about shelf circulation? what are the implications for coastal monitoring?* Based on theory and idealized models

of ocean and shelf circulation, it was shown that $\Delta\eta_c$ can be interpreted in two complementary, and dynamically consistent, ways. The coastal view is based on the time-averaged alongshore momentum equation at the coast and the regional view is based on vorticity dynamics integrated over an adjacent offshore region. The idealized ocean model of *Stommel* (1948) was used to show that $\Delta\eta_c$ can be used to estimate the coastal flow averaged along the western boundary, and also the basin-averaged, wind-forced upwelling (and hence the integrated Sverdrup transport). Furthermore, the coastally trapped wave model of *Csanady* (1982) was used to show that $\Delta\eta_c$ can be used to estimate spatially averaged upwelling caused by depth-averaged flow across a linearly sloping bathymetry.

The usefulness of the coastal and regional views was demonstrated in a more realistic setting using output from GoMSS. First, it was shown that the tilt of MDT along the coast of Nova Scotia is balanced primarily by wind stress, bottom friction, and a relatively small contribution from lateral mixing. This "frictional equilibrium" is a general characteristic of coastal circulation (*Lentz and Fewings*, 2012). This simplified momentum balance means that, if the wind setup is known, $\Delta\eta_c$ can provide a direct estimate of the average alongshore current $\langle\hat{u}_s\rangle$ between two points at the coast under the assumption that bottom friction can be approximated by a linear dependence on the depth-averaged flow. The scale factor linking $\Delta\eta_c$ and $\langle\hat{u}_s\rangle$ depends only on the mean water depth at the coast and the linear bottom drag coefficient.

The regional view is more subtle than the coastal view. As demonstrated with the idealized models, $\Delta\eta_c$ can be used to approximate the upwelling averaged over an offshore area. On the Scotian Shelf this upwelling rate (denoted by ξ) is related to vortex tube stretching caused by the combined effect of JEBAR and depth-averaged flow across isobaths. JEBAR plays a critical role and causes an overall onshore transport near the sea floor which can result in upwelling at the coast of Nova Scotia. However, there are brief periods of wind-induced downwelling.

The relationship between $\Delta\eta_c$ and the coastal and regional circulation apllies not only to the long-term mean, but also on timescales for which a quasi-steady state can be assumed. Time series of $\langle u_s\rangle$ and ξ were calculated directly from GoMSS output and also estimated from $\Delta\eta_c$ using two simple linear relationships resulting from the coastal and regional views. The parameters in these linear relationships are based on physics. The tilt-based estimates are in good agreement with the filtered time series of $\langle u_s\rangle$ and ξ calculated

directly from model output.

This has obvious implications for ocean monitoring using geodetically referenced sea level observations recorded by coastal tide gauges. For example it may be possible to use long coastal sea level records to estimate time series of upwelling rates. Such information may be of interest to biological oceanographers interested in understanding changes in nutrient cycling on the shelf over recent decades. This speculation applies not only to the Scotian Shelf. For example, in the future, it would be interesting to test the idea on the west coast of North America given the large number of long, geodetically referenced sea level records (e.g., *Lin et al.*, 2015) and the large amount of hydrographic data, e.g., the California Cooperative Oceanic Fisheries (CalCOFi) Database.

Coastal MDT can be affected by local processes, e.g., strong tidal flow around headlands. This has implications for future deployments of tide gauges if they are to be used to monitor the shelf-scale ocean circulation. Their location should be exposed to the open ocean and at distance to areas where local processes dominate.

The use of $\Delta\eta_c$ for model validation is limited to regions with long, geodetically referenced sea level records. In the upper Bay of Fundy, GoMSS predicts an unusually strong setdown in MDT that could not be directly validated because no sufficiently long sea level records exist. This will be addressed in the following chapter, where a new method will be presented which uses high-frequency tidal variations to provide information about MDT in shallow, tidally dominated regions.

CHAPTER 5

USING OBSERVATIONS OF OVERTIDES FOR MODEL VALIDATION

5.1 Introduction

As shown in the previous chapter, GoMSS predicts an unusually strong setdown of mean dynamic topography (MDT) in the upper Bay of Fundy. Due to the lack of long tide gauge records for that region, it is not possible to use the described geodetic approach to determine the reality of this setdown. (Typically hourly sea level records exceeding about 10 years in length, and with reliable vertical datum control, are required.) This motivated the development of a fundamentally different approach, based on observations of overtides, that can be applied to much shorter (one month) sea level records. This greatly increases the number of locations for which the ocean model can be validated.

Overtides result from the transfer of momentum and energy by nonlinear processes. The generation of overtides by nonlinear dynamical interactions, involving tidal variations of currents and sea level, has been studied extensively using analytical and numerical models as well as observations (e.g., *Pingree and Maddock*, 1978; *Aubrey and Speer*, 1985; *Speer and Aubrey*, 1985; *Friedrichs and Aubrey*, 1988; *Parker*, 1991; *Le Provost*, 1991). It has also been shown that the same nonlinear processes can have a direct influence on mean sea level (e.g., *Pingree et al.*, 1984; *Li and O'Donnell*, 1997, 2005). Nonlinear dynamics distort the shape of the tidal wave from a perfect sinusoid leading to a non-zero mean over a tidal cycle and a gradient in MDT. This raises the possibility of validating the mean state of an ocean model, and its representation of nonlinear interactions, by assessing the accuracy of its predicted overtides (*Pingree and Maddock*, 1978).

The asymmetry between flood and ebb in short tidal basins can either be caused by asymmetries in the tidal boundary condition or by changes in the basin geometry during a tidal cycle (*Dronkers*, 1986). Due to tidal variations in water depth, bottom friction is decreased at high water and enhanced at low water. Consequently, high water propagates faster than low water. During a tidal cycle, tidal flats and marshes store water, but do not contribute to the transport of momentum (*Speer and Aubrey*, 1985) which means they can have a counteracting effect on nonlinear tidal distortion.

The Bay of Fundy, together with the Gulf of Maine, is a near-resonant system with an extreme tidal range at the principal lunar semi-diurnal frequency M_2 (*Garrett*, 1972). The present study will focus on Minas Channel, Minas Basin and Cobequid Bay (Figure 5.1) where the highest tides in the world have been observed. In shallow, tidally dominated regions, like the upper Bay of Fundy, where M_2 is the dominant tidal constituent, the largest overtide is expected to be the first harmonic M_4 (*Speer et al.*, 1991). The periods of M_2 and M_4 are 12.42 h and 6.21 h, respectively.

Due to its uniqueness, the tidal dynamics and mean circulation of the Bay of Fundy have been the subject of numerous modelling and observation programs (e.g., *Tee*, 1977; *Greenberg*, 1983; *Dupont et al.*, 2005; *Karsten et al.*, 2008; *Hasegawa et al.*, 2011; *Wu et al.*, 2011). Many of these earlier studies were motivated by the need for reliable assessments of the impact of tidal energy extraction, including the effect on near and far field sediment transport. However, the MDT of the region has not been discussed. In this chapter, observations of the M_4 overtide will be used to check the realism of the MDT setdown predicted by GoMSS for the Bay of Fundy.

The approach described in this chapter has wider applicability than just checking the accuracy of the MDT predicted by GoMSS in the Bay of Fundy. From an oceanographer's perspective it leads to a new set of observations (overtides of sea level) that can be used to validate model predictions of the mean state predicted by ocean models in tidally dominated regions. Although overtides of tidal currents have been used in the past (e.g., *Wu et al.*, 2011), this is the first time that overtides of sea level have been used to validate the mean response predicted by regional circulation models. From a geodesist's perspective, the validation of ocean models using overtides will increase confidence in its predictions of MDT. This will be useful when selecting tide gauge locations for future long-term measurements of sea level in support of geoid model validation, and also correcting

existing mean sea levels for localized oceanographic effects.

Based on the above discussion, the following three questions will be addressed with particular emphasis on the upper Bay of Fundy and the GoMSS model. (i) Is it possible to use observations of overtides to help configure an ocean model and also validate its predictions of the mean state? (ii) What are the implications for the design of geodetic and ocean observing systems? (iii) What insights about the physical processes determining MDT can be obtained from observations of overtides?

The structure of the chapter is as follows. Section 5.2 provides a brief overview of the generation of overtides and their relationship to MDT. Particular attention is paid to tidal flow through channels and past headlands. In Section 5.3, a high-resolution model for the upper Bay of Fundy is introduced and in Section 5.4, the available observations are described. The observations are used in Section 5.5 to validate the models. The predicted MDT is described in Section 5.6 along with its sensitivity to horizontal resolution, lateral viscosity and bottom friction parameters. The results are discussed in Section 5.7.

5.2 Background and Theory

This section provides the theoretical background required to justify the use of overtides in the evaluation of ocean model predictions of the mean state with a particular focus on MDT. Following a general discussion of the generation of overtides, two situations of particular relevance to the present study are discussed: tidal flow around a headland and along a narrow channel closed at one end.

The underlying momentum and continuity equations are taken to be (*Robinson*, 1983, p. 333; see also Section 3.2):

$$\frac{\partial \overline{\mathbf{u}}}{\partial t} + \overline{\mathbf{u}} \cdot \nabla_z \overline{\mathbf{u}} + f\hat{\mathbf{k}} \times \overline{\mathbf{u}} = -g\nabla_z \eta - c_\mathrm{d} \frac{\overline{\mathbf{u}}\,|\overline{\mathbf{u}}|}{H+\eta} + A_\mathrm{h}^\mathrm{m} \nabla_z^2 \overline{\mathbf{u}}, \tag{5.1}$$

$$\frac{\partial \eta}{\partial t} + \nabla_z \cdot [\overline{\mathbf{u}}(H+\eta)] = 0. \tag{5.2}$$

Here, a quadratic bottom friction law is assumed with constant drag coefficient c_d. A_h^m is the horizontal eddy viscosity coefficient. The rest of the notation is standard. Atmospheric forcing and density variations have been ignored along with terms that arise from the vertical structure of $\mathbf{u}$ on depth-averaging the horizontal advection term (*Robinson*, 1983).

The momentum equation (5.1) has two nonlinear terms (horizontal advection and bottom

friction) and the continuity equation has a single nonlinearity involving the product of η and $\overline{\mathbf{u}}$. If the system is forced by a single tidal constituent, all three terms can generate simultaneously both overtides and a change in the mean state (e.g., *Parker*, 1991). It is important to note however that the relationship between overtides and the mean state is not straightforward and depends on the dominant nonlinearities (e.g., *Pingree et al.*, 1984).

Overtides lead to a distortion of the tidal wave. This distortion can be described by the amplitude ratio M_4/M_2 and relative phase difference $2\theta_{M_2} - \theta_{M_4}$ between the dominant M_2 constituent and its first harmonic M_4. In shallow areas, where the tidal amplitude is comparable to the water depth, larger volumes of intertidal storage lead to a decrease in the M_4/M_2 amplitude ratio and maximum tidal asymmetry at $2\theta_{M_2} - \theta_{M_4} = 90^\circ$ (*Friedrichs and Aubrey*, 1988).

More generally, the effect of the nonlinearities on the mean state can be discussed in terms of vorticity dynamics. Taking the curl of (5.1) leads to the following equation governing the change in relative vorticity ζ following the flow (e.g., *Signell and Geyer*, 1991, see also Section 3.2):

$$\frac{\partial}{\partial t}\left(f+\zeta\right) + \overline{\mathbf{u}} \cdot \nabla_z \left(f+\zeta\right) = \frac{\left(f+\zeta\right)}{h}\overline{\mathbf{u}} \cdot \nabla_z h - \hat{\mathbf{k}} \cdot \nabla \times \left(c_\mathrm{d}\frac{\overline{\mathbf{u}}\left|\overline{\mathbf{u}}\right|}{h}\right) + A_\mathrm{h}^\mathrm{m}\nabla_z^2\zeta, \quad (5.3)$$

where

$$h = H + \eta \quad (5.4)$$

is the total water depth. The terms on the right-hand side of (5.3) correspond to changes in ζ due to vortex tube stretching and the torque due to bottom stress as well as dissipation. The bottom friction term can be decomposed in a dissipation term and two generation terms associated with changes in water depth and also the speed of the current (*Signell and Geyer*, 1991). The vorticity equation will prove useful in the following discussion of flow around headlands and also the general interpretation of the observations and model predictions.

5.2.1 Tidal Flow Around a Headland

In a seminal study of the Bay of Fundy, *Tee* (1976) used a numerical model based on (5.1) and (5.2) to show how the combined effect of vorticity generation close to shore and its subsequent advection could generate strong mean flows in the vicinity of headlands where speeds can approach $1\,\mathrm{m\,s^{-1}}$. The predictions by that model were subsequently shown to

agree well with current observations (*Tee*, 1977). Similar results have been found for other locations and it is now generally accepted that strong tidal flow past a headland can lead to flow separation and two permanent, counter-rotating eddies on each side of the headland that drive a mean flow along the coast toward the tip (e.g., *Pingree and Maddock*, 1977; *Robinson*, 1983; *Geyer and Signell*, 1990). It as also been shown that tidal flow past a headland can generate overtides in addition to a mean flow (*Mardell and Pingree*, 1981; *Geyer and Signell*, 1990).

Signell and Geyer (1991, hereafter SG91) used a combination of analytical and numerical models based on (5.1) and (5.2) to examine the formation and evolution of transient eddies generated by tidal flow past an idealized headland. As a first step, SG91 used an analytical model to determine the conditions under which the flow would separate from the coast (see their Section 3.2). They used boundary layer techniques to argue that, in the absence of flow separation, the pressure gradient along the headland's coast can be approximated by

$$g\frac{\partial \eta}{\partial s} = -\frac{\partial u_1}{\partial t} - u_1\frac{\partial u_1}{\partial s} - c_{\mathrm{d}}\frac{U_0 u_1}{H}, \tag{5.5}$$

where s is the alongshore coordinate and $u_1(s,t)$ is the alongshore tidal current at the coast. To specify u_1 they assumed a large-scale irrotational flow, varying in time with tidal frequency ω as $\sin(\omega t)$, past an elliptically shaped headland that protruded from the x-axis. SG91 gave an analytic expression for $u_1(s,t)$ that satisfies the coastal boundary condition of no normal flow and approaches $U_0\sin(\omega t)$ with increasing distance from the headland. Substituting the expression for $u_1(s,t)$ into (5.5) gave an analytic expression for the time varying pressure gradient along the coast of the headland. SG91 used this pressure gradient to determine the location, and stage of the tide, at which the pressure gradient was adverse (i.e., increasing pressure in the downstream direction) and flow separation possible.

Equation (5.5) has one nonlinearity: the Bernoulli setdown of sea level, $u_1^2/2g$. Noting u_1 is a separable function of location and time implies $u_1(s,t) = U_1(s)\sin(\omega t)$. This leads to the following decomposition of the Bernoulli setdown into a change in mean sea level and an overtide of sea level varying at twice the forcing frequency:

$$\frac{u_1^2}{2g} = \frac{U_1^2}{2g} - \frac{U_1^2}{2g}\cos\left(2\omega t\right). \tag{5.6}$$

It follows that if one were to observe the overtide in sea level, it would be possible to also determine the change in mean Bernoulli setdown. This is a particularly simple demonstration of how knowledge of overtides can provide information about MDT.

As the strength of the large-scale tidal flow (U_0) increases (see *Signell and Geyer*, 1991, for conditions), Equation (5.5) eventually breaks down due to flow separation. SG91 used a numerical model, based on a discretization of (5.1) and (5.2), to examine the generation and movement of the transient eddies generated by the oscillating flow as it moves past the headland. They showed that relative vorticity is generated by bottom friction in the thin boundary layer around the headland and subsequently transported into the interior downstream where it dissipates over a tidal cycle. When the tide reverses, the same mechanism injects relative vorticity on the other side of the headland. As a consequence, the residual, tidally averaged circulation is characterized by a pair of counter-rotating eddies on either side of the promontory. These eddies drive a mean flow along both sides of the headland toward the tip.

The mean Bernoulli setdown in the numerical model of SG91 is greatest at the tip of the headland. In order to drive the mean coastal flow toward the tip of the headland, an additional setdown of sea level is needed to provide a pressure gradient to overcome friction. (The coastal boundary condition of no normal flow eliminates the Coriolis term as discussed in Chapter 4.) More quantitatively, the mean sea level gradient required to overcome the friction opposing the mean flow can be approximated by $\lambda\overline{u}/gH_0$ where λ is a linearized drag coefficient and H_0 is the depth near the coast. Taking $\lambda = 0.002\,\mathrm{m\,s^{-1}}$, $\overline{u} = 0.1\,\mathrm{m\,s^{-1}}$, and $H_0 = 10\,\mathrm{m}$ gives a gradient in mean sea level along the coast of 20 cm over 10 km. This is on the same order as typical Bernoulli setdowns. We will see exactly this type of feature in the predicted MDT.

5.2.2 Tidal Flow in a Narrow Channel

It is well known (e.g., *Pingree et al.*, 1984; *Parker*, 1991; *Li and O'Donnell*, 1997, 2005) that the nonlinear terms in the momentum equation (5.1) can generate a mean circulation in a narrow channel closed at one end. *Li and O'Donnell* (2005) used a perturbation technique to show that mean sea level over a tidal cycle always increases toward the head of the channel when forced at the mouth by a tide with a single frequency. They explained this setup in terms of the superposition of an incident and reflected wave that are both attenuated by bottom friction. Because the travel path of the reflected wave is longer, it

is more strongly attenuated than the incident wave leading to the mean setup of sea level. The magnitude of the setup depends on the length of the channel.

The nonlinear bottom friction term in (5.1) can also generate variability locally at the overtide frequency. This is another example of the link between the mean state and overtides and will be important in explaining the distribution of predicted MDT in Cobequid Bay.

5.3 Ocean Models

In addition to GoMSS, a higher resolution model of the upper Bay of Fundy, embedded in the model grid of GoMSS, is used in this study of overtides. This new model will henceforth be referred to as UBoF. The domains of both models are shown in Figure 5.1 and Table 5.1 summarizes all model runs.

5.3.1 GoMSS

A detailed description of GoMSS is given in Section 3.3. For this study of overtides, GoMSS uses the bathymetry of the original configuration of *Katavouta and Thompson* (2016). This bathymetry is based on the $2'$ global relief model ETOPO2v2 (*National Geophysical Data Center*, 2006) and was supplemented by higher resolution data in the inner Gulf of Maine.

GoMSS was initialized with temperature, salinity, sea surface height and currents from the HYCOM-NCODA system (*Chassignet et al.*, 2007). The same dataset was also used for the forcing along the lateral boundaries and supplemented with five tidal constituents (M_2, N_2, S_2, K_1, O_1) from FES2004 (*Lyard et al.*, 2006). Surface forcing at the air-sea interface was taken from CFSR (*Saha et al.*, 2010).

The model was initialized on 1 January 2010 and run for a period of 3 months. Given the initialization with full three-dimensional hydrographic information, the required spin-up time of the model depends primarily on the tides. This is estimated to be 2 days based on visual inspection of the model output. The tidal amplitudes and phases presented below have been estimated from the last month of the three month simulation.

5.3.2 UBoF

UBoF is based on the same version of NEMO as GoMSS, but only covers the upper Bay of Fundy (Figure 5.1b). In comparison to GoMSS, the UBoF horizontal grid is refined by

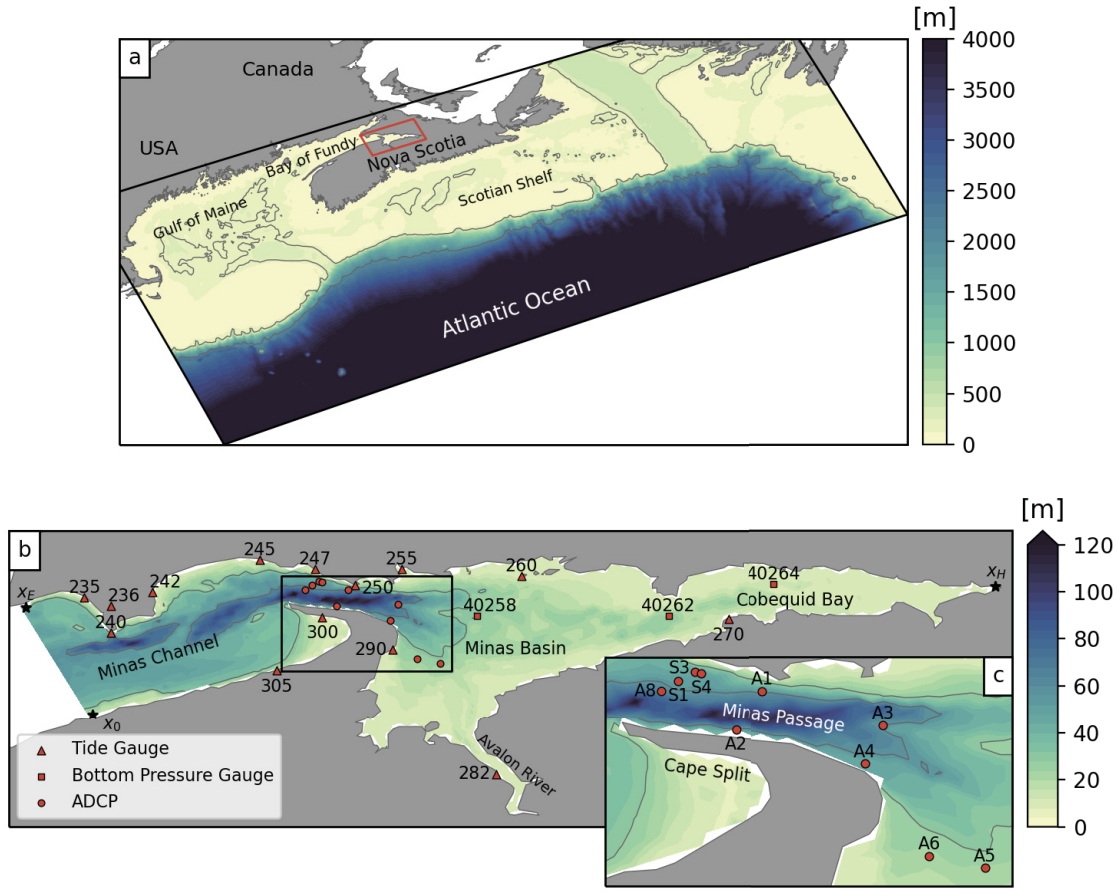

Figure 5.1: Model domains and observation locations in the Scotian Shelf, Gulf of Maine and Bay of Fundy. (a) Model domain and bathymetry of the regional GoMSS model; contours indicate the 200 and 2000 m isobaths. The red rectangle indicates the model domain of UBoF which is shown in detail in panel (b) where contours mark the 30 and 60 m isobaths. Triangles and squares show the positions of the tide gauges and bottom pressure gauges, respectively, used in this study. Circles mark the locations of ADCP measurements. Black stars are alongshore reference points used throughout this study. (c) Enlarged view of the UBoF model domain around Cape Split outlined by the black rectangle in panel (b).

a ratio of 4 resulting in an average grid spacing of 555 m in the along domain direction (roughly to the NE) and 785 m in the cross-domain direction. The vertical grid, turbulence closure schemes, and the formulation of the lateral diffusion operator, are the same as in GoMSS.

The bathymetry for UBoF was created by combining the 30″ General Bathymetric Chart of the Oceans (GEBCO, *Weatherall et al.*, 2015) with high-resolution in-situ measurements using an optimal interpolation technique. Details of the procedure are described in Appendix C. Note that NEMO version 3.6 does not allow for wetting and drying of model grid cells and therefore, a minimum water depth has to be specified. Here, the approach by *Maraldi et al.* (2013) is adopted which takes into account the local maximum tidal amplitude.

The strong tidal flow in the Bay of Fundy mixes the water column and therefore the effect of vertical stratification is negligible (*Tee*, 1977). For this reason, the temperature and salinity in UBoF were kept constant. Given the focus on nonlinear tidal processes, the atmospheric forcing was also set to zero.

The prediction of tides by non-global ocean models is strongly dependent on the quality of the open boundary conditions (*Erofeeva et al.*, 2003). UBoF was forced with tidal elevation and currents for five semi-diurnal and diurnal constituents (M_2, S_2, N_2, K_1, O_1) obtained from the Scotia-Fundy-Maine Data of WebTide (*Dupont et al.*, 2005). WebTide is a tidal prediction model that assimilates, using an inverse linear model technique, tidal amplitudes and phases estimated from satellite altimetry data at crossover points. WebTide has been shown to be in excellent agreement with observations throughout the Bay of Fundy system (see following section for details).

The control run of UBoF, henceforth CTRL (see Table 5.1), was chosen based on the validation of multiple runs. Runs B1–B3 use the same high-resolution grid and model parameters as CTRL, but the bathymetry has been replaced by the GoMSS bathymetry interpolated to the UBoF grid using three different interpolation schemes. The set of "S" runs explores the effect of varying the background lateral eddy viscosity coefficient $A_{\mathrm{h}}^{\mathrm{m}}$ and minimum bottom friction coefficient c_{d} ("S" stands for sensitivity).

The amplitude and phase of tidal elevation of the models were computed using the harmonic analysis in NEMO. Ellipse parameters of the tidal currents were estimated from the hourly predictions of depth-averaged currents using a simple (no inference) least

Table 5.1: Overview of model runs. GoMSS (1/36°) is the Gulf of Maine and Scotian Shelf regional ocean model. CTRL is the control run of the barotropic high-resolution ocean model UBoF (1/144° grid spacing) covering the upper Bay of Fundy (see Figure 5.1). Runs B1–B3 use the same high-resolution grid and model parameters as CTRL, but the bathymetry is replaced by the GoMSS bathymetry estimated using three interpolation schemes. The "S" runs explore the effect of varying the background lateral eddy viscosity coefficient $A_{\mathrm{h}}^{\mathrm{m}}$ and minimum bottom friction coefficient c_{d}. All model runs are for three months starting 1 January, 2010.

Run	Model	Bathymetry	$A_{\mathrm{h}}^{\mathrm{m}}$ [m/s^2]	c_{d} [$\times 10^{-3}$]
GoMSS	GoMSS	ETOPO2v2*	50	2.5
CTRL	UBoF	GEBCO & Observations	20	4.0
B1	UBoF	GoMSS, nearest neighbor	20	4.0
B2	UBoF	GoMSS, linear interpolation	20	4.0
B3	UBoF	GoMSS, cubic interpolation	20	4.0
S	UBoF	GEBCO & Observations	10, 20, ..., 50.0	2.5, 3.0, ..., 4.5

* Higher-resolution data were used to improve the bathymetry in the inner Gulf of Maine (*Katavouta and Thompson*, 2016).

squares method with a Rayleigh criterion of 0.95 for the selection of resolved constituents. Prior to analysis, the predicted horizontal current components, which are defined on the Arakawa C-grid of the model, were linearly interpolated to the center of each grid cell. The current vectors were then rotated from the grid coordinates to geographic coordinates (E-W, S-N). The predicted tidal ellipse parameters were then estimated from the time series at the center model grid points closest to the ADCP locations in Figure 5.1.

5.4 Observations

Tidal amplitudes and phases, estimated from sea level records from 14 coastal tide gauges, were provided by the Canadian Hydrographic Service (CHS, S. Nudds, 2017, personal communication). Additional observations made by three bottom pressure gauges were kindly made available by Dr. D. Greenberg (Bedford Institute of Oceanography, BIO, 2018, personal communication). Figure 5.1b shows the locations of all 17 observation sites.

The number of constituents resolved by the tidal analyses depends on record length. This ranges from 21 to 197 days across the 17 locations. It was possible to resolve M_2, S_2, N_2, K_1, O_1 and M_4 at all sites, except for N_2 at Spencer Island (station 242). The relatively long (168 days) sea level record from Cape D'Or (station 240, obtained from the Marine

Environmental Data Section, MEDS, Department of Fisheries and Oceans Canada, DFO) was used to quantify the uncertainty of the estimated amplitudes and phases. Specifically the 168-day time series was split into non-overlapping 29-day blocks and a tidal analysis was performed on each block. The standard deviation of the estimated amplitudes and phases was then used to obtain approximate 95% confidence intervals for 29-day records. The halfwidth of the confidence intervals was found to be about 0.09 m for the semi-diurnal amplitudes and 1°, 5° and 7° for the phases of M_2, N_2 and S_2, respectively. These values are similar to the estimates made by *Dupont et al.* (2005) based on an analysis of an 89-day observed record from Minas Basin. For the diurnal and M_4 tides, the halfwidths of the 95% confidence intervals are at the millimeter level for the amplitudes and 1°, 2° and 2° for the phases of K_1, O_1 and M_4, respectively.

Observed tidal ellipse parameters and the time mean of depth-averaged current, both obtained from *Wu et al.* (2011), are also used to validate the model predictions. These estimates are based on observations made by bottom-mounted Acoustic Doppler Current Profilers (ADCPs) deployed at ten stations in Minas Passage and Minas Basin (see Figure 5.1c for locations). The lengths of the ADCP records range between 21 and 41 days. For additional details of the ADCP observations, and the data processing, see *Wu et al.* (2011).

5.5 Model Validation for Tides and Mean Current

The first goal of this section is to show that the control run of UBoF (CTRL, see Table 5.1) provides accurate predictions of M_2, the overwhelmingly dominant tidal constituent in the study region. The model is then validated for M_4 elevation and currents, and finally mean currents. This is the first time that a tidal model of the upper Bay of Fundy has been validated using observed values of M_4 tidal elevation. The MDT, for which no reliable observations exist, is discussed in the following section.

In addition to root mean squared error (RMSE), the following metric is used to evaluate the fit of predicted tides at K stations:

$$\tilde{\gamma}^2 = \frac{\sum_{k=1}^{K} \int_0^T \left|\tilde{\mathbf{x}}_{\mathrm{o},k}(t) - \tilde{\mathbf{x}}_{m,k}(t)\right|^2 \, dt}{\sum_{k=1}^{K} \int_0^T \left|\tilde{\mathbf{x}}_{\mathrm{o},k}(t)\right|^2 \, dt}. \tag{5.7}$$

Here, $\tilde{\mathbf{x}}_{\mathrm{o},k}$ and $\tilde{\mathbf{x}}_{\mathrm{m},k}$ are the observed and predicted tidal variables, respectively. These

are expressed as sinusoidal functions with frequency $\omega = 2\pi/T$ for the tidal period T, determined by the observed and predicted amplitude and phase for station k. This metric can be used to assess the fit of either tidal elevations or currents. For the latter it takes into account errors in the principal axes of tidal current and also phase. This metric is based on *Katavouta et al.* (2016) but has been extended to summarize the fits for multiple stations.

The mean currents are validated in a similar way:

$$\overline{\gamma}^2 = \frac{\sum_{k=1}^{K} \left|\overline{\mathbf{u}}_{\mathrm{o},k} - \overline{\mathbf{u}}_{\mathrm{m},k}\right|^2}{\sum_{k=1}^{K} \left|\overline{\mathbf{u}}_{\mathrm{o},k}\right|^2}, \tag{5.8}$$

where $\overline{\mathbf{u}}_{\mathrm{o},k}$ and $\overline{\mathbf{u}}_{\mathrm{m},k}$ are the observed and predicted time mean currents at observation location k.

For both metrics, the smaller γ^2 the better the fit of the model to the observations: $\gamma^2 = 0$ implies a perfect model fit. If $\gamma^2 > 1$, the model has no useful skill. Both metrics can be used to assess fit at a single or multiple ($K > 1$) stations.

5.5.1 M_2 Elevations and Currents

The amplitude and phase of the M_2 tidal elevations predicted by CTRL are shown in Figure 5.2. The top panel shows the predicted amplitude and phase across the whole model domain and the remaining two panels show the variation of amplitude and phase along the coast. The x-axis in these two panels is alongshore distance measured counterclockwise from x_0 on the open boundary, to the head at x_{H}, and then along the north shore to x_{E} where the coastline intersects the open boundary. The black circles (triangles) in all three panels show the locations of coastal tides gauges along the south (north) shore.

Along the open boundary (clockwise from x_0 to x_{E}), the predicted mean M_2 amplitude is 4.07 m and it increases to 5.96 m at the head of Cobequid Bay (x_{H}). The tidal phase also increases toward the head with high water arriving at x_{H} with a delay of about 1.5 h relative to the open boundary. The predicted increase in M_2 amplitude and phase toward the head is consistent with previous studies (e.g., *Greenberg*, 1969; *Tee*, 1976; *Karsten et al.*, 2008; *Hasegawa et al.*, 2011; *Wu et al.*, 2011) and has been explained in terms of the resonant character of the Bay of Fundy system (*Garrett*, 1972).

The agreement between the observed and predicted M_2 elevation at the 14 coastal tide gauges is shown by the black dots (south shore) and triangles (north shore) in Figures 5.2b and c. The RMSEs in amplitude and phase are 0.12 m and 3.4°, respectively, and

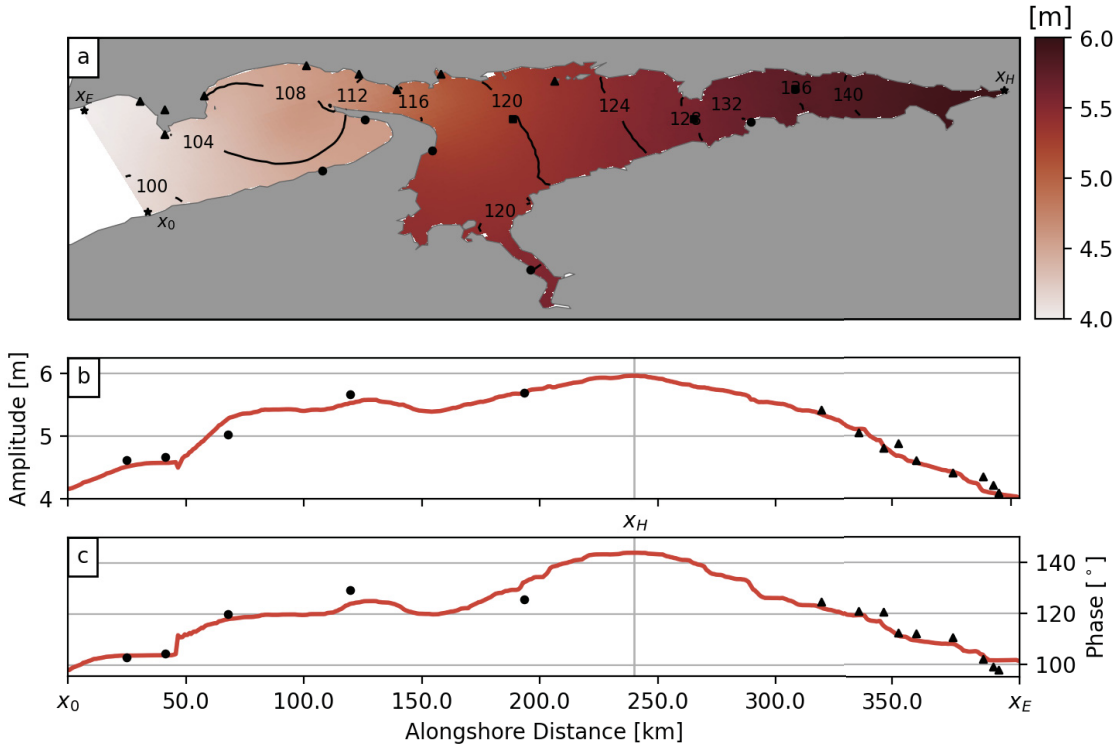

Figure 5.2: Predicted and observed amplitude and phase of M_2 tidal elevation. (a) Colors show the tidal amplitude in meters and contours show phase in degrees relative to Greenwich predicted by CTRL. Circles and triangles mark the tide gauges along the southern and northern coast, respectively, while squares indicate offshore locations. Black stars mark alongshore reference points. (b) and (c) M_2 tidal amplitude and phase as a function of alongshore distance from x_0. Black markers indicate values based on observations at the coastal tide gauges shown in panel (a).

Table 5.2: Summary of fit of model predictions to sea level and current observations using the γ^2 metric. Predicted sea level (η) and depth mean current ($\overline{\mathbf{u}}$) have been validated against observations at several tidal frequencies and the mean. The UBoF runs (CTRL, No-Slip and S runs) are defined in Table 5.1. For comparison, the same metrics have been calculated for GoMSS and WebTide (last two columns). The same observations from 14 coastal tide gauges, 3 bottom pressure gauges and 10 ADCPs were used for all models. The γ^2 metrics are defined by (5.7) and (5.8).

Variable	Constituent	CTRL	No-Slip	S runs	GoMSS	WebTide
η	M_2	0.005	0.012	0.005–0.007	0.018	0.006
η	S_2	0.022	0.033	0.021–0.024	0.325	0.022
η	N_2	0.050	0.067	0.047–0.055	0.079	0.042
η	M_4	5.577	3.994	5.089–6.072	16.887	1.841
$\mathbf{u}$	M_2	0.023	0.048	0.022–0.027	0.201	0.034
$\mathbf{u}$	M_4	0.329	1.371	0.325–0.393	1.924	0.325
$\mathbf{u}$	Mean	0.303	1.083	0.264–0.410	0.876	-

$\tilde{\gamma}^2 = 0.005$. Using observations from all 14 coastal tide gauges, and the three additional pressure gauges shown by the black squares in Figure 5.2a, the RMSEs are 0.17 m and 3.5° for amplitude and phase, respectively, and $\tilde{\gamma}^2 = 0.005$. These error metrics are similar to those of WebTide based on the same observations (RMSEs for amplitude and phase are 0.13 m and 4.03°, respectively; $\tilde{\gamma}^2 = 0.006$, see Table 5.2). This is not surprising because UBoF is forced with tidal elevations taken from WebTide (see Section 3).

Next, the fit of the model to the observed, depth-mean M_2 tidal currents is examined at the 10 ADCP locations shown in Figure 5.1c. The M_2 tidal ellipses are shown in Figure 5.3. The dots correspond to the position of the tidal current at the time of the maximum equilibrium tide at the Greenwich meridian. Strong, rectilinear M_2 tidal currents are evident in Minas Passage (locations A1–A4, A8, and S1–S3 with speeds exceeding 3 m s^{-1}). Inside Minas Basin (A5 and A6), the currents are weaker with maximum M_2 speeds of about 1 m s^{-1}. Based on visual comparison, the predictions are in good agreement with the observations and this is confirmed by the low values of $\tilde{\gamma}^2$ for each location given in the lower left corner of each subpanel. Combining results from all ADCP locations, $\tilde{\gamma}^2 = 0.023$. This is a slight improvement over WebTide ($\tilde{\gamma}^2 = 0.034$) and a significant improvement over GoMSS ($\tilde{\gamma}^2 = 0.201$).

As a further check on the model, predictions of tidal elevation for S_2 and N_2 were also compared to observations. The $\tilde{\gamma}^2$ values (Table 5.2) show the performance of CTRL is

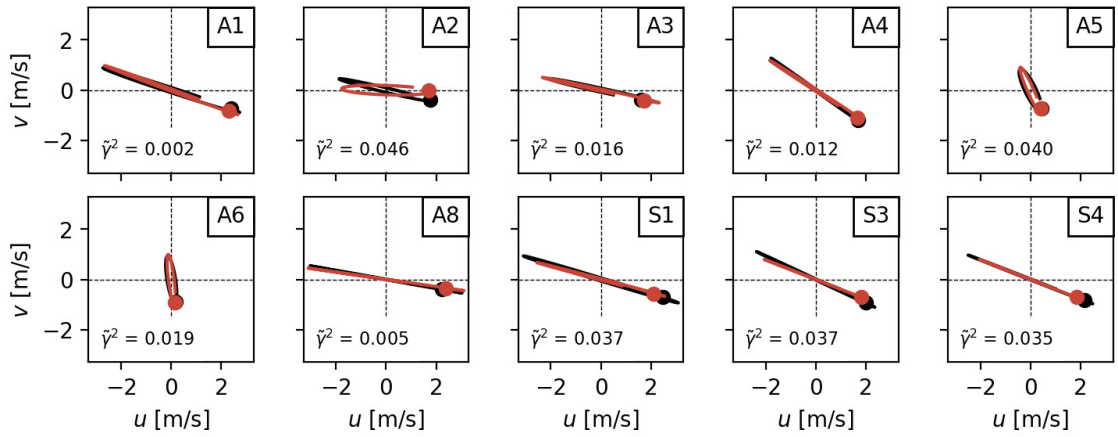

Figure 5.3: M_2 tidal ellipses of depth-averaged currents at the 10 ADCP locations shown in Figure 5.1c. The ellipses for observations and predictions by CTRL are shown in black and red, respectively. The last 10th of the tidal cycle is omitted to indicate the sense of rotation, i.e., from line to dot is forward in time. $\tilde{\gamma}^2$ for each station is given in the lower left corner of each panel. The speeds are in m s $^{-1}$.

comparable to WebTide, and slightly better than GoMSS.

Summarizing the results of this subsection, UBoF provides good predictions of M_2 tidal elevations and currents in the study region.

5.5.2 M_4 Elevation

The M_4 amplitude and phase of elevation predicted by CTRL are shown in Figure 5.4. The largest amplitudes are predicted for Cobequid Bay reaching 1.44 m at the head (x_H). Unfortunately, no observations are available for this region. At Cape Split and in Minas Passage, CTRL predicts amplitudes of 0.41 m and 0.26 m, respectively. These local maxima can be related to the Bernoulli effect as well as vorticity generation and subsequent advection due to the strong tidal currrents through the narrow strait (see Section 5.2.1).

In the Avalon River, M_4 amplitudes reach 0.43 m. The phase mapped in Figure 5.4a suggests the M_4 oscillations in the upper reaches of Cobequid Bay and the Avalon River are standing (see also Figure 5.4c). Beyond these two regions the phase suggests propagation as a shallow water wave toward the open boundary. (The same behavior is also predicted by WebTide.)

The alongshore variation of observed and predicted M_4 at the coast is shown in Figures 5.4b and c. It is clear that the overall agreement at the 14 coastal tide gauges is poor, e.g., the predicted amplitudes are generally too large, and the phase changes in

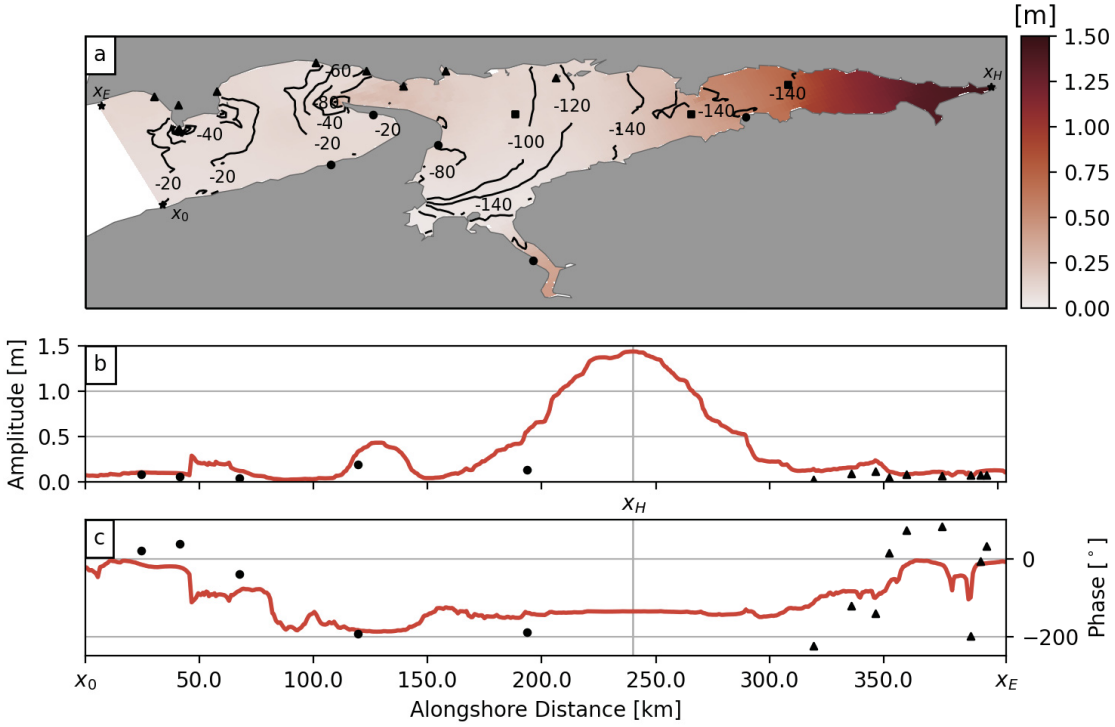

Figure 5.4: Predicted and observed amplitude and phase of M_4 tidal elevation. The format is the same as Figure 5.2.

the vicinity of Minas Passage too small, compared to the observations. This poor agreement is confirmed by large RMSEs of 0.12 m and 65.1° for M_4 amplitude and phase and $\tilde{\gamma}^2 = 3.3$. Adding observations from the three bottom pressure gauges (squares in Figure 5.4a) gives combined RMSEs for amplitude and phase of 0.19 m and 62.6° and $\tilde{\gamma}^2 = 5.6$. Clearly CTRL has no skill in predicting M_4 elevation at the coast (Table 5.2). WebTide also performs poorly with RMSEs for amplitude and phase of 0.10 m and 74.6° and $\tilde{\gamma}^2 = 1.8$ (Table 5.2).

The M_2 and M_4 amplitude and phase at the three offshore bottom pressure locations (squares in Figure 5.1b, Table 5.3) are now examined. At the most western gauge in Minas Basin (40258), the predicted M_4 amplitude is 0.12 m which corresponds to an M_4/M_2 amplitude ratio of 0.02. The observed M_4 amplitude at this location is only 0.01 m and the observed M_4/M_2 amplitude ratio is only 0.002. Moving toward the head of the basin, both the model and observations show an increase in M_4, however the predicted amplitude at the eastern most gauge in Cobequid Bay (40264) is four times larger than observed (Table 5.3). This discrepancy is also reflected in the observed and predicted M_4/M_2 ratios

Table 5.3: Observed and predicted amplitude and phase for M_4 elevation at the three bottom pressure gauges (squares in Figure 5.1b). M_4/M_2 is the amplitude ratio and $\theta_{M_2} - \theta_{M_4}$ is the phase of M_4 relative to M_2 at the same location. The row order of the stations is from west to east.

Station		M_4 Amp. [m]	M_4 Phase [°]	M_4/M_2	$2\theta_{M_2} - \theta_{M_4}$ [°]
40258	Observations	0.01	-55.1	0.00	296.8
	UBoF CTRL	0.12	-94.0	0.02	333.3
	WebTide	0.12	-134.1	0.02	383.1
40262	Observations	0.09	162.0	0.02	88.9
	UBoF CTRL	0.35	-144.6	0.06	401.5
	WebTide	0.25	-156.6	0.04	416.7
40264	Observations	0.18	164.6	0.03	94.1
	UBoF CTRL	0.72	-141.1	0.13	412.6
	WebTide	0.41	-157.9	0.07	427.9

at that station.

The observed and predicted M_4 phases at the three bottom pressure locations suggest a standing M_4 oscillation in Cobequid Bay, and westward propagation away from this region (Table 5.3). Differences exist however in the M_4 phase relative to the M_2 tide. At the two eastern bottom pressure gauges, the observed relative phase $2\theta_{M_2} - \theta_{M_4} \approx 90°$ which indicates flood dominance with maximum asymmetry between a short flood period with strong currents and longer ebb duration with weaker currents (*Friedrichs and Aubrey*, 1988). This flood dominance is also predicted by CTRL, however, the tidal distortion is less pronounced compared to the observations ($2\theta_{M_2} - \theta_{M_4} = 53°$ for the eastern station in Cobequid Bay, 40264).

As described in Section 5.1, the presence of tidal flats can have significant influence on the distortion of the tidal wave. This is not captured in UBoF because it does not include wetting and drying. (The same is true for WebTide, however, the error is less pronounced because the model does include wetting and drying but with presumably an underestimation of the overall storage area of the wetlands.)

The above discussion leads to the speculation that the M_4 tide predicted by UBoF is contaminated by an unrealistically large signal that is generated in Cobequid Bay and then propagates westward toward the open boundary. To test this speculation, the predictions of M_4 tidal elevation at all 11 tide gauges to the west of bottom pressure gauge 40258

(henceforth the reference station) were corrected as follows:

$$A'_k = A_k - A_{\text{ref}} \exp\left[i\Delta\theta\left(\frac{\lambda_k - \lambda_{\text{ref}}}{\lambda_0 - \lambda_{\text{ref}}}\right)\right], \qquad \text{with } k = 1, \ldots, 11, \tag{5.9}$$

where A_k is the complex M_4 amplitude at the kth tide gauge and A_{ref} is the complex M_4 amplitude at the reference station. λ_k, λ_{ref} and λ_0 are the longitudes of the k tide gauges, the reference station, and the most western tide gauge (235), respectively. $\Delta\theta$ is the spatial change in phase associated with a shallow water wave propagating at constant speed from the reference station to the open boundary. The optimal value of $\Delta\theta$ was found to be about $\pi/3$ corresponding to a time lag of about 1.0 h and a phase speed of 13 m s^{-1}. (The optimal value was determined by systematically varying $\Delta\theta$ to yield the maximum reduction in $\tilde{\gamma}^2$.)

Equation (5.9) was used to correct the M_4 amplitudes for the observations and predictions separately. The resulting $\tilde{\gamma}^2$ are listed in Table 5.4. It is encouraging to note that the correction significantly improves the model fit of CTRL at all but one station and thus supports the speculation that the large M_4 error is generated remotely in Cobequid Bay. This example clearly highlights a potential problem with using M_4 elevation for model validation; the fit at a given location can be swamped by remotely generated errors (*Pingree and Maddock*, 1978). The spatial referencing technique outlined above is one way of overcoming this limitation and extracting useful information from M_4 elevations.

5.5.3 M_4 Currents

The M_4 tidal ellipses calculated from observed and predicted depth-averaged currents are shown in Figure 5.5. The $\tilde{\gamma}^2$ values are given in the lower left corner of each panel. Both observations and predictions agree that the strongest M_4 currents occur in Minas Passage (A1–A4, A8, and S1–S3 where speeds approach 0.3 m s^{-1}) and are weak inside Minas Basin (A5 and A6, 0.1 m s^{-1}).

Generally, locations with strong observed M_4 currents also have strong M_4 predictions. The only exception is A2. The individual values of $\tilde{\gamma}^2$ show the model has skill in predicting M_4 currents at most locations. For all ADCP stations combined, $\tilde{\gamma}^2 = 0.329$ which is comparable to WebTide ($\tilde{\gamma}^2 = 0.325$, see Table 5.2). Note that these values of $\tilde{\gamma}^2$ are significantly better compared to M_4 tidal elevation.

As discussed in Section 5.2, both nonlinear advection and bottom friction can generate

Table 5.4: $\tilde{\gamma}^2$ for original and corrected predictions of M_4 elevation at coastal tide gauges (see Figure 5.1b). All stations are to the west of the reference bottom pressure gauge 40258. See text for details.

Station	CTRL	CTRL corr.	WebTide	WebTide corr.
235	1.484	0.161	0.177	2.584
236	0.328	1.082	0.499	5.070
240	2.224	0.151	1.370	0.935
242	3.953	0.180	1.754	0.191
245	1.892	0.019	0.677	0.329
247	4.143	0.472	7.159	1.010
250	1.829	0.202	1.343	0.371
255	1.285	0.484	0.581	0.389
290	4.475	0.891	8.683	2.241
300	2.204	0.461	1.241	1.340
305	0.569	0.358	0.810	1.062

overtides. As a result, strong M_4 currents are often observed around headlands (*Geyer and Signell*, 1990) and in regions where strong M_2 currents vary on small spatial scales (*Davies and Lawrence*, 1994). In the previous section it was shown that the strongest M_2 currents are observed (and predicted) in Minas Passage. This results in a strong inertial force, flow separation at Cape Split and Cape Blomidon, an asymmetry in the flow pattern between flood and ebb (*Tee*, 1976), and strong M_4 currents on either side of these two promontories (*Mardell and Pingree*, 1981; *Geyer and Signell*, 1990).

There is no obvious relationship between the orientation of the M_4 and M_2 currents (cf. Figure 5.3). However, it will be shown in the next section that both the predicted and observed M_4 currents are closely aligned with the *mean* circulation. This is in agreement with the figures presented by *Hasegawa et al.* (2011).

5.5.4 Mean Currents

The streamlines of the predicted time-averaged depth-mean currents are shown in Figure 5.6a. The residual circulation is strongest in and around Minas Passage where four permanent eddies can be seen (I–IV). Figure 5.6b is an enlarged view of the mean flow in Minas Passage with the predicted mean flow now shown as grey vectors at every model grid point. Black vectors show the time mean of the observed depth-averaged currents calculated from the ten ADCP stations. Overall, this circulation pattern is in agreement with the observations. The model prediction is also consistent with additional observations

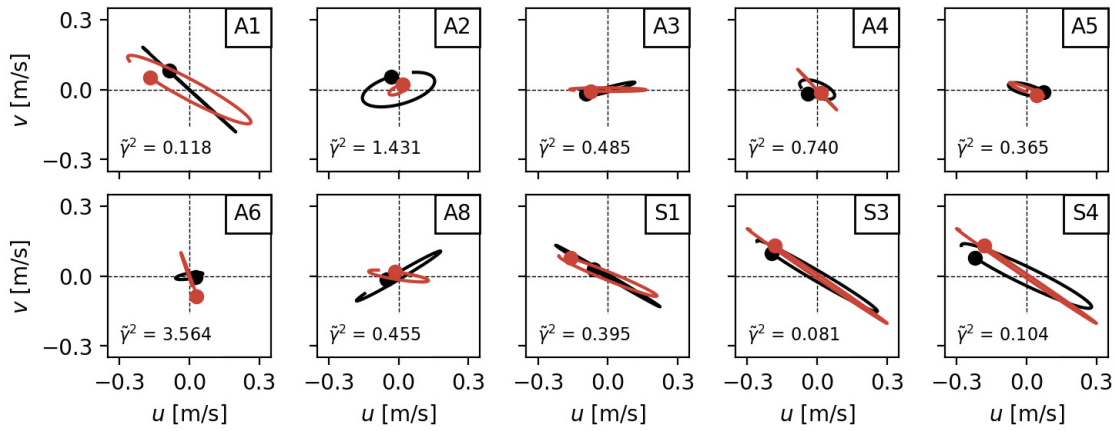

Figure 5.5: Predicted (red) and observed (black) M_4 tidal ellipses of depth-averaged currents. The format is the same as in Figure 5.3.

based on current meter measurements (*Tee*, 1977) which are not shown here.

The four permanent eddies (I–IV) have already been identified, and explained by *Tee* (1976) based on vorticity arguments, idealized model simulations, and runs with a more realistic bathymetry and coastline. He showed that the eddies are due to the combined effect of vorticity generation close to shore, subsequent advection by the tidal flow and non-local dissipation (see Section 5.2.1). Averaging over a tidal cycle results in the four permanent eddies described above. *Tee* (1976) also showed that the four eddies are due to the particular geometry of Minas Passage and Basin; he found no significant changes after setting the bathymetry to a constant value throughout the model domain, and also reducing the size of Cobequid Bay to simulate removal of the mudflats that exist in the upper part of the Bay.

A more quantitative comparison between the predicted and observed mean currents is given in Figure 5.7. The red vectors show the predicted mean depth-averaged current at center model grid points closest to the ADCP locations. Before time-averaging, the staggered velocity components defined on the C-grid were linearly interpolated to the center of the model grid cells and rotated such that the u-component of flow is positive toward the east. In each panel of Figure 5.7, the $\overline{\gamma}^2$ value for each station is given. There is general agreement between the observed and predicted mean currents at the 10 locations with the overall $\overline{\gamma}^2 = 0.303$. The reason for the large values of $\overline{\gamma}^2$ at some sites is a slight misplacement of the eddies in the model with respect to the observations (see Figure 5.6b). It is important to note that for GoMSS the fit to the mean currents is significantly worse

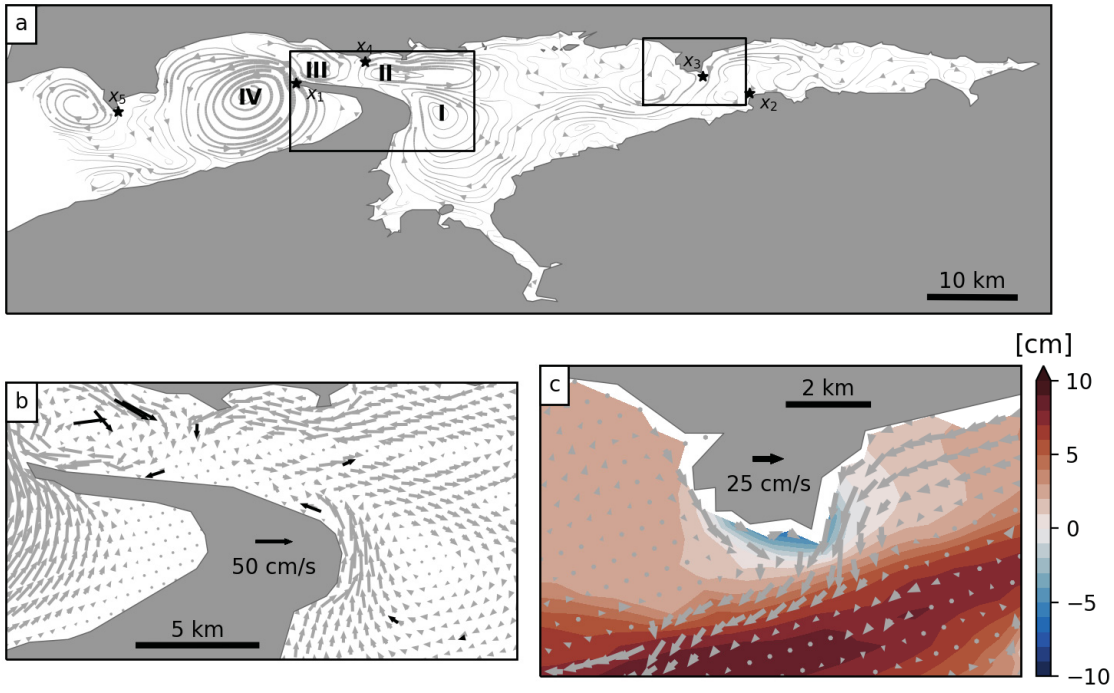

Figure 5.6: Predicted and observed time mean of depth-averaged currents. (a) Streamlines of the circulation pattern predicted by CTRL. (b) Enlarged view of the predicted mean flow around Cape Split shown as grey vectors at every model grid point. Black vectors indicate mean currents derived from high-resolution ADCP profiles. (c) Predicted mean circulation around the headland at x_3. Colors show the predicted MDT with the Bernoulli setdown removed.

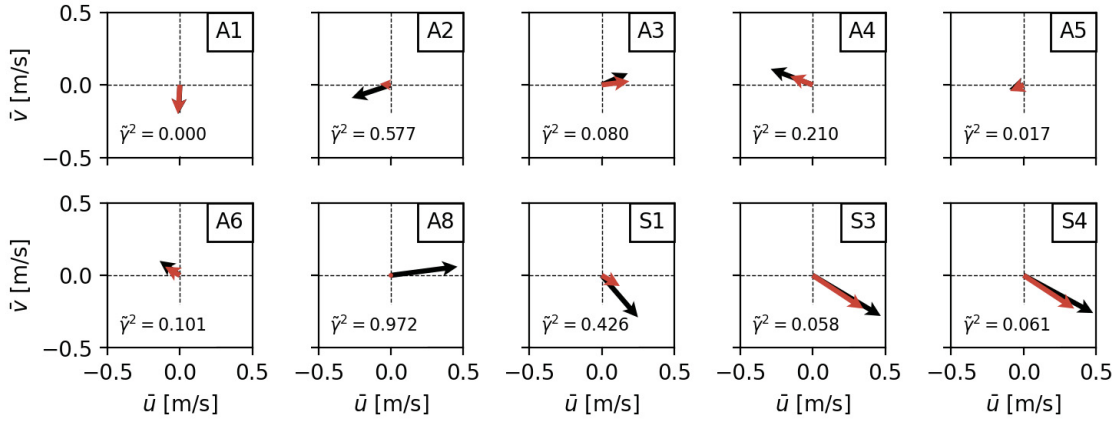

Figure 5.7: Predicted and observed time mean of depth-averaged currents at the 10 ADCP locations shown in Figure 5.1c. The vectors for observations and predictions are shown in black and red, respectively. $\overline{\gamma}^2$ for each station is given in the lower left corner of each panel.

($\overline{\gamma}^2 = 0.876$, Table 5.2). Mean currents from WebTide were not available.

Figure 5.6c is a zoom of the predicted mean around the headland at x_3. On either side of the headland, a pair of counter-rotating eddies can be identified which join to form a strong mean offshore flow away from the tip. These eddies are the result of positive (negative) vorticity generation caused by the eastward (westward) tidal flow past the headland, followed by flow separation and non-local vorticity dissipation (e.g., *Mardell and Pingree*, 1981; *Geyer and Signell*, 1990, see also Section 5.2.1). Similar arguments were used by *Tee* (1976) to explain the four gyres in Minas Passage. As discussed in Section 5.2.1, headlands can also have an important effect on MDT.

5.6 Model Prediction of MDT from UBoF

The MDT predicted by CTRL is shown in Figure 5.8. The dominant feature is the drop of almost 0.4 m in Minas Passage which can be explained by the Bernoulli effect due to the strong M_2 currents (see Section 5.2.1). This explanation is supported by the similar amplitude of M_4 elevation in this region (Figure 5.4b). More localized drops of MDT can also be seen around Cape Split and several headlands (e.g., x_3, x_4, and x_5). On the larger scale it is also clear from Figure 5.8 that the MDT inside Minas Basin is higher than in Minas Channel with an alongshore MDT difference between locations A and B of $\Delta\eta =$ 2.6 cm. (This value is in agreement with the model predictions of *Hasegawa et al.* (2011).)

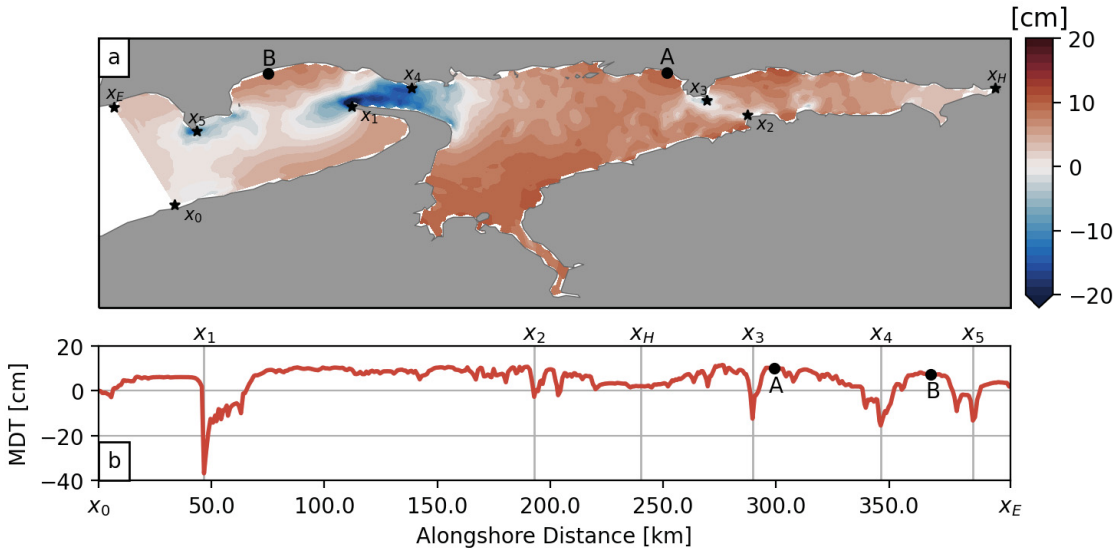

Figure 5.8: MDT relative to the value at x_0 predicted by CTRL. (a) Model prediction of MDT in the study region. Note that the minimum at Cape Split (−37 cm) is outside the range of the colorbar. The two black dots A and B indicate the model grid points between which the mean sea level difference $\Delta\eta$ has been computed. Stars mark alongshore reference points. (b) Predicted MDT as a function of alongshore distance from x_0.

$\Delta\eta$ will subsequently be used as a measure of the large-scale slope of MDT in the upper Bay of Fundy.

The predicted MDT after correction for the Bernoulli effect is shown in Figure 5.9. This correction reduces the overall variability, but $\Delta\eta$ remains positive (equal to 2.0 cm) and local depressions of MDT remain in the vicinity of Cape Split and the headlands mentioned above. At the head of Cobequid Bay a small setdown is predicted.

In order to explain this setdown, the *Li and O'Donnell* (2005) channel model (see Section 5.2.2) was extended to allow for forcing with multiple tidal constituents. If the tidal wave prescribed at the open boundary is the sum of a main tidal constituent and its first harmonic, e.g., M_2 and M_4, the model can predict a setdown in mean sea level toward the end of the channel (not shown). This setdown can be explained in terms of the asymmetry in the forcing due to the inclusion of the overtide.

Given the predicted tidal wave entering Cobequid Bay is already distorted due to a significant M_4 amplitude (0.72 m at the western most bottom pressure gauge 40264, see Table 5.3), its strong and short inflow is balanced by weaker outflow over a longer period. Consequently, mean bottom stress over the tidal cycle is established and this must be

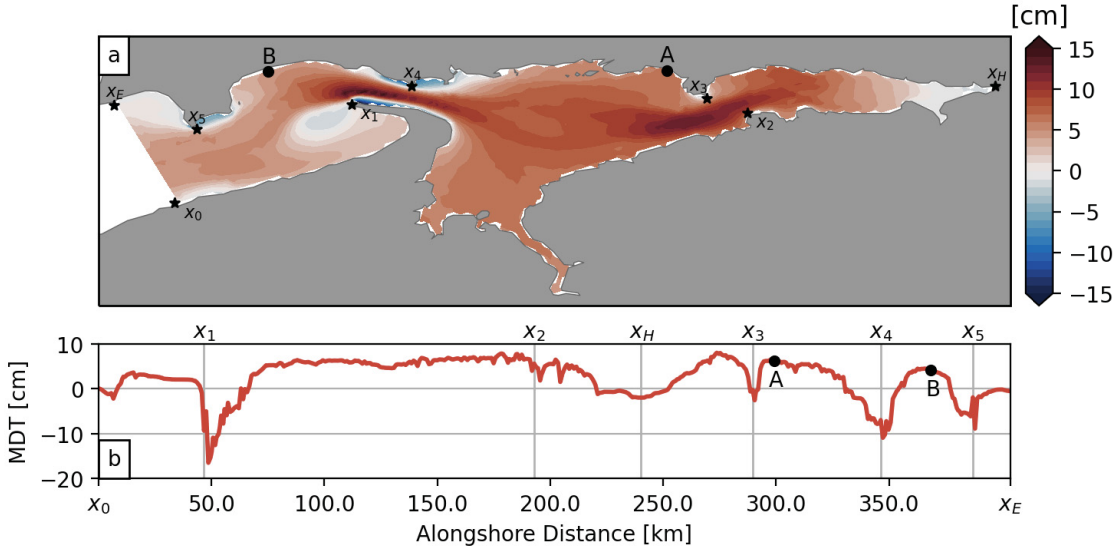

Figure 5.9: MDT prediction by CTRL with Bernoulli setdown $-\overline{\mathbf{u}}/2g$ subtracted. The format is the same as in Figure 5.8.

balanced by a drop in mean sea level toward the head.

Figure 5.6c shows the Bernoulli-corrected MDT around the headland at x_3. A setdown at the tip of the headland is evident. As discussed in Section 5.2, tidal flow around a headland generates not only a mean Bernoulli setdown, but also a pair of two counter-rotating gyres on either side of the promontory. Along the coast, a pressure gradient is required to drive the mean flow toward the tip of the headland. An analysis of the momentum balance shows that this pressure gradient is primarily balanced by bottom friction as expected. Note that these detailed results are consistent with the "back-of-the-envelope" calculation in Section 5.2.1 that showed frictional and Bernoulli contributions to the setdown at the tip can be comparable. There is also a secondary contribution from the time mean of the $\zeta\hat{\mathbf{k}} \times \overline{\mathbf{u}}$ term in the momentum equation, associated with the transient eddies generated either side of the headland. (The use of an Arakawa C-grid means the model sea level is not exactly at the coast where the $\zeta\hat{\mathbf{k}} \times \overline{\mathbf{u}}$ term vanishes.) The same momentum balance holds for the predicted MDT setdowns at Cape Split (x_1) and in Minas Passage (x_4).

5.6.1 Using Overtides to Identify Errors in MDT

As mentioned in the Introduction and shown in Chapter 4, GoMSS predicts a large setdown of MDT in the upper Bay of Fundy. Given the lack of long tide gauge records for this region, it is not possible to use observed, geodetically referenced mean sea levels to check the

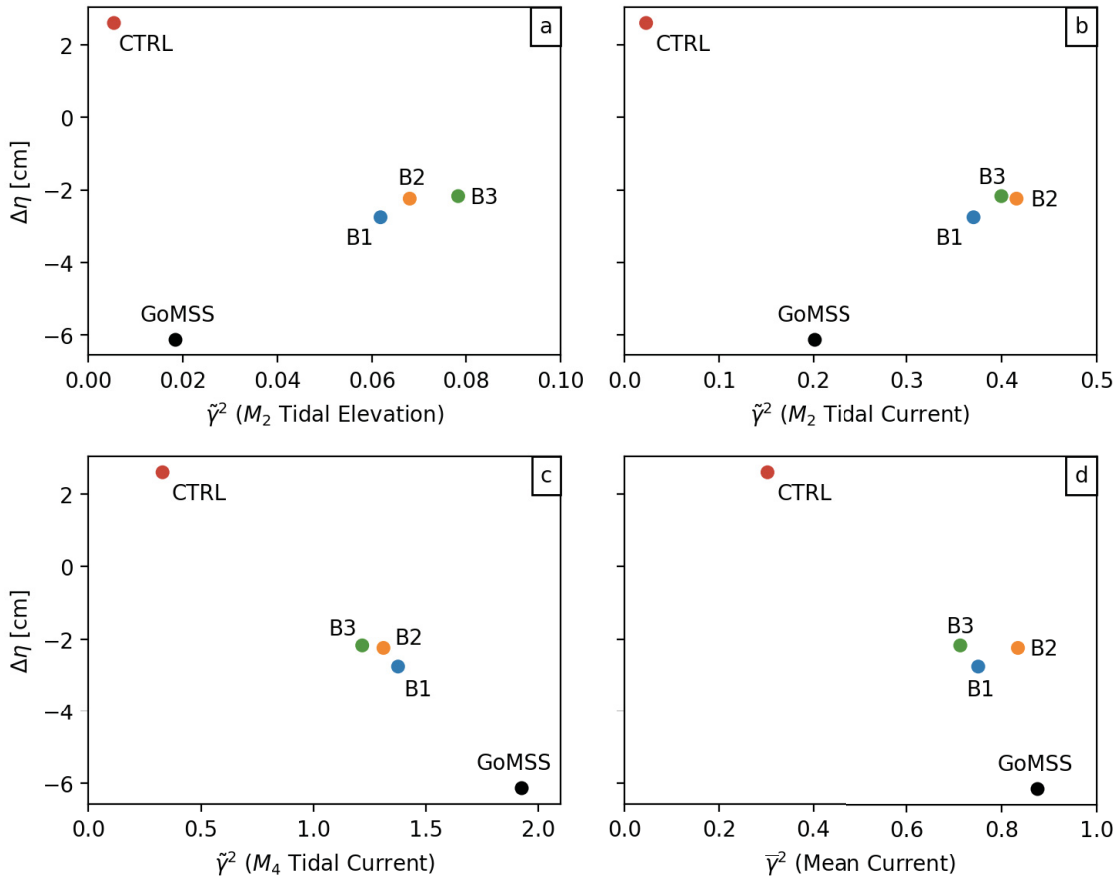

Figure 5.10: MDT difference $\Delta\eta$ as a function of γ^2 for models with different horizontal resolution and bathymetry. The metrics are $\tilde{\gamma}^2$ for M_2 tidal elevation (a) as well as M_2 and M_4 currents (b and c). (d) Relationship between $\Delta\eta$ and $\overline{\gamma}^2$. Black dots show the results for GoMSS. UBoF B1–B3 use the same high-resolution grid and model parameters as CTRL, but the bathymetry is replaced by the GoMSS bathymetry using different interpolation schemes (see Table 5.1 for details). Note the range of the x-axis varies among the panels.

realism of this setdown. Here, a question raised in the Introduction will be addressed: Can observations of overtides be used to assess the accuracy of MDT predictions? Particular attention is paid to the effect of spatial resolution and bathymetry, the main differences between GoMSS and UBoF, on the large-scale alongshore tilt of MDT $\Delta\eta$ and γ^2. As discussed in Section 5.5.2, none of the models considered here has skill in predicting M_4 elevation (Table 5.2) and therefore it has been excluded from the discussion below.

The predicted $\Delta\eta$ by GoMSS, and its values of $\tilde{\gamma}^2$ for M_2 elevation and current, are shown in Figure 5.10a and b (black dots, the values on the y-axis are the same). GoMSS predicts a 6.1 cm setdown going into Minas Basin through Minas Passage. There is nothing

in the fit of the observed and predicted M_2 elevations and currents that raises concern about the accuracy of this drop in mean sea level. The corresponding plot for M_4 currents (Figure 5.10c) tells a different story: $\tilde{\gamma}^2$ is close to 2 indicating no predictive skill for the dominant overtide. Given the intrinsic relationship between MDT and overtides due to nonlinearities in the governing equations, this high value of γ^2 means that the GoMSS setdown must be considered suspect. This is further supported by the $\overline{\gamma}^2$ for mean currents (Figure 5.10d).

The values of $\Delta\eta$ and γ^2 for CTRL are also shown in Figure 5.10 (red dots). This control run of UBoF predicts a 2.6 cm setup of mean sea level. The low values of γ^2 for M_4 and mean currents provide strong support in favor of the CTRL prediction of a small setup of MDT, and not the 6.1 cm setdown predicted by GoMSS.

Why does CTRL provide more accurate predictions of the overtides and mean currents at the ADCP locations? The most obvious explanation is that GoMSS has a relatively coarse resolution (two model grid points in Minas Passage) and a poorly resolved bathymetry in the study region. The CTRL configuration is superior to GoMSS in two respects: (i) its horizontal grid is refined by a factor of 4 compared to GoMSS, (ii) its bathymetry has been generated specifically for UBoF, taking into account more than 122 000 in-situ measurements using a specifically tuned optimal interpolation technique (Section 5.3.2 and Appendix C). The runs B1–B3 were designed to assess the effect of (ii). They all have the same high-resolution grid and model parameters as CTRL, and differ only in the way the GoMSS bathymetry was interpolated to the UBoF grid (see Table 5.1 for details).

The values of $\Delta\eta$ and $\tilde{\gamma}^2$ for the runs B1–B3 are shown in Figure 5.10 (blue, orange and green dots). Interpolating the coarse bathymetry of GoMSS to the UBoF model grid degrades the model fit for M_2 elevation and current but improves slightly the fit for M_4 and mean currents (presumably because nonlinearities are better represented with the increased spatial resolution). However, the $\tilde{\gamma}^2$ for M_4 and mean currents remain much higher than the values for CTRL implying increased horizontal resolution alone is not sufficient.

The runs B1–B3 all predict $\Delta\eta$ between -2 and -3 cm. This setdown is smaller than the GoMSS prediction, but still of opposite sign to the CTRL prediction. Based on the poor performance of runs B1–B3 in predicting overtides and the mean currents, these predicted setdowns also have to be considered suspect.

In summary, the use of overtides has led to conclusion that the large setdown in MDT predicted by GoMSS is highly suspect and the 2.6 cm setup predicted by the control run of

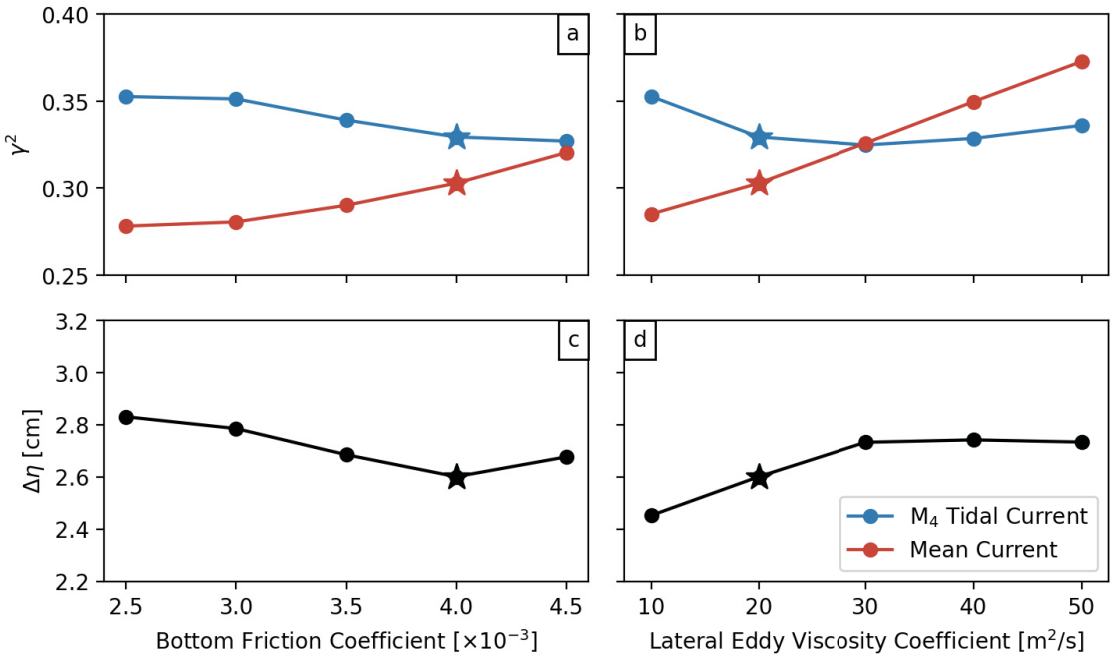

Figure 5.11: γ^2 and predicted mean sea level difference ($\Delta\eta$) for a subset of the UBoF S runs with varying bottom friction (a and c) and lateral eddy viscosity coefficient (b and d), respectively. The star indicates the UBoF control run (CTRL, see Table 5.1 for details) which has been validated in Section 5.5.

UBoF is more realistic. It is important to note that just increasing horizontal resolution did not necessarily improve model performance in the study region. This is at odds with the sensitivity studies by *Tee* (1976) discussed in Section 5.5.4 which showed that setting the bathymetry to a constant value did not have a significant effect on the four permanent eddies in the study region. The conclusion reached here is that a realistic bathymetry is critical. These conclusions could only have been reached by using observations at multiple frequencies, including overtides, to validate the models.

5.6.1.1 Sensitivity of MDT prediction to Model Parameters

Numerical ocean models typically have multiple parameters that can be adjusted to improve the agreement with observations. How sensitive are predictions of the large-scale MDT to model parameters?

The sensitivity of MDT and model performance has been analyzed with respect to different parameters. Here, the focus is on lateral eddy viscosity and bottom friction which appeared to have the biggest effect. (The results were insensitive to variations in the vertical mixing coefficient. This can be explained by the mainly barotropic character of

the circulation in the study region.)

UBoF was run with systematic variations of background lateral eddy viscosity $A_{\mathrm{h}}^{\mathrm{m}}$ and minimum bottom friction coefficients c_{d} over a realistic range, keeping all other model parameters fixed as in CTRL (see Table 5.1 for details). The overall range of $\Delta\eta$ of these runs is between 2.4 and 2.8 cm which shows that the predicted MDT is robust to varying these model parameters.

In Table 5.2, the range of γ^2 in the "S" runs is summarized for each variable. While values of $\tilde{\gamma}^2$ for tidal elevation and currents on semi-diurnal frequencies show very little sensitivity, there is some effect of lateral viscosity and bottom friction on the prediction of the overtides and mean currents. For M_4 tidal elevation, $\tilde{\gamma}^2 > 1$ for all model runs, indicating that none of the "S" runs has predictive skill for sea level variations at this frequency.

For M_4 and mean currents, γ^2 shows a considerable spread that warrant further examination. Figure 5.11 shows γ^2 and $\Delta\eta$, for a subset of the "S" runs with varying bottom friction (panels a and c) and lateral eddy viscosity coefficient (panels b and d). In all panels, the star indicates the control run of UBoF (CTRL) which has been validated in Section 5.5.

The agreement between predicted and observed mean currents improves with smaller bottom friction and lateral viscosity coefficient. All UBoF runs generally underestimate the speed of the mean currents. Reducing the bottom friction and viscosity gives faster currents and, consequently, lead to a stronger residual circulation which fits the observations better. However, this also leads to an overestimation of the tidal currents and their harmonics which is indicated by the higher $\tilde{\gamma}^2$ values for M_4 currents.

Sea level is mostly recorded by tide gauges near the coast where the water depth tends to zero and currents are weaker due to increased friction. This cannot be accurately captured in UBoF because the model requires a minimum depth and therefore, the coastal bathymetry is not well resolved in the model. Instead, a partial slip lateral boundary condition is applied to reduce the current along the coast.

Sensitivity experiments were conducted with varying strength of the partial slip boundary condition including the extreme cases of no-slip and free-slip. Applying a no-slip boundary condition led to a reduction of the model error for M_4 tidal elevation, but $\tilde{\gamma}^2 > 1$ and furthermore, the fit of the other variables deteriorated (see Table 5.2). This suggests that UBoF overestimates the nearshore currents which generates stronger overtides in these

regions.

The contrasting effect of different variables shows that there is not one "best" set of model parameters. In order to tune an ocean model, it is important to validate different variables at multiple (tidal) frequencies. This supports the idea by *Pingree and Maddock* (1978) that overtides can add useful information because they are directly related to the nonlinearities in the system.

5.7 Summary and Discussion

The prediction of an unexpectedly large setdown of MDT predicted by GoMSS in the upper Bay of Fundy raised concern about the ability of the model to provide accurate predictions of coastal MDT, and the mean ocean state in general. Obviously, this would have implications for using GoMSS to downscale the quasi-steady circulation on S2S timescales. Due to the lack of sufficiently long tide gauge records for the upper Bay of Fundy, it is not possible to validate the setdown predicted by GoMSS using the geodetic approach. This motivated a fundamentally different way of assessing predictions of MDT using observations of overtides. To capture the nonlinear dynamics responsible for the connection between overtides and the mean state, a new high-resolution model (UBoF) was embedded within the GoMSS grid.

Extensive model validation showed that the control run of UBoF (CTRL) generally agrees well with tidal observations of elevation and currents at semi-diurnal frequencies and also the dominant overtide M_4 (Table 5.2). The performance of UBoF is comparable to WebTide, a data-assimilating tidal model of the Scotian Shelf and Gulf of Maine region, and a significant improvement over GoMSS. (WebTide was used to prescribe the open boundary conditions of UBoF.) Both UBoF and WebTide gave poor predictions of M_4 elevation and this was explained in terms of an error generated in the upper reaches of Cobequid Bay, related to wetting and drying, that propagated throughout the model domain as a shallow water wave. A statistical method, based on station referencing, was developed to remove such remotely generated errors from the tidal observations and predictions before attempting to validate the model. This approach potentially has wider applicability to other studies and regions.

UBoF predicts a mean sea level difference between Minas Basin and Minas Channel of $\Delta\eta = 2.6\,\text{cm}$. This setup is of the opposite sign, and much smaller in magnitude, than the

corresponding prediction by GoMSS ($\Delta\eta = -6.1$ cm). A set of sensitivity studies showed that the UBoF prediction is robust to changes in the coefficients used to parameterize lateral and vertical mixing, and bottom friction. The overall performance of UBoF on multiple timescales, and its robustness, increase confidence in its prediction of MDT. The MDT prediction by GoMSS for the same region should be considered suspect based on its poor predictions of M_4 and mean currents.

Sensitivity studies showed that the difference in the performance of GoMSS and UBoF is not due solely to differences in horizontal resolution, but also the choice of method for generating the UBoF bathymetry. Both factors are critical for the accurate representation of nonlinearities in the ocean model and thus predictions of overtides and the mean state. It was shown that predictions of semi-diurnal tides are relatively insensitive to model resolution and bathymetry. This means that validating an ocean model using only diurnal and semi-diurnal tidal constituents may fail to identify important model deficiencies at other frequencies.

The most accurate version of UBoF, the control run CTRL, used a bathymetry that was a blend of a publicly available, gridded relief model (GEBCO) and more than 122 000 in-situ observations of water depth. The nominal grid spacing of global gridded datasets like GEBCO does not necessarily give an indication of its effective resolution which strongly depends on data availability (*Weatherall et al.*, 2015). The optimal interpolation scheme used here to generate the bathymetry for CTRL (see Appendix C) is both computationally efficient and robust. This means it could be used to generate high resolution models "on the fly" for relocatable ocean models deployed in response to environmental emergencies (e.g., *Chegini et al.*, 2018).

High resolution models like UBoF, validated by overtides and mean currents, can provide valuable information to geodesists. The present study has shown that the strongest signals in alongshore MDT occur in Minas Passage and in the vicinity of headlands. Here, the generation and subsequent advection of vorticity by the tidal flow leads to a pair of counter-rotating, mean gyres either side of the promontory. This results in local setdowns of coastal MDT at the tip of the headlands caused primarily by bottom friction and the transport of vorticity. When combined with the Bernoulli effect the total setdown can be of order 10 cm, an amount that greatly exceeds the standard error of the recent generation of geoid models. This has implications for future deployments of tide gauges in support of

geoid model validation; high resolution models like UBoF, validated in part by overtides, can be used to select optimal tide gauge locations.

To conclude this chapter, the three research questions raised in the Introduction are now answered:

(i) Is it possible to use observations of overtides to help configure an ocean model and also validate its predictions of the mean state? Overtides were critical in selecting the optimal bathymetry for UBoF. They also helped show that the MDT predicted by GoMSS for the upper Bay of Fundy is likely incorrect. More generally, model validation based on overtides can be a useful complement to traditional model-observation comparisons at principal tidal frequencies in shallow, tidally dominated regions.

(ii) What are the implications for the design of geodetic and ocean observing systems? From a geodesist's perspective, a high resolution ocean model, validated by overtides and mean currents, can be used to determine optimal locations for long-term sea level measurements in support of geoid model validation. From an oceanographer's perspective, a major advantage of validating an ocean model using overtides is that the observed record can be relatively short (order one month) and its vertical datum does not need to be specified. Reliable observations of mean sea level for MDT validation using the standard geodetic approach require decades of hourly sea levels and continuous vertical datum control. On the negative side, sea level predictions of overtides can be contaminated by remotely generated errors and care must be taken in the selection of the coastal tide gauge or offshore bottom pressure locations in order to minimize such errors (or remove them using the referencing approach described in Section 5.5.2). If the errors propagate as a shallow water wave, they will have a relatively weak signature in currents compared to sea level. This implies that overtides in currents are potentially more useful than overtides in sea level.

(iii) What insights about the physical processes determining MDT can be obtained from observations of overtides? The MDT predicted by UBoF for the upper Bay of Fundy is strongly coupled to local features in the coastline (e.g., headlands) and bathymetry. Horizontal advection is the dominant nonlinear process through the Bernoulli effect and also the generation of a secondary mean circulation that requires a sea level gradient to overcome the associated frictional drag. It is therefore important that these features are captured in the model.

CHAPTER 6

DOWNSCALING THE OCEAN RESPONSE TO THE MADDEN-JULIAN OSCILLATION

6.1 Introduction

Previous studies (*Katavouta and Thompson*, 2016; *Katavouta et al.*, 2016) and the validation described in Chapters 4 and 5 have shown that the regional ocean model GoMSS has useful skill in predicting the circulation and hydrography of the Gulf of Maine and Scotian Shelf. In this chapter, GoMSS is used for subseasonal-to-seasonal (S2S) prediction through dynamical downscaling of the mean ocean circulation in response to the Madden-Julian Oscillation (MJO).

As shown in Chapter 2, large-scale anomalies in sea surface temperature (SST) occur along the eastern seaboard of North America in response to the MJO during boreal winter (December–February, DJF). These anomalies reach their maximum 20–25 days after phases 3 and 7 defined by the Real-Time Multivariate MJO (RMM) index. Predictions by a simplified surface mixed layer model demonstrated that this SST response is caused by net heat flux anomalies which arise from the teleconnection between the MJO and the extratropical atmospheric circulation at higher latitudes. This identifies a potential temporal "window of opportunity" of enhanced S2S predictability for the ocean.

In contrast to the mixed layer model, GoMSS is a high-resolution regional model which captures all relevant physical processes that influence the ocean and shelf circulation, e.g., advection by large-scale currents, tidal mixing, and stirring by mesoscale variability. Therefore, it is a suitable tool to further explore the ocean response related to the MJO

and its interaction with other ocean processes. Due to its three-dimensional model grid, GoMSS can also be used to analyze how the surface signal is projected vertically into the ocean interior. Compared to most global ocean circulation models and reanalyses, GoMSS has a relatively high spatial resolution (1/36° grid spacing) and also includes tides. These properties are needed to better and more accurately predict the circulation and hydrography in the study region.

Regional ocean models like GoMSS require forcing along the lateral and surface boundaries including variability on S2S timescales. Hence, atmospheric perturbations caused by the MJO can be included in the surface forcing of GoMSS. Additionally, changes in the large-scale ocean circulation due to the MJO can enter the model through the open boundary conditions.

In this study, a signal related to the MJO, and based on composited forcing variables with respect to a specific MJO phase, is added to the forcing of the model. The predicted ocean response can then be attributed directly to the additional forcing and thus the MJO.

The following research questions will be addressed: (i) Can GoMSS reproduce the three-dimensional, time-varying response of the ocean to the MJO? (ii) What are the main physical processes that shape the mean ocean response to the MJO? (iii) How is the effect of atmospheric forcing in response to the MJO vertically projected into the subsurface ocean? (iv) What is the importance of including forcing at higher frequencies than the MJO (e.g., tides and weather)?

Section 6.2 gives an overview of the configuration of GoMSS and the idealized boundary forcing used for the model experiments in this study. In Section 6.3, the model predictions of the mean hydrographic conditions during winter are presented. The atmospheric forcing related to the MJO is discussed in Section 6.4 and Section 6.5 describes the ocean response to this forcing predicted by GoMSS. A summary and discussion of the results is given in Section 6.6.

6.2 Model Experiment Design

A detailed description of GoMSS is provided in Chapter 3 and the configuration used here is described in Section 4.2.2.

For the present study, idealized forcing based on climatology and composites of atmospheric and ocean reanalyses conditioned on the state of the MJO was used. Here, the

focus is on phases 3 and 7 during winter. These phases have been shown to lead to a large-scale ocean response in the North Atlantic (Chapter 2). The ocean initial conditions and lateral boundary forcing were computed from the global GLORYS12v1 reanalysis (*Fernandez and Lellouche*, 2018, daily data available for the period 1993–2018). At the air-sea interface, the atmospheric forcing is based on the NCEP Climate Forecast System Reanalysis (CFSR, *Saha et al.*, 2010, hourly data available for the period 1979–2010). Data for the common period of the datasets, 1993–2010, have been used. The surface fluxes of heat and momentum are calculated internally by GoMSS based on the CORE bulk formulae (*Large and Yeager*, 2004). The following atmospheric variables are used: 10 m wind, air temperature and specific humidity at 2 m, downward short and outgoing longwave radiation as well as precipitation. More details on the open boundary and surface forcing are given in the following subsection.

Three model experiments have been performed with GoMSS. Each model run was for the period 1 October to 18 February with the first three months discarded to avoid contamination by model spin-up. Details of the experiment design are given below.

6.2.1 Boundary Forcing and Model Experiments

As discussed in Section 1.2 of the Introduction to the thesis, interaction across scales plays a dominant role in shaping the ocean and shelf circulation. This has to be taken into account in the specification of the boundary forcing of GoMSS. For the present study, the idealized model forcing F along the open boundaries and at the air-sea interface is decomposed into contributions from four frequency bands

$$F = \overline{F} + F'_{\mathrm{a}} + \tilde{F}_{\mathrm{o}} + \hat{F}(j, \delta), \tag{6.1}$$

where $\overline{F}$ is the seasonal climatology, F'_{a} is high-frequency atmospheric variability with timescales of 10 days or less, $\tilde{F}_{\mathrm{o}}$ are tidal variations (only applied at the lateral ocean boundaries), and $\hat{F}(j, \delta)$ is the forcing on S2S timescales (15–100 days) depending on the lag δ after a given MJO phase $\Phi_{\mathrm{RMM}} = j$. Using this decomposition, it is possible to identify the effect of the different forcing timescales on the circulation and hydrography in the GoMSS domain. In order to isolate the predicted mean ocean response to the MJO, model sensitivity runs with and without forcing on S2S timescales are performed.

It is important to recognize $\overline{F}$ describes a smoothly varying seasonal mean of the

atmosphere-ocean system. (Due to the higher heat capacity of water, the surface ocean does not fully adjust to the cooling by the atmosphere during winter.) Therefore, it is important to include the seasonal cycle in $\overline{F}$ as opposed to a seasonal mean value which would lead to an overestimation of the winter cooling. The daily climatology of the forcing variables was computed for the period 1993–2010 using the methodology of *Hobday et al.* (2016) as described in Section 2.2.2. The forcing on synoptic and S2S timescales is extracted by applying filters to the anomalies which were calculated by subtracting the climatology from the respective original fields of the ocean and atmosphere reanalyses.

Stochastic, high-frequency variability in the atmospheric forcing F'_{a} is necessary for a realistic prediction of the hydrography, particularly the mixed layer depth (see below). F'_{a} includes weather events on synoptic timescales, e.g., storms passing through the study area. In order to compute F'_{a}, a third order Butterworth highpass-filter (*Butterworth*, 1930) with a 10-day cutoff was applied to the anomalies at each grid point of the atmospheric forcing. The filtered anomalies for the period 1 October 1993 to 18 February 1993 were then used to define the high-frequency atmospheric forcing F'_{a}. This period was chosen based on the reduced activity of the MJO (mean A_{RMM} = 1.2). Given the known connection between the MJO and the El-Niño Southern Oscillation (ENSO, e.g., *Lee et al.*, 2019) the period for the high-frequency forcing was also chosen to be a during a neutral year indicated by the Oceanic Niño Index of 0.1 °C during DJF 1992/93. Sensitivity studies using anomalies from a different year showed that all results presented in this chapter are robust to changes in the period of the high-frequency forcing.

The atmospheric and ocean forcing on S2S timescales $\hat{F}$ is based on lagged composites with respect to the MJO which were calculated following the methodology outlined in Section 2.3. Prior to compositing, the variability of the forcing variables in the MJO frequency band was extracted by applying a third order Butterworth bandpass filter with a 15–100-day passband to the anomalies. Additionally, any remaining interannual variability was removed by subtracting the mean anomaly of each winter season. The forcing composites $\hat{F}(j, \delta)$ were then created by computing the mean bandpass-filtered anomalies conditioned on MJO phase $\Phi_{\mathrm{RMM}} = j$ during winter when the RMM amplitude $A_{\mathrm{RMM}} > 1$. Composites of the atmospheric forcing variables are shown and discussed in Section 6.4. The impact of $\hat{F}$ along the lateral boundaries is assumed to be smaller than the atmospheric forcing and will not be further discussed.

Table 6.1: Overview of boundary forcing for model experiments with GoMSS. Each column refers to atmospheric and ocean forcing in a frequency band defined in (6.1). The checkmarks indicate which forcing frequencies are applied. See text for details.

	Spin-Up Period 1 October – 31 December				Analysis Period 1 January – 18 February			
Run	$\overline{F}$	F'_{a}	$\tilde{F}_{\mathrm{o}}$	$\hat{F}$	$\overline{F}$	F'_{a}	$\tilde{F}_{\mathrm{o}}$	$\hat{F}$
P0	✓	✓	✓		✓	✓	✓	
P3	✓	✓	✓		✓	✓	✓	$\hat{F}(3,\delta)$
P7	✓	✓	✓		✓	✓	✓	$\hat{F}(7,\delta)$

The ocean reanalysis does not include tides and therefore predictions by the global tide model FES2004 (*Lyard et al.*, 2006) have been used to specify the tidal forcing $\tilde{F}_{\mathrm{o}}$. This includes tidal elevation and depth-averaged currents for five tidal constituents (M_2, N_2, S_2, K_1, O_1).

An alternative approach to the decomposition of F in (6.1) would be the specification of $\hat{F}$ by extracting the MJO-related forcing using a linear regression of the raw reanalysis fields onto the RMM index (e.g., *Oliver*, 2015). The difference between a model experiment using the full reanalysis fields as forcing F and a run using $F-\hat{F}$ would allow the response to the MJO to be quantified. This approach can be useful to identify the ocean response to a canonical cycle or individual episodes of the MJO. However, it is not straightforward to specify the known time lag between a specific MJO phase and the atmospheric and ocean response which can vary with location. For this reason, the composite-based approach is used in this study; it provides a prediction of the mean ocean response to the MJO and its lagged behaviour can be directly assessed with respect to a particular phase. It is also a natural extension of the composite analysis of the SST observations in Chapter 2.

Three model experiments were performed to downscale the mean ocean response with focus on MJO phases 3 and 7 during winter. The response to each phase is predicted in a separate model run (P3 and P7) which is then compared to a control run (P0) without $\hat{F}$ (see Table 6.1). All model runs were initialized with the climatology for 1 October and spun up over three months until 31 December using the neutral forcing

$$F_{\mathrm{n}} = \overline{F} + F'_{\mathrm{a}} + \tilde{F}_{\mathrm{o}}. \tag{6.2}$$

The control run P0 is based on continued forcing with F_{n}, whereas for P3 and P7, the composites $\hat{F}(j,\delta)$ were added for $j = 3$ and $j = 7$, respectively. It is assumed that the MJO occurs in a given phase on 1 January and thus the contemporaneous composites ($\delta = 0$) were included in the forcing for that day. This added forcing is small enough that no additional spin-up was necessary. For the subsequent days, composites for increasing lags $\delta > 0$ were added. Each model run was continued until 18 February which is equivalent to a lag δ = 48 days after a given phase and corresponds to the mean period of the MJO. The downscaled mean ocean response to forcing in the MJO frequency band is then obtained by subtracting the control run P0 from P3 and P7, respectively. In the following, only the 49-day, post spin-up period will be discussed.

6.3 Predictions of Mean Hydrography during Winter

Figure 6.1 shows the mean sea surface temperature and salinity predicted by the control run P0 for the analysis period focusing on the model grid points with water depth <2000 m. In the study region, colder, less salty waters can be seen off the coast of Newfoundland and warmer, slightly more saline waters in the Gulf of Maine (GoM) and on Georges Bank (GB). Cold and relatively fresh water enters the model domain through the western Cabot Strait and follows the Nova Scotia Current along the coast toward the Gulf of Maine. The outer edge of the current can be identified by the strong gradients of temperature and salinity confining this water mass to the nearshore on the Scotian Shelf.

This separation is also visible in mean hydrographic conditions along the section across the Scotian Shelf marked by the black line and shown in Figure 6.2. Henceforth, this will be referred to as the Scotian Shelf section. The horizontal density gradient in the surface mixed layer marks the front separating the colder and fresher water mass associated with the Nova Scotia Current from the rest of the shelf. Across the entire Shelf, the water column is stratified with colder, fresher water in the surface mixed layer with depth of about 60–80 m. This is in close qualitative agreement with the winter climatology computed from glider-based observations by *Dever et al.* (2016). The realism of the seasonal mean state predicted by the control run P0 is further supported by its similarity to the results of *Katavouta and Thompson* (2016) and *Katavouta et al.* (2016) who demonstrated the good performance of GoMSS using a variety of observations.

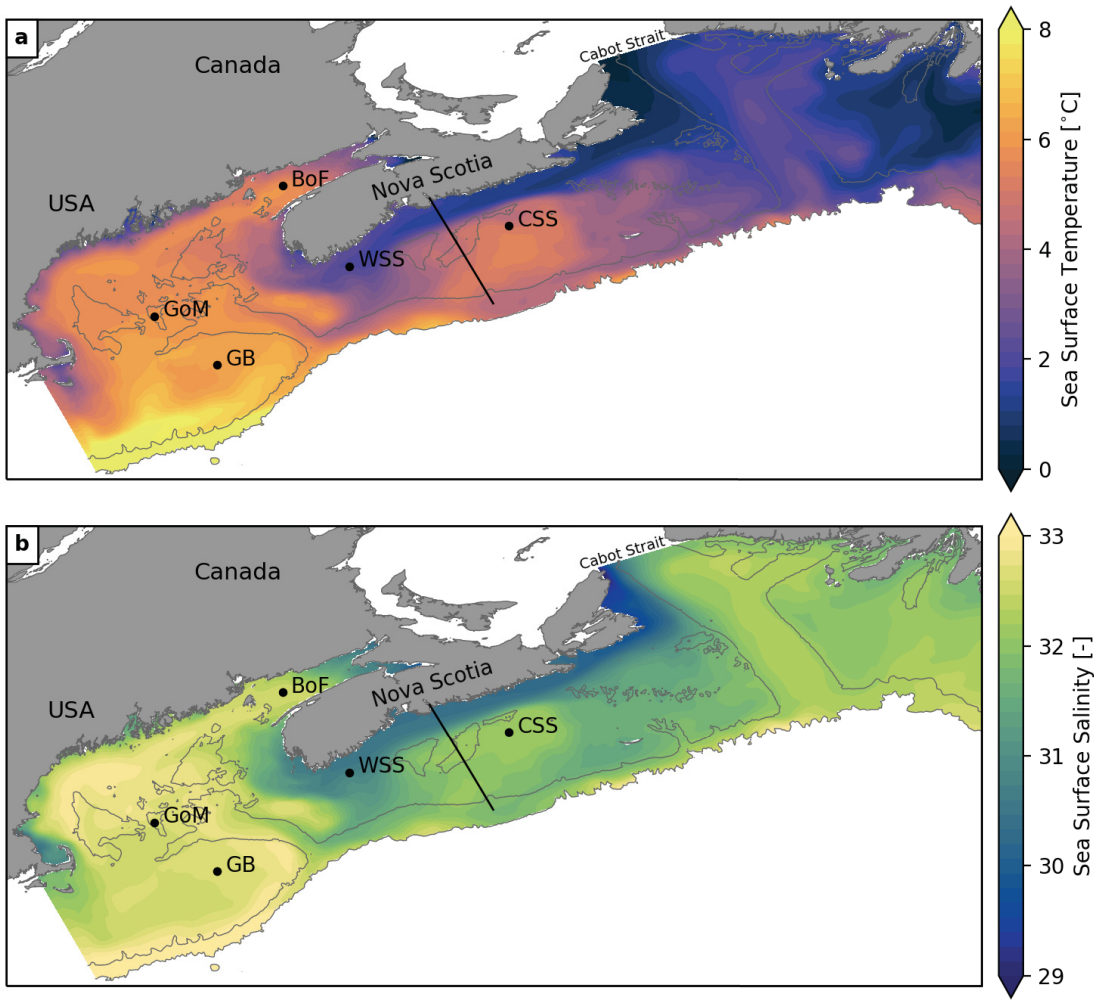

Figure 6.1: Mean sea surface temperature (a) and salinity (b) predicted by the GoMSS control run P0. Only model grid points are shown where the water depth $<$2000 m. The line marks the Scotian Shelf section. Black dots mark five representative locations where the model predictions are further analyzed.

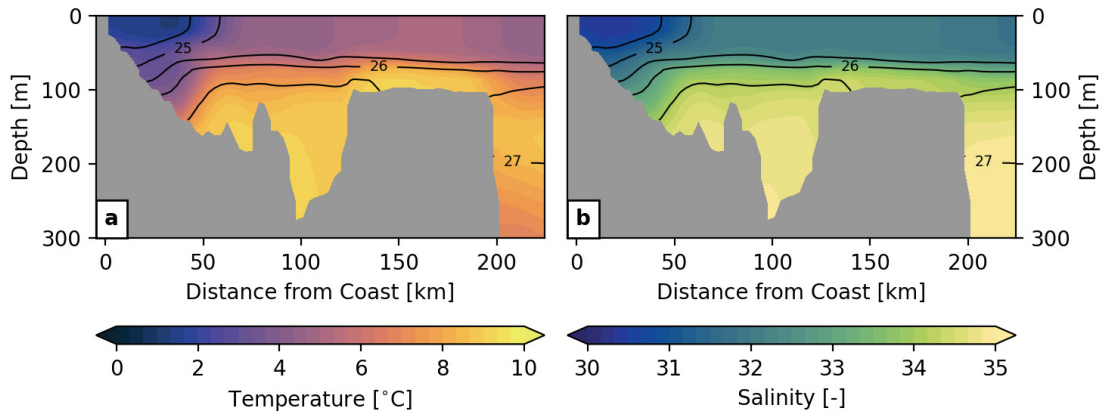

Figure 6.2: Mean hydrographic conditions along the Scotian Shelf section predicted by the GoMSS control run P0. (a) Ocean temperature. (b) Salinity. The contours show the associated in-situ density $\sigma = \rho - 1000\,\mathrm{kg\,m^{-3}}$.

6.3.1 The Importance of High-Frequency Atmospheric Forcing

Model test runs showed that stochastic, high-frequency variability in the atmospheric forcing is needed for GoMSS to realistically predict the hydrography in the study region, particularly the mixed layer depth. Figure 6.3 shows the mean hydrographic conditions along the Scotian Shelf section predicted by a GoMSS run with neutral forcing F_n, but excluding atmospheric variations on synoptic timescales F'_a. It is obvious that the colder and fresher surface water mass is constrained to a thin layer with depth of order 10 m. This leads to a strong stratification of the top 100 m of the water column and a less pronounced pycnocline which can be related to the absence of enhanced mixing due to strong wind forcing.

The predictions by a simplified surface mixed layer model in Chapter 2 showed that SST variability on S2S timescales is determined by net heat flux anomalies in response to the MJO. In that model, the mixed layer depth is an important parameter that determines the strength of the SST response. This shows that a correct representation of the mixed layer is critical for S2S predictions of the ocean and therefore, it is important to include high-frequency atmospheric variations in the forcing of GoMSS. Note that the mixed layer depths independently estimated by the statistical model (70–100 m, see Figure 2.8b in Chapter 2) are comparable to the prediction by GoMSS P0. This is remarkable given the simplified dynamics in the mixed layer model.

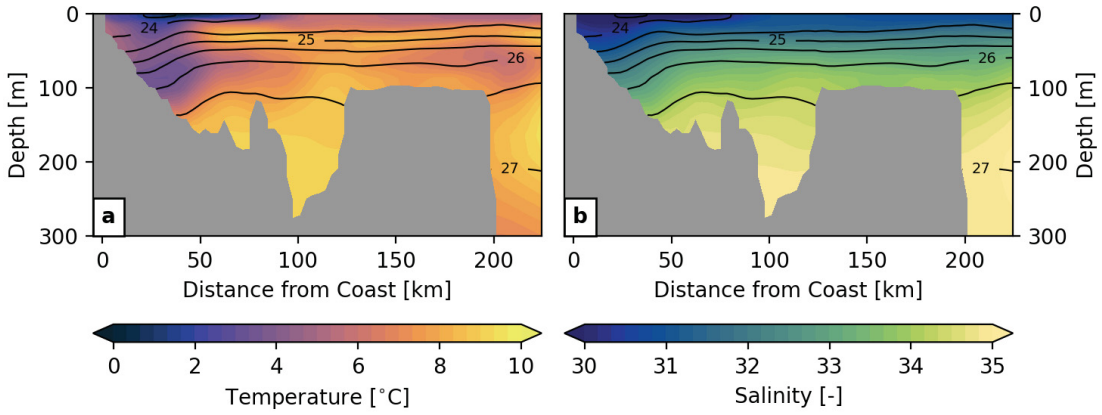

Figure 6.3: Mean hydrographic conditions along the Scotian Shelf section predicted by a GoMSS test run without high-frequency atmospheric forcing F'_{a}. The format is the same as Figure 6.2.

6.4 Composites of Atmospheric Forcing Conditioned on the MJO

Before the downscaled ocean response to forcing on S2S timescales is discussed, it is worthwhile analyzing the MJO-related signal in the atmospheric surface forcing itself. Here, the focus is on the air temperature and wind fields.

Figure 6.4 shows composite maps of bandpass-filtered 2 m air temperature and 10 m wind anomalies at lags $\delta = 6$, 12, ..., 30 days with respect to MJO phases 3 and 7 when $A_{\mathrm{RMM}} > 1$ during winter. It can be seen that during the weeks following phase 3, a strong warm anomaly occurs throughout the study region with near-surface temperatures over land that are up to 2 °C higher than the climatology. Over the ocean, the signal becomes weaker with increasing distance from the coast. Another band of slightly higher temperature anomalies can be seen along the track of the Gulf Stream at lag $\delta = 12$ days. The elevated near-surface temperatures are accompanied by anomalous winds over the ocean from the southeast and south.

At lag $\delta = 30$ days after phase 3, a cold anomaly and northerly winds occur in the study area. Given that the MJO spends, on average, 6 days in one phase, this time is equivalent to a lag $\delta = 6$ days after phase 7. Note that after half a cycle of the MJO, there is still a significant amount of autocorrelation in the RMM index (see Section 2.2.2 in Chapter 2). This is apparent by comparing the last panel in the left column with the first composite in

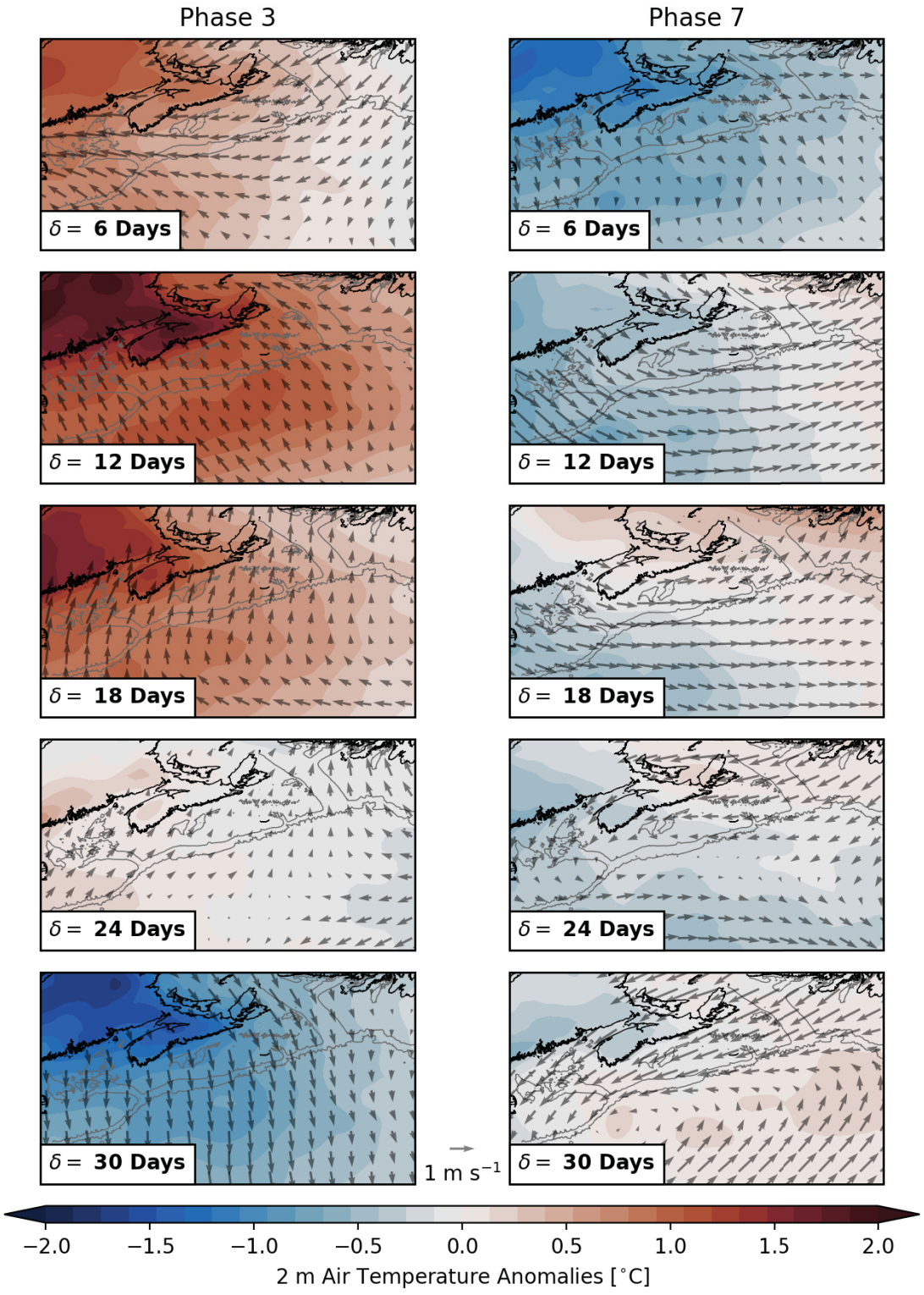

Figure 6.4: Composites of bandpass-filtered anomalies of 2 m air temperature and 10 m wind for MJO phases 3 and 7 when $A_{\mathrm{RMM}} > 1$ during winter. The wind vectors are shown at every third grid point over the ocean.

the right column of Figure 6.4. Interestingly, the signal appears stronger at long lags after phase 3. With increasing lag after phase 7, the cold anomaly weakens, but the anomalous wind is still predominantly in the offshore direction. The strongest wind anomalies occur over the Gulf of Maine and Georges Bank at lag $\delta = 12$ days after phase 7.

Overall, these surface temperature and wind composites are in agreement with previous studies (e.g., *Lin and Brunet*, 2009; *Seo et al.*, 2016) and the atmospheric circulation anomalies presented in Chapter 2 (see Figure 2.11). The warm (cold) anomalies in Figure 6.4 generally coincide with positive (negative) anomalies of specific humidity 2 m above ground (not shown). These changes in the forcing variables lead to changes in the air-sea fluxes. In the following section, the predicted ocean response to these changes in the forcing on S2S timescales will be analyzed.

6.5 Predicted Ocean Response to MJO-Related Forcing

The ocean response in the Gulf of Maine and Scotian Shelf to forcing on S2S timescales is analyzed by comparing the deviations of the GoMSS model runs P3 and P7 from the control run P0. These differences will henceforth be referred to as anomalies. First, the predicted SST response in the study area will be analyzed and compared to the observed composites presented in Chapter 2. Next, the penetration of the signal into the ocean interior will be explored. Finally, the predicted bottom salinity will be analyzed for changes in the circulation on the Scotian Shelf due to the forcing related to the MJO.

6.5.1 Sea Surface Temperature

The spatial structure of the surface ocean response to MJO phase 3 in the Northwest Atlantic shelf region is shown in Figure 6.5. In the left column, composite maps of bandpass-filtered, observed SST anomalies relative to zero lag are shown for $\delta = 6$, 12, ..., 30 days. These are the same composites computed in Section 2.3, but here they have been referenced to the anomalies at lag $\delta = 0$ days, to make them more comparable to the results of the sensitivity experiments with GoMSS. As illustrated in Chapter 2, a wide-spread warm anomaly occurs in the study region 2–3 weeks after the MJO is in phase 3.

The panels in the right column of Figure 6.5 show SST anomalies predicted by GoMSS in response to the composite forcing calculated as the difference P3 $-$ P0. It can be seen that the forcing on S2S timescales leads to a large-scale surface warming in the study area

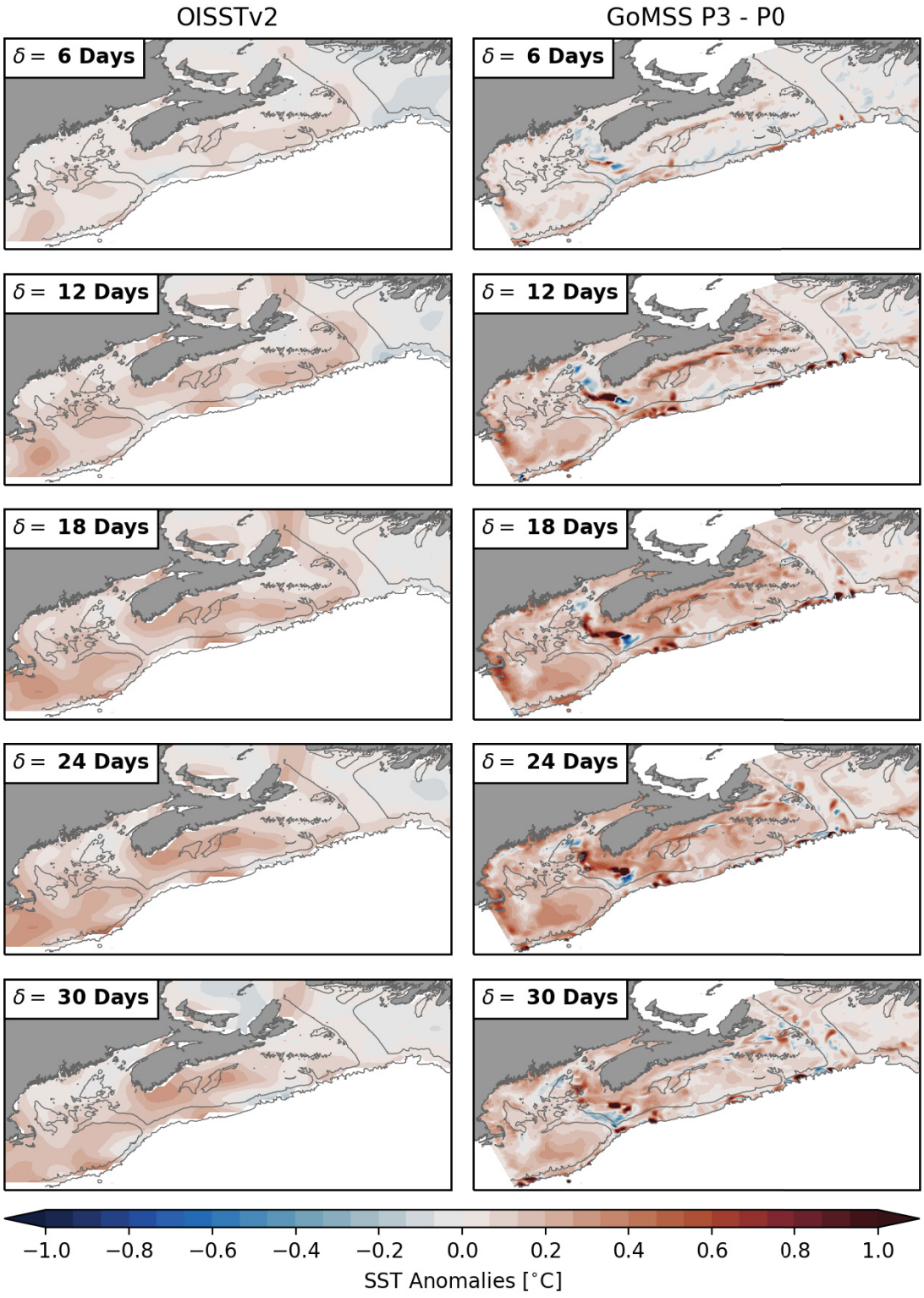

Figure 6.5: Observed composites and predictions of SST anomalies with respect to MJO phase 3. Left column: composite maps of bandpass-filtered, observed SST anomalies when $A_{\text{RMM}} > 1$ during winter. Right column: SST anomalies predicted by GoMSS (P3 − P0). All anomalies are relative to lag $\delta = 0$ days.

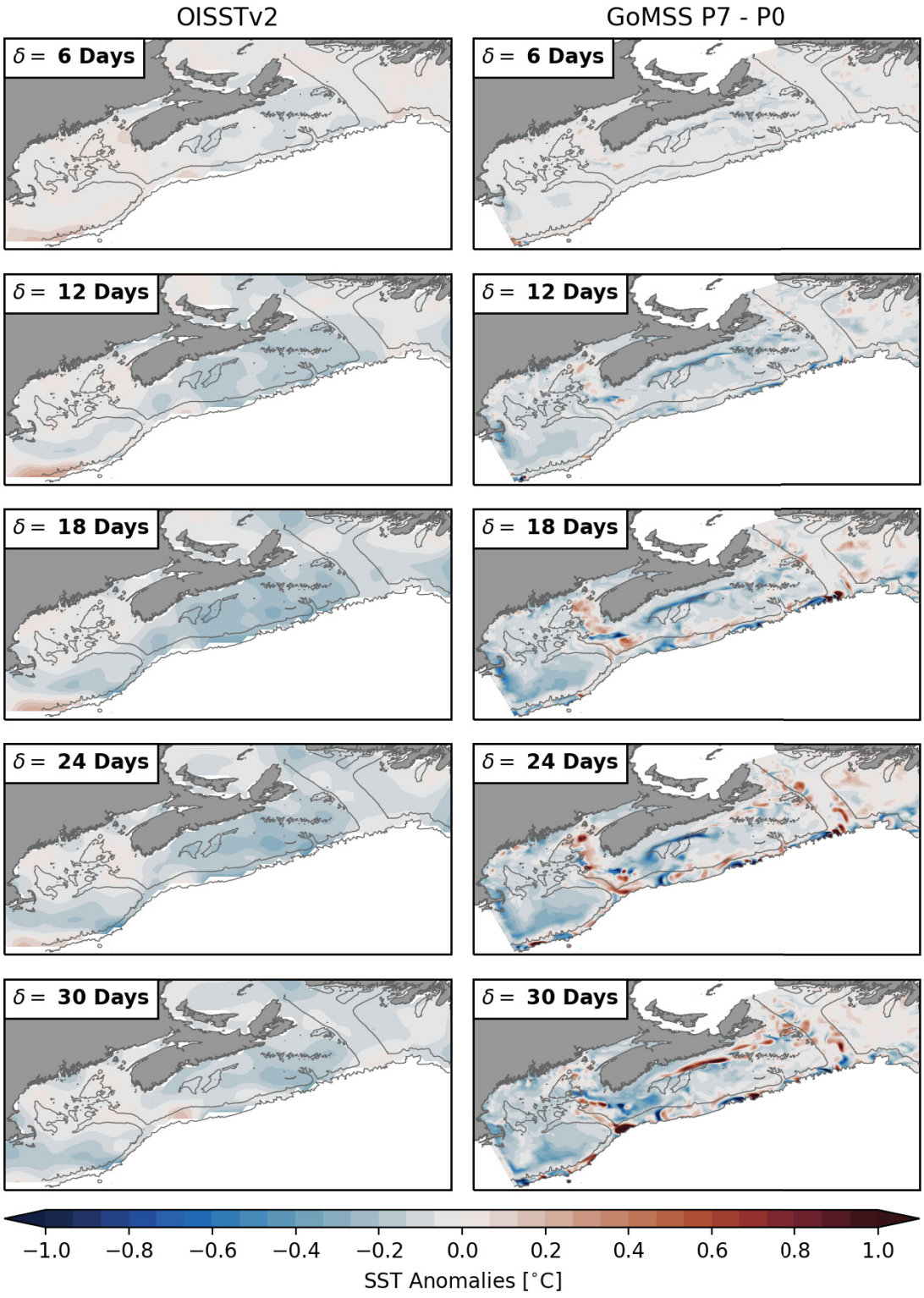

Figure 6.6: Observed composites and predictions of SST anomalies with respect to MJO phase 7. The format is the same as Figure 6.5.

reaching its maximum 18–24 days after the MJO is in phase 3. This predicted increase in SST is broadly consistent with the observed composites. The strongest response is found on Georges Bank and on the Scotian Shelf. Generally, the maximum surface warming predicted by GoMSS is slightly stronger and contains small-scale features that cannot be captured in the gridded observations due to their coarser resolution.

Similarly, GoMSS is able to capture the large-scale cooling trend after MJO phase 7 which is evident in the observed composites in the left column of Figure 6.6. The strongest decrease in SST is observed on the eastern Scotian Shelf at lags $\delta = 18$–24 days. In the panels on the right of 6.6, the predicted SST anomalies (P7 $-$ P0) are shown for the period after MJO phase 7. GoMSS slightly underestimates this cooling and, contrary to the observations, predicts a stronger response on the western Scotian Shelf to occur later at δ = 24–30 days. Furthermore, the model predicts an overall surface cooling throughout the Gulf of Maine which is not seen in the observations.

The predicted SST response is consistent with forcing due to the large-scale atmospheric anomalies following MJO phases 3 and 7 shown in Figure 6.4. This furthermore confirms the results of the simplified surface mixed layer model in Chapter 2.

Due to its higher horizontal resolution, GoMSS is also able to predict localized features, e.g., a narrow band of large anomalies along the outer edge of the Nova Scotia Coastal Current and off the coast of southwest Nova Scotia. In these areas, strong SST gradients exists (see Figure 6.1). Due to the MJO-related forcing, these gradients are shifted horizontally leading to anomalies of >1 °C. This is further discussed below in Section 6.5.2. The horizontal resolution of OISSTv2 (1/4° grid spacing) is too coarse to resolve these features.

The temporal evolution of the SST anomalies in response to the MJO is now further discussed at the five representative locations in the GoMSS model domain defined in Figure 6.1. In the left column of Figure 6.7, SST composites of bandpass-filtered observations and the global ocean reanalysis are shown with respect to MJO phase 3 when $A_{\mathrm{RMM}} > 1$ during winter. The observed composites on Georges Bank and on the Scotian Shelf are the same as in Figure 2.3, but here they are shown relative to the anomalies at lag $\delta = 0$ days. At all locations, an increase in SST can be observed, but the signal is negligible in the Bay of Fundy. The timing of the maximum response varies among the locations, but is generally at lags $\delta = 12$–30 days which is in overall agreement with the results presented

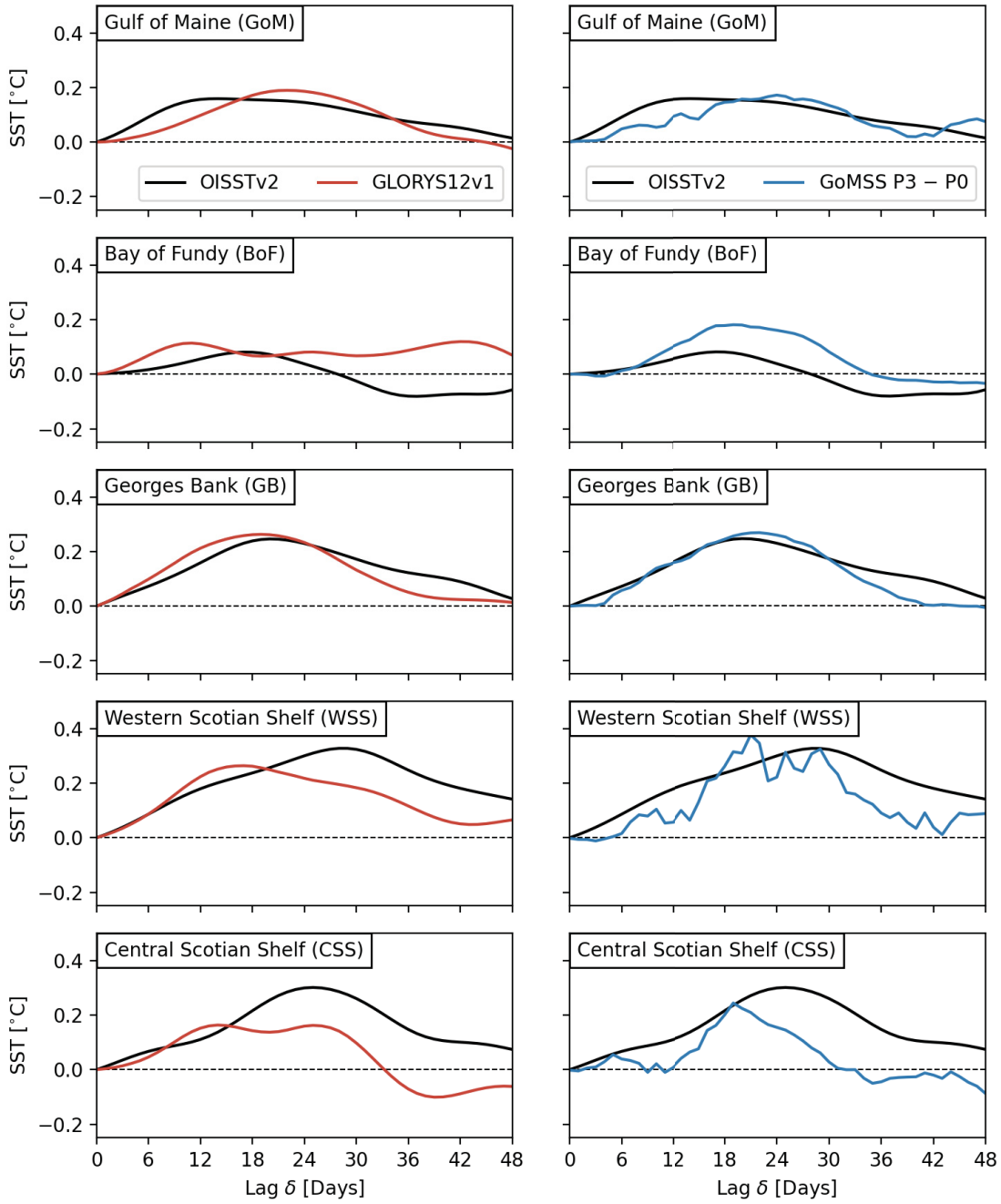

Figure 6.7: Composites and predictions of SST anomalies at the five representative locations defined in Figure 6.1 with respect to MJO phase 3. Left column: composites of bandpass-filtered SST anomalies from observations (OISSTv2) and the global reanalysis GLORYS12v1 with respect to MJO phase 3 when $A_{\text{RMM}} > 1$ during winter. Right column: Observed SST composites and anomalies predicted by GoMSS (P3 − P0). All anomalies are relative to lag $\delta = 0$ days. The observed composites for Georges Bank and Scotian Shelf are the same as in as in Figure 2.3.

in Chapter 2.

These warm anomalies are also captured in the ocean reanalysis GLORYS12v1. However, at some locations, the lag of the maximum response is different (Gulf of Maine and Western Scotian Shelf) or the signal is weaker compared to the observations (Central Scotian Shelf). Note that the temperature observations in OISSTv2 have also been assimilated in GLORYS12v1.

In the panels on the right of Figure 6.7, the observed SST composites are compared to the anomalies predicted by GoMSS (P3 − P0). The model generally captures the temporal evolution and strength of the warm anomalies following MJO phase 3. At all locations, GoMSS predicts a localized peak in SST with comparable timing to the observations. The weaker observed signal in the Bay of Fundy can be attributed to the coarser resolution of the OISSTv2 dataset (the grid spacing of OISSTv2 is four times larger compared to GoMSS). Additionally, the predicted anomalies show some superimposed high-frequency variability which is related to the atmospheric forcing on synoptic timescales. Note the composites are based on bandpass-filtered SST observations whereas no filtering was applied to the GoMSS predictions.

The observed SST composites are only partly comparable to the model predictions because the GoMSS runs are based on idealized, composited forcing. Additionally, the observed composites were calculated for the period 1981–2019 and the model forcing was for 1993–2010. Nevertheless, the qualitative agreement between the predicted large-scale anomalies and the results from Chapter 2 provides further confidence that the ocean response is driven by atmospheric perturbations caused by the MJO. In the following section, the vertical penetration of the surface signal into the ocean interior will be examined.

6.5.2 Vertical Penetration of the Surface Signal

How deep does the signal at the surface penetrate into the subsurface ocean? This is one of the questions that can now be addressed with GoMSS. Figure 6.8 shows depth profiles of temperature anomalies after MJO phase 3 predicted by GoMSS (P3 − P0) at the five representative locations in the model domain. The black line shows the base of the mixed layer predicted by P3 here defined as the depth where the change in potential density $\Delta\sigma_\theta = 0.01$ with respect to the density at 10 m. Note that the differences in the mixed layer depth predicted by P0 and P3 are negligible. (If the mixed layer depth from P0 was plotted in Figure 6.8 it would be indistinguishable from the line shown.)

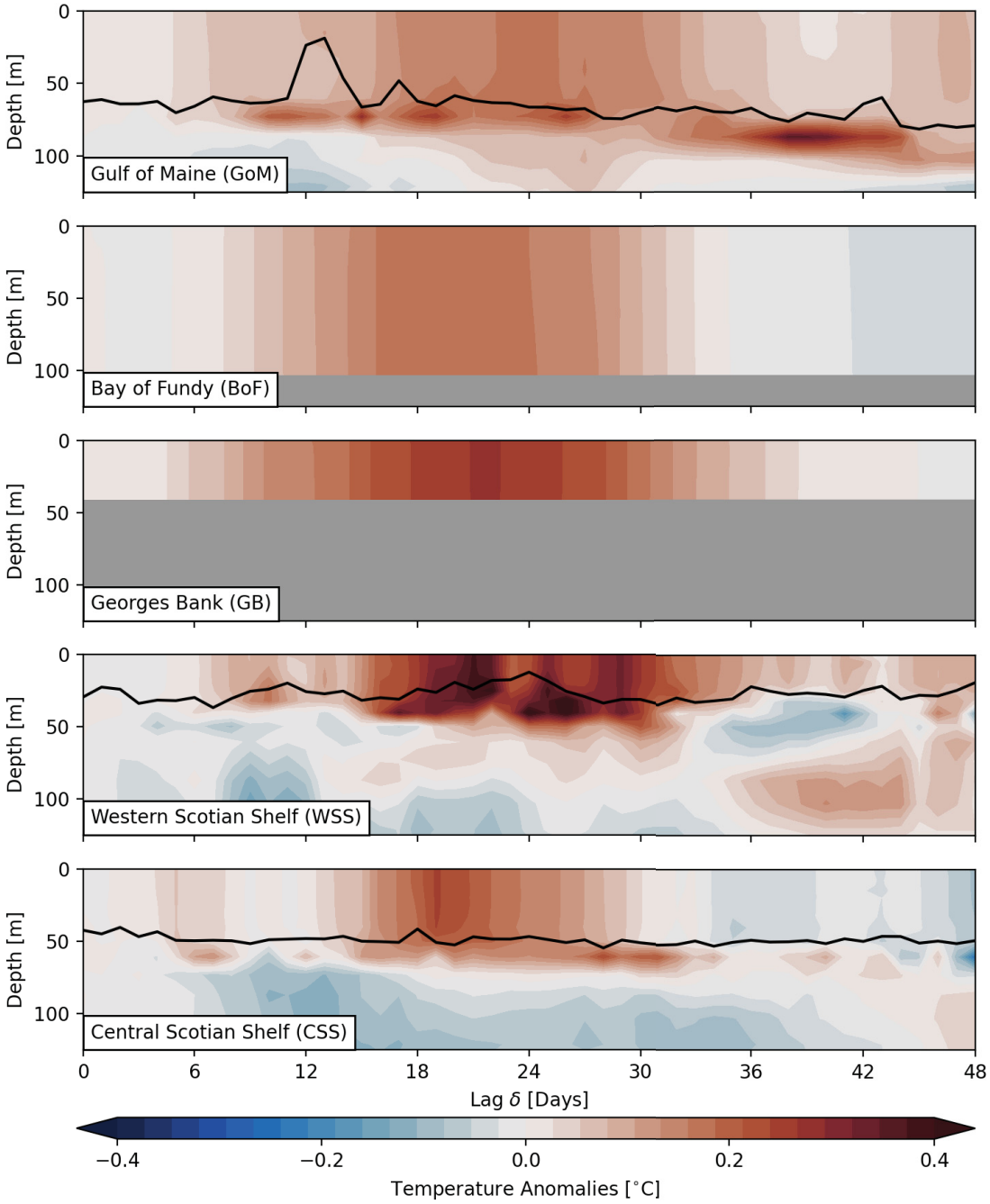

Figure 6.8: Depth profiles of temperature anomalies with respect to MJO phase 3 predicted by GoMSS (P3 − P0) at the representative locations defined Figure 6.1. Only the top 125 m are shown. The black lines shows the base of the mixed layer predicted by P3 if it is shallower than the local water depth. Grey shading shows the seafloor.

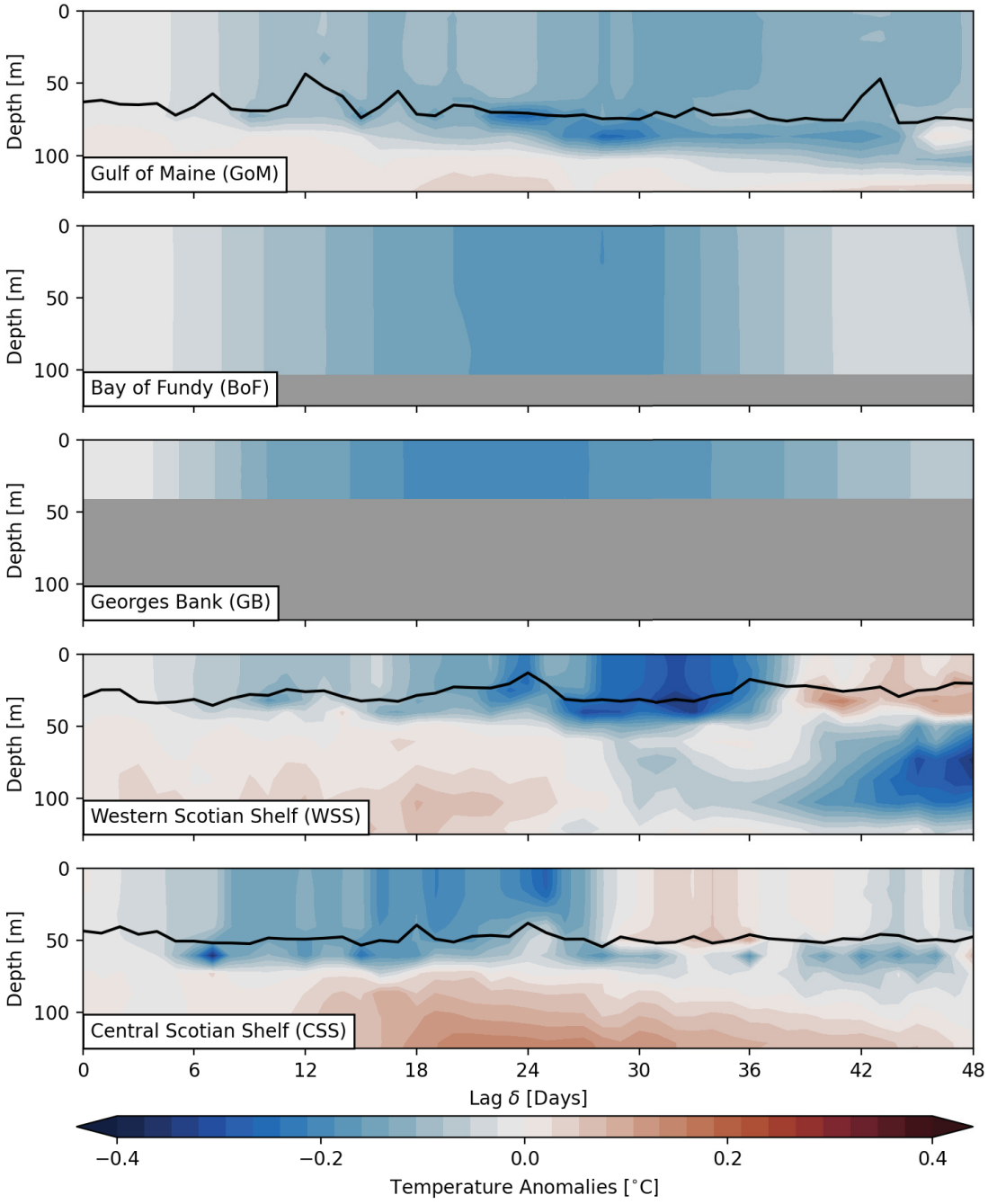

Figure 6.9: Depth profiles of temperature anomalies with respect to MJO phase 7 predicted by GoMSS (P7 − P0) at the representative locations defined in Figure 6.1. The format is the same as Figure 6.8.

The temporal evolution of the subsurface temperature anomalies shows a warming predicted to occur throughout the model domain 2–3 weeks after MJO phase 3. Furthermore, this anomaly extends throughout the surface mixed layer. In the Gulf of Maine and at both locations on the Scotian Shelf, the warm anomaly reduces the temperature gradient of the thermocline indicated by the strong localized anomalies below the mixed layer.

The cold anomaly predicted by GoMSS (P7 $-$ P0) following phase 7 also does not penetrate beyond the base of the mixed layer (Figure 6.9). The strong anomalies just below the mixed layer are due to the increased temperature gradient of the thermocline.

The apparent deepening of the mixed layer in the Gulf of Maine with increasing lag after both phases 3 and 7 is primarily a feature of the seasonal climatology. While initially the temperature profile is uniform as a result of the breakdown of a thin, warm surface layer during the model spin-up representative of conditions in the fall, a cold surface layer develops and deepens throughout the rest of the winter. As shown in the time series, the anomalies in response to the MJO are spread across this layer.

On Georges Bank and in the Bay of Fundy the whole water column is well mixed due to strong tides and shallow bathymetry. Consequently, the warm and cold anomalies in response to MJO phases 3 and 7, respectively, penetrate to the sea floor. Due to the smaller water depth on Georges Bank, the warming is faster and therefore a stronger anomaly occurs. The homogeneity of the signal throughout the water column is not captured in composites of GLORYS12v1 temperature profiles (not shown). This demonstrates the importance of tides at these locations as tidal mixing can change the thermal inertia of the ocean and thus directly affect air-sea heat fluxes.

After MJO phases 3 and 7, an anomaly of the opposite sign compared to the mixed layer occurs at depths below about 100 m at both locations on the Scotian Shelf. This can be best explained by looking at the ocean response to the MJO along the Scotian Shelf section (Figures 6.10 and 6.11).

Clearly, the warm anomaly with its maximum at $\delta = 18$–24 days after phase 3 extends from the coast beyond the shelf break, but is generally confined to the surface mixed layer. As noted in Section 6.5.1, the wide-spread cold anomaly in response to phase 7 is predicted to occur mainly on the western Scotian Shelf at longer lags. Therefore, this signal is more dominant along the section at $\delta = 30$ days, but also does not penetrate beyond the pycnocline.

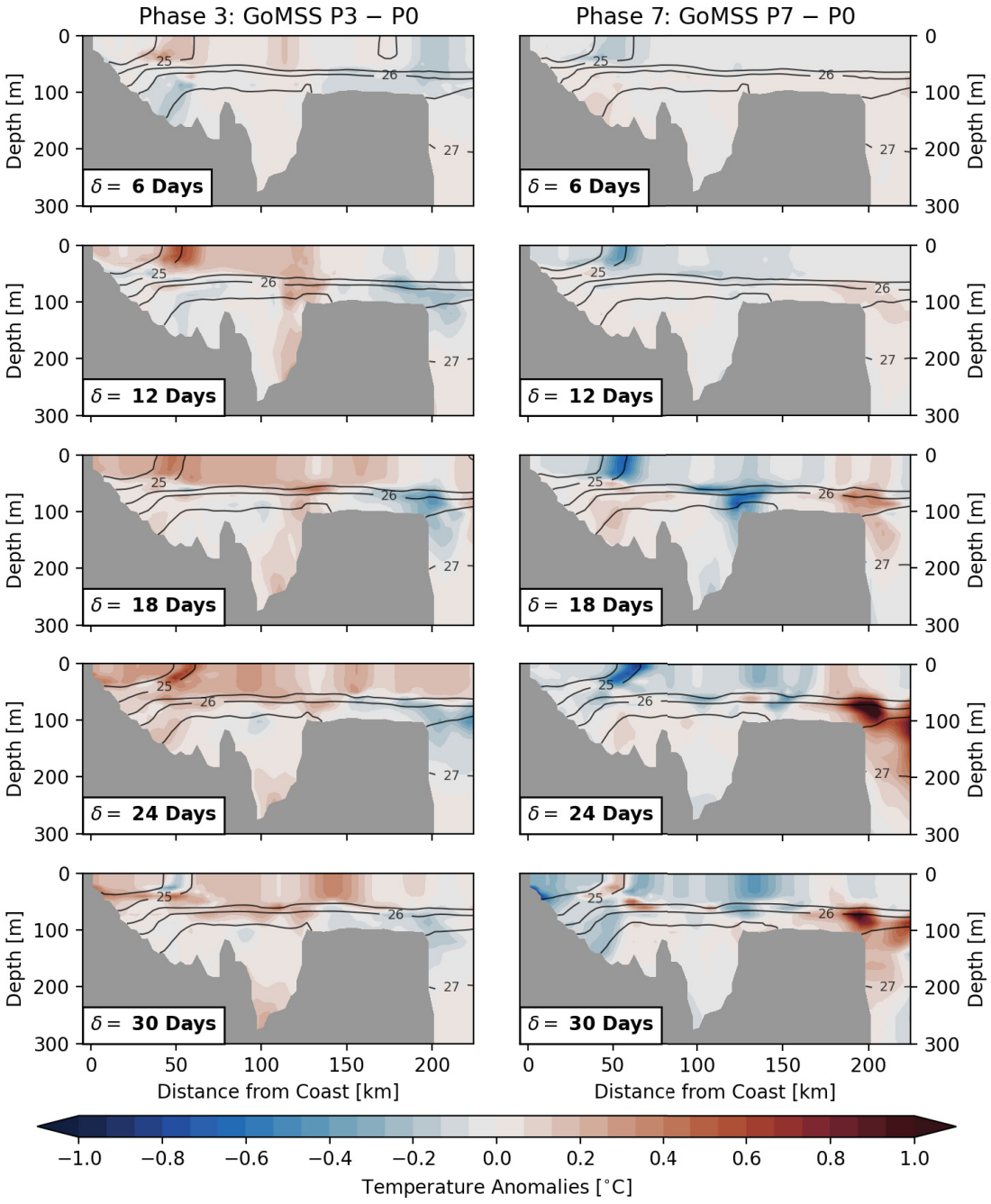

Figure 6.10: Ocean temperature anomalies and density along the Scotian Shelf section with respect to MJO phases 3 and 7. Colors show the temperature anomalies predicted by GoMSS (left column: P3 − P0, right column: P7 − P0). Contours show the predicted in-situ density σ.

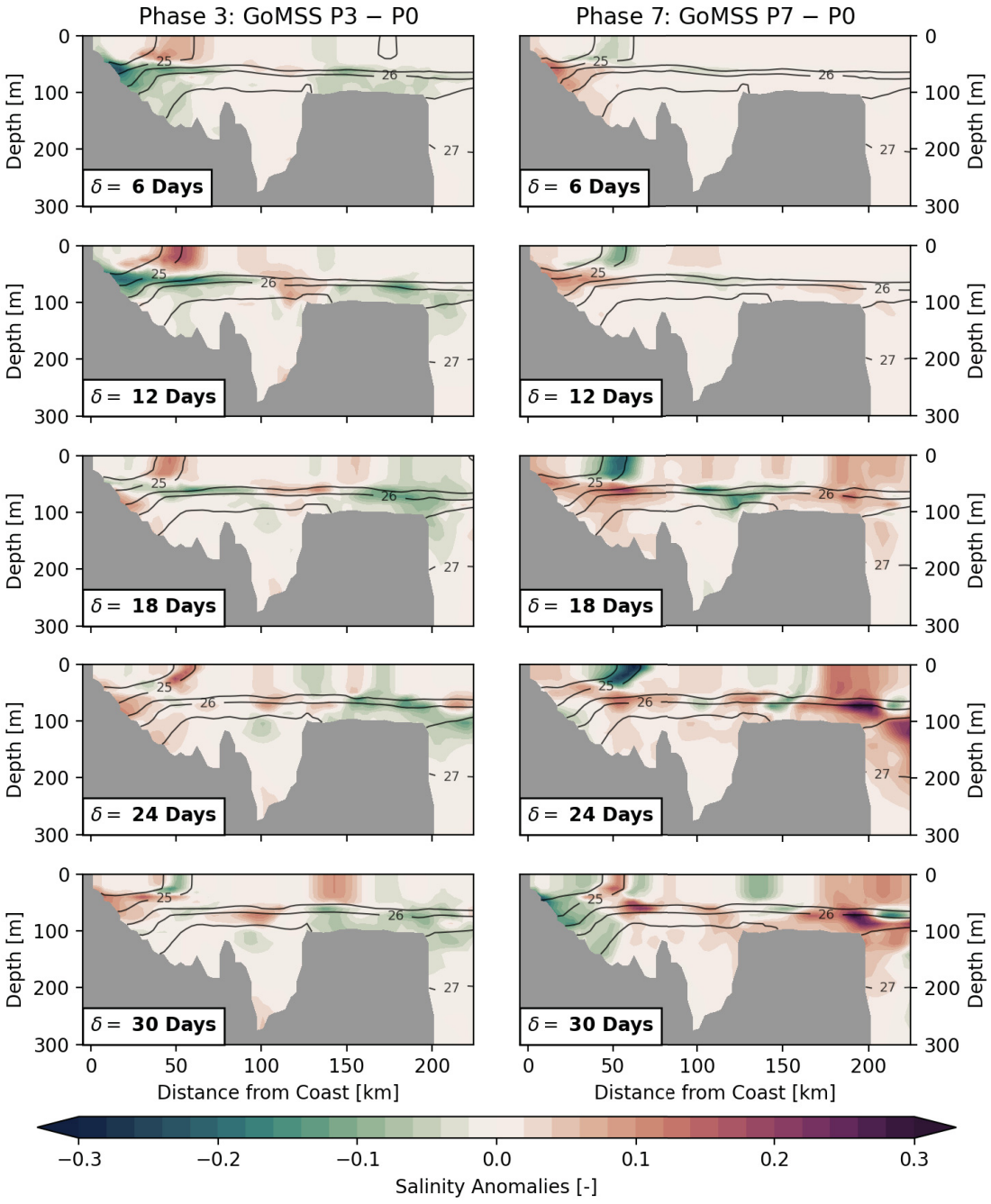

Figure 6.11: Salinity anomalies and density along the Scotian Shelf section with respect to MJO phases 3 and 7. The format is the same as Figure 6.10.

After both MJO phases 3 and 7, a strong and localized temperature anomaly occurs along the density front at the outer edge of the Nova Scotia Current at lags $\delta = 12$–24 days. These correspond to the narrow anomaly parallel to the coastline seen in Figures 6.5 and 6.6. Similar anomalies can be seen in the salinity along the Scotian Shelf section shown in Figure 6.11. This suggests a horizontal displacement of the density front due to advection toward and away from the coast after phase 3 and 7, respectively.

As shown in Figure 6.4, the 10 m wind anomalies after phase 3 are directed predominantly in the onshore direction. The anomalous wind forcing causes the density front to move toward the coast where anomalous downwelling of colder and fresher surface water occurs. This is particularly apparent in the negative salinity anomalies where the isopycnals intersect the bathymetry near the coast at lags $\delta = 6$–12 days (Figure 6.11). An offshore flow below the mixed layer advects this water mass leading to a deep anomaly of the opposite sign to the surface signal. This feature is also captured in the depth profiles in Figure 6.8.

The opposite effect can be seen after MJO phase 7 when the near-surface wind anomalies lead to upwelling-favourable conditions. As a result, the Nova Scotia Current widens and the density front along its outer edge is moved offshore. Positive salinity anomalies near the seafloor and along the coast at lags $\delta = 6$–18 days indicate more saline water is upwelled into the surface layer. The order of magnitude of the predicted upwelling-related salinity anomalies is consistent with an advective change $D\frac{\partial S}{\partial z}$ assuming a salinity gradient $\frac{\partial S}{\partial z} = -0.03\,\mathrm{m}^{-1}$ and a vertical displacement over 10 days of $D = 10\,\mathrm{m}$. The upwelled water mass, which is also warmer, is partly advected by an offshore flow near the pycnocline leading to the warm anomalies below the mixed layer at the locations on the Scotian Shelf (Figure 6.9).

At the shelf break, strong upwelling occurs after phase 7 leading to intrusions of warm and salty waters onto the shelf. This is consistent with observations by *Petrie* (1983) who showed that this intense upwelling is the response to transient winds in alongshelf direction over a period of two days or longer. Similarly, downwelling occurs after phase 3, but the resulting anomalies are less pronounced.

With increasing lag after MJO phases 3 and 7, the direction of the wind anomalies reverses leading to anomalous downwelling and upwelling, respectively, at lag $\delta = 30$ days. The coastal upwelling and downwelling signatures are less apparent in the temperature

profile along the Scotian Shelf section. This is likely because the temperature changes in the surface mixed layer are mitigated by anomalous heat fluxes.

6.5.3 Bottom Salinity

In regions where the surface mixed layer does not extend throughout the water column, bottom salinity can act as a tracer for the ocean circulation at depth. Figure 6.12 shows the bottom salinity anomalies on the Scotian Shelf following MJO phases 3 and 7 predicted by GoMSS. The composites of bandpass-filtered CFSR wind anomalies at 10 m height are also shown. As discussed above, the anomalous wind forcing at lags $\delta = 6$–12 days after phase 3 leads to conditions that favour anomalous downwelling. The resulting fresh anomaly occurs initially along the entire Atlantic coastline of mainland Nova Scotia, but is more pronounced along the South Shore at $\delta = 12$ days. With increasing lag, the direction of the near-surface wind anomalies changes and a positive salinity anomaly occurs.

Given the mean period of a MJO cycle of 48 days, a lag of $\delta = 24$ days after phase 3 roughly corresponds to the time when the MJO is in phase 7. Therefore, there is a similarity in the bottom salinity anomaly along the coast in the bottom left and top right panel of Figure 6.12.

Following MJO phase 7, near-surface wind anomalies over the Scotian Shelf have a north-westerly and westerly direction. This leads to anomalous upwelling of more saline waters along the coast causing a maximum anomaly at lag $\delta = 18$ days.

Overall, it is apparent that the atmospheric perturbations caused by the MJO not only lead to a large-scale surface signal, but also affect the ocean circulation on smaller horizontal scales and the ocean interior. This demonstrates the benefits of a high-resolution ocean model like GoMSS which is able to better resolve the coastline and nearshore bathymetry.

6.6 Summary and Discussion

In this chapter, GoMSS was used to investigate the feasibility of ocean downscaling for S2S prediction. Following the results in Chapter 2, the mean ocean response to the MJO in the Gulf of Maine and Scotian Shelf region was predicted. Consistent with *Katavouta and Thompson* (2016) and *Katavouta et al.* (2016), GoMSS was shown to be able to predict the main features of the observed mean circulation and hydrography in the study region during winter.

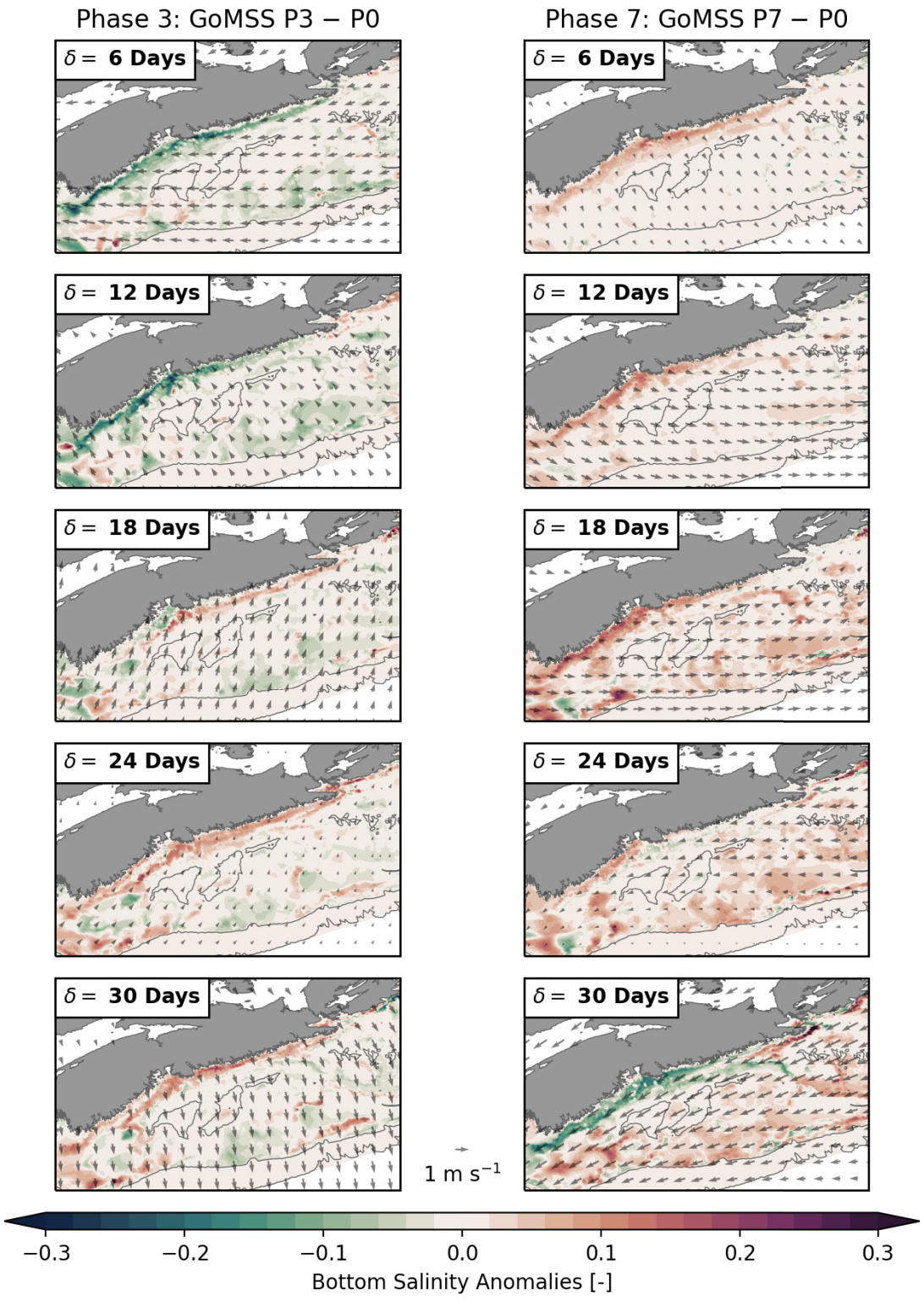

Figure 6.12: Bottom salinity anomalies predicted by GoMSS (left column: P3 − P0, right column: P7 − P0). Vectors show the composites of bandpass-filtered CFSR wind anomalies at 10 m height with respect to MJO phases 3 (left column) and 7 (right column) when $A_{\mathrm{RMM}} > 1$ during winter. Note that the Bay of Fundy region has been masked out.

Three model experiments were performed using idealized forcing decomposed into contributions from four frequency bands. To explicitly include the effect of the MJO, composites with respect to a specific phase were added to the time-varying neutral forcing. This neutral forcing consisted of contributions from the seasonal climatology, high-frequency atmospheric variability, and tidal variations in the ocean. It was shown that all three components are needed to accurately predict the circulation and hydrography in the GoMSS region.

Based on the results of the model experiments, it is now possible to answer the research questions raised in the Introduction:

(i) Can GoMSS reproduce the three-dimensional, time-varying response of the ocean to the MJO? GoMSS predicts a large-scale positive SST anomaly following phase 3 and a widespread cooling of the sea surface after phase 7. In both cases, the maximum response occurs at lag $\delta = 18$–24 days. Overall, the spatial structure, magnitude, and timing of the anomalies predicted by GoMSS are in agreement with the composite analysis of the SST observations with respect to the MJO presented in Chapter 2. This shows GoMSS can reproduce the mean ocean response to the MJO. It furthermore shows that it is feasible, and of value, to use regional high-resolution ocean models like GoMSS to downscale global S2S predictions of the ocean by global systems. Due to their higher resolution and inclusion of tides, these regional models can better predict the circulation on the shelf and in coastal regions, and thus the ocean response to the MJO.

(ii) What are the main physical processes that shape the mean ocean response to the MJO? The large-scale anomalies throughout the whole model domain can be directly related to surface forcing on S2S timescales. Composites of the atmospheric forcing variables conditioned on the MJO showed a strong warm anomaly peaking around 12 days after phase 3 accompanied by onshore wind anomalies. After phase 7, a cold anomaly and offshore wind anomalies occur. Consequently, GoMSS computes anomalous sensible and latent heat fluxes into the ocean causing the predicted SST anomalies. This is consistent with the predictions by a simplified mixed layer model in Chapter 2.

In response to the anomalous wind forcing related to the MJO, horizontal advection leads to a lateral displacement of the density front that separates the Nova Scotia Current from the rest of the shelf. This is expressed by a narrow band of strong SST anomalies parallel to the coast which is neither captured in the observations nor in the mixed layer

model. The predicted small-scale response demonstrates the added value of the high spatial resolution and the additional physical processes captured in GoMSS.

Other important processes for the ocean response to the MJO include mixing by tidal variations and stochastic wind forcing as well as up- and downwelling leading to a penetration of the MJO-related signal into the ocean interior. These processes are further discussed below.

(iii) How is the effect of atmospheric forcing in response to the MJO vertically projected into the subsurface ocean? Predicted temperature profiles at representative locations and along the Scotian Shelf section showed the surface warming and cooling in response to the MJO generally do not extend beyond the mixed layer. However, in shallow areas (e.g., Georges Bank and Bay of Fundy) where strong tidal mixing occurs, the signal can penetrate to the seafloor. This can have biological impacts as groundfish, lobster and other benthic species as well as their habitats have to adjust to these changes in temperature (e.g., *Crossin et al.*, 1998; *Donaldson et al.*, 2008; *Burdett et al.*, 2019).

The anomalous wind forcing in response to the MJO leads to anomalous downwelling and upwelling along the coast of Nova Scotia and at the shelf edge after phases 3 and 7, respectively. If the intrusion of nutrient-rich slope water occurs toward the end of the winter, this could potentially contribute to a more pronounced spring bloom of phytoplankton on the Scotian Shelf. It is therefore possible that the MJO can also have an effect on biological processes.

(iv) What is the importance of including forcing at higher frequencies than the MJO (e.g., tides and weather)? Although the focus of this study is on S2S timescales, it was shown that atmospheric forcing at higher frequencies is essential to realistically predict the mean ocean circulation and hydrography during winter. This was shown to be of particular importance for the surface mixed layer depth in GoMSS.

During winter, episodic wind bursts on synoptic timescales related to passing storm systems lead to a deepening of the surface mixed layer. Consequently, heat and freshwater entering the ocean through the air-sea interface are quickly spread throughout the surface layer. This direct influence of the high-frequency atmospheric forcing on the mean seasonal ocean circulation is a striking example of coupling across scales. Since a significant part of the ocean variability on S2S timescales is determined by atmospheric variations through the air-sea interface, a correct representation of the surface mixed layer is critical for S2S

prediction.

The wind mixing can be further enhanced by tidal variations, especially in shallow regions where, as a consequence, the surface signal is able to penetrate through the entire water column to the seafloor (see above). Tides can both increase and decrease predictability depending on location (including depth) and the background state of the ocean. This again illustrates the role of interactions across space and time scales for S2S prediction.

This study is not exhaustive. Based on the conceptual framework using composite forcing, it was possible to determine the mean ocean response to forcing conditioned on the MJO. In the future, this could be further explored by analysis of a hindcast over multiple years, or case studies in response to individual MJO episodes. This could also provide useful insights into the possibility of extreme events.

CHAPTER 7

SUMMARY AND DISCUSSION

In this thesis, the feasibility of subseasonal-to-seasonal (S2S) predictions of the ocean has been explored using a variety of tools ranging from simple, statistically based models to regional, high-resolution ocean circulation models based on physical principles. The overall objectives were to (i) improve the understanding of extratropical ocean variability and predictability on S2S timescales and (ii) increase the predictive skill of high-resolution, regional ocean models. A detailed summary of the results was given in each chapter. Here, the key findings of the research are summarized and their contribution toward meeting the objectives is discussed. Directions of future research are also presented. As indicated in the Introduction, the thesis is broadly divided into three themes which also guide the following summary and discussion of the main results.

7.1 Theme 1: Identification of "Windows of Opportunity"

Teleconnections play an important role for S2S prediction of the extratropical atmosphere and ocean. In Chapter 2, composites of gridded sea surface temperature (SST) observations in the North Atlantic were used to analyze the mean response of the surface ocean to the Madden-Julian Oscillation (MJO) during winter. A statistically significant, spatially coherent SST signal that covaries with the MJO was found. Specifically, a large-scale warm anomaly occurs along the eastern seaboard of North America, and extends to the Sargasso Sea, about 20 days after MJO phase 3. Similarly, a cold anomaly occurs in these regions, and at the same lag, after phase 7.

Based on a simplified surface mixed layer model, it was shown that air-sea heat fluxes

are the primary drivers of SST variability on S2S timescales for the study region. The spatial structure of the heat flux anomalies can be related to known patterns of atmospheric variability (e.g., PNA and NAO) for which teleconnections with the MJO have been documented (e.g., *Cassou*, 2008; *Lin et al.*, 2009). These patterns are associated with anomalous wind speeds as well as advection of warm and cold air masses. Both lead to anomalies in sensible and latent heat flux in the extratropical North Atlantic and thus influence the SST.

It is important to recognize that the composite analysis only provides an estimate of the average SST response to the MJO which is generally $< 0.5\,^{\circ}\mathrm{C}$. Individual MJO episodes can lead to a much stronger response that can be further influenced by other modes of variability, e.g., ENSO or stratospheric processes. This can lead to extreme events like marine heat waves with potentially severe ecological and socioeconomic impacts. However, it is not straightforward to quantify the effect of an individual MJO episode because of the multiple timescales at play. Additionally, the quasi-periodicity of the MJO and related differences in its propagation speed can have an influence on the downstream effects and thus would have to be taken into account.

The quasi-periodicity of the RMM index is, in part, due to the way it is calculated using EOF analysis. Given the multi-scale and non-stationary nature of the large-scale MJO convection and propagation, tracking of "large-scale precipitation objects" using satellite observations (e.g., *Kerns and Chen*, 2016, 2020) could be used instead. This would provide an alternative MJO metric that does not rely on EOF analysis and therefore would avoid the introduction of any artificial quasi-periodicity. This could provide more insightful information about the ocean response to individual MJO episodes.

Overall, the results presented in Chapter 2 improve understanding of S2S variability of the North Atlantic. The robust relationship between the MJO and SST in the North Atlantic, mediated by local air-sea interactions, provides evidence that the atmospheric variability in the tropics is a source of S2S predictability for the extratropical ocean. This leads to the possibility of temporal "windows of opportunity" that will ultimately enable more accurate ocean predictions on S2S timescales.

7.2 Theme 2: Model Validation

Ocean predictions are of greatest interest in coastal regions where most socioeconomic activities (e.g., aquaculture, shipping, tourism, etc.) take place. Regional, high-resolution models are often used to downscale the large-scale ocean circulation predicted by global models. These models generally do not resolve all relevant physical processes (e.g., tides). In principle, such dynamical downscaling is straightforward because it only requires a model and large-scale information from a global system for forcing at the boundaries. However, it first has to be demonstrated that the regional model has useful skill in predicting the circulation and hydrography across the relevant spatial and temporal scales and also adds value to global models. Therefore, a significant part of this thesis was concerned with the validation of the Gulf of Maine and Scotian Shelf (GoMSS) model with particular focus on the mean state and low-frequency changes.

In Chapter 4, it was shown that GoMSS predicts the main features of the mean circulation including the outflow of relatively cold and fresh water forming the Nova Scotia Current and tidal rectification in the Gulf of Maine and Bay of Fundy. The associated mean dynamic topography (MDT) predicted by GoMSS was compared with geodetically referenced mean sea levels observed by coastal tide gauges. These novel observations are based on one of the latest generation of geoid models which have unprecedented accuracy due to the inclusion of new satellite-based measurements of the Earth's gravity field. Overall, the MDT prediction was shown to be in good agreement with the observations. Between the tide gauges in North Sydney and Yarmouth, GoMSS predicts an alongshore MDT difference $\Delta\eta_c = 8.3\,\text{cm}$ which is slightly larger than the geodetically estimated value of $\Delta\eta_c = 5.9 \pm 2.0\,\text{cm}$. The convergence of the two independent approaches demonstrates that geodetically referenced sea level measurements by tides gauges can help validate high-resolution ocean models. Simultaneously, it also increases the confidence in the geoid models. Thus, Chapter 4 extends previous studies (e.g., *Woodworth et al.*, 2012; *Higginson et al.*, 2015; *Lin et al.*, 2015) that focus on global and basin-scale variability of MDT at the coast.

Tilts of MDT along the coast have value beyond model validation. In Chapter 4, two complementary, and dynamically consistent, interpretations of $\Delta\eta_c$ were developed and illustrated using idealized models of wind-driven ocean and shelf circulation. The coastal view is based on the time-averaged alongshore momentum equation and can be

used to estimate the mean flow averaged along the coast. The regional view, based on vorticity dynamics integrated over an adjacent offshore region, relates $\Delta\eta_c$ to area-averaged upwelling due to cross-isobath flow. Using the validated GoMSS model, it was shown that these views also hold in a three-dimensional, baroclinic ocean model with realistic bathymetry and forcing. This also demonstrates the usefulness of the geodetic MDT estimates for model validation with respect to integrated offshore dynamics. The two views also highlight the value of $\Delta\eta_c$ for ocean monitoring as discussed below.

The geodetic approach to estimating coastal MDT is limited to locations where decades of sea level observations by tide gauges and continuous vertical datum control exist. It can therefore be difficult to validate features on smaller scales, e.g., the MDT setdown in the upper Bay of Fundy predicted by GoMSS. This motivated the development of a new approach presented in Chapter 5 for the validation of MDT in shallow, tidally dominated regions where no sufficiently long sea level records exist. The new approach is based on observations of overtides which arise from tidal currents along the coastline or nonlinear interactions of the flow with the bathymetry. Both of these processes can also cause changes in the mean ocean state. To demonstrate the approach, the barotropic, higher-resolution model UBoF was developed for the upper Bay of Fundy with grid spacing four times smaller than GoMSS.

Predictions of tidal elevation and currents for the dominant M_2 constituent, and its first harmonic M_4, as well as mean currents, were validated against available observations. It was shown that the predictions by UBoF are a significant improvement over GoMSS. In contrast to GoMSS, UBoF is able to accurately predict M_4 currents and the mean circulation in the upper Bay of Fundy. Furthermore, UBoF predicts a sea level difference between Minas Basin an Minas Channel of $\Delta\eta = 2.6\,\text{cm}$ which is of opposite sign and smaller magnitude than the corresponding prediction by GoMSS ($\Delta\eta = -6.1\,\text{cm}$). Due to the superior performance of UBoF over GoMSS on multiple timescales, the MDT predicted by GoMSS for the upper Bay of Fundy should be considered suspect. The improvement of the predictions is not solely due to the higher spatial resolution of UBoF; it is also due to the improved bathymetry which was specifically designed for the model. This ensures that the nonlinear interactions between the tidal circulation and the bathymetry are better resolved in the model.

The largest alongshore variations in MDT are predicted to occur in Minas Passage and

around headlands where generation and advection of relative vorticity leads to a pair of counter-rotating gyres either side of the promontory. At the coast, this is expressed by a local setdown in MDT. The Bernoulli effect can further enhance this setdown. Typically, these regions also show enhanced overtides thereby illustrating the intrinsic relationship between the mean state and higher harmonics of the tidal circulation through nonlinear processes. Thus, the new approach of validating predictions of MDT using observations of overtides complements the validation of ocean models with geodetically referenced sea level measurements. Both methods highlight the fact that coastal MDT is a direct measure of ocean dynamics on multiple scales. They also demonstrate the value of sea level observations by tide gauges for model validation.

Coastal tide gauges are easy to maintain and provide a low-cost opportunity for continuous long-term ocean monitoring (e.g., *Pugh and Woodworth*, 2014, pp. 18). Many existing sea level records are several decades long and can be used for the validation of ocean models on both global and regional scales. On the other hand, they also provide an opportunity to reconstruct recent variability in shelf circulation based on the coastal and regional views. However, depending on the scale of interest, the influence of the local circulation (e.g., tidal flow around a headland) has to be taken into account. The approaches presented in Chapters 4 and 5 can be used to identify suitable locations for future deployments of tide gauges to monitor either the circulation on regional scales or in small tidal bays.

The validation of GoMSS using new observations (Chapter 4) and a new method (Chapter 5) extend the previous validation of the model by *Katavouta and Thompson* (2016) and *Katavouta et al.* (2016). All of these studies demonstrate that GoMSS has useful skill in predicting the mean and seasonal ocean circulation and hydrography in the Northwest Atlantic and adjacent shelf region. This shows that the model is a suitable tool for S2S prediction of the ocean.

7.3 Theme 3: Downscaling Case Studies

In Chapter 6, sensitivity model experiments with the validated GoMSS model were used to explore the feasibility of downscaling the large-scale ocean circulation in a global system for S2S prediction. Based on the "windows of opportunity" identified in Chapter 2, the mean ocean responses to MJO phases 3 and 7 were predicted using GoMSS and model

forcing from global atmosphere (CFSR) and ocean (GLORYS12v1) reanalyses. The model forcing was decomposed into four timescales and model runs, with and without forcing on S2S timescales, were compared. The forcing was based on composites of the atmospheric and large-scale ocean circulation with respect to the MJO.

It was shown that GoMSS is able to predict the large-scale positive SST anomalies after phase 3 and widespread cold anomalies after phase 7. In agreement with the observations, the maximum response occurs at lag $\delta = 18$–24 days. This timing is consistent with anomalies of sensible and latent heat flux associated with previously documented, large-scale changes in near-surface air temperature, humidity, and wind speed in response to the MJO (e.g., *Lin and Brunet*, 2009; *Seo et al.*, 2016). Predicted temperature profiles at representative locations in the GoMSS domain indicated that the anomalies are constrained to the surface mixed layer which can extend throughout the entire water column in shallow areas where tidal mixing plays a dominant role (e.g., Georges Bank and Bay of Fundy). On the Scotian Shelf, the added atmospheric forcing related to the MJO leads to anomalous downwelling and upwelling after phases 3 and 7, respectively. This is associated with a lateral shift of the outer edge of the Nova Scotia Current leading to a narrow band of strong anomalies parallel to the coast. The upwelled and downwelled water masses are subsequently advected offshore thereby creating anomalies below the thermocline of opposite sign to the surface anomalies.

The results in Chapter 6 demonstrate that it is generally possible, and of value, to use regional, high-resolution models for S2S prediction of the ocean on continental shelves and in coastal regions. Clearly, the ocean response to the MJO is not only a large-scale warming or cooling of the sea surface due to anomalous heat fluxes, but is also characterized by changes on smaller scales due to, e.g., tidal mixing, advection, and upwelling. In order to accurately capture these processes, a model with sufficiently high spatial resolution and realistic bathymetry is needed. Furthermore, the model should include physical processes related to tides which is often not the case for global ocean models. It has been shown that GoMSS fulfills these requirements and additionally has useful skill in predicting the circulation and hydrography in the Gulf of Maine and Scotian Shelf region. This clearly demonstrates the added value that such a model can provide, and highlights its potential for downscaling global S2S predictions.

7.4 Future Work

In this thesis, the feasibility and potential of regional ocean models for S2S prediction of the ocean has been shown. This provides a foundation for future research that will ultimately lead to operational predictions of coastal and shelf circulation on S2S timescales. Recent research efforts by the climate community are centered on the S2S Prediction Project Database (*Vitart et al.*, 2017) which contains hindcasts and historical S2S forecasts by eleven global models. Most of these are coupled atmosphere-ocean models and thus provide an opportunity for future downscaling experiments with physically consistent forcing at the surface and lateral boundaries. It has been shown that these coupled models are generally able to predict the known teleconnections between the MJO and the extratropical atmosphere, although they are often underestimated in the North Atlantic sector (*Vitart*, 2017). However, it remains to be seen whether the ocean response described in Chapter 2 is captured by these coupled models. Once this is demonstrated, the large-scale information from the models in the S2S database can be downscaled using regional, high-resolution models like GoMSS.

Given the great uncertainty of predictions on S2S and longer timescales, it is important to deal with them in a probabilistic framework, i.e., the predictions should be issued in terms of predictive probability distributions (e.g., *Kantz et al.*, 2006; *Gneiting and Katzfuss*, 2014). The models in the S2S database are ensemble prediction systems with multiple model runs for the same period based on slightly perturbed initial conditions or parameterizations of subgrid-scale processes. These perturbations can lead to small differences that can grow with increasing lead time due to the nonlinearities of the ocean-atmosphere system and model imperfections. The ensemble members provide distinct realizations of possible future states of the system and can be used to estimate predictive probability distributions and thus the uncertainty of the forecast. Dynamical downscaling of the ensemble runs with validated models like GoMSS further improves the S2S predictions of the ocean.

Ensemble predictions will also help improve our understanding of the physical basis of ocean variability and predictability on S2S timescales. Downscaling experiments with ensemble forcing limited to either the surface or lateral model boundaries will allow us to assess the relative importance of atmospheric forcing in comparison to the large-scale ocean circulation. Additionally, downscaling will allow us to quantify how effectively atmospheric predictability is transferred into the ocean.

Ensemble predictions can also be used to explore temporal limits of S2S predictability. Under the perfect model assumption, where the ensemble spread is assumed to evolve solely due to the intrinsic chaotic behaviour of the climate system, the predictability limit is the lead time at which the differences between the ensemble runs become as large as the model signal itself (e.g., *Lorenz*, 1982; *Neena et al.*, 2014). It would be interesting to explore approaches based on dynamical system theory, where predictability is assessed by estimating the instantaneous dimension and stability of the underlying attractor of the system (e.g., *Faranda et al.*, 2017).

Future research should also address the predictability of ocean extreme events, e.g., storm surges, marine heatwaves or cold spells, on S2S timescales. In this context, the extratropical ocean response to large MJO events could be explored to further understand the different timescales at play and their influence on the strength and timing of the signal. Additionally, the interaction of the MJO with other modes of climate variability, e.g., ENSO or stratospheric variations, and their joint effect on the ocean needs to be better understood.

In addition to S2S prediction systems, observations can provide valuable information on multiple timescales and play a critical role in understanding ocean variability and model validation. To further investigate the predicted anomalous upwelling on the Scotian Shelf in response to the MJO, an array of benthic pods to measure bottom temperature and salinity could be deployed. In combination with glider-based measurements of physical and biogeochemical variables, it would be interesting to explore possible effects on biological processes and the ecosystem on the shelf.

The results presented in this thesis provide strong arguments for deploying and maintaining coastal tide gauges with permanent vertical datum control. Clearly, the locations of future deployments have to be chosen carefully taking into account to the spatial scales of interest. Regional ocean models such as GoMSS will be able to provide useful guidance in the selection of suitable tide gauge locations.

APPENDIX A

SUPPLEMENTARY FIGURES FOR CHAPTER 2

This appendix contains supplementary Figures for Chapter 2.

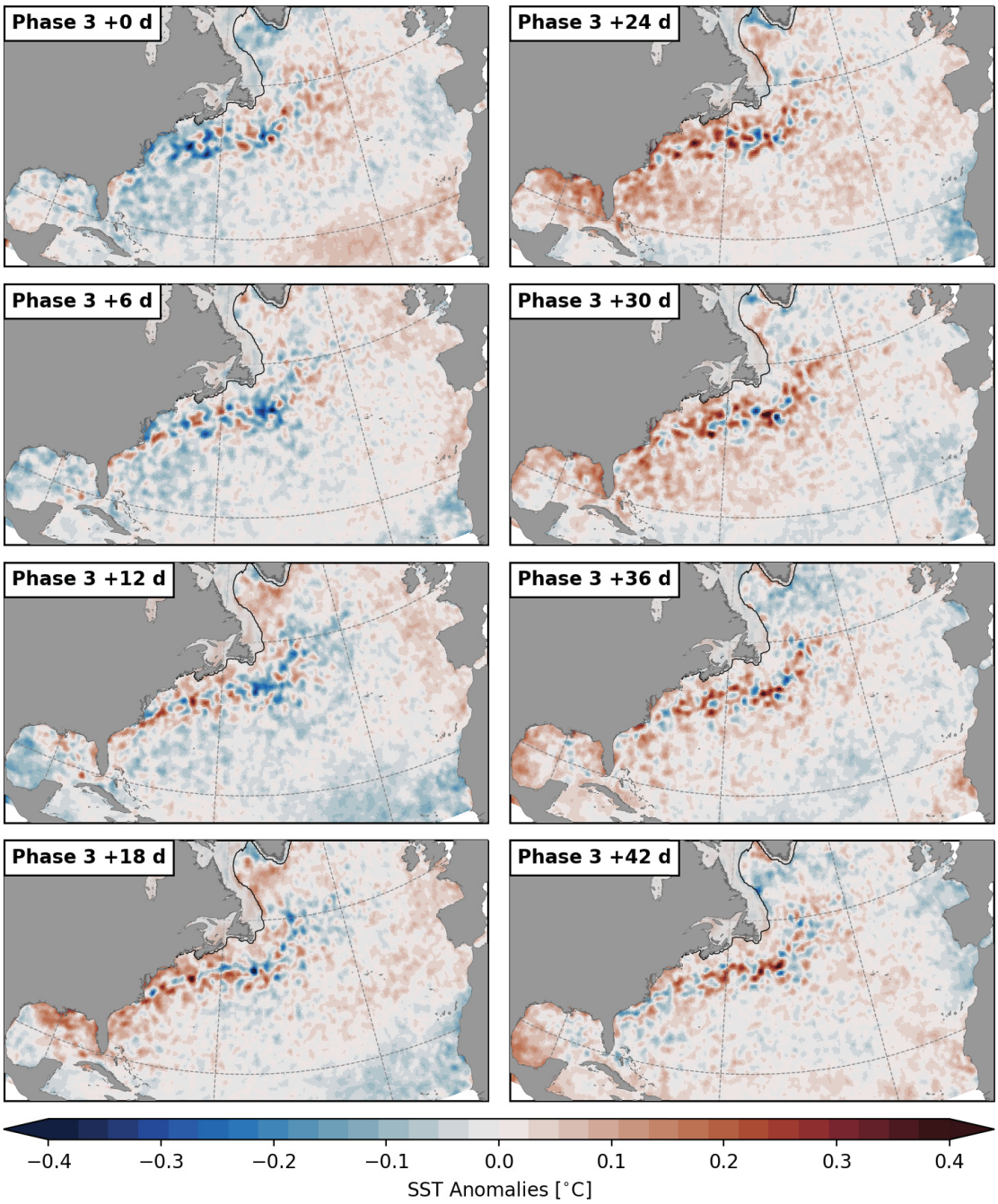

Figure A.1: Lagged composites of bandpass-filtered SST anomalies $\overline{T}_a$ with respect to MJO phases 3 during winter (DJF) when $A_{\text{RMM}} > 1$. Maps show the spatial structure of the composites for the whole study area (top panels) and in the Middle Atlantic Bight, Gulf of Maine, and Scotian Shelf region (bottom panels). Each map is a composite for lags $\delta =$ 0, 6, ..., 42 days after phase 3. Shaded areas near the coast show the climatological sea ice cover.

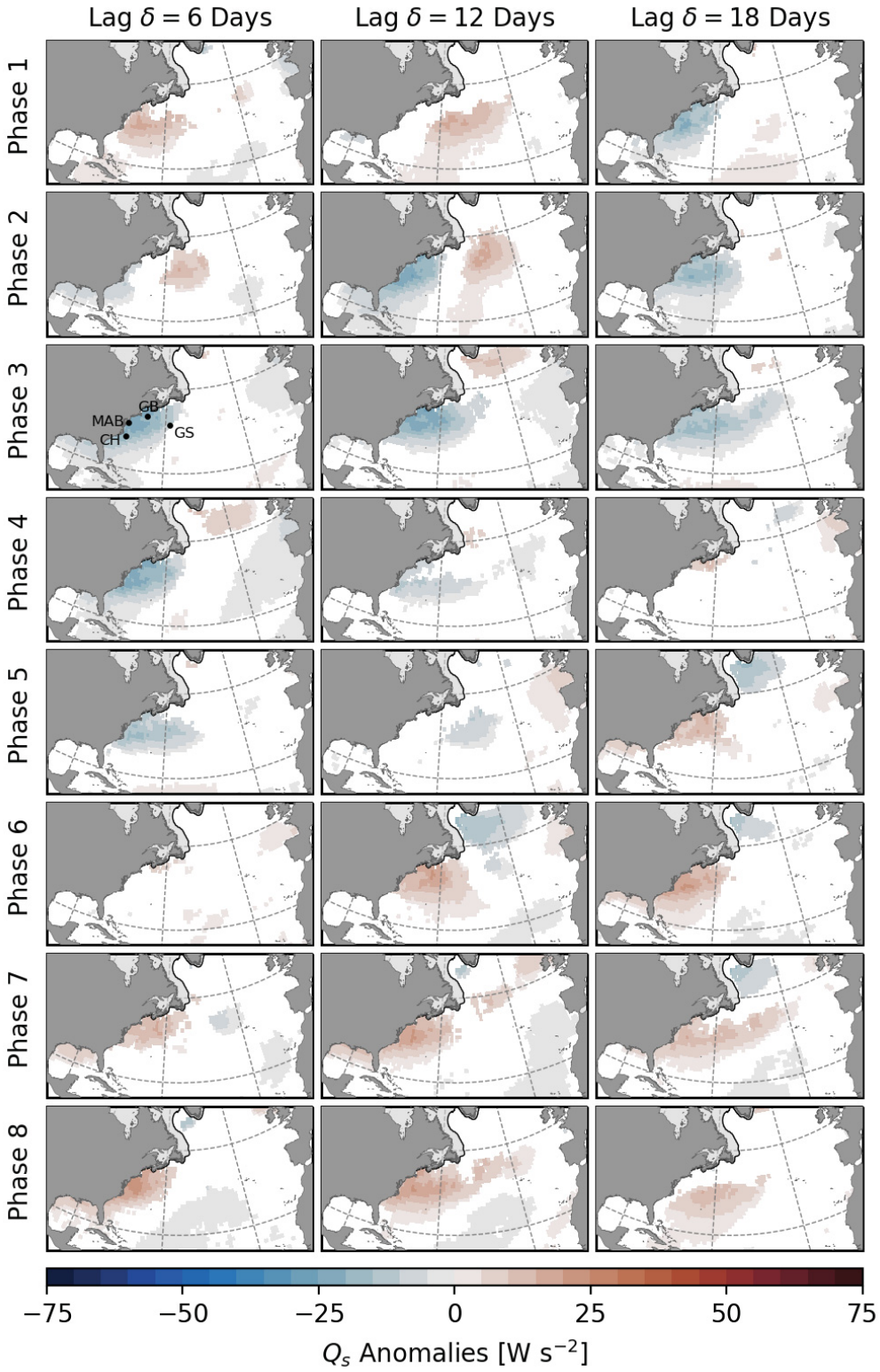

Figure A.2: Composites of bandpass-filtered sensible heat flux anomalies (positive upward) for all MJO phases during winter (DJF) when $A_{\mathrm{RMM}} > 1$. All shown anomalies are statistically different from zero at the 10% significance level. Shaded areas near the coast show the climatological sea ice cover.

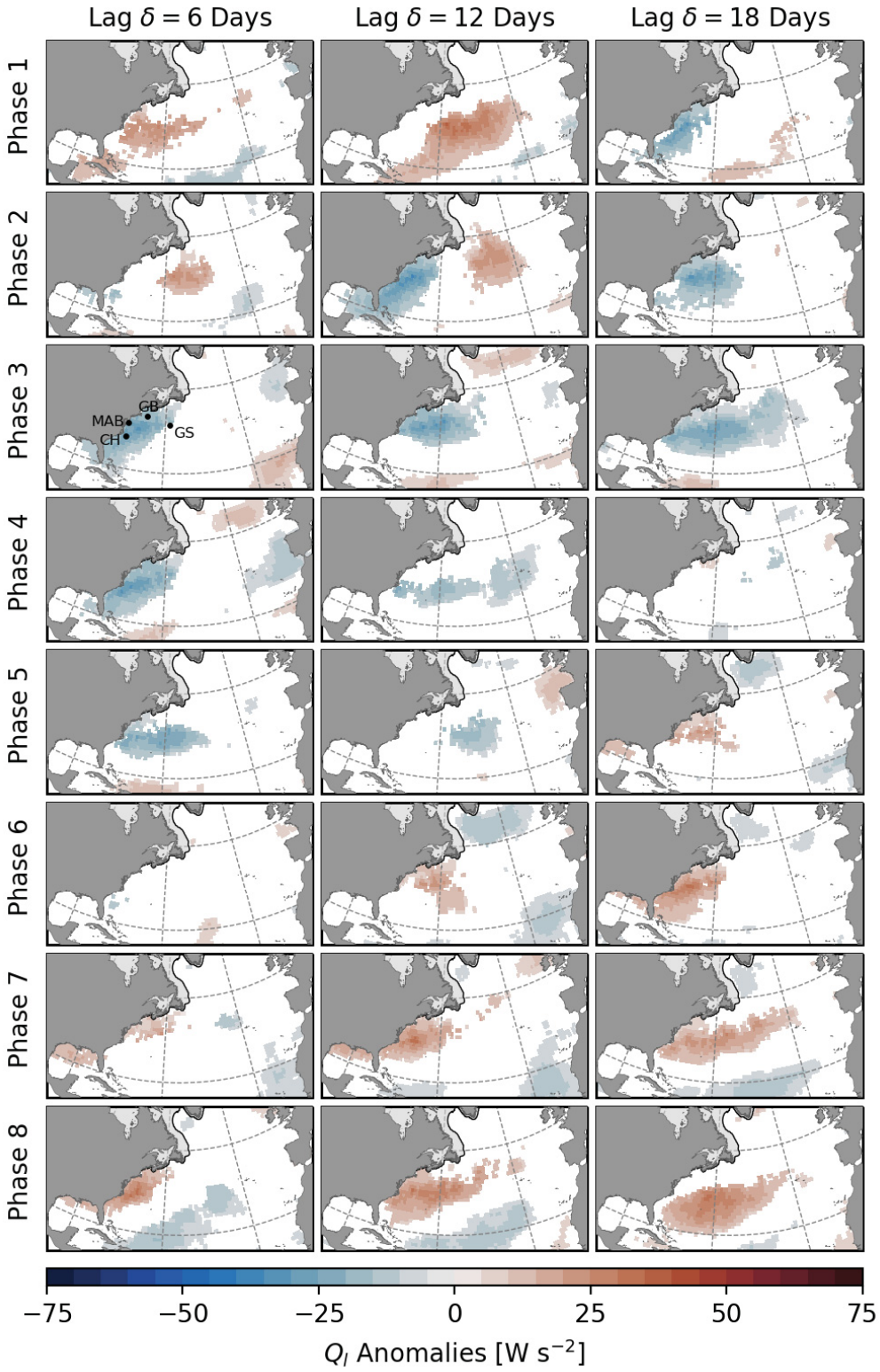

Figure A.3: Composites of bandpass-filtered latent heat flux anomalies (positive upward) for all MJO phases during winter (DJF) when $A_{\mathrm{RMM}} > 1$. All shown anomalies are statistically different from zero at the 10% significance level. Shaded areas near the coast show the climatological sea ice cover.

APPENDIX B

THE DEPTH-AVERAGED PRESSURE GRADIENT TERM AND ITS CURL

Under the hydrostatic approximation, the vertical pressure gradient is balanced by the buoyancy force (e.g., *Gill*, 1982, p. 47)

$$\frac{\partial p}{\partial z} = -\rho g. \tag{B.1}$$

The pressure at any depth z can be obtained by integrating (B.1) from z to the sea surface η relative to $z = 0$. Writing the density as constant reference density and a pertubation, $\rho = \rho_0 + \rho'$, the hydrostatic pressure is

$$p(z) = p_a + g\rho_0(\eta - z) + g\int_z^\eta \rho'\, dz, \tag{B.2}$$

where $p_a = p(\eta)$ is the atmospheric pressure at the air-sea interface.

In the momentum equation, the horizontal pressure gradient $\nabla_z p$ appears which can be integrated from the sea floor at $z = -H$ to the sea surface

$$\frac{1}{\rho_0}\int_{-H}^{\eta} \nabla_z p\, dz = \int_{-H}^{\eta} \nabla_z \left(\frac{p_a}{\rho_0} + g(\eta - z) + g\int_z^\eta \epsilon\, dz'\right) dz, \tag{B.3}$$

where ϵ is the normalized density pertubation.

Note that the upper limit of the integral in (B.3) is often set to zero under the assumption that density variations between $z = 0$ and the sea surface are negligible (e.g., *Csanady*, 1982, p. 7). Without this assumption, an exact solution for the depth-averaged pressure gradient is still possible. However, this can have consequences for the vorticity equation of

the depth-averaged flow.

The gradient of the first two terms inside the parentheses in (B.3) is independent of z and therefore, it is straightforward to integrate them:

$$\frac{1}{\rho_0}\int_{-H}^{\eta}\nabla_z p\,dz = h\nabla_z\left(\frac{p_a}{\rho_0}\right) + gh\nabla_z\eta + g\int_{-H}^{\eta}\nabla_z\int_{z}^{\eta}\epsilon\,dz'\,dz. \tag{B.4}$$

Here,

$$h = H + \eta \tag{B.5}$$

Is the total water depth.

Using Leibniz' integral rule, the last term becomes

$$\int_{-H}^{\eta}\nabla_z\int_{z}^{\eta}\epsilon\,dz'\,dz = \nabla_z\int_{-H}^{\eta}\int_{z}^{\eta}\epsilon\,dz'\,dz - \nabla_z H\int_{-H}^{\eta}\epsilon\,dz. \tag{B.6}$$

The double integral in the first term on the right-hand side can be simplified using integration by parts (e.g., *Csanady*, 1979):

$$\nabla_z\int_{-H}^{\eta}\int_{z}^{\eta}\epsilon\,dz'\,dz = \nabla_z\int_{-H}^{\eta}z\epsilon\,dz + \nabla_z\left[z\int_{z}^{\eta}\epsilon\,dz'\right]_{-H}^{\eta} \tag{B.7}$$

$$= \nabla_z\int_{-H}^{\eta}z\epsilon\,dz + \nabla_z\left(H\int_{-H}^{\eta}\epsilon\,dz\right) \tag{B.8}$$

$$= \nabla_z\int_{-H}^{\eta}(z+H)\epsilon\,dz. \tag{B.9}$$

In the last step, use has been made of the fact that H is independent of z and thus can be moved inside the integral.

By combining (B.4) and (B.6) with (B.9) and (B.8), respectively, two forms of the depth-averaged pressure gradient term arise:

$$\frac{1}{\rho_0 h}\int_{-H}^{\eta}\nabla_z p\,dz = \nabla_z\left(\frac{p_a}{\rho_0}\right) + g\nabla_z\eta + \frac{g}{h}\int_{-H}^{\eta}(z+H)\nabla_z\epsilon\,dz \tag{B.10}$$

$$= \nabla_z\left(\frac{p_a}{\rho_0}\right) + g\nabla_z\eta + \frac{1}{h}\nabla_z\chi - g\frac{H}{h}\nabla_z\eta_{\mathrm{s}}, \tag{B.11}$$

where

$$\eta_{\mathrm{s}} = -\int_{-H}^{\eta}\epsilon\,dz \tag{B.12}$$

is the steric contribution to the sea level and

$$\chi = g \int_{-H}^{\eta} z\epsilon \, dz \tag{B.13}$$

is the vertically integrated potential energy anomaly.

Equations (B.10) and (B.11) differ in the way the density anomalies are weighted in the vertical. In (B.10), $z + H$ is decreasing linearly with depth and thus the gradient of density variations at the surface are weighted more. Therefore, this form is particularly suitable for the estimation of surface currents from surface density fields. On the other hand, given the definition of χ in (B.13) shows that density variations at depth are weighted more and therefore, (B.11) is more suitable for transports or depth-averaged currents.

Note that the factor H/h in the last term in (B.11) arises from the integral over the whole water column. In deep water where $\eta \ll H$, this factor is approximately one and the steric height gradient in its traditional form is recovered.

Including this factor is has consequences for the vorticity equation. Taking the curl of (B.11) gives

$$\hat{\mathbf{k}} \cdot \nabla \times \left(\frac{1}{\rho_0 h} \int_{-H}^{\eta} \nabla_z p \, dz \right) = J\left(\chi, \frac{1}{h} \right) - \nabla \left(\frac{H}{h} \right) \times \nabla \eta_s, \tag{B.14}$$

where

$$J(A, B) = \frac{\partial A}{\partial x}\frac{\partial B}{\partial y} - \frac{\partial B}{\partial x}\frac{\partial A}{\partial y} \tag{B.15}$$

is the Jacobian determinant. Note that the curl of the gradient terms is identically zero. The first term on the right-hand side in (B.14) is the Joint Effect of Baroclinicity and Relief (JEBAR, *Sarkisyan and Ivanov*, 1971).

The second term is a nonlinear term which results from depth-integrating the pressure gradient over the whole water column. Using a Taylor series expansion, this can be approximated by

$$\nabla \left(\frac{H}{h} \right) \times \nabla \eta_s \approx \nabla \left(\frac{\eta}{H} \right) \times \nabla \eta_s. \tag{B.16}$$

Noting that gradients in sea level, steric height and bathymetry are often aligned, this term becomes negligible. Furthermore, η_s is generally small in shallow water and in deeper water, $\eta/H \approx 1$. This shows that the traditional approach of neglecting density variations between $z = 0$ and the sea surface is valid.

APPENDIX C

AN OPTIMAL INTERPOLATION TECHNIQUE TO CREATE AN OCEAN MODEL BATHYMETRY

This appendix describes the approach that was used to create the bathymetries for GoMSS and UBoF.

C.1 Introduction

As shown throughout the thesis, ocean models need a realistic bathymetry to accurately predict circulation, particularly in shallow coastal and shelf regions. These bathymetries are usually generated by interpolating (global) gridded relief models to the grid of the ocean model. Global datasets are typically based on satellite measurements of gravity anomalies and sea surface height which are complemented with bathymetric soundings. Where available, regional relief models are incorporated to increase the spatial resolution, particularly in coastal regions. Because of the reduced accuracy of satellite measurements and limited incorporation of high-resolution soundings along coastlines, the resulting level of detail of the bathymetry in these regions can be limited.

The horizontal grid spacing of relief models is often on the same order or even bigger compared to regional ocean models. However, it is important to note that this is not necessarily an indication of the effective spatial resolution which depends on data availability. Even where in-situ measurements exist, the gridding procedures for relief models lead to loss of information. In order to overcome these limitations, it is necessary to create bathymetries explicitly for a given model grid using available observations. However,

the incorporation of in-situ depth measurements is not straightforward and can lead to discontinuities in the resulting bathymetry.

Here a modified form of optimal interpolation was used to create an ocean model bathymetry. This approach was used to generate the bathymetries for GoMSS and UBoF. It can be applied for any ocean circulation model provided in-situ observations of water depth exist. This can be very useful for relocatable models which can be set up quickly to respond to environmental emergencies.

C.2 Optimal Interpolation

In general, the true state of a variable $\mathbf{x}$ is unknown. Models can only provide an approximation of $\mathbf{x}$ due to underlying assumptions and finite resolution of the model grid. Observations, on the other hand, are only available at a few locations, sparsely distributed over a large area, and usually contain uncertainties based on the measurement technique. Optimal Interpolation (OI) aims at combining both models and observations to generate an analysis $\mathbf{x}_\mathrm{a}$ which minimizes the error $\boldsymbol{\varepsilon}_\mathrm{a} = \mathbf{x} - \mathbf{x}_a$ in a least squares sense.

However, the errors are generally unknown, but assumptions about their statistical properties can be made. If the model and observations are unbiased, i.e., the means of their errors are zero, and the error covariances are known, the analysis can be computed as (e.g., *Kalnay*, 2002, p. 157)

$$\mathbf{x}_\mathrm{a} = \mathbf{x}_\mathrm{b} + \mathbf{W}\left[\mathbf{y} - \mathcal{H}(\mathbf{x}_\mathrm{b})\right] \tag{C.1}$$

where $\mathbf{x}_\mathrm{b}$ is the gridded background field based on the model and $\mathbf{y}$ are the observations. $\mathcal{H}(\mathbf{x}_\mathrm{b})$ is the forward observational operator. The weight matrix $\mathbf{W}$, also referred to as gain matrix, is defined as

$$\mathbf{W} = \mathbf{B}\mathbf{H}^\mathrm{T}\left(\mathbf{H}\mathbf{B}\mathbf{H}^\mathrm{T} + \mathbf{R}\right)^{-1} \tag{C.2}$$

where $\mathbf{B}$ and $\mathbf{R}$ are the error covariance matrices of the background and observations, respectively. The linear observation operator $\mathbf{H}$ and its transpose $\mathbf{H}^\mathrm{T}$ transform values on the model grid to the observation space and vice versa. Let m and n be the number of model grid points and observations, respectively.

It is assumed that the observation errors are uncorrelated which implies that $\mathbf{R}$ is a diagonal matrix of size $n \times n$.

$\mathbf{B}$ is a $m \times m$ matrix. The background errors are assumed to have spatial structure. It is sometimes assumed that the background error covariance follows a Gaussian distribution over distance. This raises computational problems resulting from the need to manipulate large matrices. In order to overcome this limitation, the background error covariance matrix is limited in spatial extent using the approach of *Gaspari and Cohn* (1999). This effectively truncates the Gaussian distribution using the following functional form:

$$r(z) = \begin{cases} -\frac{1}{4}|z|^5 + \frac{1}{2}|z|^4 + \frac{5}{8}|z|^3 + \frac{5}{3}|z|^2 + 1 & \text{for } |z| < c \\ \frac{1}{12}|z|^5 - \frac{1}{2}|z|^4 + \frac{5}{8}|z|^3 + \frac{5}{3}|z|^2 - 5|z| - \frac{2}{3}|z|^{-1} & \text{for } c \leq |z| < 2c \end{cases} \tag{C.3}$$

where z is the distance between two grid points and c is a length scale such that the correlation is zero for $z > 2c$. This allows for applying the OI block-wise to subsets of the model domain which decreases the computational demand.

The weight matrix (C.2) depends on the variance of the background and observation errors. Consider the case of an observation co-located with a single grid point. If the background and observation error variances are σ_B^2 and σ_R^2, respectively, the scalar weight is given by

$$W = \frac{1}{1 + \sigma_R^2/\sigma_B^2} \tag{C.4}$$

In case the observations are accurate and perfectly known, $\sigma_R = 0$ and $W = 1$. Thus, the analysis is equal to the observed values, $x_\mathrm{a} = y$. On the other hand, if the observations are poorly known or do not exist ($\sigma_R \to \infty$), $W = 0$ and the analysis is equal to the background value, $x_\mathrm{a} = x_\mathrm{b}$.

In the present study, it proved difficult to specify a priori choices for σ_B^2 and σ_R^2. One of the issues is that the observation error includes a so-called "error of representativeness" which refers to variations in observed values occuring on length scales much shorter that the model grid spacing. (In the present context this could refer to high-wavenumber ripples which can affect depth soundings.) After experimentation with different weighting schemes and visually assessing the realism of the analyzed bathymetry it was decided to set $\sigma_B = \sigma_R$.

C.3 Datasets

In the following, the datasets used to create model bathymetries for GoMSS and UBoF are introduced and the pre-processing to prepare the data for the OI is described.

C.3.1 General Bathymetric Charts of the Oceans (GEBCO)

The background field is based on the 2014 version of the General Bathymetric Charts of the Oceans (GEBCO, *Weatherall et al.*, 2015). This dataset provides a global ocean bathymetry and land topography based on SRTM30_PLUS (*Becker et al.*, 2009) and is supplemented by regional gridded products, altimetry measurements, and bathymetric soundings. (For details about the data sources, see *Weatherall et al.* (2015).)

The grid spacing of GEBCO_2014 is 30″ (in the area of interest, this is approximately 650 m in longitudinal and 920 m in latitudinal direction). However, it is important to note that the resolution of individual bathymetric features depends on the underlying data density.

In order to create the background field for the OI procedure, the GEBCO data were linearly interpolated to the destination grid of the ocean model.

C.3.2 Northwest Atlantic Bathymetry Dataset (NABD)

The multi-source Northwest Atlantic Bathymetry Dataset (NABD) was collected by the Bedford Institute of Oceanography (BIO) and kindly made available by Dr. David Greenberg (BIO, 2017, personal communication). It was compiled from digital charts, digitized field sheets, and recent surveys. NABD includes most of the available bathymetry observations from Canadian sources including ship measurements, single- and multibeam sonar, as well as LIDAR data. Overall, the dataset contains water depth of more than 70 000 000 data points from both direct measurements and gridded data.

Besides water depth, each data point contains information about the date and time, the geographic location, and type of measurement (e.g., seismic, multibeam, singlebeam, lidar, gridded, digitized, etc.). Additionally, the vertical datum, measurement campaign, and the data source are specified.

Initially, the data went through the following subsetting and a quality control procedure. As a first step, data points from gridded sources such as ETOPO, the International Bathymetric Chart of the Arctic Ocean (IBCAO), and other interpolated datasets were removed.

From the remaining in-situ observations, only data points within area of interest were selected. Observations with incomplete information or water depth greater than 10 000 m were excluded. Visual inspection of the remaining data showed some inconsistent depth values compared to measurements nearby. The suspicious data can be related individual to measurement campaigns and therefore all data associated with them, were omitted.

The NABD provides water depth with respect to two different vertical datums. While some of the measurements are with respect to mean sea level (MSL), others are referenced to Lower Low Water Low Tide (LLWLT). A tidal datum correction was applied to the latter group to homogenize the vertical datum of NABD and make it compatible with the vertical coordinate system of ocean circulation models.

The correction requires knowledge about the local tidal amplitude at each observation location. Here, the HRglobal data of WebTide were used. This dataset is based on the data-assimilative FES2004 model (*Lyard et al.*, 2006) and provides predictions of amplitude and phase for nine tidal constituents on an unstructured grid. For each model grid point, the maximum tidal amplitude was computed by adding the amplitudes of the M_2, S_2, N_2, K_1, and O_1 constituents.

In order to correct the vertical datum, the maximum tidal amplitude at the model grid point nearest to the observation location was added to the measured water depth. Note that this correction was only applied to observations with respect to LLWLT and water depth less than 200 m. In deeper regions, the tidal correction does not affect the water depth significantly.

Figure C.1a shows the homogenized in-situ observations in and around the GoMSS domain outlined in black. In total, 22 687 092 measurements are available, but they are distributed unevenly throughout the region. In some areas, the spatial density of observations is very high such that multiple data points fall within one grid cell of GoMSS or UBoF.

In order to further reduce the dataset, the depth values were represented on the destination grid using the "super observation" approach. For every grid point of the model, the median of the observations within the associated grid cell was computed. The advantage of mapping the observations directly on the destination grid is that no information is lost on scales that can be resolved by the model. Figure C.1b shows the super observations on the GoMSS model. Note that in-situ measurements are not available everywhere in the model

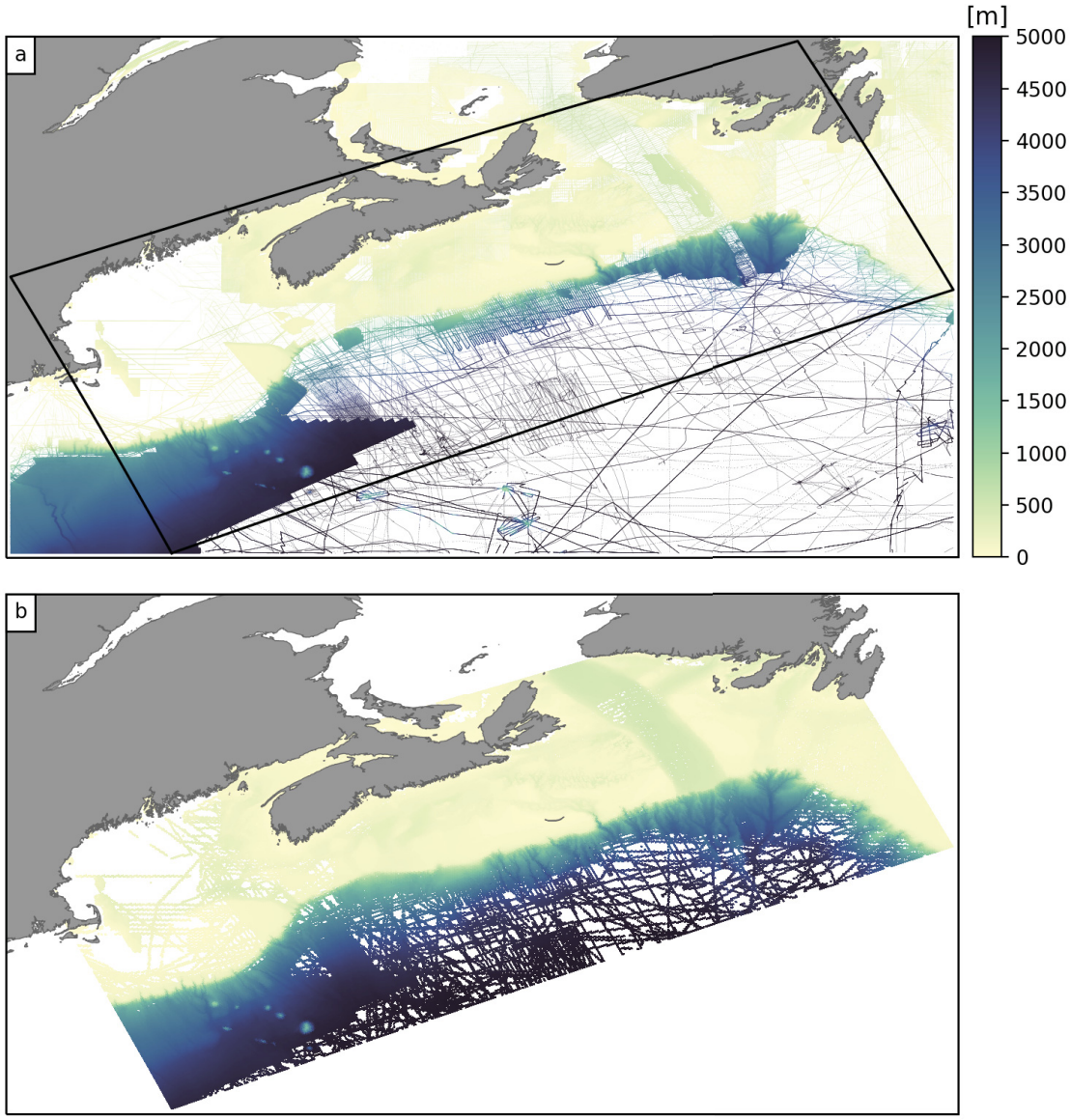

Figure C.1: Quality-controlled and homogenized in-situ observations of water depth from NABD in the GoMSS region. (a) Water depth at original location where measurements were taken. (b) Super observation of measurements mapped on the GoMSS model grid.

domain which illustrates the need for the OI approach to fill these gaps.

C.4 Bathymetry Creation and Postprocessing

The bathymetry creation using the OI procedure is illustrated here for the GoMSS model, but the same steps also apply for UBoF. Differences will be highlighted below.

After the quality control and pre-processing described above, it is straightforward to blend the background field based on GEBCO with the in-situ observations using (C.1). The background error covariance matrix $\mathbf{B}$ was created using the Gaspari-Cohn localization in (C.3) with $c = 10\,\text{km}$. (For the UBoF bathymetry, $c = 2\,\text{km}$ was used.)

The resulting bathymetry requires some post-processing to use it for ocean model simulations. All grid points which are considered to represent land were set to zero. In order to ensure compatibility with the original GoMSS configuration by *Katavouta and Thompson* (2016), the land-sea mask of their bathymetry was used. For UBoF, the dry grid cells in the model were determined using the 1:10 m coastline of the Natural Earth dataset.

Since NEMO version 3.6 does not capture wetting and drying processes of tidal flats, a minimum water depth has to be specified at the wet grid points in the model domain. Instead of choosing a constant value, the minimum depth H_{min} was determined depending on the local tidal amplitude. Following the approach of *Maraldi et al.* (2013), H_{min} was calculated as

$$H_{\text{min}}(x, y) = \max\left[H_0, 1.5 \times A_{\text{max}}(x, y)\right] \tag{C.5}$$

This ensures that the model bathymetry is deep enough in regions where the maximum tidal amplitude A_{max} exceeds the constant minimum depth H_0. In GoMSS, $H_0 = 2.5\,\text{m}$, whereas in UBoF, $H_0 = 5\,\text{m}$. The maximum tidal amplitude was determined using the Northwest and Atlantic and Scotia-Fundy-Maine Data of WebTide (*Dupont et al.*, 2005) for GoMSS and UBoF, respectively. Additionally, the maximum depth in GoMSS was set to 4000 m in consistency with the original configuration.

BIBLIOGRAPHY

Adames, Á. F., J. M. Wallace, and J. M. Monteiro, Seasonality of the structure and propagation characteristics of the MJO, *Journal of the Atmospheric Sciences*, *73*, 3511–3526, 2016.

Altamimi, Z., X. Collilieux, and L. Métivier, ITRF2008: An improved solution of the international terrestrial reference frame, *Journal of Geodesy*, *85*, 457–473, 2011.

Andersen, O. B., and R. Scharroo, Range and Geophysical Corrections in Coastal Regions: And Implications for Mean Sea Surface Determination, in *Coastal Altimetry*, edited by S. Vignudelli, A. G. Kostianoy, P. Cipollini, and J. Benveniste, pp. 103–145, Springer, 2011.

Arakawa, A., and V. R. Lamb, Computational Design of the Basic Dynamical Processes of the UCLA General Circulation Model, in *Methods in Computational Physics: Advances in Research and Applications*, edited by J. Chang, vol. 17 of *General Circulation Models of the Atmosphere*, pp. 173–265, Academic Press, 1977.

Aubrey, D. G., and P. E. Speer, A Study of Non-linear Tidal Propagation in shallow Inlet/Estuarine Systems Part I: Observations, *Estuarine, Coastal and Shelf Science*, *21*, 185–205, 1985.

Bach, E., S. Motesharrei, E. Kalnay, and A. Ruiz-Barradas, Local Atmosphere–Ocean Predictability: Dynamical Origins, Lead Times, and Seasonality, *Journal of Climate*, *32*, 7507–7519, 2019.

Barnes, E. A., S. M. Samarasinghe, I. Ebert-Uphoff, and J. C. Furtado, Tropospheric and Stratospheric Causal Pathways Between the MJO and NAO, *Journal of Geophysical Research: Atmospheres*, *124*, 9356–9371, 2019.

Bauer, P., A. Thorpe, and G. Brunet, The quiet revolution of numerical weather prediction, *Nature*, *525*, 47–55, 2015.

Baxter, S., S. Weaver, J. Gottschalck, and Y. Xue, Pentad Evolution of Wintertime Impacts of the Madden–Julian Oscillation over the Contiguous United States, *Journal of Climate*, *27*, 7356–7367, 2014.

Becker, J. J., D. T. Sandwell, W. H. F. Smith, J. Braud, B. Binder, J. Depner, D. Fabre, J. Factor, S. Ingalls, S.-H. Kim, R. Ladner, K. Marks, S. Nelson, A. Pharaoh, R. Trimmer, J. V. Rosenberg, G. Wallace, and P. Weatherall, Global Bathymetry and Elevation Data at 30 Arc Seconds Resolution: SRTM30_PLUS, *Marine Geodesy*, *32*, 355–371, 2009.

Bjerknes, V., Das Problem der Wettervorhersage: betrachtet vom Standpunkte der Mechanik und der Physik, *Meteorologische Zeitschrift*, *21*, 1–7, 1904.

Bryan, K., A numerical method for the study of the circulation of the world ocean, *Journal of Computational Physics*, *4*, 347–376, 1969.

Bryan, K., and M. D. Cox, A numerical investigation of the oceanic general circulation, *Tellus*, *19*, 54–80, 1967.

Buckley, M. W., R. M. Ponte, G. Forget, and P. Heimbach, Low-Frequency SST and Upper-Ocean Heat Content Variability in the North Atlantic, *Journal of Climate*, *27*, 4996–5018, 2014.

Burdett, H. L., H. Wright, and D. A. Smale, Photophysiological Responses of Canopy-Forming Kelp Species to Short-Term Acute Warming, *Frontiers in Marine Science*, *6*, 2019.

Butler, A., A. Charlton-Perez, D. I. V. Domeisen, C. Garfinkel, E. P. Gerber, P. Hitchcock, A. Y. Karpechko, A. C. Maycock, M. Sigmond, I. Simpson, and S.-W. Son, Chapter 11 - Sub-seasonal Predictability and the Stratosphere, in *Sub-Seasonal to Seasonal Prediction*, edited by A. W. Robertson and F. Vitart, pp. 223–241, Elsevier, 2019.

Butman, B., R. C. Beardsley, B. Magnell, D. Frye, J. A. Vermersch, R. Schlitz, R. Limeburner, W. R. Wright, and M. A. Noble, Recent Observations of the Mean Circulation on Georges Bank, *Journal of Physical Oceanography*, *12*, 569–591, 1982.

Butterworth, S., On the Theory of Filter Amplifiers., *Experimental Wireless & Wireless Engineer*, *7*, 536–514, 1930.

Byrne, D., M. Münnich, I. Frenger, and N. Gruber, Mesoscale atmosphere ocean coupling enhances the transfer of wind energy into the ocean, *Nature Communications*, *7*, 1–8, 2016.

Cartwright, D. E., Oceanic tides, *Reports on Progress in Physics*, *40*, 665–708, 1977.

Cassou, C., Intraseasonal interaction between the Madden-Julian Oscillation and the North Atlantic Oscillation, *Nature*, *455*, 523–527, 2008.

Cayan, D. R., Latent and Sensible Heat Flux Anomalies over the Northern Oceans: The Connection to Monthly Atmospheric Circulation, *Journal of Climate*, *5*, 354–369, 1992a.

Cayan, D. R., Latent and Sensible Heat Flux Anomalies over the Northern Oceans: Driving the Sea Surface Temperature, *Journal of Physical Oceanography*, *22*, 859–881, 1992b.

Chapman, D. C., and R. C. Beardsley, On the Origin of Shelf Water in the Middle Atlantic Bight, *Journal of Physical Oceanography*, *19*, 384–391, 1989.

Chapman, D. C., J. A. Barth, R. C. Beardsley, and R. G. Fairbanks, On the Continuity of Mean Flow between the Scotian Shelf and the Middle Atlantic Bight, *Journal of Physical Oceanography*, *16*, 758–772, 1986.

Charney, J. G., R. Fjörtoft, and J. V. Neumann, Numerical Integration of the Barotropic Vorticity Equation, *Tellus*, *2*, 237–254, 1950.

Chassignet, E. P., H. E. Hurlburt, O. M. Smedstad, G. R. Halliwell, P. J. Hogan, A. J. Wallcraft, R. Baraille, and R. Bleck, The HYCOM (HYbrid Coordinate Ocean Model) data assimilative system, *Journal of Marine Systems*, *65*, 60–83, 2007.

Chegini, F., Y. Lu, A. Katavouta, and H. Ritchie, Coastal Upwelling Off Southwest Nova Scotia Simulated With a High-Resolution Baroclinic Ocean Model, *Journal of Geophysical Research: Oceans*, *123*, 2318–2331, 2018.

Chen, K., G. G. Gawarkiewicz, S. J. Lentz, and J. M. Bane, Diagnosing the warming of the Northeastern U.S. Coastal Ocean in 2012: A linkage between the atmospheric jet stream variability and ocean response, *Journal of Geophysical Research: Oceans*, *119*, 218–227, 2014.

Chen, K., Y.-O. Kwon, and G. Gawarkiewicz, Interannual variability of winter-spring temperature in the Middle Atlantic Bight: Relative contributions of atmospheric and oceanic processes, *Journal of Geophysical Research: Oceans*, *121*, 4209–4227, 2016.

Clarke, A. J., *An Introduction to the Dynamics of El Nino and the Southern Oscillation*, Academic Press, 2008.

Crossin, G. T., S. A. Al-Ayoub, S. H. Jury, W. H. Howell, and W. H. Watson, Behavioral thermoregulation in the American lobster Homarus americanus., *Journal of Experimental Biology*, *201*, 365–374, 1998.

Csanady, G. T., The Arrested Topographic Wave, *Journal of Physical Oceanography*, *8*, 47–62, 1978.

Csanady, G. T., The pressure field along the western margin of the North Atlantic, *Journal of Geophysical Research*, *84*, 4905, 1979.

Csanady, G. T., *Circulation in the Coastal Ocean*, Springer, 1982.

Davies, A. M., and J. Lawrence, A three-dimensional model of the M_4 tide in the Irish Sea: The importance of open boundary conditions and influence of wind, *Journal of Geophysical Research*, *99*, 16197, 1994.

Davies, H. C., A lateral boundary formulation for multi-level prediction models, *Quarterly Journal of the Royal Meteorological Society*, *102*, 405–418, 1976.

de Boyer Montégut, C., G. Madec, A. S. Fischer, A. Lazar, and D. Iudicone, Mixed layer depth over the global ocean: An examination of profile data and a profile-based climatology, *Journal of Geophysical Research: Oceans*, *109*, 2004.

Dee, D. P., A Pragmatic Approach to Model Validation, in *Quantitative Skill Assessment for Coastal Ocean Models*, edited by D. R. Lynch and A. M. Davies, vol. 47 of *Coastal and Estuarine Studies*, pp. 1–13, American Geophysical Union (AGU), 1995.

DeMott, C. A., N. P. Klingaman, and S. J. Woolnough, Atmosphere-ocean coupled processes in the Madden-Julian oscillation, *Reviews of Geophysics*, *53*, 1099–1154, 2015.

Deser, C., and M. S. Timlin, Atmosphere–Ocean Interaction on Weekly Timescales in the North Atlantic and Pacific, *Journal of Climate*, *10*, 393–408, 1997.

Deser, C., M. A. Alexander, and M. S. Timlin, Understanding the Persistence of Sea Surface Temperature Anomalies in Midlatitudes, *Journal of Climate*, *16*, 57–72, 2003.

Dever, M., D. Hebert, B. J. W. Greenan, J. Sheng, and P. C. Smith, Hydrography and Coastal Circulation along the Halifax Line and the Connections with the Gulf of St. Lawrence, *Atmosphere-Ocean*, *54*, 199–217, 2016.

Donaldson, M. R., S. J. Cooke, D. A. Patterson, and J. S. Macdonald, Cold shock and fish, *Journal of Fish Biology*, *73*, 1491–1530, 2008.

Dronkers, J., Tidal asymmetry and estuarine morphology, *Netherlands Journal of Sea Research*, *20*, 117–131, 1986.

Dupont, F., C. G. Hannah, and D. A. Greenberg, Modelling the sea level of the upper Bay of Fundy, *Atmosphere-Ocean*, *43*, 33–47, 2005.

Ekman, M., Impacts of geodynamic phenomena on systems for height and gravity, *Bulletin Géodésique*, *63*, 281–296, 1989.

Ekman, M., A concise history of the theories of tides, precession-nutation and polar motion (from antiquity to 1950), *Surveys in Geophysics*, *14*, 585–617, 1993.

El-Sabh, M. I., Oceanographic Features, Currents, and Transport in Cabot Strait, *Journal of the Fisheries Research Board of Canada*, *34*, 516–528, 1977.

Engedahl, H., Use of the flow relaxation scheme in a three-dimensional baroclinic ocean model with realistic topography, *Tellus A*, *47*, 365–382, 1995.

Erofeeva, S. Y., G. D. Egbert, and P. M. Kosro, Tidal currents on the central Oregon shelf: Models, data, and assimilation, *Journal of Geophysical Research*, *108*, 3148, 2003.

Fairall, C. W., E. F. Bradley, J. E. Hare, A. A. Grachev, and J. B. Edson, Bulk Parameterization of Air–Sea Fluxes: Updates and Verification for the COARE Algorithm, *Journal of Climate*, *16*, 571–591, 2003.

Faranda, D., G. Messori, and P. Yiou, Dynamical proxies of North Atlantic predictability and extremes, *Scientific Reports*, *7*, 1–10, 2017.

Feldstein, S. B., and C. L. E. Franzke, Atmospheric Teleconnection Patterns, in *Nonlinear and Stochastic Climate Dynamics*, edited by C. L. E. Franzke and T. J. O'Kane, pp. 54–104, Cambridge University Press, 2017.

Fernandez, E., and J. Lellouche, Product User Manual for the Global Ocean Physical Reanalysis product GLOBAL_REANALYSIS_PHY_001_030, *Tech. rep.*, EU Copernicus Marine Service, Toulouse, 2018.

Fewings, M. R., and S. J. Lentz, Momentum balances on the inner continental shelf at Martha's Vineyard Coastal Observatory, *Journal of Geophysical Research: Oceans*, *115*, 2010.

Filmer, M. S., C. W. Hughes, P. L. Woodworth, W. E. Featherstone, and R. J. Bingham, Comparison between geodetic and oceanographic approaches to estimate mean dynamic topography for vertical datum unification: Evaluation at Australian tide gauges, *Journal of Geodesy*, *92*, 1413–1437, 2018.

Flather, R. A., A Storm Surge Prediction Model for the Northern Bay of Bengal with Application to the Cyclone Disaster in April 1991, *Journal of Physical Oceanography*, *24*, 172–190, 1994.

Frankignoul, C., Sea surface temperature anomalies, planetary waves, and air-sea feedback in the middle latitudes, *Reviews of Geophysics*, *23*, 357–390, 1985.

Frankignoul, C., and K. Hasselmann, Stochastic climate models, Part II Application to sea-surface temperature anomalies and thermocline variability, *Tellus*, *29*, 289–305, 1977.

Frederikse, T., K. Simon, C. A. Katsman, and R. Riva, The sea-level budget along the Northwest Atlantic coast: GIA, mass changes, and large-scale ocean dynamics, *Journal of Geophysical Research: Oceans*, *122*, 5486–5501, 2017.

Friedrichs, C. T., and D. G. Aubrey, Non-linear Tidal Distortion Estuaries in Shallow Well-mixed Estuaries: A Synthesis, *Estuarine, Coastal and Shelf Science*, *27*, 521–545, 1988.

Frisinger, H. H., Aristotle and his "Meteorologica", *Bulletin of the American Meteorological Society*, *53*, 634–638, 1972.

Garrett, C., Tidal Resonance in the Bay of Fundy and Gulf of Maine, *Nature*, *238*, 441–443, 1972.

Garrett, C. J. R., and H. Loucks, Upwelling Along the Yarmouth Shore of Nova Scotia, *Journal of the Fisheries Research Board of Canada*, *33*, 116–117, 1976.

Gaspari, G., and S. E. Cohn, Construction of correlation functions in two and three dimensions, *Quarterly Journal of the Royal Meteorological Society*, *125*, 723–757, 1999.

Gawarkiewicz, G. G., R. E. Todd, A. J. Plueddemann, M. Andres, and J. P. Manning, Direct interaction between the Gulf Stream and the shelfbreak south of New England, *Scientific Reports*, *2*, 2012.

Geyer, W. R., and R. Signell, Measurements of tidal flow around a headland with a shipboard acoustic Doppler current profiler, *Journal of Geophysical Research*, *95*, 3189, 1990.

Gill, A. E., *Atmosphere-Ocean Dynamics*, vol. 30 of *International Geophysics*, Academic Press, 1982.

Gneiting, T., and M. Katzfuss, Probabilistic Forecasting, *Annual Review of Statistics and Its Application*, *1*, 125–151, 2014.

Green, G., *An Essay on the Application of Mathematical Analysis to the Theories of Electricity and Magnetism*, Nottingham, 1828.

Greenberg, D. A., Modification of the M_2 Tide due to Barriers in the Bay of Fundy, *Journal of the Fisheries Research Board of Canada*, *26*, 2775–2783, 1969.

Greenberg, D. A., Modeling the Mean Barotropic Circulation in the Bay of Fundy and Gulf of Maine, *Journal of Physical Oceanography*, *13*, 886–904, 1983.

Gregory, J. M., S. M. Griffies, C. W. Hughes, J. A. Lowe, J. A. Church, I. Fukimori, N. Gomez, R. E. Kopp, F. Landerer, G. L. Cozannet, R. M. Ponte, D. Stammer, M. E. Tamisiea, and R. S. W. van de Wal, Concepts and Terminology for Sea Level: Mean, Variability and Change, Both Local and Global, *Surveys in Geophysics*, *40*, 1251–1289, 2019.

Haidvogel, D., H. Arango, W. Budgell, B. Cornuelle, E. Curchitser, E. Di Lorenzo, K. Fennel, W. Geyer, A. Hermann, L. Lanerolle, J. Levin, J. McWilliams, A. Miller, A. Moore, T. Powell, A. Shchepetkin, C. Sherwood, R. Signell, J. Warner, and J. Wilkin, Ocean forecasting in terrain-following coordinates: Formulation and skill assessment of the Regional Ocean Modeling System, *Journal of Computational Physics*, *227*, 3595–3624, 2008.

Hallberg, R., Using a resolution function to regulate parameterizations of oceanic mesoscale eddy effects, *Ocean Modelling*, *72*, 92–103, 2013.

Hannah, C. G., J. A. Shore, J. W. Loder, and C. E. Naimie, Seasonal Circulation on the Western and Central Scotian Shelf, *Journal of Physical Oceanography*, *31*, 591–615, 2001.

Hansen, W., Theorie zur Errechnung des Wasserstandes und der Strömungen in Randmeeren nebst Anwendungen, *Tellus*, *8*, 287–300, 1956.

Hasegawa, D., J. Sheng, D. A. Greenberg, and K. R. Thompson, Far-field effects of tidal energy extraction in the Minas Passage on tidal circulation in the Bay of Fundy and Gulf of Maine using a nested-grid coastal circulation model, *Ocean Dynamics*, *61*, 1845–1868, 2011.

Heaps, N. S., and J. Proudman, A two-dimensional numerical sea model, *Philosophical Transactions of the Royal Society of London. Series A, Mathematical and Physical Sciences*, *265*, 93–137, 1969.

Henderson, S. A., E. D. Maloney, and E. A. Barnes, The influence of the Madden-Julian Oscillation on Northern Hemisphere Winter Blocking, *Journal of Climate*, *29*, 4597–4616, 2016.

Herbertson, A. J., *Outlines of Physiography: An Introduction to the Study of the Earth*, Edward Arnold, 1901.

Hickey, B. M., and N. E. Pola, Seasonal Alongshore Pressure Gradient on the West Coast of the United States., *Journal of Geophysical Research*, *88*, 7623–7633, 1983.

Higginson, S., K. R. Thompson, P. L. Woodworth, and C. W. Hughes, The tilt of mean sea level along the east coast of North America, *Geophysical Research Letters*, *42*, 1471–1479, 2015.

Hobday, A. J., L. V. Alexander, S. E. Perkins, D. A. Smale, S. C. Straub, E. C. Oliver, J. A. Benthuysen, M. T. Burrows, M. G. Donat, M. Feng, N. J. Holbrook, P. J. Moore, H. A. Scannell, A. Sen Gupta, and T. Wernberg, A hierarchical approach to defining marine heatwaves, *Progress in Oceanography*, *141*, 227–238, 2016.

Holt, J., P. Hyder, M. Ashworth, J. Harle, H. T. Hewitt, H. Liu, A. L. New, S. Pickles, A. Porter, E. Popova, J. Icarus Allen, J. Siddorn, and R. Wood, Prospects for improving the representation of coastal and shelf seas in global ocean models, *Geoscientific Model Development*, *10*, 499–523, 2017.

Hoskins, B., The potential for skill across the range of the seamless weather-climate prediction problem: A stimulus for our science, *Quarterly Journal of the Royal Meteorological Society*, *139*, 573–584, 2013.

Hu, W., P. Liu, Q. Zhang, and B. He, Dominant patterns of winter-time intraseasonal surface air temperature over the CONUS in response to MJO convections, *Climate Dynamics*, *53*, 3917–3936, 2019.

Huang, J., Determining Coastal Mean Dynamic Topography by Geodetic Methods, *Geophysical Research Letters*, *44*, 11,125–11,128, 2017.

Hughes, C., R. Bingham, et al., An oceanographer's guide to GOCE and the geoid, *Ocean Science Discussions*, *3*, 1543–1568, 2006.

Hughes, C. W., R. J. Bingham, V. Roussenov, J. Williams, and P. L. Woodworth, The effect of Mediterranean exchange flow on European time mean sea level, *Geophysical Research Letters*, *42*, 466–474, 2015.

Hughes, C. W., I. Fukumori, S. M. Griffies, J. M. Huthnance, S. Minobe, P. Spence, K. R. Thompson, and A. Wise, Sea Level and the Role of Coastal Trapped Waves in Mediating the Influence of the Open Ocean on the Coast, *Surveys in Geophysics*, *40*, 1467–1492, 2019.

Huthnance, J. M., Ocean-to-shelf signal transmission: A parameter study, *Journal of Geophysical Research: Oceans*, *109*, 1–11, 2004.

Jayne, S. R., and J. Marotzke, The Oceanic Eddy Heat Transport, *Journal of Physical Oceanography*, *32*, 3328–3345, 2002.

Jones, C., and L. M. V. Carvalho, Spatial–Intensity Variations in Extreme Precipitation in the Contiguous United States and the Madden–Julian Oscillation, *Journal of Climate*, *25*, 4898–4913, 2012.

Kalnay, E., *Atmospheric Modeling, Data Assimilation and Predictability*, Cambridge University Press, 2002.

Kanamitsu, M., W. Ebisuzaki, J. Woollen, S.-K. Yang, J. J. Hnilo, M. Fiorino, and G. L. Potter, NCEP–DOE AMIP-II Reanalysis (R-2), *Bulletin of the American Meteorological Society*, *83*, 1631–1644, 2002.

Kantz, H., E. G. Altmann, S. Hallerberg, D. Holstein, and A. Riegert, Dynamical Interpretation of Extreme Events: Predictability and Predictions, in *Extreme Events in Nature and Society*, edited by S. Albeverio, V. Jentsch, and H. Kantz, The Frontiers Collection, pp. 69–93, Springer, 2006.

Kara, A. B., P. A. Rochford, and H. E. Hurlburt, Mixed layer depth variability over the global ocean, *Journal of Geophysical Research: Oceans*, *108*, 2003.

Karsten, R. H., J. M. McMillan, M. J. Lickley, and R. D. Haynes, Assessment of tidal current energy in the Minas Passage, Bay of Fundy, *Proceedings of the Institution of Mechanical Engineers, Part A: Journal of Power and Energy*, *222*, 493–507, 2008.

Katavouta, A., and K. R. Thompson, Downscaling ocean conditions with application to the Gulf of Maine, Scotian Shelf and adjacent deep ocean, *Ocean Modelling*, *104*, 54–72, 2016.

Katavouta, A., K. R. Thompson, Y. Lu, and J. W. Loder, Interaction between the Tidal and Seasonal Variability of the Gulf of Maine and Scotian Shelf Region, *Journal of Physical Oceanography*, *46*, 3279–3298, 2016.

Kerns, B. W., and S. S. Chen, Large-scale precipitation tracking and the MJO over the Maritime Continent and Indo-Pacific warm pool, *Journal of Geophysical Research: Atmospheres*, *121*, 8755–8776, 2016.

Kerns, B. W., and S. S. Chen, A 20-Year Climatology of Madden-Julian Oscillation Convection: Large-Scale Precipitation Tracking From TRMM-GPM Rainfall, *Journal of Geophysical Research: Atmospheres*, *125*, e2019JD032142, 2020.

Kidston, J., A. A. Scaife, S. C. Hardiman, D. M. Mitchell, N. Butchart, M. P. Baldwin, and L. J. Gray, Stratospheric influence on tropospheric jet streams, storm tracks and surface weather, *Nature Geoscience*, *8*, 433–440, 2015.

Klotzbach, P., S. Abhik, H. H. Hendon, M. Bell, C. Lucas, A. G. Marshall, and E. C. J. Oliver, On the emerging relationship between the stratospheric Quasi-Biennial oscillation and the Madden-Julian oscillation, *Scientific Reports*, *9*, 2981, 2019.

Klotzbach, P. J., E. C. J. Oliver, R. D. Leeper, and C. J. Schreck, The Relationship between the Madden–Julian Oscillation (MJO) and Southeastern New England Snowfall, *Monthly Weather Review*, *144*, 1355–1362, 2016.

Lagerloef, G. S. E., R. Lukas, R. A. Weller, and S. P. Anderson, Pacific Warm Pool Temperature Regulation during TOGA COARE: Upper Ocean Feedback, *Journal of Climate*, *11*, 2297–2309, 1998.

Large, G., and S. Yeager, Diurnal to decadal global forcing for ocean and sea-ice models: The data sets and flux climatologies, *Tech. Rep. NCAR/TN-460+STR*, University Corporation for Atmospheric Research, 2004.

Le Provost, C., Generation of Overtides and Compound Tides (Review), in *Tidal Hydrodynamics*, edited by B. B. Parker, pp. 269–295, Wiley, 1991.

Lee, R. W., S. J. Woolnough, A. J. Charlton-Perez, and F. Vitart, ENSO Modulation of MJO Teleconnections to the North Atlantic and Europe, *Geophysical Research Letters*, *46*, 13535–13545, 2019.

Lentz, S. J., Observations and a Model of the Mean Circulation over the Middle Atlantic Bight Continental Shelf, *Journal of Physical Oceanography*, *38*, 1203–1221, 2008.

Lentz, S. J., and M. R. Fewings, The Wind- and Wave-Driven Inner-Shelf Circulation, *Annual Review of Marine Science*, *4*, 317–343, 2012.

Levier, B., A.-M. Tréguier, G. Madec, and V. Garnier, Free surface and variable volume in the NEMO code, *Tech. rep.*, Ifremer, Brest, 2007.

Li, C., and J. O'Donnell, Tidally driven residual circulation in shallow estuaries with lateral depth variation, *Journal of Geophysical Research: Oceans*, *102*, 27915–27929, 1997.

Li, C., and J. O'Donnell, The Effect of Channel Length on the Residual Circulation in Tidally Dominated Channels, *Journal of Physical Oceanography*, *35*, 1826–1840, 2005.

Li, Y., R. He, and D. J. McGillicuddy, Seasonal and interannual variability in Gulf of Maine hydrodynamics: 2002–2011, *Deep Sea Research Part II: Topical Studies in Oceanography*, *103*, 210–222, 2014a.

Li, Y., R. Ji, P. S. Fratantoni, C. Chen, J. A. Hare, C. S. Davis, and R. C. Beardsley, Wind-induced interannual variability of sea level slope, along-shelf flow, and surface salinity on the Northwest Atlantic shelf, *Journal of Geophysical Research: Oceans*, *119*, 2462–2479, 2014b.

Liebmann, B., and C. A. Smith, Description of a Complete (Interpolated) Outgoing Longwave Radiation Dataset, *Bulletin of the American Meteorological Society*, *77*, 1275–1277, 1996.

Lin, H., and G. Brunet, The Influence of the Madden–Julian Oscillation on Canadian Wintertime Surface Air Temperature, *Monthly Weather Review*, *137*, 2250–2262, 2009.

Lin, H., G. Brunet, and J. Derome, An observed connection between the North Atlantic oscillation and the Madden-Julian oscillation, *Journal of Climate*, *22*, 364–380, 2009.

Lin, H., G. Brunet, and R. Mo, Impact of the Madden–Julian Oscillation on Wintertime Precipitation in Canada, *Monthly Weather Review*, *138*, 3822–3839, 2010.

Lin, H., K. R. Thompson, J. Huang, and M. Véronneau, Tilt of mean sea level along the Pacific coasts of North America and Japan, *Journal of Geophysical Research: Oceans*, *120*, 6815–6828, 2015.

Lin, H., J. Frederiksen, D. Straus, and C. Stan, Chapter 7 - Tropical-Extratropical Interactions and Teleconnections, in *Sub-Seasonal to Seasonal Prediction*, edited by A. W. Robertson and F. Vitart, pp. 143–164, Elsevier, 2019.

Loder, J. W., Topographic Rectification of Tidal Currents on the Sides of Georges Bank, *Journal of Physical Oceanography*, *10*, 1399–1416, 1980.

Lorenz, E. N., Deterministic Nonperiodic Flow, *Journal of the Atmospheric Sciences*, *20*, 130–141, 1963.

Lorenz, E. N., A study of the predictability of a 28-variable atmospheric model, *Tellus*, *17*, 321–333, 1965.

Lorenz, E. N., Climatic Predictability, in *The Physical Basis of Climate and Climate Modelling: Report of the International Study Conference in Stockholm, 29 July - 10 August 1974*, no. 16 in GARP Publications Series, pp. 132–136, 1975.

Lorenz, E. N., Atmospheric predictability experiments with a large numerical model, *Tellus*, *34*, 505–513, 1982.

Lyard, F., F. Lefevre, T. Letellier, and O. Francis, Modelling the global ocean tides: Modern insights from FES2004, *Ocean Dynamics*, *56*, 394–415, 2006.

Madden, R. A., and P. R. Julian, Detection of a 40–50 Day Oscillation in the Zonal Wind in the Tropical Pacific, *Journal of the Atmospheric Sciences*, *28*, 702–708, 1971.

Madden, R. A., and P. R. Julian, Description of Global-Scale Circulation Cells in the Tropics with a 40–50 Day Period, *Journal of the Atmospheric Sciences*, *29*, 1109–1123, 1972.

Madec, G., B.-B. Romain, B. Pierre-Antoine, B. Clément, B. Diego, C. Daley, C. Jérôme, C. Emanuela, A. Coward, D. Damiano, E. Christian, F. Simona, G. Tim, H. James, I. Doroteaciro, L. Dan, L. Claire, L. Tomas, M. Nicolas, M. Sébastien, M. Silvia, P. Julien, R. Clément, S. Dave, S. Andrea, and V. Martin, NEMO ocean engine version 3.6 stable, *Tech. Rep. 27*, Pôle de modélisation de l'Institut Pierre-Simon Laplace (IPSL), Paris, 2017.

Mandelbrot, B. B., *The Fractal Geometry of Nature*, W.H. Freeman and Company, 1982.

Mantua, N. J., and S. R. Hare, The Pacific Decadal Oscillation, *Journal of Oceanography*, *58*, 35–44, 2002.

Maraldi, C., J. Chanut, B. Levier, N. Ayoub, P. De Mey, G. Reffray, F. Lyard, S. Cailleau, M. Drévillon, E. A. Fanjul, M. G. Sotillo, P. Marsaleix, and the Mercator Research and Development Team, NEMO on the shelf: Assessment of the Iberia-Biscay-Ireland configuration, *Ocean Science*, *9*, 745–771, 2013.

Mardell, G. T., and R. D. Pingree, Half-wave rectification of tidal vorticity near headlands as determined from current meter measurements, *Oceanologica Acta*, *4*, 63–68, 1981.

Mariotti, A., P. M. Ruti, and M. Rixen, Progress in subseasonal to seasonal prediction through a joint weather and climate community effort, *npj Climate and Atmospheric Science*, *1*, 4, 2018.

Marshall, A. G., and H. H. Hendon, Impacts of the MJO in the Indian Ocean and on the Western Australian coast, *Climate Dynamics*, *42*, 579–595, 2014.

Marshall, A. G., H. H. Hendon, T. H. Durrant, and M. A. Hemer, Madden Julian Oscillation impacts on global ocean surface waves, *Ocean Modelling*, *96*, 136–147, 2015.

Matthews, A. J., B. J. Hoskins, and M. Masutani, The global response to tropical heating in the Madden-Julian oscillation during the northern winter, *Quarterly Journal of the Royal Meteorological Society*, *130*, 1991–2011, 2004.

Merryfield, W. J., J. Baehr, L. Batté, E. J. Becker, A. H. Butler, C. A. S. Coelho, G. Danabasoglu, P. A. Dirmeyer, F. J. Doblas-Reyes, D. I. V. Domeisen, L. Ferranti, T. Ilynia, A. Kumar, W. A. Müller, M. Rixen, A. W. Robertson, D. M. Smith, Y. Takaya, M. Tuma, F. Vitart, C. J. White, M. S. Alvarez, C. Ardilouze, H. Attard, C. Baggett, M. A. Balmaseda, A. F. Beraki, P. S. Bhattacharjee, R. Bilbao, F. M. de Andrade, M. J. DeFlorio, L. B. Díaz, M. A. Ehsan, G. Fragkoulidis, S. Grainger, B. W. Green, M. C. Hell, J. M. Infanti, K. Isensee, T. Kataoka, B. P. Kirtman, N. P. Klingaman, J.-Y. Lee, K. Mayer, R. McKay, J. V. Mecking, D. E. Miller, N. Neddermann, C. H. Justin Ng, A. Ossó, K. Pankatz, S. Peatman, K. Pegion, J. Perlwitz, G. C. Recalde-Coronel, A. Reintges, C. Renkl, B. Solaraju-Murali, A. Spring, C. Stan, Y. Q. Sun, C. R. Tozer, N. Vigaud, S. Woolnough, and S. Yeager, Current and Emerging Developments in Subseasonal to Decadal Prediction, *Bulletin of the American Meteorological Society*, *101*, E869–E896, 2020.

Mertz, G., and D. G. Wright, Interpretations of the JEBAR Term, *Journal of Physical Oceanography*, *22*, 301–305, 1992.

Miyakoda, K., T. Gordon, R. Caverly, W. Stern, J. Sirutis, and W. Bourke, Simulation of a Blocking Event in January 1977, *Monthly Weather Review*, *111*, 846–869, 1983.

Miyakoda, K., J. Sirutis, and J. Ploshay, One-Month Forecast Experiments—without Anomaly Boundary Forcings, *Monthly Weather Review*, *114*, 2363–2401, 1986.

Munk, W. H., On the wind-driven ocean circulation, *Journal of Meteorology*, *7*, 80–93, 1950.

Naimie, C. E., Georges Bank residual circulation during weak and strong stratification periods: Prognostic numerical model results, *Journal of Geophysical Research: Oceans*, *101*, 6469–6486, 1996.

Naimie, C. E., J. W. Loder, and D. R. Lynch, Seasonal variation of the three-dimensional residual circulation on Georges Bank, *Journal of Geophysical Research: Oceans*, *99*, 15967–15989, 1994.

National Geophysical Data Center, 2-minute Gridded Global Relief Data (ETOPO2) v2, 2006.

Navier, C. L. M. H., Sur le lois des mouvemens des fluides, en ayant égard à l'adhésion des molécules, *Annales de chimie et de physique*, *19*, 244–260, 1821.

Navier, M., Sur les lois du movement des fluides, *Mémoires de l'Académie (royale) des sciences de l'Institut (imperial) de France*, *6*, 389–440, 1827.

Neena, J. M., J. Y. Lee, D. Waliser, B. Wang, and X. Jiang, Predictability of the Madden-Julian oscillation in the Intraseasonal Variability Hindcast Experiment (ISVHE), *Journal of Climate*, *27*, 4531–4543, 2014.

Olbers, D., J. Willebrand, and C. Eden, *Ocean Dynamics*, Springer, 2012.

Oliver, E. C., S. J. Wotherspoon, M. A. Chamberlain, and N. J. Holbrook, Projected Tasman Sea extremes in sea surface temperature through the twenty-first century, *Journal of Climate*, *27*, 1980–1998, 2014.

Oliver, E. C. J., Multidecadal variations in the modulation of Alaska wintertime air temperature by the Madden–Julian Oscillation, *Theoretical and Applied Climatology*, *121*, 1–11, 2015.

Ophaug, V., K. Breili, and C. Gerlach, A comparative assessment of coastal mean dynamic topography in Norway by geodetic and ocean approaches, *Journal of Geophysical Research: Oceans*, *120*, 7807–7826, 2015.

Parker, B. B., The relative importance of the various nonlinear mechanisms in a wide range of tidal interactions (Review), in *Tidal Hydrodynamics*, edited by B. B. Parker, pp. 237–268, Wiley, 1991.

Pearson, C., and R. Snay, Introducing HTDP 3.1 to transform coordinates across time and spatial reference frames, *GPS Solutions*, *17*, 1–15, 2013.

Pedlosky, J., *Geophysical Fluid Dynamics*, second ed., Springer, 1987.

Peña, M., E. Kalnay, and M. Cai, Statistics of locally coupled ocean and atmosphere intraseasonal anomalies in Reanalysis and AMIP data, *Nonlinear Processes in Geophysics*, *10*, 245–251, 2003.

Petrie, B., Does the north Atlantic oscillation affect hydrographic properties on the Canadian Atlantic continental shelf?, *Atmosphere-Ocean*, *45*, 141–151, 2007.

Petrie, B. D., Current response at the shelf break to transient wind forcing, *Journal of Geophysical Research: Oceans*, *88*, 9567–9578, 1983.

Pettigrew, N. R., D. W. Townsend, H. Xue, J. P. Wallinga, P. J. Brickley, and R. D. Hetland, Observations of the Eastern Maine Coastal Current and its offshore extensions in 1994, *Journal of Geophysical Research: Oceans*, *103*, 30623–30639, 1998.

Pettigrew, N. R., J. H. Churchill, C. D. Janzen, L. J. Mangum, R. P. Signell, A. C. Thomas, D. W. Townsend, J. P. Wallinga, and H. Xue, The kinematic and hydrographic structure of the Gulf of Maine Coastal Current, *Deep Sea Research Part II: Topical Studies in Oceanography*, *52*, 2369–2391, 2005.

Pinardi, N., L. Cavaleri, G. Coppini, P. De Mey, C. Fratianni, J. Huthnance, P. F. J. Lermusiaux, A. Navarra, R. Preller, and S. Tibaldi, From weather to ocean predictions: An historical viewpoint, *Journal of Marine Research*, *75*, 103–159, 2017.

Pingree, R., D. Griffiths, and L. Maddock, Quarter diurnal shelf resonances and tidal bed stress in the English Channel, *Continental Shelf Research*, *3*, 267–289, 1984.

Pingree, R. D., and L. Maddock, Tidal eddies and coastal discharge, *Journal of the Marine Biological Association of the United Kingdom*, *57*, 869, 1977.

Pingree, R. D., and L. Maddock, The M_4 tide in the English Channel derived from a nonlinear model of the M_2 tide, *Deep-Sea Research*, *25*, 53–63, 1978.

Priestley, M. B., *Spectral Analysis and Time Series*, Probability and Mathematical Statistics, Academic Press, 1981.

Pugh, D., and P. Woodworth, *Sea-Level Science: Understanding Tides, Surges, Tsunamis and Mean Sea-Level Changes*, Cambridge University Press, 2014.

Reynolds, R. W., T. M. Smith, C. Liu, D. B. Chelton, K. S. Casey, and M. G. Schlax, Daily High-Resolution-Blended Analyses for Sea Surface Temperature, *Journal of Climate*, *20*, 5473–5496, 2007.

Richardson, L. F., *Weather Prediction by Numerical Process*, Cambridge University Press, 1922.

Riddle, E. E., M. B. Stoner, N. C. Johnson, M. L. L'Heureux, D. C. Collins, and S. B. Feldstein, The impact of the MJO on clusters of wintertime circulation anomalies over the North American region, *Climate Dynamics*, *40*, 1749–1766, 2013.

Robinson, I., Chapter 7: Tidally Induced Residual Flows, in *Physical Oceanography of Coastal and Shelf Seas*, edited by B. Johns, vol. 35 of *Elsevier Oceanographhy Series*, pp. 321–356, Elsevier, 1983.

Rodi, W., Examples of calculation methods for flow and mixing in stratified fluids, *Journal of Geophysical Research*, *92*, 5305, 1987.

Rutherford, K., and K. Fennel, Diagnosing transit times on the northwestern North Atlantic continental shelf, *Ocean Science*, *14*, 1207–1221, 2018.

Saha, S., et al., The NCEP Climate Forecast System Reanalysis, *Bulletin of the American Meteorological Society*, *91*, 1015–1058, 2010.

Saha, S., S. Moorthi, X. Wu, J. Wang, S. Nadiga, P. Tripp, D. Behringer, Y. T. Hou, H. Y. Chuang, M. Iredell, M. Ek, J. Meng, R. Yang, M. P. Mendez, H. Van Den Dool, Q. Zhang, W. Wang, M. Chen, and E. Becker, The NCEP climate forecast system version 2, *Journal of Climate*, *27*, 2185–2208, 2014.

Saji, N. H., B. N. Goswami, P. N. Vinayachandran, and T. Yamagata, A dipole mode in the tropical Indian Ocean, *Nature*, *401*, 360–363, 1999.

Saravanan, R., and P. Chang, Chapter 9 - Midlatitude Mesoscale Ocean-Atmosphere Interaction and Its Relevance to S2S Prediction, in *Sub-Seasonal to Seasonal Prediction*, edited by A. W. Robertson and F. Vitart, pp. 183–200, Elsevier, 2019.

Sardeshmukh, P. D., and B. J. Hoskins, The Generation of Global Rotational Flow by Steady Idealized Tropical Divergence, *Journal of the Atmospheric Sciences*, *45*, 1228–1251, 1988.

Sarkisyan, A. S., and V. F. Ivanov, The joint effect of baroclinicity and the bottom relief as an important factor in the sea current dynamics, *Atmosphere and Ocean Physics*, *7*, 116–124, 1971.

Schlesinger, M. E., N. Ramankutty, and N. Andronova, Temperature Oscillations in the North Atlantic, *Science*, *289*, 547–548, 2000.

Schwing, F. B., Subtidal response of the Scotian shelf bottom pressure field to meteorological forcing, *Atmosphere-Ocean*, *27*, 157–180, 1989.

Scott, J. T., and G. T. Csanady, Nearshore currents off Long Island, *Journal of Geophysical Research*, *81*, 5401–5409, 1976.

Seager, R., Y. Kushnir, M. Visbeck, N. Naik, J. Miller, G. Krahmann, and H. Cullen, Causes of Atlantic Ocean Climate Variability between 1958 and 1998, *Journal of Climate*, *13*, 2845–2862, 2000.

Semtner, A. J., Modeling Ocean Circulation, *Science*, *269*, 1379–1385, 1995.

Seo, K.-H., and H.-J. Lee, Mechanisms for a PNA-Like Teleconnection Pattern in Response to the MJO, *Journal of the Atmospheric Sciences*, *74*, 1767–1781, 2017.

Seo, K.-H., and S.-W. Son, The Global Atmospheric Circulation Response to Tropical Diabatic Heating Associated with the Madden–Julian Oscillation during Northern Winter, *Journal of the Atmospheric Sciences*, *69*, 79–96, 2012.

Seo, K.-H., H.-J. Lee, and D. M. W. Frierson, Unraveling the Teleconnection Mechanisms that Induce Wintertime Temperature Anomalies over the Northern Hemisphere Continents in Response to the MJO, *Journal of the Atmospheric Sciences*, *73*, 3557–3571, 2016.

Sharpies, J., J. H. Simpson, D. G. Aubrey, and C. T. Friedrichs, The Influence of the Springs-Neaps Cycle on the Position of Shelf Sea Fronts, in *Buoyancy Effects on Coastal and Estuarine Dynamics*, no. 53 in Coastal and Estuarine Studies, pp. 71–82, American Geophysical Union (AGU), 1996.

Shchepetkin, A. F., and J. C. McWilliams, The regional oceanic modeling system (ROMS): A split-explicit, free-surface, topography-following-coordinate oceanic model, *Ocean Modelling*, *9*, 347–404, 2005.

Sheng, J., and K. R. Thompson, A robust method for diagnosing regional shelf circulation from scattered density profiles, *Journal of Geophysical Research: Oceans*, *101*, 25647–25659, 1996.

Signell, R. P., and W. R. Geyer, Transient eddy formation around headlands, *Journal of Geophysical Research: Oceans*, *96*, 2561–2575, 1991.

Smith, P. C., The Mean and Seasonal Circulation off Southwest Nova Scotia, *Journal of Physical Oceanography*, *13*, 1034–1054, 1983.

Smith, P. C., and F. B. Schwing, Mean circulation and variability on the eastern Canadian continental shelf, *Continental Shelf Research*, *11*, 977–1012, 1991.

Somavilla Cabrillo, R., C. González-Pola, M. Ruiz-Villarreal, and A. Lavín Montero, Mixed layer depth (MLD) variability in the southern Bay of Biscay. Deepening of winter MLDs concurrent with generalized upper water warming trends?, *Ocean Dynamics*, *61*, 1215, 2011.

Speer, P. E., and D. G. Aubrey, A Study of Non-linear Tidal Propagation in Shallow Inlet/Estuarine Systems Part II: Theory, *Estuarine, Coastal and Shelf Science*, *12*, 207–224, 1985.

Speer, P. E., D. G. Aubrey, and C. T. Friedrichs, Nonlinear hydrodynamics in shallow tidal inlet/bay systems, in *Tidal Hydrodynamics*, pp. 321–339, 1991.

Spiegel, E. A., and G. Veronis, On the Boussinesq Approximation for a Compressible Fluid., *The Astrophysical Journal*, *131*, 442, 1960.

Stan, C., D. M. Straus, J. S. Frederiksen, H. Lin, E. D. Maloney, and C. Schumacher, Review of Tropical-Extratropical Teleconnections on Intraseasonal Time Scales, *Reviews of Geophysics*, *55*, 902–937, 2018.

Stewart, R. W., The no-slip constraint and ocean models, *Atmosphere-Ocean*, *27*, 542–552, 1989.

Stokes, G. G., On the Steady Motion of Incompressible Fluids, *Transactions of the Cambridge Philosophical Society*, *7*, 439–453, 1848.

Stommel, H., The westward intensification of wind-driven ocean currents, *Transactions, American Geophysical Union*, *29*, 202, 1948.

Stommel, H., Varieties of Oceanographic Experience, *Science*, *139*, 572–576, 1963.

Subramanian, A. C., M. A. Balmaseda, L. Centurioni, R. Chattopadhyay, B. D. Cornuelle, C. DeMott, M. Flatau, Y. Fujii, D. Giglio, S. T. Gille, T. M. Hamill, H. Hendon, I. Hoteit, A. Kumar, J.-H. Lee, A. J. Lucas, A. Mahadevan, M. Matsueda, S. Nam, S. Paturi, S. G. Penny, A. Rydbeck, R. Sun, Y. Takaya, A. Tandon, R. E. Todd, F. Vitart, D. Yuan, and C. Zhang, Ocean Observations to Improve Our Understanding, Modeling, and Forecasting of Subseasonal-to-Seasonal Variability, *Frontiers in Marine Science*, *6*, 2019.

Sverdrup, H. U., Wind-Driven Currents in a Baroclinic Ocean; with Application to the Equatorial Currents of the Eastern Pacific, *Proceedings of the National Academy of Sciences*, *33*, 318–326, 1947.

Tee, K. T., Tide-induced residual current, a 2-D nonlinear numerical tidal model, *Journal of Marine Research*, *34*, 603–628, 1976.

Tee, K. T., Tide-Induced Residual Current—Verification of a Numerical Model, *Journal of Physical Oceanography*, *7*, 396–402, 1977.

Tee, K.-T., P. C. Smith, and D. Lefaivre, Estimation and Verification of Tidally Induced Residual Currents, *Journal of Physical Oceanography*, *18*, 1415–1434, 1988.

Tee, K. T., P. C. Smith, and D. Lefaivre, Topographic Upwelling off Southwest Nova Scotia, *Journal of Physical Oceanography*, *23*, 1703–1726, 1993.

Thompson, K. R., North Atlantic sea-level and circulation, *Geophysical Journal International*, *87*, 15–32, 1986.

Thompson, K. R., and J. Sheng, Subtidal circulation on the Scotian Shelf: Assessing the hindcast skill of a linear, barotropic model, *Journal of Geophysical Research: Oceans*, *102*, 24987–25003, 1997.

Thompson, P. R., and G. T. Mitchum, Coherent sea level variability on the North Atlantic western boundary, *Journal of Geophysical Research: Oceans*, *119*, 5676–5689, 2014.

Towe, R., E. Eastoe, J. Tawn, and P. Jonathan, Statistical downscaling for future extreme wave heights in the North Sea, *The Annals of Applied Statistics*, *11*, 2375–2403, 2017.

Umlauf, L., and H. Burchard, A generic length-scale equation for geophysical turbulence models, *Journal of Marine Research*, *61*, 235–265, 2003.

Umlauf, L., and H. Burchard, Second-order turbulence closure models for geophysical boundary layers. A review of recent work, *Continental Shelf Research*, *25*, 795–827, 2005.

Vallis, G. K., *Atmospheric and Oceanic Fluid Dynamics: Fundamentals and Large-Scale Circulation*, second ed., Cambridge University Press, 2017.

Vanhatalo, J., A. J. Hobday, L. R. Little, and C. M. Spillman, Downscaling and extrapolating dynamic seasonal marine forecasts for coastal ocean users, *Ocean Modelling*, *100*, 20–30, 2016.

Vecchi, G. A., and N. A. Bond, The Madden-Julian Oscillation (MJO) and northern high latitude wintertime surface air temperatures, *Geophysical Research Letters*, *31*, 2004.

Véronneau, M., and J. Huang, The Canadian Geodetic Vertical Datum of 2013 (CGVD2013), *GEOMATICA*, *70*, 9–19, 2016.

Visbeck, M., E. P. Chassignet, R. G. Curry, T. L. Delworth, R. R. Dickson, and G. Krahmann, The Ocean's Response to North Atlantic Oscillation Variability, in *The North Atlantic Oscillation: Climatic Significance and Environmental Impact*, edited by J. W. Hurrell, Y. Kushnir, G. Ottersen, and M. Visbeck, vol. 134 of *Geophysical Monograph Series*, pp. 113–145, American Geophysical Union (AGU), 2003.

Vitart, F., Evolution of ECMWF sub-seasonal forecast skill scores, *Quarterly Journal of the Royal Meteorological Society*, *140*, 1889–1899, 2014.

Vitart, F., Madden-Julian Oscillation prediction and teleconnections in the S2S database, *Quarterly Journal of the Royal Meteorological Society*, *143*, 2210–2220, 2017.

Vitart, F., and A. W. Robertson, Chapter 1 - Introduction: Why Sub-seasonal to Seasonal Prediction (S2S)?, in *Sub-Seasonal to Seasonal Prediction*, edited by A. W. Robertson and F. Vitart, pp. 3–15, Elsevier, 2019.

Vitart, F., C. Ardilouze, A. Bonet, A. Brookshaw, M. Chen, C. Codorean, M. Déqué, L. Ferranti, E. Fucile, M. Fuentes, H. Hendon, J. Hodgson, H.-S. Kang, A. Kumar, H. Lin, G. Liu, X. Liu, P. Malguzzi, I. Mallas, M. Manoussakis, D. Mastrangelo, C. MacLachlan, P. McLean, A. Minami, R. Mladek, T. Nakazawa, S. Najm, Y. Nie, M. Rixen, A. W. Robertson, P. Ruti, C. Sun, Y. Takaya, M. Tolstykh, F. Venuti, D. Waliser, S. Woolnough, T. Wu, D.-J. Won, H. Xiao, R. Zaripov, and L. Zhang, The Subseasonal to Seasonal (S2S) Prediction Project Database, *Bulletin of the American Meteorological Society*, *98*, 163–173, 2017.

Von Neumann, J., Some Remarks on the Problem of Forecasting Climatic Fluctuations, in *Dynamics of Climate: The Proceedings of a Conference on the Application of Numerical Integration Techniques to the Problem of the General Circulation Held October 26–28, 1955*, edited by R. L. Pfeffer, pp. 9–11, Pergamon, 1960.

Waliser, D., Predictability and forecasting, in *Intraseasonal Variability in the Atmosphere-Ocean Climate System*, edited by K. M. Lau and D. E. Waliser, pp. 389–423, Springer, 2005.

Wallace, J. M., and D. S. Gutzler, Teleconnections in the Geopotential Height Field during the Northern Hemisphere Winter, *Monthly Weather Review*, *109*, 784–812, 1981.

Weatherall, P., K. M. Marks, M. Jakobsson, T. Schmitt, S. Tani, J. E. Arndt, M. Rovere, D. Chayes, V. Ferrini, and R. Wigley, A new digital bathymetric model of the world's oceans, *Earth and Space Science*, *2*, 331–345, 2015.

Werner, F. E., and B. M. Hickey, The Role of a Longshore Pressure Gradient in Pacific Northwest Coastal Dynamics, *Journal of Physical Oceanography*, *13*, 395–410, 1983.

Wheeler, M. C., and H. H. Hendon, An All-Season Real-Time Multivariate MJO Index: Development of an Index for Monitoring and Prediction, *Monthly Weather Review*, *132*, 1917–1932, 2004.

White, C. J., H. Carlsen, A. W. Robertson, R. J. Klein, J. K. Lazo, A. Kumar, F. Vitart, E. Coughlan de Perez, A. J. Ray, V. Murray, S. Bharwani, D. MacLeod, R. James, L. Fleming, A. P. Morse, B. Eggen, R. Graham, E. Kjellström, E. Becker, K. V. Pegion, N. J. Holbrook, D. McEvoy, M. Depledge, S. Perkins-Kirkpatrick, T. J. Brown, R. Street, L. Jones, T. A. Remenyi, I. Hodgson-Johnston, C. Buontempo, R. Lamb, H. Meinke, B. Arheimer, and S. E. Zebiak, Potential applications of subseasonal-to-seasonal (S2S) predictions, *Meteorological Applications*, *24*, 315–325, 2017.

Wilks, D. S., *Statistical Methods in the Atmospheric Sciences*, Academic Press, 2011.

Woodworth, P. L., C. W. Hughes, R. J. Bingham, and T. Gruber, Towards worldwide height system unification using ocean information, *Journal of Geodetic Science*, *2*, 302–318, 2012.

Woodworth, P. L., M. Gravelle, M. Marcos, G. Wöppelmann, and C. W. Hughes, The status of measurement of the Mediterranean mean dynamic topography by geodetic techniques, *Journal of Geodesy*, *89*, 811–827, 2015.

Woollings, T., C. Franzke, D. L. R. Hodson, B. Dong, E. A. Barnes, C. C. Raible, and J. G. Pinto, Contrasting interannual and multidecadal NAO variability, *Climate Dynamics*, *45*, 539–556, 2015.

Woolnough, S. J., Chapter 5 - The Madden-Julian Oscillation, in *Sub-Seasonal to Seasonal Prediction*, edited by A. W. Robertson and F. Vitart, pp. 93–117, Elsevier, 2019.

World Meteorological Organization, Manual on the Global Data-processing and Forecasting System: Annex IV to the WMO Technical Regulations, *Tech. Rep. WMO-No. 485*, World Meteorological Organization, Geneva, 2018.

Wu, Y., J. Chaffey, D. A. Greenberg, K. Colbo, and P. C. Smith, Tidally-induced sediment transport patterns in the upper Bay of Fundy: A numerical study, *Continental Shelf Research*, *31*, 2041–2053, 2011.

Xu, F.-H., and L.-Y. Oey, The Origin of Along-Shelf Pressure Gradient in the Middle Atlantic Bight, *Journal of Physical Oceanography*, *41*, 1720–1740, 2011.

Yu, L., Sea Surface Exchanges of Momentum, Heat, and Fresh Water Determined by Satellite Remote Sensing, in *Encyclopedia of Ocean Sciences (Second Edition)*, edited by J. H. Steele, pp. 202–211, Academic Press, 2009.

Yu, L., and R. A. Weller, Objectively Analyzed Air–Sea Heat Fluxes for the Global Ice-Free Oceans (1981–2005), *Bulletin of the American Meteorological Society*, *88*, 527–540, 2007.

Yuan, X., M. R. Kaplan, and M. A. Cane, The Interconnected Global Climate System—A Review of Tropical-Polar Teleconnections, *Journal of Climate*, *31*, 5765–5792, 2018.

Zhang, C., Madden-julian oscillation: Bridging weather and climate, *Bulletin of the American Meteorological Society*, *94*, 1849–1870, 2013.

Zhang, C., and M. Dong, Seasonality in the Madden-Julian oscillation, *Journal of Climate*, *17*, 3169–3180, 2004.

Zhang, Y., W. B. Rossow, A. A. Lacis, V. Oinas, and M. I. Mishchenko, Calculation of radiative fluxes from the surface to top of atmosphere based on ISCCP and other global data sets: Refinements of the radiative transfer model and the input data, *Journal of Geophysical Research: Atmospheres*, *109*, 2004.

Zhou, S., M. L'Heureux, S. Weaver, and A. Kumar, A composite study of the MJO influence on the surface air temperature and precipitation over the Continental United States, *Climate Dynamics*, *38*, 1459–1471, 2012.